

edited by

**Marco Anni**

**Sandro Lattante**

# Organic Lasers

**Fundamentals, Developments,  
and Applications**



A grayscale abstract background featuring a central glowing lens element that emits radial light rays, creating a starburst effect. The background has a subtle, organic, undulating texture.

# Organic Lasers



Taylor & Francis  
Taylor & Francis Group  
<http://taylorandfrancis.com>

# **Organic Lasers**

## **Fundamentals, Developments, and Applications**

edited by  
**Marco Anni**  
**Sandro Lattante**

*Published by*

Pan Stanford Publishing Pte. Ltd.  
Penthouse Level, Suntec Tower 3  
8 Temasek Boulevard  
Singapore 038988

Email: [editorial@panstanford.com](mailto:editorial@panstanford.com)  
Web: [www.panstanford.com](http://www.panstanford.com)

**British Library Cataloguing-in-Publication Data**

A catalogue record for this book is available from the British Library.

**Organic Lasers: Fundamentals, Developments, and Applications**

Copyright © 2018 Pan Stanford Publishing Pte. Ltd.

*All rights reserved. This book, or parts thereof, may not be reproduced in any form or by any means, electronic or mechanical, including photocopying, recording or any information storage and retrieval system now known or to be invented, without written permission from the publisher.*

For photocopying of material in this volume, please pay a copying fee through the Copyright Clearance Center, Inc., 222 Rosewood Drive, Danvers, MA 01923, USA. In this case permission to photocopy is not required from the publisher.

ISBN 978-981-4774-46-8 (Hardcover)  
ISBN 978-1-315-10233-7 (eBook)

We dedicate this book to our beloved families:  
thank you for your strong and affectionate  
support in every day of our life.

We also dedicate this book to the people  
who contributed to the growth of our love for  
science and physics and to the development of  
the physics community of Università del Salento,  
especially to Prof. Mario Leo and to the memory  
of Prof. Raimondo Anni and Prof. Giulio Soliani,  
whose teaching and messages are  
a continuous guide for us.



Taylor & Francis  
Taylor & Francis Group  
<http://taylorandfrancis.com>

# Contents

<i>Preface</i>	xiii
<b>1 Basic Concepts of Stimulated Emission and Lasing in Organic Materials</b>	<b>1</b>
<i>Sandro Lattante</i>	
1.1 Introduction	1
1.2 Electronic Structure	3
1.2.1 Energetic Levels	3
1.2.2 Primary Excitations	4
1.2.3 Electronic Transitions and Relaxation Processes	5
1.3 Stimulated Emission and Line Narrowing	7
1.4 Optical Gain Measurement: Experimental Setup	11
1.5 A More Detailed Analysis of the VSL Method	12
1.6 Two Key Parameters: The Threshold Length and the Saturation Length	15
1.7 Effects of Waveguiding in the VSL Method	18
1.8 Conclusion	19
<b>2 Physics Behind Amplified Spontaneous Emission in Organic Active Waveguides</b>	<b>23</b>
<i>Marco Anni</i>	
2.1 Introduction	23
2.2 Waveguide Operation	25
2.2.1 Ray Optics	25
2.2.2 Wave Optics	30
2.3 Understanding the Intrinsic Gain Properties of an Active Material by ASE Measurements	35

2.4	Gain Cross Section and ASE Threshold: The Case of Poly(9,9-dioctylfluorene)	36
2.5	ASE Dependence on the Waveguide Thickness	44
2.5.1	ASE Thickness Dependence in Diluted Polystyrene Matrix	46
2.5.2	ASE Thickness Dependence in Poly(9,9-dioctylfluorene) Neat Films	49
2.6	ASE Dependence on the Molecule Alignment	59
2.7	ASE Dependence on the Film Morphology	61
2.7.1	Minimization of the Amplified Spontaneous Emission Threshold by Optimization of the Micromorphology	63
2.7.2	Unexpected Composition Dependence of the ASE Properties of Polymer:Polymer Blends—The Case of PF8:F8BT	72
<b>3</b>	<b>State-of-the-Art Active Materials for Organic Lasers</b>	<b>85</b>
<i>Luis Cerdán</i>		
3.1	Introduction	85
3.2	Dyes	88
3.2.1	Synthetic Molecules	89
3.2.1.1	BODIPYs	89
3.2.1.2	Perylenediimides	94
3.2.1.3	Xanthenes	97
3.2.1.4	Miscellanea	98
3.2.2	Biomolecules	98
3.3	Molecular Single Crystals	100
3.3.1	Oligomeric Compounds	102
3.3.2	Non-oligomeric Molecules	105
3.3.2.1	Excited-state intramolecular proton transfer	106
3.4	Molecular Glasses	108
3.4.1	Linear, Branched, and Spiro Compounds	110
3.4.2	Star-Shaped Oligomers	113
3.5	Conjugated Polymers	115
3.5.1	Homopolymers	116
3.5.2	Copolymers	118
3.6	Hybrid Compounds	122
3.7	Final Remarks	126

<b>4 Basic Physics and Recent Developments of Organic Random Lasers</b>	<b>151</b>
<i>Ilenia Viola, Luca Leuzzi, Claudio Conti, and Neda Ghofraniha</i>	
4.1 Introduction	151
4.2 Random Laser	152
4.2.1 Random-Laser Materials	155
4.2.2 Applications	157
4.3 Organic Semiconductor Materials in Random Lasers	158
4.4 Patterning Organic Compounds for Random Lasing	161
4.5 Thiophene-Based Compounds: Engineered Random Lasers and Replica Symmetry Breaking	164
4.5.1 Lithographed Random Lasers	164
4.5.2 Intensity Fluctuations in Random Lasers	170
4.6 Biocompatible and Biologically Inspired Random Lasers	174
<b>5 Cavity–Matter Interaction in Weak- and Strong-Coupling Regime: From White OLEDs to Organic Polariton Lasers</b>	<b>193</b>
<i>Marco Mazzeo, Fabrizio Mariano, Armando Genco, Claudia Triolo, and Salvatore Patanè</i>	
5.1 Light–Matter Coupling: Classical and Quantum Theory	195
5.1.1 A Classical Toy Model	195
5.1.2 Optical Resonators: The Case of Optical Microcavity	198
5.1.3 Cavity–Exciton Interaction in Weak-Coupling Regime	201
5.1.4 Quantum Description of Strong Coupling	203
5.1.5 Strong Coupling with Damping	209
5.2 Organic Light-Emitting Diodes: From Weak- to Strong-Coupling Regime	211
5.2.1 OLED in a Cavity	211
5.2.2 Weak-Coupling Interaction for Lighting Applications	213
5.2.3 Electroluminescence of Organic Microcavities in Strong-Coupling and USC Regimes	220
5.3 Toward Electrically Pumped Organic Lasers	228
5.3.1 Organic Laser under Weak-Coupling Regime	228

5.3.2	The Way of Polariton Laser	231
5.3.3	Electrical Polariton Lasers: A Brief Overlook in Inorganic World	237
<b>6</b>	<b>Vertical External-Cavity Organic Lasers: State of the Art and Application Perspectives</b>	<b>245</b>
	<i>Sébastien Chénais and Sébastien Forget</i>	
6.1	Introduction: Context and General Description of Vertical External-Cavity Surface-Emitting Organic Lasers	245
6.2	General Properties of VECOSOLs	249
6.2.1	Setup Description and Fabrication	249
6.2.2	Conversion Efficiency under Laser and Diode Pumping	249
6.2.3	Beam Quality and Brightness	251
6.2.4	Influence of the Cavity Length on Performance and Pulse Buildup Dynamics	254
6.2.5	Spectrum of VECOSOLs	258
6.2.6	Power Scaling and Photodegradation	260
6.2.7	Thermal Limitations	262
6.3	VECSOLs for Applications: Three Examples of Intracavity Laser Spectrum Engineering	264
6.3.1	VECSOLs as Tunable and High Beam Quality “Low-Cost” Lasers over the Visible Spectrum	264
6.3.2	VECSOLs as Ultrananow Linewidth Single-Mode Organic Lasers	271
6.3.3	VECSOLs as Deep-UV Lasers by Intracavity Nonlinear Optics	275
<b>7</b>	<b>Organic Lasers with Distributed Feedback: Threshold Minimization and LED Pumping</b>	<b>285</b>
	<i>Guy L. Whitworth and Graham A. Turnbull</i>	
7.1	Introduction	285
7.2	A Simple Model for Distributed Feedback	286
7.3	Coupled Mode Theory	288
7.3.1	First-Order Distributed Feedback	288
7.3.2	Second-Order Distributed Feedback	291
7.3.3	DFB Modal Structure	292

7.4	Experimental Characteristics	294
7.4.1	Spectral Characteristics	294
7.4.2	Second-Order Outcoupling Characteristics	295
7.5	Fabrication Techniques	298
7.5.1	Electron Beam Lithography	299
7.5.2	Holography	299
7.5.3	UV Nanoimprint Lithography	300
7.5.4	Solvent Imprint Lithography	302
7.5.5	Thermal Imprint Lithography	304
7.6	Minimizing DFB Lasing Threshold	304
7.6.1	Mixed-Order Gratings	305
7.6.2	Controlling Fourier Coefficients	306
7.6.3	Sub-structured Gratings	308
7.7	LED-Pumped Organic DFB Lasers	310
7.8	Conclusion	312
	<i>Index</i>	317



Taylor & Francis  
Taylor & Francis Group  
<http://taylorandfrancis.com>

## Preface

After the first demonstration of amplified spontaneous emission (ASE) and optically pumped lasing from thin films of conjugated polymers about 20 years ago, substantial attention has been given to the investigation of light amplification and lasing in organic molecules. This has resulted in important advances in all aspects related to laser realization, starting from active materials to the development of laser prototypes, including a lot of interesting research on their chemical and physical aspects. Many research groups have been active in the development of new molecules that show optical gain and have explored non-conductive dyes, semiconducting oligomers, dendrimers, and polymers, which has led to considerable extension of a number of potential active molecules for organic lasers, with special attention to several complementary aspects, such as high gain, wavelength tunability, and operational stability.

A lot of research has also been focused on the photophysics of the optical gain process, involving experiments being performed with several spectroscopic techniques, such as steady-state photoluminescence, ultrafast time-resolved photoluminescence, pump and probe, and photoluminescence measurements under strong pumping. This has allowed a deep understanding of the physical processes occurring between molecular excitation and the eventual spontaneous and stimulated emission.

Last but not the least, tremendous efforts have also been made to develop optical resonators with a large variety of explored geometries, which has resulted in the application of optically pumped organic lasers in microcavities, distributed feedback (DFB) lasers, external cavity lasers, whispering gallery mode microdisks, microrings and microspheres, and also scattering-assisted coherent random lasers.

All this has led to important demonstrations of the feasibility of optically pumped organic lasers by using many different active systems and resonators, with progressive optimization of the performances up to the one requested for applications to real devices. The actual values of the state-of-the-art lasing threshold and operational stability clearly demonstrate that an optically pumped organic laser can be effectively realized by combining low-cost nanofabrication techniques and cheap pumping source, fully maintaining the promises of low-cost and broadly tunable devices.

Even if the realization of an organic laser under electrical pump is still missing, and a debate still exists on the real possibility to reach this result, the amazing improvement in the performances of optically pumped organic lasers makes them extremely interesting for various applications. In particular, the lasing threshold of organic DFBs has been considerably reduced, recently allowing the demonstration of lasing from a polymeric DFB laser, pumped by a UV light-emitting diode. In this book, experts who have been doing research on organic materials for lasing applications have presented reviews of the recent advances in their research fields.

The book covers the basic aspects of the measurement techniques of optical gain and ASE in organic films as well as the photophysics of organic materials that can be understood using ASE measurements. It reviews the recent advances in the development of new active materials for organic lasers as well as the actual state of the art of scattering-assisted random lasers and of strongly coupled organic microcavities, both promising interesting developments in the near future. Finally, it gives a detailed review of the state of the art of the organic lasers actually closest to real applications, namely external cavity lasers and DFB lasers.

This book is the result of the work of many distinguished experts and colleagues who devoted their time and experience to write excellent state-of-the-art review chapters. We kindly acknowledge all of them for their valuable contribution.

**Marco Anni  
Sandro Lattante**  
Summer 2018

# Chapter 1

## Basic Concepts of Stimulated Emission and Lasing in Organic Materials

**Sandro Lattante**

*Dipartimento di Matematica e Fisica “Ennio De Giorgi”, Università del Salento,  
Via per Arnesano, 73100 Lecce, Italy*  
[sandro.lattante@unisalento.it](mailto:sandro.lattante@unisalento.it)

### 1.1 Introduction

Organic conjugated polymers and oligomers, since the discovery in 1977 of high conductivity in chemical-doped polyacetylene [1], have attracted lot of research interest in the last couple of decades due to their unique mechanical, optical, and electrical properties. Such properties depend on the molecular chemical structure and on the supra-molecular organization in solid state, making possible to obtain insulating, conducting, or semi-conducting behavior by properly modifying the chemical backbone consisting of alternating carbon single and double bonds that originate  $\pi$  and  $\pi^*$  molecular orbitals with various degree of electron delocalization. The typical energy gap of this class of materials is in the range near UV–near IR. Because of the large density of states associated with

---

*Organic Lasers: Fundamentals, Developments, and Applications*

Edited by Marco Anni and Sandro Lattante

Copyright © 2018 Pan Stanford Publishing Pte. Ltd.

ISBN 978-981-4774-46-8 (Hardcover), 978-1-315-10233-7 (eBook)

[www.panstanford.com](http://www.panstanford.com)

the  $\pi \rightarrow \pi^*$  transition, the absorption and thus the stimulated emission cross sections are very large. Moreover, the emission spectra of conjugated polymers are, in general, red shifted compared to the absorption spectra; thus, the auto-absorption is strongly reduced. These systems can be optically excited to obtain population inversion by pumping the  $\pi \rightarrow \pi^*$  transition, being the absorption process and the stimulated emission ones separated in energy due to the spectral shift mentioned above. Optical gain has been demonstrated in a large variety of organic compounds [2–10], so making these materials very interesting compounds as gain material for laser devices.

At the moment, a variety of organic optoelectronic devices have been demonstrated such as highly efficient organic light-emitting diodes (OLEDs) [11–13], solar cells [14, 15], field-effect transistors (FETs) [16–18], and optically pumped organic lasers in different cavity configurations [19–23]. However, it must be pointed out that, to date, an important organic optoelectronic device is still missing: the organic semiconductor laser diode (OSLD). OSLDs would possess a lot of advantages compared to their inorganic counterparts based on III-V family of semiconductor materials, like the possibility to integrate them on arbitrary and flexible substrates, the low cost devices fabrication, and the wide tuneability on the entire visible range by simple chemical processing. Moreover, basic research on this subject has influenced other research fields of technological importance: The development in defining and processing nano-imprinting and holography on organic layers and the subsequent demonstration of organic pumped lasing in nanodevices such as distributed Bragg reflector (DBR) and distributed feedback (DFB) have encouraged the same research on the inorganic laser processing and fabrication.

In this chapter, a brief description about the processes of stimulated emission and optical gain in organic compounds will be given, followed by a detailed description of the experimental technique broadly used in order to check the presence of optical gain in organic materials and to quantitatively measure its value.

## 1.2 Electronic Structure

Non-conductive organic polymers originate from the bonding of carbon atoms in  $sp^3$  hybrid configuration along the molecular chain. *Conjugated* polymers, instead, originate from the alternating bonding of carbon atoms in  $sp^2$  hybrid configuration, leaving two  $p_z$  atomic orbitals belonging to two adjacent carbons to originate a  $\pi$  molecular orbital: such compounds possess semiconducting properties due to the delocalization of  $\pi$  electrons along the chain structure. The energy gap between the two frontier orbitals, namely the highest occupied molecular orbital (HOMO) and the lowest unoccupied molecular orbital (LUMO) is in the near infrared–near ultraviolet range. Theoretical and semi-empirical calculations [24, 25] attributed the HOMO and LUMO to the  $\pi$  and  $\pi^*$  molecular orbitals.

### 1.2.1 Energetic Levels

A single molecule possesses energetic states corresponding to electronic, vibronic, rotational, and translational quantum states. Ground state of conjugated polymers consists of a completely filled  $\pi$  orbital (HOMO) (see Fig. 1.1).

Molecular excited states can be populated by an external perturbation that promotes an electron to a higher energetic level. The first excited state is the LUMO (see Fig. 1.1). Spin configuration can originate either a singlet or a triplet state (indicated by  $S_n$  or  $T_n$ , respectively, where  $n$  is an integer denoting the energy order). When the isolated molecules interact each other to form a crystal structure, the effects of the interactions have to be taken into account when describing the solid-state electronic structure; differently from inorganic crystals where strong covalent bond are formed, molecular crystal structures are generally characterized by dynamic dipole interactions of van der Waals type (with binding energy of the order of  $10^{-2}$  eV). Thus, it is possible to approximate the energetic level structure of such solid-state materials with the energetic level structure of the single molecule introducing second-order corrections that account for the molecular interaction. These corrections introduce energy-level splitting and energy gap

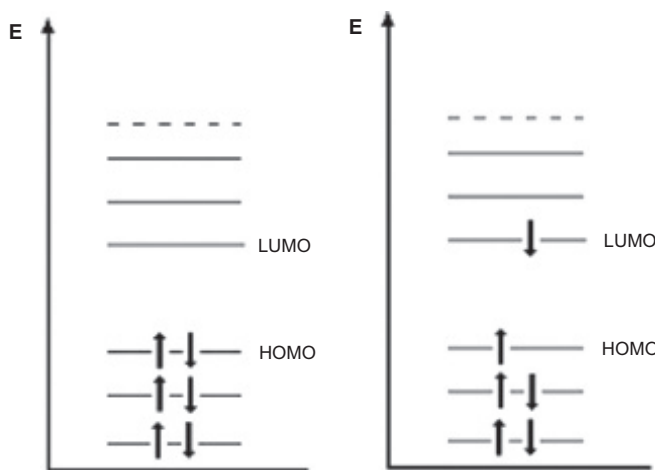


**Figure 1.1** Energetic ground state and first excited state of a conjugated polymer.

reduction due to the perturbation on the single molecule by neighbor molecules' potentials.

### 1.2.2 Primary Excitations

Excitons are the basis for the description of primary elementary excitation in semiconductor crystals. An exciton can be defined as an elementary excitation constituted by a hole into the ground state and an electron into an excited state, bound together by Coulomb interaction. Excitons can be delocalized on a great number of atomic or molecular units as in the case of strongly covalent bounded crystals (Wannier–Mott excitons) or localized on a small number of units or even on a single molecule (Frenkel excitons) as, for instance, in the case of organic disordered thin films. In the particular case of organic compounds, it is possible to distinguish different excited states, which are:

- *Neutral excited states*: are the Frenkel excitons, both singlets and triplets;
- *Aggregates*: macromolecular ensembles with a wavefunction delocalized on several units. They possess both ground

and excited states, thus being an intermolecular absorbing channel, usually at lower energy than the  $S_0 \rightarrow S_1$  transition due to the delocalization of wavefunctions;

- *Excimers or excited dimers:* They are dimers stable only in the excited state and constituted by an excitation formed on one molecule and, after a local variation of the molecular geometry, delocalized on a neighbor molecule. They cannot be optically excited because of the lack of a ground state; thus, direct self-absorption is not possible. Moreover, the excimer emission is typically at lower energy than the component molecules absorption;
- *Charge transfer excitons:* an intermediate case between the Frenkel exciton and the Wannier–Mott exciton, being the two charges forming the exciton delocalized on two different close molecules; usually they represent an intermediate state before the possible exciton dissociation into free charges.

### 1.2.3 Electronic Transitions and Relaxation Processes

Electronic transitions in organic solid compounds usually occur with a variation of both the electronic and the vibrational state. The most probable transitions can be singled out by the Franck–Condon rule (see Fig. 1.2 where the energy diagrams of two electronic states are depicted as a function of the inter-nuclear distance  $r$ , with respective vibrational energy levels), which states that the vibrational transition between two electronic states occurs vertically as the atomic nuclei distance has to remain unchanged during the short time duration of the electronic transition, and in such a way to involve the maxima of the wavefunctions.

Moreover, transitions follow the usual selection rules on parity (the transition can occur only between wavefunctions of different symmetry for spatial inversion) and spin (the transition, in the dipole approximation, occurs with no variation of the spin configuration). After the absorption of one photon, an electron is promoted to a vibrational level of the excited electronic state, following these rules; then it relaxes very fast (hundreds of femtoseconds) into the lowest vibrational state from which it relaxes radiatively

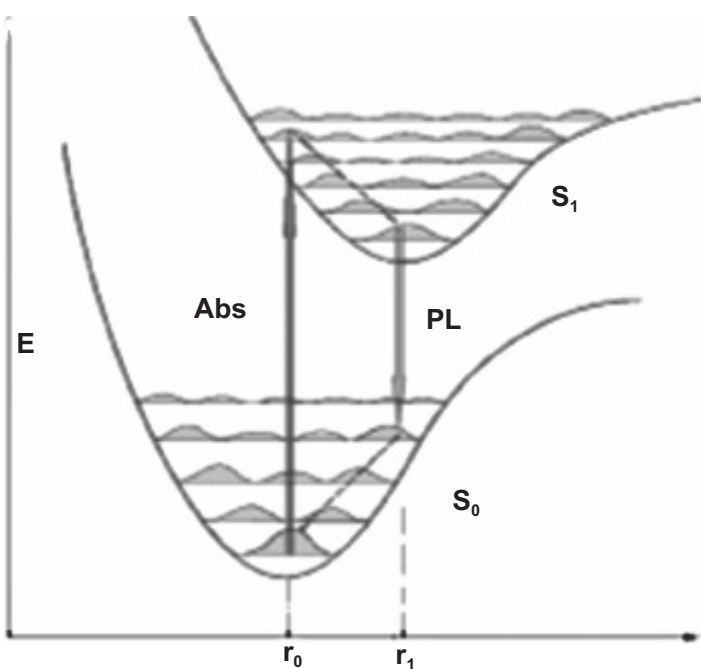


**Figure 1.2** Franck–Condon rule for electro-vibronic transitions on organic solid-state compounds.

(luminescence, PL in Fig. 1.2) or non-radiatively into a vibronic level of the ground state (in the range of nanoseconds). Finally, it quickly relaxes non-radiatively to the first vibronic level of the ground state. In the case of radiative relaxation, the consequence is a red-shifted emission to respect the absorption with a Stokes shift of the order of the eV. Thus, it is possible to consider this class of compounds as four level system emitters. Moreover, due to the Stokes shift, a very low auto-absorption affects these materials.

Figure 1.3 reports a simplified summary scheme of the electronic and vibronic processes in organic compounds, with radiative [fluorescence (Fl) and phosphorescence (Ph)] and non-radiative decay channels being included, in particular:

- *Internal conversion (IC)*: an intramolecular process; an electron migrates from a vibronic level that lies within an

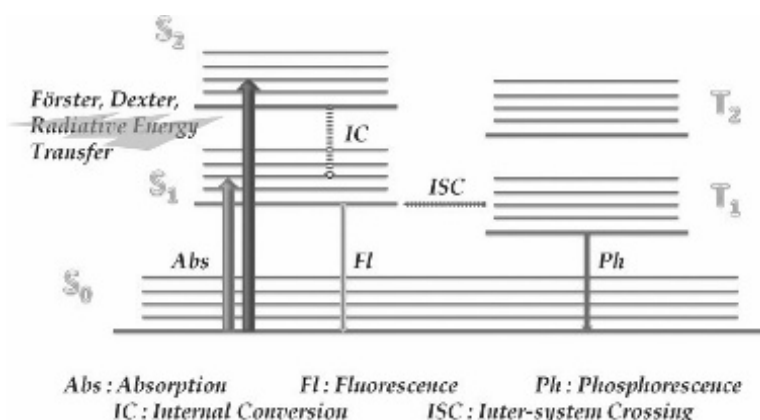


**Figure 1.3** Jablonsky diagram: different energetic exchange channels are depicted, both radiative and non-radiative (the different vibrational relaxations are not depicted for the sake of clarity).

electronic level to another vibronic level that lies within a different electronic level;

- **Intersystem crossing (ISC)**: excitation transfers from a singlet to a triplet state that overlaps in energy.

### 1.3 Stimulated Emission and Line Narrowing

In the previous section, a brief summary of absorption and spontaneous emission processes, and non-radiative decay channels, has been given. In this section, the stimulated emission properties of organic compounds will be briefly described. Let us consider a two-level system composed by the ground state  $|0\rangle$  and the excited state  $|1\rangle$ , and let us assume that after an absorption process, the system is in the excited state  $|1\rangle$ . A second photon interacting with the system can stimulate the excited electron to relax to its ground state with the subsequent emission of a second photon with the same phase, energy, and polarization state of the incident one. Various events of such type generate an output radiation that is coherent, monochromatic, and highly energetic. Being absorption, spontaneous and stimulated emission concomitant events in a real

system, the radiation intensity variation  $dI$  due to an interaction with a differential thickness  $dz$  of material, neglecting spontaneous emission, is

$$dI = \gamma I(n_1 - n_0)\hbar\omega dz \quad (1.1)$$

where  $\gamma$  is the Einstein absorption or stimulated emission rate coefficient,  $n_0$  and  $n_1$  are the  $|0\rangle$  and  $|1\rangle$  population, respectively, and  $\hbar\omega$  is the photon energy. At thermodynamic equilibrium,  $n_0 > n_1$  and the system mainly absorbs the radiation. On the contrary, if due to some pumping process, an inverted population  $n_1 > n_0$  has been created, the output intensity will be higher than the input one. It is easy to understand that such two-level system cannot amplify the radiation in continuous pumping situation because  $n_1$  can never become higher than  $n_0$  when increasing continuous pump intensity: when  $n_1$  becomes higher than  $n_0$ , the propagating radiation interacting with the system stimulates more transition from level 1 to level 0 than that from level 0 to level 1; thus  $(n_1 - n_0)$  decreases and the populations of the two levels tend to become equal. In order to have stimulated emission, it is then necessary to operate with a three- or a four-level system, being the latter more efficient due to the absence of initial population between the two intermediate energy levels (see Fig. 1.4).

As anticipated in the previous section, organic compounds constitute a natural efficient four-level system, being the non-radiative decay process (IC) between the respective high and low vibronic levels of the ground and excited electronic states very

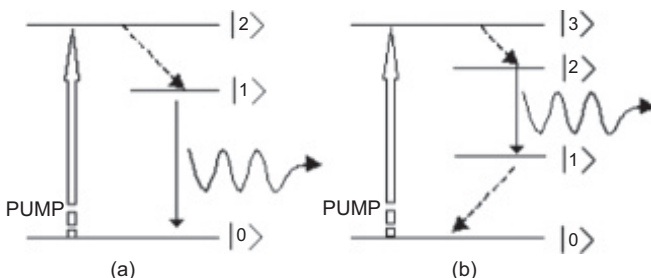


**Figure 1.4** Stimulated emission system: (a) three levels, (b) four levels. Dashed lines indicate fast non-radiative decay.

fast, on the femtoseconds order and the luminescence mean life time of the order of nanoseconds. The capacity of amplifying radiation is quantified by the optical gain coefficient of the material, defined as

$$g = \sigma(n_1 - n_0) \quad (1.2)$$

where  $\sigma$  is the gain cross section of the considered material. In a real system, the optical gain is reduced by several loss channels, quantified by the loss coefficient  $\alpha$ . It is possible to define a net optical gain given by

$$g' = g - \alpha \quad (1.3)$$

As  $\sigma$  is a function of the wavelength, also  $g$  is wavelength dependent. When the gain in the material compensates the losses, the threshold for amplifying radiation has been reached.

Three different physical processes can lead to light amplification, namely superradiance, superfluorescence, and amplified spontaneous emission. The first two processes are *cooperative* processes of spontaneous emission from an ensemble of dipoles and are characterized by a clear threshold. On the contrary, amplified spontaneous emission (ASE) is a *collective* effect: spontaneous emission stimulates further emission, resulting in light amplification if high enough optical gain is present [26]. An intense radiation is emitted in a solid angle around the active region axis without any need of a resonant cavity. ASE intensity depends on the geometry of the medium, besides its optical properties. The effect of ASE presence on the emission spectra as a function of excitation density is a line narrowing around the wavelength of maximum gain (see Fig. 1.5).

ASE process strictly is a threshold-less process, but it is usual to define as ASE threshold the excitation density value at which the spectrum full width at half maximum (FWHM) starts to decrease with the excitation density [27]. This convention allows to compare the gain properties of different classes of compounds. The mechanism of line narrowing in organic compounds was argument of debate some years ago, but now it is generally recognized that ASE is the most common amplifying process in organic thin slab

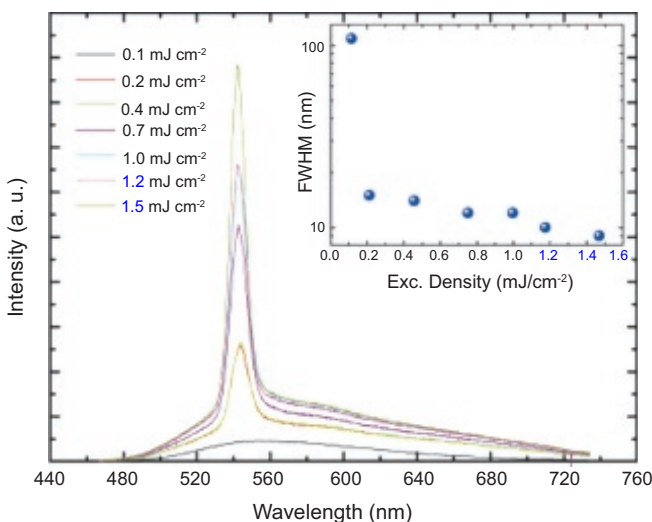


**Figure 1.5** Line-narrowing effect around the maximum gain wavelength on the emission spectra for increasing excitation density. Inset: FWHM as a function of excitation density.

waveguides [28–31] and can be used for the determination of optical gain.

Thus, in photonics, the term *gain* is used to quantify the amplification of optical amplifiers. Different meanings occur in literature:

- The gain can simply be an amplification factor, that is, the ratio of output power and input power.
- Particularly for small gains, the gain is often specified in percent, for example 3% refers to an amplification factor of 1.03.
- Particularly large gains are often specified in decibel (dB), that is, 10 times the logarithm (with base 10) of the amplification factor.
- Often a gain per unit length it is specified, more precisely the natural logarithm of the amplification factor per unit length.

## 1.4 Optical Gain Measurement: Experimental Setup

In traditional laser systems, the optical gain of active material is measured by coupling a probe radiation with the excited active region, then analyzing the difference between input and output probe light intensity due to the propagation of the radiation inside the material. However, it is difficult to apply this technique to structures whose active region is concentrated in a very thin layer. Moreover, typically the stimulated emission is so intense to make problematic the correct measurement of the probe intensity that is spectrally overlapped.

A common alternative technique to measure the optical gain spectrum avoiding the previous problems is based on the dependence of the emission spectra (in the presence of optical gain) on the excited region geometry. As it has been reported in [Section 1.3](#), ASE is the most frequent amplifying process. In this configuration, the differential variation of the radiation intensity  $I(\lambda)$  due to the interaction with a slab of active material with length  $dx$  is given by:

$$dI(\lambda) = [I(\lambda)g' + I_0(\lambda)]dx \quad (1.4)$$

where  $I_0$  is the spontaneous emission intensity per unitary length and  $g'$  is the net gain coefficient. If the excited region shape is a stripe with total length  $l$  (see [Fig. 1.6](#)), it is straightforward to demonstrate that the intensity of the light emitted from the sample edge is

$$I(\lambda, g', l) = \frac{I_0(\lambda)}{g'(\lambda)}(e^{g'(\lambda)l} - 1) \quad (1.5)$$

Thus, by measuring the emission spectra as a function of the excitation stripe length, it is possible to extract  $g'$  by fitting, for each wavelength, the experimental emission spectra intensity to [Eq. 1.5](#), thus obtaining the gain spectrum of the material [[32](#)]. This method is typically named the variable stripe length (VSL) method. The stripe-shaped excitation spot is obtained by means of a cylindrical lens, usually coupled with one or two spherical lenses in order to improve the focusing onto the sample, so that the stripe is characterized by a very low width in the range 100–200  $\mu\text{m}$ , and a typical length in the few millimeters range. The guided emitted radiation from

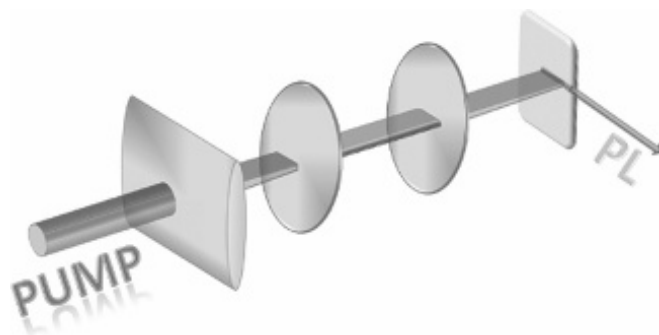


**Figure 1.6** Experimental excitation geometry for optical gain measurements.

the sample edge is collected by an optical system coupled with an optical fiber connected to a computer-controlled spectrometer. This arrangement is characterized by several parameters that can affect the results of the experiment: We will discuss this important point in details in the next sections.

## 1.5 A More Detailed Analysis of the VSL Method

The gain measurement method described in the previous section is clearly based on the so-called one-dimensional amplifier (rod) model, but it strictly works only if a number of simplifying hypotheses are assumed. For the one-dimensional rod amplifier of length  $l$  and section  $S$ , the spatial dependence of the intensity of the spontaneous emission can be described by the following equation [33]:

$$\frac{dI}{dx} = (\Gamma g - \alpha)I + (A_{sp} N^* h\nu)[\Omega(x)/4\pi]] \quad (1.6)$$

being  $g$  the gain,  $\Gamma$  the confinement factor of the waveguide,  $\alpha$  the optical loss coefficient,  $A_{sp}$  the spontaneous emission rate,  $N^*$  the density of the excited states,  $h\nu$  the emitted photon energy, and  $\Omega(x)$  the rod exit solid angle as seen from  $dx$  (see Fig. 1.7) [33].

Thus, the portion of the spontaneous emission that propagates along the axis of the one-dimensional rod is described by the

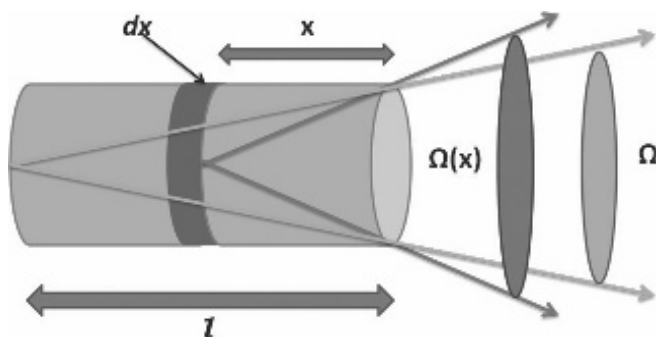


**Figure 1.7** Schematic of the one-dimensional rod amplifier model at the basis of Eq. 1.6.

factor  $\Omega(x)/4\pi$ . Equation 1.6 can be analytically integrated under a number of simplifying assumptions [33]:

- (1) The light collection efficiency is independent on the pumping length. That is to say considering  $\Omega$  as a constant independent on  $x$  and equal to  $S/l^2$ .
- (2) Both the gain coefficient and the pumping intensity are homogeneous all over the pumped region.

If these assumptions are taken into account, Eq. 1.5 is the solution to Eq. 1.6, where  $I_0 = (A_{sp} N^* h\nu)\Omega/4\pi$  is the intensity of the spontaneous emission (emitted within the angle  $\Omega$ ) and  $g' = \Gamma g - \alpha$  is the *net gain* (wavelength dependent). Thus, a measure of the intensity of the emitted radiation as a function of the variable stripe length  $l$  allows the calculation of the net gain  $g'$  by fitting the measured data with Eq. 1.5.

The above described hypotheses (1) and (2) are actually very *strong* hypotheses. Indeed the assumption of constant collection efficiency can be straightforwardly applied to an actual rod amplifier (for example rod-like optical fibers), but hardly applicable to a planar waveguide where the optical modes are not confined in the pumped region, but on the contrary spread in the waveguide plane [33]. Moreover, the light emitted from near the edge of the planar waveguide is actually characterized by a very large  $\Omega$  compared to the light that comes from the farther region of the illuminated stripe

(thus involving as an important parameter the acceptance angle of the collection system). Also the focal plane is different for different regions of the stripe (that is of the order of quite a few millimeters). Finally, an angle misalignment between the waveguide optical axis and the collection system optical axis (the two axes form an angle different from 0) can strongly influence the collection efficiency of the system.

The pump excitation intensity, moreover, cannot be considered actually constant nor homogeneous due to the nature of the laser radiation: The laser spot ideally has a Gaussian profile of the intensity. Even if the external region of the profile is cut from the mechanical slit in the optical gain measurement setup, still the profile cannot be considered constant in intensity. Furthermore, it should be considered that there is a diffraction effect from the mechanical slit edges [34] when the slit itself is far away from the sample surface, that is, the standard experimental situation with organic planar waveguide since they are usually measured under vacuum condition inside a vacuum chamber, in order to prevent degradation and photo-oxidation. The intensity of the pumping beam increases exponentially in the region where the diffraction effects are important [33]: since the optical gain depends on the pumping intensity, considering in the fit process with Eq. 1.5 the experimental VSL data corresponding to the stripe length where the diffraction effects are dominating can give erroneous values for the net optical gain.

At the same time, the assumptions of constant gain is easily not fulfilled, first of all due to inappropriate experimental setup or morphological inhomogeneities in the organic waveguide (macroscopic aggregates, thickness fluctuation, macroscopic phase separation in blends, etc.). Moreover, the process of stimulated emission itself can influence the temporal behavior of the gain coefficient. The depletion of the excited state population reduces the gain value (gain saturation) [33, 35]. This process is reflected in a non-exponential growth of the ASE intensity as the stripe length exceeds a certain value (the *ASE saturation length*), with the ASE intensity that tends toward a constant value as a function of increasing stripe length. In this saturation region, obviously the application of Eq. 1.5 would give as a result a net gain value strongly underestimated.

In order to overcome all the aforementioned drawbacks, Dal Negro and coworkers have proposed a more complex equation to be applied in the measurement of optical gain in planar waveguides [33]. They have generalized the simple one-dimensional rod model by adding to the original equation a number of spatial dependent coefficients, obtaining a new equation for the emitted light propagation as follows [33]:

$$\frac{dI}{dx} = [g(x)\xi(x) - \alpha]I + [\xi(x)A_{sp}N^*(x)hv] \cdot [\beta_1(x) + \beta_2(x)] \quad (1.7)$$

Here the Fresnel diffraction effect is taken into account by the term  $\xi(x)$  and both the gain  $g$  and the excited state population density  $N^*$  are dependent on the position  $x$ . The spatial dependence of the coupling between the wave-guided emission and the collection system as well as the Gaussian profile of the pumping laser beam are condensed in the two factors  $\beta_1$  and  $\beta_2$ . Although this equation cannot be solved analytically, a numeric integration for a least square fit to the measured data with the VSL technique gives by far more reliable results compared to the simple one-dimensional model. The choice of the precise analytical form of  $\xi$ ,  $\beta_1$ , and  $\beta_2$  strongly depends on the particular system under investigation.

## 1.6 Two Key Parameters: The Threshold Length and the Saturation Length

We have previously cited the ASE saturation length. Indeed the process of ASE is characterized by two key parameters, that are the *ASE threshold length* ( $L_{th}$ ) and the *ASE saturation length* ( $L_s$ ). The first indicate the minimum length of the pumping stripe for ASE to occur, and the second is the length of the stripe for which a saturation of the ASE intensity  $I_{ASE}$  occurs ( $I_{ASE}^s$ ). These two parameters define the lower and the upper bounds for the stripe length to be used in VSL measurements in order to have the most reliable data to be used in the fitting process described in the previous section. We have already given a definition of ASE threshold in [Section 1.3](#). Actually that is one possible definition: In fact, the specific literature is characterized by several ASE threshold

definitions, with actually a lack of agreement among different authors. Apart from the already given definition, some authors prefer to consider as ASE threshold the pumping energy density at which the slope of the emitted radiation intensity as a function of the pumping energy density starts to increase superlinearly [31, 36]. Other still use the FWHM as a criterion but consider the threshold to set in when the FWHM reaches half or  $1/e$  of the initial fluorescence spectrum FWHM [37, 38]. Another possible definition comes from considering as the ASE threshold the excitation density for which the intrinsic optical gain equals the optical losses, thus giving a net gain equal to 0 [39].

Peters and Allen [40] proposed that as threshold definition, one should consider the excitation density for which a photon spontaneously emitted at one end of the amplifier stimulate a second photon at the other end, thus giving the following expression for the  $L_{\text{th}}$ :

$$L_{\text{th}} = \frac{8\pi \Delta\nu \tau}{N^* \lambda^2 \phi} \quad (1.8)$$

where  $\Delta\nu$  is the fluorescence bandwidth,  $\tau$  is the fluorescence lifetime,  $N^*$  is the population inversion density,  $\lambda$  is the photon wavelength, and  $\phi$  is the fluorescence quantum yield [40]. Since  $N^*$  depends on the excitation density,  $L_{\text{th}}$  decreases as the excitation density increases.

Thus, it is clear that depending on the used criterion for establishing the ASE threshold, the value of  $L_{\text{th}}$  can also vary on a wide range for the same system.

The same uncertainties persist in the determination of  $L_s$  and the ASE saturation intensity  $I_{\text{ASE}}^s$ . These uncertainties are reflected in the values that different authors consider for determining the ASE saturation, taking into account the product between the net gain  $g'$  and  $L_s$ : This product can have values ranging from 4 to 10 [33, 39].

In order to eliminate the subjectivity in the determination of such parameters, Cerdán and coworkers proposed an analytical method to determine  $L_{\text{th}}$  and  $L_s$ , based on the experimental VSL data [41]. They started their analysis from the same one-dimensional amplifier model, basically rewriting Eq. 1.6 in order to include also the saturation effects as:

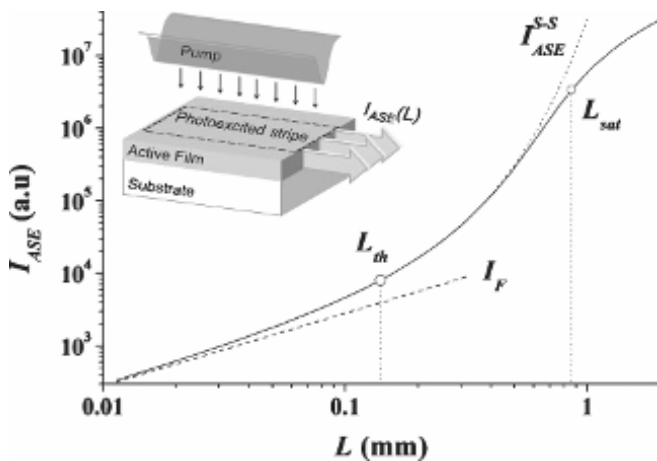


**Figure 1.8** ASE intensity versus stripe length. Reproduced from Ref. [41] with permission of the Optical Society of America.

By inserting the parameter  $I_{\text{ASE}}^{\text{S}}$ :

$$L = \frac{I_{\text{ASE}}(L)/I_s}{g' + \Omega/I_s} + \frac{g'}{(g' + \Omega/I_s)^2} \ln \left| \frac{\Omega + (g' + \Omega/I_s) I_{\text{ASE}}(L)}{\Omega} \right| \quad (1.9)$$

where  $I_{\text{ASE}}(L)$  is the ASE intensity at the length  $L$ ,  $I_s$  is a parameter accounting for saturation,  $\Omega$  is a fluorescence growing parameter, and  $g'$  is the net gain.

In the small-signal regime, far from saturation, their equation simply becomes Eq. 1.5. A summary of their results is reported in Fig. 1.8, where the  $I_{\text{ASE}}$  is plotted against the pumping stripe length.

It can be seen that up to a certain value of the stripe length, the intensity of the emitted light grows linearly with the stripe length itself (fluorescence emission). As soon the stripe length exceeds this value ( $L_{\text{th}}$ ), a super-linear behavior of the light intensity is detected, up to a stripe length for which the intensity tends toward a limit value (saturation,  $L_s$ ).

By using their modified model and reinterpreting Eq. 1.8, Cerdán and collaborators found that an objective criterion for the determination of  $L_{\text{th}}$  and  $L_s$  is given by

$$g' L_{\text{th}} \approx 1.256 \quad (1.10)$$

and

$$g' L_s \approx 1 + \ln \frac{g' I_{\text{ASE}}^s}{\Theta} \quad (1.11)$$

where  $\Theta$  is the fluorescence growing parameters that depend on  $\Gamma$ ,  $N^*$ ,  $\tau$ , and from the normalized fluorescence spectrum [41]. Thus, by determining  $g'$ ,  $I_{\text{ASE}}^s$  and  $\Theta$  from the fit of the VSL measured data with their model, the threshold length and the saturation length can be easily calculated from 1.10 and 1.11. Following in an iterative way, this procedure—that is, to recalculate each time the optical gain considering each time only the data comprised in the  $L_{\text{th}}$  and  $L_s$  calculated in the previous iteration—the optical gain can be calculated with the requested accuracy.

## 1.7 Effects of Waveguiding in the VSL Method

We have already cited how waveguiding effects on planar waveguides can affect the output of the VSL technique. Actually, if particular care is neglected in setting up the experimental conditions and instrumentations, false optical gain behavior can show up as demonstrated by Valenta and coworkers [42]. We have seen that a fundamental hypothesis for the VSL technique to be correctly applied on planar waveguides is the constant coupling of the sample emission to the detecting system, independent on the position of the pumping region on the sample. Valenta et al. checked the validity of this assumption using a slightly modified VSL arrangement setup [42], measuring the guided TE and TM modes output of a layer of Si nanocrystals. Apparently, both the TE and TM signals showed an exponential increase in the output intensity as the stripe length increased from 0 to 0.45 mm, giving unrealistic optical gain coefficient of about  $30 \text{ cm}^{-1}$  by fitting with Eq. 1.5 in this stripe length range. Thus, the assumption of constant output-detecting system coupling seems to be unrealistic. They checked this by implementing what they called the “shifting excitation spot” (SES) technique, where only a tiny rectangular region of the sample is excited while moving the excitation spot far from the sample edge. In these conditions, an exponential decrease in the output intensity is expected due to optical losses. Surprisingly, they detected, on the contrary, an *increase* in the output intensity as the spot was

moved far from the sample edge, up to a distance of about 0.5 mm (coherently with the previous findings on the VSL measurements). By comparing the VSL and SES findings, they concluded that the apparent optical gain in the sample for stripe lengths lower than a certain value is an artifact due to the non-constant coupling of the guided modes in the sample plane to the detection system. The important parameter that determines the accuracy of the constant coupling assumption was identified in the numerical aperture (NA) of the detection optic system: The higher the NA, the more realistic the VSL results. Thus, their suggestion was to perform the SES and the VSL measurements in the same condition on the same region of the sample: If the SES measurements show an initial increase in the guided signal while moving the spot far from the sample edge, then there is a problem in the output-detection coupling that should be taken into account in analyzing the VSL data.

Considering all these findings, the most reliable method for qualitatively and preliminarily determining if the particular sample is characterized by optical gain is to check if there is a switch between loss and gain as the excitation density increases (onset of ASE band) [33], using a reasonable stripe length  $l$ , since all the possible sources of false gain signal are independent from the excitation density.

## 1.8 Conclusion

In conclusion, many organic materials (lots of polymers and oligomers in particular) are very flexible systems that have demonstrated to be characterized by great optical gain properties, with stimulated emission bands that span the whole visible spectrum. The more diffused technique for measuring the gain coefficient is the planar waveguide VSL method, with all its corrections and variations. In order to avoid any mistake or inappropriate experimental conditions, as well as any improper use of the technique itself, one should ensure that a series of requirements are fulfilled: first of all the validity of the simplified hypothesis at the base of the VSL method itself should be carefully checked for the particular system (sample plus experimental conditions).

Then the sample itself should consist of a good planar waveguide, which means a homogeneous layer of the same thickness. The substrate itself should be as smooth as possible, thus avoiding losses and scattering due to a high roughness, as well as characterized by an index of refraction lower than that of the material to be characterized (for waveguiding). The excitation stripe should be well focused on the sample surface with a width much lower than its length in order to minimize the emission leakage from the side borders. Moreover, the intensity profile of the laser stripe should be as homogeneous as possible, selecting the central region of the Gaussian-shaped original laser spot. The laser source itself should be chosen according to the absorption spectrum of the particular material under investigation, using pulsed laser sources due to the high excitation density required in the VSL measurements, hard to obtain using a cw laser. However, the laser pulse should be characterized by a duration higher than the emission lifetime of the material (typically of a few nanoseconds), thus operating in a quasi-cw conditions, together with a low operation rate to avoid sample damage (usually the 10 Hz region is the optimum). Finally, one should conveniently protect the sample from photodegradation that typically affects organic materials, thus operating in a proper vacuum chamber.

## References

1. Chiang, C. K., Fincher, C. R., Park, Y. W., Heeger, A. J., Shirakawa, H., Louis, E. J., Gua, S. C., and MacDiarmid, A. G. (1977). *Phys. Rev. Lett.* **39**, p. 1098.
2. Anni, M., Gigli, G., Zavelani-Rossi, M., Gadermaier, C., Lanzani, G., Barbarella, G., Favaretto, L., and Cingolani, R. (2001). *Appl. Phys. Lett.* **78**, p. 2679.
3. Brouwer, H. J., Krasnikov, V. V., Pham, T. A., Gill, R. E., and Hadzioannou, G. (1998). *Appl. Phys. Lett.* **73**, p. 708.
4. Graupner, W., Leising, G., Lanzani, G., Nisoli, M., Silvestri, S. D., and Scherf, U. (1996). *Phys. Rev. Lett.* **76**, p. 847.
5. Hassan, M. U., Liu, Y.-C., Butt, H., Hasan, K. U., Chang, J.-F., Olawoyin, A. A., and Friend, R. H. (2016). *J. Pol. Sci. B Pol. Phys.* **54**, pp. 15–21.
6. Heliotis, G., Bradley, D. C., Turnbull, G. A., and Samuel, I. D. W. (2002). *Appl. Phys. Lett.* **81**, p. 3534.

7. Hide, F., Garcia, M. D., Schwartz, B. J., Andersson, M. R., Qibing, P., and Heeger, A. J. (1996). *Science* **273**, p. 1833.
8. Kazlauskas, K., Kreiza, G., Bobrovas, O., Adoméniené, O., Adoménas, P., Jankauskas, V., and Jursnas, S. (2015). *Appl. Phys. Lett.* **107**.
9. Sang, M., Cao, S., Yi, J., Huang, J., Lai, W.-Y., and Huang, W. (2016). *RSC Adv.* **6**, pp. 6266–6275.
10. Stagira, S., Nisoli, M., Cerullo, G., Zavelani-Rossi, M., Silvestri, S. D., Lanzani, G., Graupner, W., and Leising, G. (1998). *Chem. Phys. Lett.* **289**, p. 205.
11. Feng, X. J., Peng, J., Xu, Z., Fang, R., Zhang, H., Xu, X., Li, L., Gao, J., and Wong, M. S. (2015). *ACS App. Mater. Interf.* **7**, pp. 28156–28165.
12. Sun, D., Zhou, X., Liu, J., Sun, X., Li, H., Ren, Z., Ma, D., Bryce, M. R., and Yan, S. (2015). *ACS Appl. Mater. Interf.* **7**, pp. 27989–27998.
13. Zhang, M., Hofle, S., Czolk, J., Mertens, A., and Colsmann, A. (2015). *Nanoscale* **7**, pp. 20009–20014.
14. Jung, J. W., Jo, J. W., Jung, E. H., and Jo, W. H. (2016). *Organic Electronics* **31**, pp. 149–170.
15. Mehmood, U., Al-Ahmed, A., and Hussein, I. A. (2016). *Renew. Sustainable Energy Rev.* **57**, pp. 550–561.
16. Chiu, C.-Y., Wang, H., Phan, H., Shiratori, K., Nguyen, T.-Q., and Hawker, C. J. (2016). *J. Pol. Sci. A Pol. Chem.* **54**, pp. 889–899.
17. Han, S., Zhuang, X., Shi, W., Yang, X., Li, L., and Yu, J. (2016). *Sensor. Actuat. B Chem.* **225**, pp. 10–15.
18. Wang, H., Zhu, Y., Liu, Z., Zhang, L., Chen, J., and Cao, Y. (2016). *Org. Electronics* **31**, pp. 1–10.
19. Anni, M., Lattante, S., Gigli, G., Barbarella, G., Favaretto, L., and Cingolani, R. (2003). *Appl. Phys. Lett.* **83**, p. 2754.
20. Berggren, M., Dodabalapur, A., Slusher, R. E., Timko, A., and Nalamasu, O. (1997). *Appl. Phys. Lett.* **72**, p. 410.
21. Foucher, C., Guilhabert, B., Kanibolotsky, A. L., Skabara, P. J., Laurand, N., and Dawson, M. D. (2016). *Opt. Express* **24**, pp. 2273–2280.
22. Goldenberg, L. M., Lisinetskii, V., and Schrader, S. (2015). *Appl. Phys. B* **120**, pp. 271–277.
23. Rogers, J. A., Meier, M., and Dodabalapur, A. (1998). *Appl. Phys. Lett.* **73**, p. 1766.
24. Bredas, J. L., Elsemrauer, R. L., Chance, R. R., and Silbey, R. (1983). *J. Chem. Phys.* **78**, p. 5656.

25. Champagne, B., Mosley, D. H., and Anré, J. M. (1994). *J. Chem. Phys.* **100**, p. 2034.
26. Frolov, S. V., Gellermann, W., Ozaki, M., Yoshino, K., and Vardeny, Z. V. (1997). *Phys. Rev. Lett.* **78**, p. 729.
27. Azuma, H., Kobayashi, T., Shim, Y., Mamedov, N., and Naito, H. (2007). *Org. Electron.* **8**, pp. 184–188.
28. Brouwer, H. J., Krasnikov, V. V., Hilberer, A., and Hadzioannou, G. (1996). *Adv. Mater.* **8**, p. 935.
29. Denton, G. J., Tessler, N., Stevens, M. A., and Friend, R. H. (1997). *Adv. Mater.* **9**, p. 547.
30. Frolov, S. V., Vardeny, Z. V., Yoshino, K., Zakhidov, A., and Baughman, R. H. (1999). *Phys. Rev. B* **59**, p. R5284.
31. McGehee, M. D., Gupta, R., Veenstra, S., Miller, E. K., Díaz-García, M. A., and Heeger, A. J. (1998). *Phys. Rev. B* **58**, pp. 7035–7039.
32. Shaklee, K. L., Nahory, R. E., and Leheny, R. F. (1973). *J. Luminescence* **7**, pp. 284–309.
33. Dal Negro, L., Bettotti, P., Cazzanelli, M., Pacifici, D., and Pavesi, L. (2004). *Opt. Comm.* **229**, pp. 337–348.
34. Born, M. and Wolf, E. (1999). *Principles of Optics* (Cambridge University Press).
35. Milonni, P. W. and Eberly, J. H. (1988). *Lasers* (John Wiley and Sons).
36. Yamashita, K., Kuro, T., Oe, K., and Yanagi, H. (2006). *Appl. Phys. Lett.* **88**, p. 241110.
37. Holzer, W., Penzkofer, A., Schmitt, T., Hartmann, A., Bader, C., Tillmann, H., Raabe, D., Stockmann, R., and Hörrhold, H. H. (2001). *Opt. Quantum Electron.* **33**, pp. 121–150.
38. Lahoz, F., Oton, C. J., Capuj, N., Ferrer-González, M., Cheylan, S., and Navarro-Urrios, D. (2009). *Opt. Express* **17**, pp. 16766–16775.
39. Cerdán, L., Costela, A., García-Moreno, I., García, O., and Sastre, R. (2009). *Appl. Phys. B* **97**, pp. 73–83.
40. Peters, G. I. and Allen, L. (1971). *J. Phys. A* **4**, pp. 238–243.
41. Cerdán, L., Costela, A., and García-Moreno, I. (2010). *J. Opt. Soc. Am. B* **27**, pp. 1874–1877.
42. Valenta, J., Pelant, I., and Linnros, J. (2002). *Appl. Phys. Lett.* **81**, pp. 1396–1398.

## Chapter 2

# Physics Behind Amplified Spontaneous Emission in Organic Active Waveguides

**Marco Anni**

*Dipartimento di Matematica e Fisica “Ennio De Giorgi”, Università del Salento,  
Via per Arnesano, 73100 Lecce, Italy  
[marco.anni@unisalento.it](mailto:marco.anni@unisalento.it)*

### 2.1 Introduction

The characterization of the amplified spontaneous emission (ASE) properties of an organic thin film exploits light waveguiding in the active film and it is experimentally relatively easy. Waveguiding takes place in films with refractive index larger than the ambient and the substrate ones, and with a thickness larger than a cutoff value. As organic compounds typically show refractive index around 2, and as the refractive index of glass is around 1.5, the cutoff thickness for an organic film on glass is typically between 50 nm and 100 nm. Film thicknesses in this range can be obtained by several easy deposition techniques from solution, like spin coating, drop casting, and doctor blading. Thus, a standard film deposition from solution, on glass substrates, typically leads to a film supporting waveguiding.

---

*Organic Lasers: Fundamentals, Developments, and Applications*

Edited by Marco Anni and Sandro Lattante

Copyright © 2018 Pan Stanford Publishing Pte. Ltd.

ISBN 978-981-4774-46-8 (Hardcover), 978-1-315-10233-7 (eBook)

[www.panstanford.com](http://www.panstanford.com)

Concerning the excitation source, ASE experiments require pulsed lasers with high enough pulse energy, in order to reach and overcome the ASE threshold. Anyway, as the ASE thresholds of organic films are typically well below  $1 \text{ mJcm}^{-2}$ , not particular high pulse energy and, thus, not particularly expensive lasers are generally necessary to succeed in observing ASE from organic films.

Finally, concerning the detector, as the ASE intensity is generally high and the ASE band linewidth is on the scale of a few nanometers, even minispectrometers can be enough to successfully measure ASE spectra. Overall the equipment and the know-how necessary to design and perform ASE measurements in organic waveguides are then relatively easy, thus justifying, together with the high potentiality of organic materials for laser applications, the high number of research groups active in the investigation of the optical gain, ASE, and lasing, in organic materials. However, the experimental easiness of measuring the eventual presence of ASE in organic films, and of quantifying the ASE threshold, does not mean that the ASE properties are physically trivial to investigate and to understand. Beyond the value of the gain cross section of the material, that directly determines the possible optical gain of a material, the strength and even the presence of ASE are determined by the interplay between several physical processes. A careful investigation of the processes affecting ASE in potential active materials for lasers is thus extremely interesting from a fundamental science point of view, but it is also very important for potential laser applications, as the knowledge of these processes and their potential control gives an extremely powerful way to optimize the light amplification properties of a given material, that is the first step for the realization of lasers with optimized performances.

In this chapter, we will thus investigate the several processes affecting the ASE properties of organic active waveguides, beyond their dependence on the gain cross section of the active material. In particular, we will start from the fundamental aspects of the waveguide operation, addressing the importance of the dielectric properties of the active layer and of its thickness on the waveguide modes number and structure. We will then provide several examples of processes able to modify the ASE properties of a given active molecule.

We will start by discussing the role of the waveguide thickness, for molecules dispersed in an inert matrix or in a neat film.

Then we will discuss the role of the active molecules alignment, and we will finally discuss the role of the active film morphology.

This discussion is expected to allow the reader to have a clear picture of the potential complexity of a direct correlation between the final ASE properties and the active material intrinsic gain cross section but also, on the other side, of how much nice physics can be understood starting from ASE experiments.

## 2.2 Waveguide Operation

In this section, we will describe the main features of light waveguiding, starting from a simple ray optic description, and then moving to an electromagnetic wave description based on the Maxwell equations.

### 2.2.1 Ray Optics

Let us consider a system of three parallel dielectric slabs: the bottom slab will be the substrate, the intermediate one the active film, and the top one the cover, with refractive index  $n_s$ ,  $n_f$ , and  $n_c$  (see Fig. 2.1), respectively, and let us consider a ray propagating in the active film. According to geometrical optics, the ray will be partially reflected and partially refracted any time that it reaches the film-substrate or the film-cover interface.

Calling  $\theta_i$  the angle between the propagation direction of the ray in medium  $i$  and the normal to the interface, the propagation direction in the cover and in the substrate will be related to the propagation direction in the film by Snell's law:

$$n_f \sin \theta_f = n_c \sin \theta_c \quad (2.1)$$

$$n_f \sin \theta_f = n_s \sin \theta_s \quad (2.2)$$

When  $n_f < n_c$  and  $n_f < n_s$ , light will be partially reflected at both the c-f and f-s interface for any incidence angle. Thus, part of the light will be lost at any interface, and the light will be not confined in the active film. On the contrary, if  $n_f > n_c$  and  $n_f > n_s$ , the light

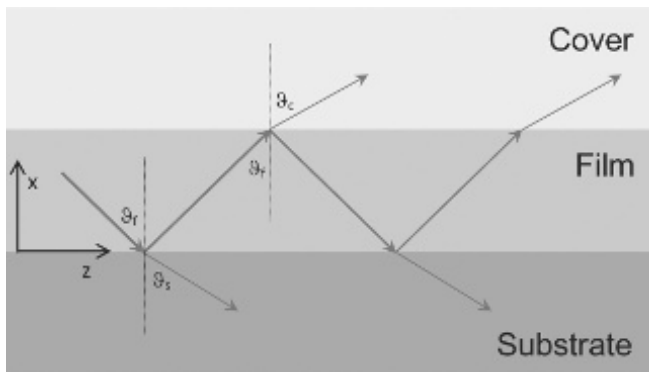


**Figure 2.1** Ray optics description of light propagation in a film of refractive index  $n_f$ , realized on a substrate with refractive index  $n_s$  and with a cover with refractive index  $n_c$  (in the figure, the refractive index of the film is higher than the ones of the substrate and the cover; thus, the refraction angles are larger than the incidence one). Light propagates along a zig-zag path, with sequential reflection and refraction at any interface. The partial refraction for incidence angles below the critical angle for total reflection leads to a progressive intensity decrease during propagation.

will be partially reflected at the interfaces only for small incidence angles, while it will be totally reflected at the f-i interface when  $\theta_f > \text{arc sin}(n_i/n_f)$  (critical angle for total internal reflection) (see Fig. 2.2). In this case, the light intensity will not be attenuated when it reaches the interfaces between the film and the surrounding layers, and thus the light will propagate in the film, ideally without losses if all the media are perfectly transparent and the interfaces perfectly smooth. The light will propagate along the periodic zig-zag direction visible in Fig. 2.2.

Anyway not all the propagation angles above the critical angle are allowed. This can be understood considering the wave nature of light. Considering the reference system in Fig. 2.2, the zig-zag propagation evidences a propagation along the increasing z, a partial propagation along the increasing x-direction (when light moves toward the cover), and a partial propagation along the decreasing x-direction (when light moves toward the substrate). This behavior can be obtained with the superposition of two plane waves, of the

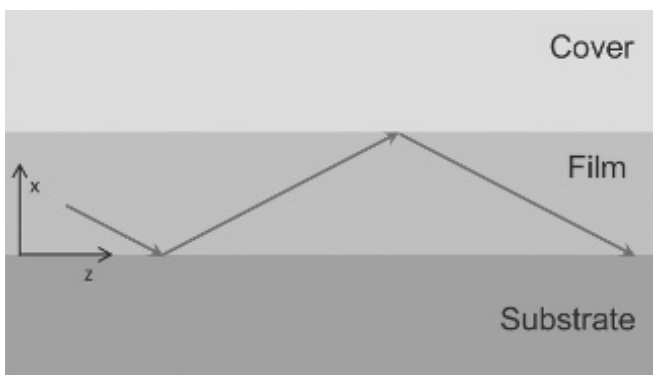


**Figure 2.2** Ray optics description of light propagation in a film for incidence angle above the total internal reflection one, both at the film–substrate and the film–cover interfaces. In this case, the light intensity does not decrease during propagation, and no energy is lost due to refraction at the interfaces.

same wavelength and frequency, and with a spatial dependence given by  $\exp(ik(\pm x \cos \theta_f + z \sin \theta_f))$ . For a guided wave, the ray optics picture predicts a propagation constant along the  $z$ -direction,  $\beta = k \sin \theta_F$ , that is, the  $z$ -component of the wavevector  $\vec{k}$ . As the wave must be able to propagate back and forth along the  $x$ -direction, a transverse resonance condition has to be imposed, asking that the total wave phase variation for a complete round trip along  $x$  in the film is equal to an integer multiple of  $2\pi$ . Part of this phase variation comes from the transversal propagation of twice the film thickness “ $d$ ”, and part from the wave phase variation due to the two reflections ( $\phi_c$  at the film–cover interface and  $\phi_s$  at the film–substrate interface). Actually above the total reflection critical angle, the reflected wave intensity is equal to the incident one, but the electric field phase changes upon reflection. In other terms, the reflection coefficient, defined as the ratio between the reflected electric field and the incident one, is a complex number with modulus 1 but nonzero phase (called  $\phi$  in the following). The phase variation due to total reflection depends on the wave polarization. For electric field perpendicular of the plane formed by the incidence propagation direction and the surface normal (plane

of incidence), called TE polarization, we have:

$$\tan\left(\frac{\phi_{TEi}}{2}\right) = -\frac{\sqrt{n_f^2 \sin^2 \theta_f - n_i^2}}{n_f \cos \theta_f} \quad (2.3)$$

For TM polarization (when the magnetic field is perpendicular to the plane of incidence), the dephasing is given by:

$$\tan\left(\frac{\phi_{TMI}}{2}\right) = -\frac{n_f^2}{n_i^2} \frac{\sqrt{n_f^2 \sin^2 \theta_f - n_i^2}}{n_f \cos \theta_f} \quad (2.4)$$

The transversal resonance condition then becomes:

$$2kd \cos \theta_f + \phi_c + \phi_s = 2v\pi \Leftrightarrow 2kd \cos \theta_f = 2v\pi - \phi_c - \phi_s \quad (2.5)$$

where  $v$  is an integer (including 0) identifying the mode number.

A graphical solution to Eq. 2.5 can be obtained by plotting the angular dependence of  $2kd \cos \theta_f$  and  $-\phi_c - \phi_s$ . A solution will be found any time that the plot of  $2kd \cos \theta_f - 2v\pi$  crosses the plot of  $-\phi_c - \phi_s$ .

The behavior of the waveguide can be understood by looking at the angular dependence of the two dephasing contributions (see Fig. 2.3), and remembering that the reflection phase variation is a function of the propagation angle and of the refractive indexes of the three media, while the propagation dephasing also depends on the film thickness. In Fig. 2.3 and in the others of this subsection, we fixed the substrate refractive index to 1.5, the film refractive index to 2 (typical of many organic films), and the cover refractive index to 1, which are reasonable values for an organic film deposited on glass and with air as cover layer.

If the cover and the substrate refractive index are the same, the waveguide is symmetric and the reflection phase variation is  $-2\phi_c$ . Once the refractive indexes of the three media are fixed, the angular dependence of  $-2\phi_c$  is fixed, while the angular dependence of the propagation dephasing also depends on the film thickness. Whatever the fixed thickness, it is evident from the graphics that there is always at least one solution of Eq. 2.5, as the propagation dephasing is a decreasing positive function reaching 0 for  $\theta_f = 90^\circ$ , and the reflection dephasing is an increasing positive function for any angle above the total reflection critical angle  $\theta_{cc}$ . Thus, a symmetric waveguide supports at least a guided mode, for any thickness of the guiding layer.

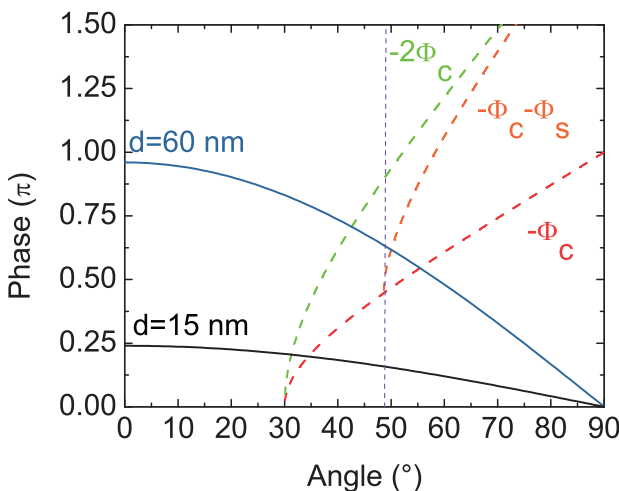


**Figure 2.3** Graphical solution of the waveguide propagation transversal resonance condition at  $\lambda = 500 \text{ nm}$  for a film with refractive index 2 (reasonable for organic films), deposited on a glass substrate ( $n_s \approx 1.5$ ) and with air as cover ( $n_c = 1$ ). The black and blue decreasing functions are the propagation dephasing for thickness of 15 nm and 60 nm, respectively. The red dashed line is the dephasing due to total reflection at the film-cover interface. The orange dashed line is the total value of reflection dephasing at both interfaces in the asymmetric waveguide, while the green dashed line is the total value of reflection dephasing at both interfaces in the symmetric waveguide in air. The vertical line evidences the critical total reflection angle at the film-substrate interface, limiting the minimum acceptable value of the propagation angle in the waveguide.

On the contrary, in an asymmetric waveguide, the existence of the solution requires the crossing of  $2kd \cos \theta_f$  and  $-\phi_c - \phi_s$  above the highest of the two critical angles for total internal reflection (vertical line in Fig. 2.3). As evident from Fig. 2.3, this condition can be obtained only for thick enough guiding film. Thus, an asymmetric structure can show waveguiding only above a cutoff thickness.

When the thickness increases, the propagation dephasing increases linearly with the thickness, and for high enough  $d$  values, also the plot of  $2kd \cos \theta_2 - 2\pi$  crosses the plot of  $-\phi_c - \phi_s$  (see Fig. 2.4). In this case, two guided modes exist. For even higher  $d$  values, further solutions can be found, leading to the conclusion

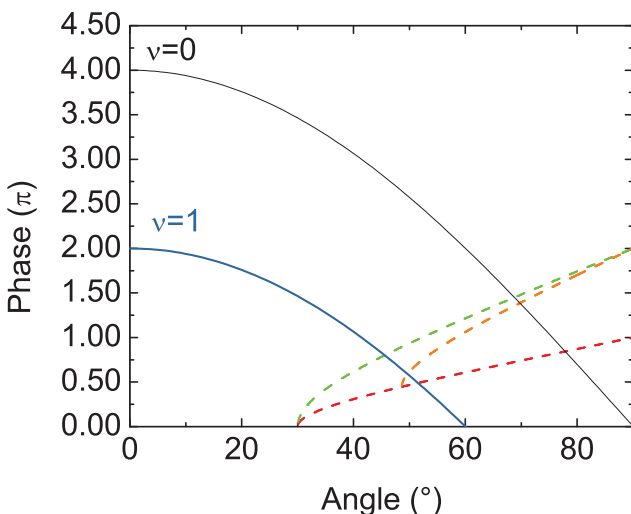


**Figure 2.4** Graphical demonstration of the existence of multiple solutions to Eq. 2.5 for thick enough films. In this case, a thickness of 250 nm has been assumed, for the same refractive indexes of Fig. 2.3, leading to a solution for both  $v = 0$  (black line) and  $v = 1$  (blue line).

that the number of guided modes increases with the guiding layer thickness.

Qualitatively identical conclusions can be obtained investigating the transversal resonance condition for TM polarization, with numerical differences in the cutoff thickness for asymmetric waveguides, and different values of the critical thickness for the increase in the number of guided modes. The mode number evolution as a function of the film thickness, for both polarizations, is reported in Fig. 2.5, evidencing that for film thickness of hundreds of nanometers, typical of spin coated films, more than one guided mode is generally allowed.

## 2.2.2 Wave Optics

The formally correct description of the guiding properties of a film requires the solution of the Maxwell equations for the system of three dielectric slabs, imposing the proper continuity conditions at

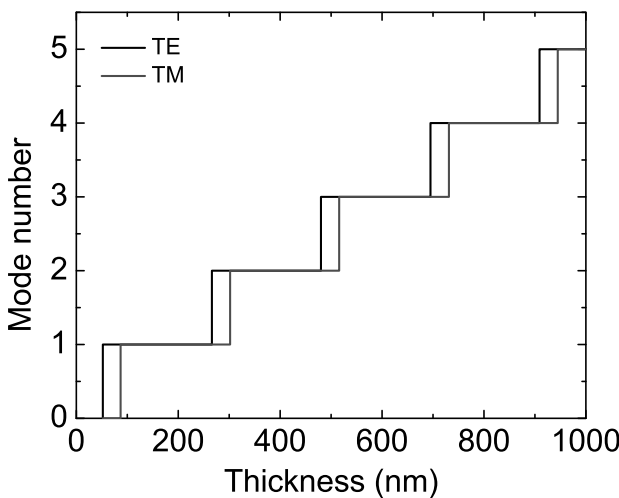


**Figure 2.5** Number of guided modes for TE and TM polarization as a function of the film thickness.

any interface:

$$\nabla \times \vec{E} = -\frac{\partial \vec{B}}{\partial t} \quad (2.6)$$

$$\nabla \times \vec{H} = -\frac{\partial \vec{D}}{\partial t} \quad (2.7)$$

where  $\nabla$  is the nabla operator ( $\partial/\partial x, \partial/\partial y, \partial/\partial z$ );  $\vec{E}$ ,  $\vec{B}$ ,  $\vec{D}$ , and  $\vec{H}$  are the electric field, magnetic induction, electric displacement, and magnetic field, respectively. Considering only isotropic and transparent materials with scalar dielectric constant  $\epsilon$  and scalar magnetic permeability  $\mu$ , we have:

$$\vec{D} = \epsilon \vec{E} \quad (2.8)$$

$$\vec{B} = \mu \vec{H} \quad (2.9)$$

Finally, looking for solutions periodic in time, thus with a time dependence  $\exp(i\omega t)$ , Eq. 2.6 and 2.7 become:

$$\nabla \times \vec{E} = -i\omega\mu\vec{H} \quad (2.10)$$

$$\nabla \times \vec{H} = i\omega\epsilon\vec{E} \quad (2.11)$$

The above equations have to be solved taking into account the proper boundary conditions at the interface, i.e., continuity of the  $\vec{E}$  and  $\vec{H}$  components tangential to the interface, and of the  $\vec{D}$  and  $\vec{B}$  components normal to the interface. If all the media are not magnetic, we have  $\mu = \mu_0$ ; thus,  $\vec{H}$  has to be continuous at any interface.

A mode of the waveguide is a solution containing a propagating wave term along the  $z$ -direction, thus:

$$\vec{E}(x, y, z) = \vec{E}_v(x, y) e^{i\beta_v z} \quad (2.12)$$

$$\vec{H}(x, y, z) = \vec{H}_v(x, y) e^{i\beta_v z} \quad (2.13)$$

In a planar waveguide, the optical properties and thus the modal fields change only as a function of the  $x$ -coordinate. The wave equations can thus be simplified by fixing  $\partial/\partial y = 0$ . In this case, the wave equations admit solutions with electric field transverse to the propagation direction (TE modes, with  $E_z = 0$ ) and with magnetic field transverse to the propagation direction (TM modes, with  $H_z = 0$ ).

The wave equation for TE modes can be obtained from the scalar projections of [Eqs. 2.10](#) and [2.11](#) along the three axes obtaining, after some straightforward steps:

$$\frac{\partial^2 E_y}{\partial x^2} = (\beta^2 - k^2 n^2) E_y \quad (2.14)$$

where  $k = \omega/c$  and  $n^2 = \epsilon/\epsilon_0$ .

The general solution of [Eq. 2.14](#) is a linear combination of exponential function, with real argument if  $(\beta^2 - k^2 n^2) > 0$  and with complex argument in the opposite case.

The complex exponential solutions represent traveling waves in the corresponding layer, while the real exponential solutions represent exponentially decreasing solutions in layers in which light propagation is forbidden. For example, the solutions oscillating in all the layers will represent solutions not confined in any layer, corresponding to light not totally reflected at any of the interfaces. The solutions oscillating in the film and in the substrate, but not in the cover, will instead represent light totally reflected at the film-cover interface, but not at the film-substrate one (substrate

solutions), while the solutions oscillating only in the film will represent waveguide modes, corresponding to light totally reflected both at the film–substrate and at the film–cover interfaces.

We define the following transverse decay ( $\gamma_i$ ) and propagation constants ( $k_i$ ):

$$k_c^2 = n_c^2 k^2 - \beta^2 = -\gamma_c^2 \quad (2.15)$$

$$k_f^2 = n_f^2 k^2 - \beta^2 \quad (2.16)$$

$$k_s^2 = n_s^2 k^2 - \beta^2 = -\gamma_s^2 \quad (2.17)$$

Fixing the 0 of the  $x$ -axis at the substrate–film interface, and calling  $d$  the film thickness, the general solution for waveguide modes will be of the kind:

$$E_y = E_c e^{-\gamma_c(x-d)} \quad x > d \text{ (cover)} \quad (2.18)$$

$$E_y = E_{1f} e^{ik_f x} + E_{2f} e^{-ik_f x} \quad 0 < x < d \text{ (film)} \quad (2.19)$$

$$E_y = E_s e^{\gamma_s x} \quad x < 0 \text{ (substrate)} \quad (2.20)$$

where the subscripts c, f, and s indicate cover, film, and substrate, respectively, and the amplitudes of the real exponential solutions diverging for  $x \rightarrow \pm\infty$  have been fixed to 0.

From the continuity condition at  $x = 0$  and  $x = d$  of both  $E_y$  and  $dE_y/dx$ , the following relations are obtained:

$$\tan \frac{\phi_s}{2} = -\frac{\gamma_s}{k_f} \quad (2.21)$$

$$\tan \frac{\phi_c}{2} = -\frac{\gamma_c}{k_f} \quad (2.22)$$

$$k_f d + \phi_s + \phi_c = \nu\pi \quad (2.23)$$

The obtained equations are identical to the ray optics one, thus allowing to easily understand the presence of a discrete number of guided modes solutions, with the mode number increasing with the film thickness.

In order to better understand the obtained solution from a different perspective, we observe that the structure of the final wave equation is formally identical to the time-independent Schrödinger equation in a monodimensional potential well:

$$\frac{\hbar^2}{2m} \frac{\partial^2 \Phi}{\partial x^2} = (V - E) \Phi \quad (2.24)$$

In this case, fixing the potential to 0 in the well and calling the potential barrier height  $V_0$ , the solutions are real exponentials in the barrier regions if  $E < V_0$ , while we find complex exponential (thus sine or cosine function) if  $E > V_0$ . The system will then show a finite number of solutions with exponential decay outside the well, and oscillating behavior inside the well, which are the bound states, at discrete energies. These states are the solutions equivalent to the guided modes.

In the potential well, the number of confined modes depend on the barrier height (related in the optical case to the refractive index discontinuity) and on the well width, equivalent to the film thickness. Moreover, infinite solutions for the Schrödinger equation are found at energies above  $V_0$ , representing free states with continuous energies, equivalent to the unguided wave solutions.

In a similar way, the wave equation solutions will exponentially decrease outside the film if  $\beta > kn$ , while they will be oscillating functions if  $\beta < kn$ . The solutions with oscillating behavior only in the film are the guided modes that will exist only for discrete and finite values of  $\beta$ . With this analogy, the presence of at least one guided mode solution in the symmetric waveguide case can be easily understood, as the Schrödinger equation always admits at least one bound solution, whatever the well thickness and the barrier eight, if the quantum well is symmetric. The TM modes can be obtained starting from the wave equation:

$$\frac{\partial^2 H_y}{\partial x^2} = (\beta^2 - k^2 n^2) H_y \quad (2.25)$$

With the boundary conditions of continuity of  $H_y$  and  $1/n^2 \partial H_y / \partial x$ . In this case, the continuity conditions lead to the following equations:

$$\tan \frac{\phi_s}{2} = - \frac{n_f^2}{n_s^2} \frac{\gamma_s}{k_f} \quad (2.26)$$

$$\tan \frac{\phi_c}{2} = - \frac{n_f^2}{n_c^2} \frac{\gamma_c}{k_f} \quad (2.27)$$

$$2k_f d + \phi_s + \phi_c = 2\nu\pi \quad (2.28)$$

## 2.3 Understanding the Intrinsic Gain Properties of an Active Material by ASE Measurements

According to the previous description, the realization of a thick enough uniform layer of an emitting material between two materials with lower refractive index is enough to allow waveguiding in the film of the photoluminescence obtained by optical pumping. If the material shows optical gain, the investigation of the PL spectra as a function of the excitation density will allow to observe line narrowing and light amplification by ASE as soon as the pumping density makes the optical gain stronger than the waveguide losses. In these terms, the ASE threshold, that is the minimum excitation density necessary to observe ASE in the spectra, can be considered a quantifier of the excitation density required to have a material that, inside a proper resonant cavity, can lead to lasing.

In the field of developing active materials for organic lasers, the pumping regime required for lasing is obviously extremely important, as low threshold means cheap pumping source and also high emission stability (the organic photodegradation becomes faster under stronger pumping).

The simplicity of ASE measurements proposes these experiments as a simple starting step in the characterization of new materials for laser applications. Actually if ASE is observed, many important information can be obtained. First of all ASE is a direct consequence of optical gain, thus the presence of ASE indicates that the material can be used in a laser. Moreover, the ASE dependence on the pumped region geometry allows the quantitative measurement of the gain spectrum, and thus of the obtainable gain values and of the possible laser tunability range.

By looking at the literature, it can be effectively observed that the first evaluation of a novel material for lasers is often based on ASE measurements. Rather interestingly, the results obtained for the ASE threshold are often used as an indicator of the laser application potentiality of the investigated material, assuming that a low ASE threshold indicates a good material while a high threshold characterizes bad materials.

This argument is apparently meaningful as a low ASE threshold indicates that low pumping energy is necessary to have gain.

In the following sections, we will provide several examples that should allow the reader to realize that, as often happens in physics, reasonable arguments are not always correct arguments. In particular, we will discuss recent results obtained in the literature demonstrating that the ASE properties depend on many properties of the investigated films, sometimes resulting in huge variations of the ASE threshold even in a fixed material, evidencing that a wide systematic investigation on the role of these parameters must be performed in order to be able to correctly understand what are the potentiality of a novel material for lasers.

## 2.4 Gain Cross Section and ASE Threshold: The Case of Poly(9,9-dioctylfluorene)

The first evidence that the simple correlation of the ASE threshold to the intrinsic gain properties, and thus to the gain cross section, exposes to high risks of committing mistakes concerns the optical gain properties of active waveguides of poly(9,9-dioctylfluorene) (PF8). The family of polyfluorenes received large attention in the literature, showing interesting active materials for a wide range of devices, such as light-emitting diodes [1], field-effect transistors [2], sensors [3], and solar cells [4].

Moreover, poly-alkyl-fluorenes are interesting mesomorphic molecules, presenting two different chain conformations, called glassy and  $\beta$  phases, with distinct emission spectra, allowing several basic experiments on the photophysics dependence on the chain conformation. For example, it has been demonstrated that triplet exciton generation and intermolecular charge separation are strongly different between glassy and  $\beta$  phases [5]. Concerning lasers, tunable optical gain has been demonstrated in polyfluorene derivatives [6] as well as efficient distributed feedback lasing [7].

The films in which the two phases coexist are typically characterized by a  $\beta$ -phase content of a few percent. Since the  $\beta$ -phase emits at lower energy than the glassy phase, with a good spectral overlap

between the glassy phase emission and the  $\beta$  absorption, efficient glassy to  $\beta$ -phase, Förster resonance energy transfer (FRET) is present, allowing PF8 to give self-doped host guest films emitting in the blue. This property is extremely interesting for laser applications as host:guest blends interacting by FRET are typically realized to maximize the gain of a given molecule. The basic idea of this approach is that the photoluminescence quantum yield (PLQY) of a molecule in neat films is lower than the PLQY of the isolated molecule, due to the presence of intermolecular energy migration toward defects and/or molecule aggregation. This effect is very evident for dye molecules, typically showing extremely high PLQY and gain in diluted solutions, and strong PL and gain concentration quenching in concentrated solutions and films.

A further contribution to the gain decrease in neat films comes from the active molecule self-absorption, which is particularly relevant when a waveguide geometry configuration is used, as the collected light propagates for several millimeters along the pumped stripe. The molecule dilution in an inert matrix, which would improve the gain properties of the active molecules, on the other side decreases the absorption (thus lowering the fraction of the pump laser absorbed light), as well as the volume density of active molecules (and thus the possibly obtainable gain). On the contrary, blends between two active molecules in which the one majority component (the host) efficiently absorbs the pump light and then transfers the excitation to the minority component (the guest) by FRET allow to obtain high absorption due to the host absorption, efficient guest excitation by FRET, and high guest gain and low self-absorption due to the dilution. On this point of view, PF8 is a unique system in which the same molecule can act in the film both as the host and as the guest, due to the chain conformation dependence of the optical properties.

For all these reasons, several experiments have been performed in order to characterize the gain performances of the two PF8 phases leading, rather surprisingly, to strikingly inconsistent results. The first work on the PF8 ASE reported that ASE is present at room temperature only in films in which a thermal treatment induces the  $\beta$ -phase formation [8]. It was later demonstrated that a copolymer with controlled amount of  $\beta$  phase shows an

ASE threshold increasing with the  $\beta$ -phase content [9], while the comparison between thin films of glassy phase and films containing also the  $\beta$  phase leads to the observation of similar ASE thresholds in one case [10], and in lower threshold for the  $\beta$ -phase sample [11] in the other. Quite interestingly, this large spread of results of the ASE measurements is obtained even if the measurement of the peak gain cross section of the PF8 glassy and  $\beta$  phase [12], by pump-probe experiments, showed that the  $\beta$ -phase gain cross section is about four times larger than the glassy phase one. Considering that the samples used in the previously cited ASE experiments are apparently comparable systems, the inconsistencies of the results prove how the final ASE properties depend not only on the intrinsic gain properties of the employed active molecule.

In order to understand the origin of the previous contrasting results, and to correlate the ASE properties of PF8 to the gain cross section of the phase dominating the emission spectra, we investigated in details the ASE properties of four samples with different  $\beta$ -phase contents between 0 and 6.4% [13].

The glassy phase samples were prepared by spin coating PF8 thin films from a  $10^{-4}$  M chloroform solution. In order to induce the formation of different amounts of  $\beta$  phase, the glassy phase samples were exposed to toluene vapors for different times in steps of about 10 min. In order to avoid effects on the ASE wavelength and threshold, all the samples have been realized with a comparable thickness of  $350 \pm 20$  nm, well above the waveguide threshold thickness of about 50 nm and 40 nm for the glassy and  $\beta$  phases, respectively.

The different composition of the samples is evidenced by the absorption spectra (see inset of Fig. 2.6) that show a main resonance peaked at about 385 nm, due to the  $S_0 \rightarrow S_1$  glassy phase absorption and, in the toluene exposed samples a further resonance at higher wavelengths, peaked at about 432 nm with a linewidth of about 14 nm, with an intensity increasing with the toluene vapors exposure time, which is due to the  $S_0 \rightarrow S_1$   $\beta$ -phase absorption. The  $\beta$  phase content of all the samples was estimated by calculating the ratio between the  $S_0 \rightarrow S_1$  glassy phase resonance integrated absorbance and the  $S_0 \rightarrow S_1$   $\beta$ -phase resonance one (see Table 2.1).

The PL spectra of the glassy phase sample (see Fig. 2.6 a) show the typical peaks of the PF8 glassy phase, with a 0-0 resonance at about 425 nm, followed by the 0-1 and 0-2 vibronic bands at about 451 nm and 481 nm, respectively. As the excitation density increases, an ASE band appears at about 451 nm, and progressively dominates the emission, leading to a clear line narrowing of the 0-1 vibronic band (see Fig. 2.7). The ASE threshold (estimated as the excitation density at which the 0-1 band linewidth decreases at 80% of the low excitation density value  $\pm 5\%$ ) is about  $0.70 \pm 0.08 \text{ mJcm}^{-2}$ .

The PL spectra of the  $\beta_1-\beta_3$  samples show, at low excitation density, the typical features of the  $\beta$ -phase PL, with a 0-0 line peaked at about 440 nm, followed by the 0-1 and 0-2 vibronic bands at about 470 nm and 500 nm, respectively (see Fig. 2.6b)). As the excitation density increases, ASE is observed in correspondence of the 0-1 band in all the three samples with a threshold decreasing with the increase in the  $\beta$ -phase content down to  $0.48 \pm 0.04 \text{ mJcm}^{-2}$  for the  $\beta_1$  sample, and about  $0.25 \pm 0.02 \text{ mJcm}^{-2}$  for the  $\beta_2$  and  $\beta_3$  samples (see the inset of Fig. 2.7 and Table 2.1).

In order to determine the origin of the observed decrease in the ASE threshold with the  $\beta$ -phase content, we considered that ASE is observed only if  $g' = g - \alpha > 0$ , where  $g'$  is the net gain,  $\alpha$  the waveguide losses, and  $g$  the gain coefficient. As the gain coefficient is given by  $g = n\sigma$ , where  $n$  is the volumetric density of molecules with population inversion and  $\sigma$  is the gain cross section, ASE will be observed in the spectra as soon as  $n\sigma > \alpha$ . Differences in the ASE threshold can be then due to difference in the waveguide losses, in the gain cross section, and in the efficiency of

**Table 2.1**  $\beta$ -phase content, ASE threshold, waveguide losses, net gain, gain of the investigated samples (at a pump density of  $4.0 \text{ mJcm}^{-2}$ )

Sample	$\beta$ phase %	ASE thr. $\text{mJcm}^{-2}$	Losses $(\text{cm}^{-1})$	Net gain $(\text{cm}^{-1})$	Gain $(\text{cm}^{-1})$
Glassy	0.0	$0.70 \pm 0.08$	$5.1 \pm 0.1$	$4.0 \pm 0.2$	$9.1 \pm 0.3$
$\beta_1$	1.5	$0.48 \pm 0.04$	$3.0 \pm 0.2$	$5.4 \pm 0.2$	$8.3 \pm 0.4$
$\beta_2$	3.3	$0.24 \pm 0.02$	$3.3 \pm 0.2$	$5.7 \pm 0.2$	$9.0 \pm 0.4$
$\beta_3$	6.4	$0.26 \pm 0.02$	$3.5 \pm 0.1$	$5.8 \pm 0.2$	$9.3 \pm 0.3$

Source: Reprinted from Ref. [13] with the permission of AIP Publishing.

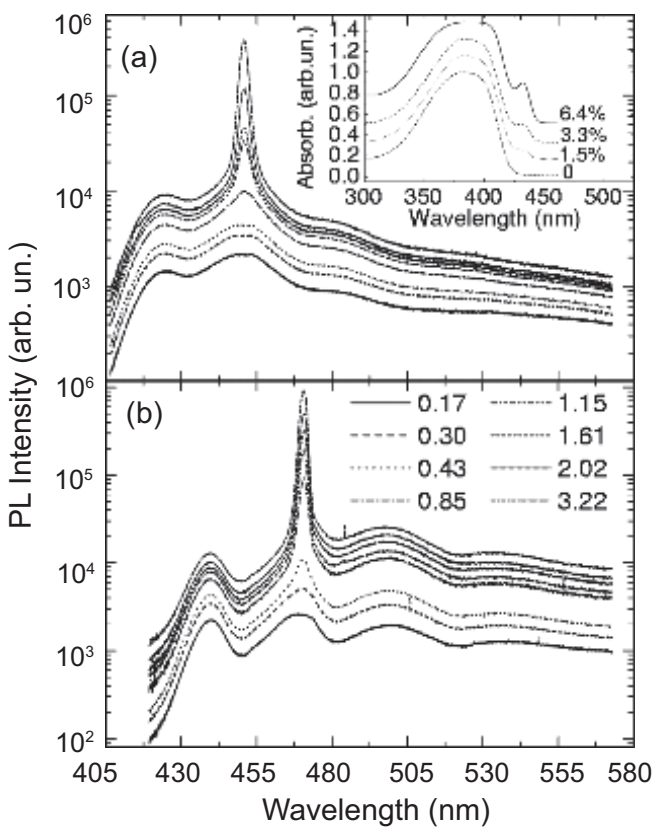


**Figure 2.6** PL spectra as a function of the excitation density (in  $\text{mJcm}^{-2}$ ) of the glassy phase film (a) and  $\beta_3$  ( $\beta$ -phase content of 6.4%). In sample,  $\beta_3$  ASE is peaked at about 471 nm, and it is clearly visible for excitation densities higher than about 0.4  $\text{mJcm}^{-2}$ . Inset: absorption spectra of the investigated samples (normalized to the peak value and vertically translated for clarity). Reprinted from Ref. [13], with the permission of AIP Publishing.

the active molecule pumping process (which determine the relation between the excitation density and  $n$ ). We then measured the waveguide losses  $\alpha$  and the net gain  $g'$  (at an excitation density of 4.0  $\text{mJcm}^{-2}$ ) for all the samples. The obtained results (see Fig. 2.8 and Table 2.1) clearly show that  $g'$  progressively increases from  $4.0 \pm 0.2 \text{ cm}^{-1}$  of the glassy phase sample up to  $5.7 \pm 0.2 \text{ cm}^{-1}$  of the  $\beta_3$  sample, consistently with the corresponding ASE threshold

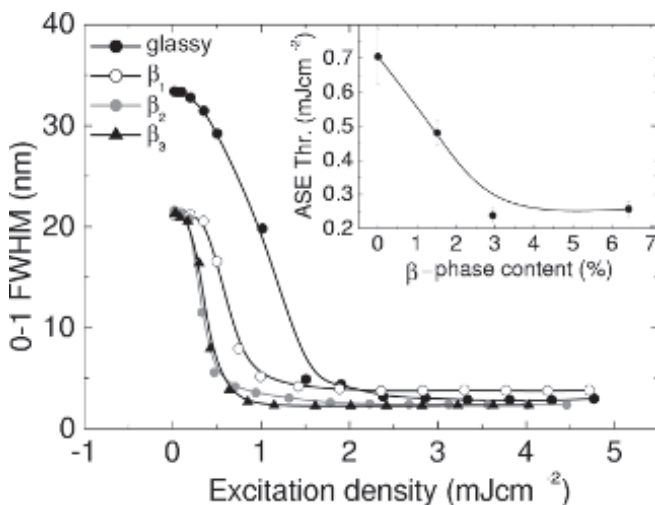


**Figure 2.7** Full width at half maximum (FWHM) of the 0-1 line as a function of the excitation density for all the investigated samples. Inset: ASE threshold as a function of the  $\beta$ -phase content in the films. Reprinted from Ref. [13], with the permission of AIP Publishing.

decrease. However, this increase in net gain is not due to a higher gain coefficient of the  $\beta$ -phase samples, but it is mainly due to the losses reduction from  $5.1 \pm 0.14 \text{ cm}^{-1}$  of the glassy phase, down to about  $3.3 \pm 0.2 \text{ cm}^{-1}$  of the  $\beta_1-\beta_3$  samples. The  $\alpha$  reduction is ascribed to the improvement in the morphology uniformity induced by the toluene vapors exposure [14], and to the increase in the refractive index in the films with  $\beta$  phase, improving the mode confinement in the active waveguides, estimated in about 13% in [11].

Concerning the gain coefficient, our results show that  $g$  in the  $\beta_1$  and  $\beta_2$  samples is *smaller* than the glassy phase one. The increase in the  $\beta$ -phase content leads to a progressive increase in  $g$ , which anyway becomes higher than the glassy phase one only for  $\beta$ -phase contents higher than about 4.7% (see Fig. 2.8). The origin of this  $g$  increase with the  $\beta$ -phase content has been investigated by modeling the excitation density dependence of the glassy and  $\beta$ -phase excited molecules density  $n_g$  and  $n_\beta$  with the following rate

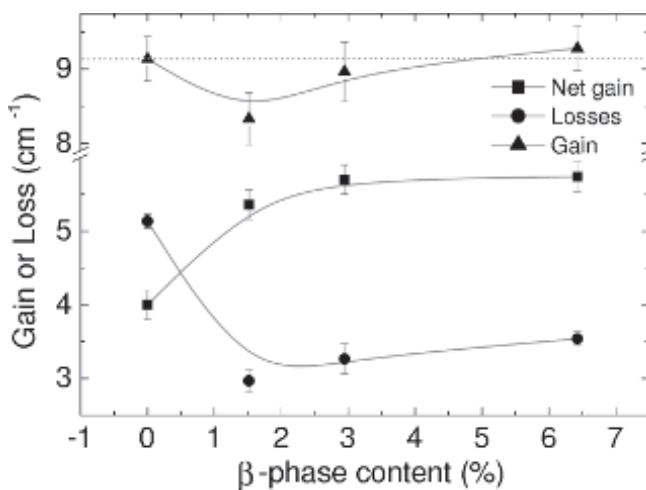


**Figure 2.8** Waveguide losses, net gain, and gain as a function of the  $\beta$ -phase content. Reprinted from Ref. [13], with the permission of AIP Publishing.

equations:

$$\frac{dn_g}{dt} = \rho_{\gamma\text{abs}} - \frac{n_g}{\tau_g} - \frac{n_g}{\tau_{\text{fret}}} \quad (2.29)$$

$$\frac{dn_\beta}{dt} = -\frac{n_\beta}{\tau_\beta} + \frac{n_g}{\tau_{\text{fret}}} \quad (2.30)$$

where  $\rho_{\gamma\text{abs}} = D / (d \Delta t E_\gamma)$  is the density of photons absorbed by the glassy phase per unit of time ( $D$  is the excitation density in  $\text{Jcm}^{-2}$ ,  $E_\gamma$  the pump laser photon energy,  $\Delta t$  the pulsedwidth, and  $d$  the film thickness),  $\tau_g$  and  $\tau_\beta$  are the glassy and  $\beta$ -phase excited state lifetime, respectively, and  $1/\tau_{\text{fret}}$  is the total glassy  $\rightarrow$   $\beta$ -phase FRET rate given by:

$$\frac{1}{\tau_{\text{fret}}} = \int_{2a}^{\infty} \frac{1}{\tau_g} \frac{R_0^6}{r^6} \rho_\beta 4\pi r^2 dr = \frac{\pi \rho_\beta}{6\tau_g a^3} R_0^6 \quad (2.31)$$

where  $\rho_\beta$  is the density of  $\beta$ -phase molecules (acceptors),  $R_0$  is the Förster radius, and  $a$  is the donor and acceptor radius (in a spherical donor and acceptor approximation). As the excitation laser delivers 3 ns pulses, which is a time much larger than the lifetime of both the glassy and  $\beta$  phases, solving Eqs. 2.29 and 2.30 in the steady state

and imposing the threshold condition  $n\sigma = \alpha$ , we find:

$$D_g^{\text{th}} = \frac{\alpha_g d \Delta t E_\gamma}{\tau_g \sigma_g} \quad (2.32)$$

$$D_\beta^{\text{th}} = \frac{\alpha_\beta d \Delta t E_\gamma}{\tau_\beta \sigma_\beta} \left( 1 + \frac{6a^3}{\pi \rho_\beta R_0^6} \right) = D_\infty^{\text{th}} \left( 1 + \frac{B}{\rho_\beta} \right) \quad (2.33)$$

The previous expressions of  $D^{\text{th}}$  show that in order to correlate the ASE threshold to the gain coefficient value, the gain cross section is not the only parameter to look at as, for a given  $\sigma$ , different excited state lifetime results in different ASE threshold, as  $D^{\text{th}}$  is inversely proportional to  $\sigma\tau$ . For the glassy phase sample, we estimated  $\sigma_g \tau_g = (4.5 \pm 0.9) 10^{-28} \text{ cm}^2\text{s}$  by using the experimental values of  $\alpha_g$ ,  $D_g^{\text{th}}$ ,  $\Delta t = 3 \text{ ns}$ , and  $E_\gamma = 3.68 \text{ eV}$ . The value of  $\sigma_\beta \tau_\beta$  was instead obtained from a best fit of the experimental dependence of  $D_\beta^{\text{th}}$  on  $\rho_\beta$  to Eq. 2.33, which is obtained for  $D_\infty^{\text{th}} = 150 \pm 20 \mu\text{Jcm}^{-2}$  and  $B = (2.7 \pm 0.6) 10^{20} \text{ cm}^{-3}$ , thus obtaining  $\sigma_\beta \tau_\beta = (14 \pm 3) 10^{-28} \text{ cm}^2 \text{s} \approx (3.2 \pm 1.2) \sigma_g \tau_g$ , indicating that the  $\beta$ -phase molecules, for a given pump density, have higher gain than the glassy phase ones. This conclusion is fairly consistent with the gain cross section values obtained by pump probe in [12], proving that the  $\beta$  phase has a gain cross section about four times larger than the glassy phase one.

Finally, we used Eq. 2.33 and the correspondence between  $\rho_\beta$  and the  $\beta$ -phase content of Ref. [15], to estimate the  $\beta$ /glassy-phase relative ASE threshold as a function of the  $\beta$ -phase content of the film and of  $\alpha_\beta/\alpha_g$  (see Fig. 2.9). Our results indicate that an increase in the  $\beta$ -phase content from 1% to 10% decreases the threshold by about three times, while, for a fixed  $\beta$ -phase content, a reduction in the relative glassy/ $\beta$  losses from 0.5 to 2 increases the  $\beta$ -phase ASE threshold of about four times. Overall in this range (of  $\beta$ -phase content and loss), threshold variations of about one order of magnitude are obtained, indicating that no conclusions can be obtained about the glassy and  $\beta$ -phase molecular gain by considering only the ASE threshold, without taking into account the waveguide losses and the effects of the  $\beta$ -phase content on the *glassy*  $\rightarrow$   $\beta$ -phase FRET. In other terms, the absence of quantitative understanding of the role of the  $\beta$ -phase content and of the losses value can lead to completely different results on the

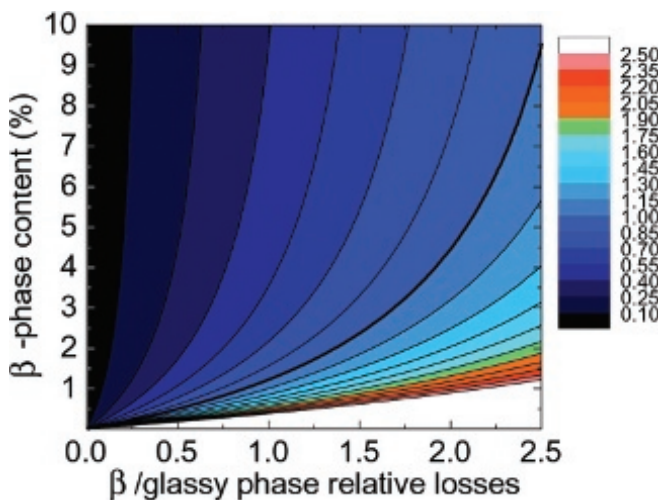


**Figure 2.9**  $\beta$ /glassy phase relative ASE threshold as a function of the relative waveguide losses  $\alpha_\beta/\alpha_g$  and of the  $\beta$ -phase content of the film. The thickest line is the line of equal ASE threshold of glassy and  $\beta$ -phase samples. Reprinted from Ref. [13], with the permission of AIP Publishing.

relative threshold value of apparently comparable samples made by the same materials.

## 2.5 ASE Dependence on the Waveguide Thickness

According to the previous description, the waveguiding properties of any active film are a function of the cover, film, and substrate refractive indexes and of the film thickness. A variation of the thickness of the active layer changes the wavelength of the possible guided modes, their number, both for TE and TM polarization, and the electric field profile in the active layer. On an applicative point of view, almost all the realized organic active waveguides are asymmetric, being made by an active film deposited on a solid substrate (most of the times glass), with air working as cover layer. Thus once that the working wavelength  $\lambda_0$  of the waveguide has been chosen, obviously within the spectral range in which

the molecule shows optical gain, an active layer with thickness above a cutoff value  $d_{\min}$  has to be realized, where  $d_{\min}$  is the waveguide thickness allowing waveguiding for wavelengths up to  $\lambda_0$ . The relationship between film thickness and spectral range of waveguiding can be exploited to tune the maximum ASE wavelength of the waveguide. Actually, calling  $\lambda_{g\max}$  the wavelength of maximum optical gain, a waveguide will show ASE peaked at  $\lambda_{g\max}$ , if thick enough to allow efficient waveguiding at this wavelength. A reduction in the waveguide thickness leads to the decrease in the maximum wavelength that is guided in the active film,  $\lambda_{w\max}$ . When  $\lambda_{w\max}$  becomes smaller than  $\lambda_{g\max}$ , light propagation at  $\lambda_{g\max}$  is no more allowed, thus the ASE band shifts toward the blue, being peaked at the wavelength of maximum gain below  $\lambda_{w\max}$ .

Assuming a bell-shaped gain spectrum, and thus a continuous gain decrease below  $\lambda_{g\max}$ , the ASE peak will be at  $\lambda_{w\max}$ , when  $\lambda_{w\max} < \lambda_{g\max}$ . This result can be used to tune the ASE band at lower wavelength, as successfully demonstrated in literature [16–18]. The tunability range coincides with the gain range below  $\lambda_{g\max}$  and is typically on the scale of 10–20 nm.

This approach, which is based on basic properties of waveguiding, smartly allows to change the amplification spectral range by only changing a geometrical parameter of the active film.

Moreover, from a qualitative point of view, it is also rather straightforward to guess that the film thickness has to affect the ASE threshold. First of all, it could be expected that, in order to have efficient stimulated emission, the mode electric field in the active layer has to be as large as possible. Moreover, it should also be reasonable to observe the lowest ASE threshold in waveguides supporting only one guided mode as the presence of many modes should lead to an energy redistribution across the modes, thus leading to mode competition. In standard laser cavities this guess is actually correct, as the threshold typically increases in cavities with a high number of resonant modes.

Despite the possible strong dependence of the waveguiding properties of the active films on its thickness, and despite the obvious correlation between waveguiding properties and light amplification efficiency along the waveguide, the experimental investigation of the thickness effect on ASE properties has been to

date relatively scarce, and only a few articles appeared in the last years on this topic. In particular, the active film thickness variation has been to date mainly used to tune the ASE peak wavelength [16–18], while the thickness effects on the ASE threshold have been to date investigated only in a few cases [16, 18], finding a decrease in the ASE threshold as the active film thickness increases. In the following subsections, we will address in details the role of the film thickness on the ASE properties of both short molecules in diluted inert polymer matrix, and of polymeric neat films.

### 2.5.1 ASE Thickness Dependence in Diluted Polystyrene Matrix

The first systematic investigation of the ASE thickness dependence has been reported in [16], investigating the role of the active film thickness on the ASE threshold and wavelength in polystyrene films containing 15 wt % of *N,N'*-bis(3-methylphenyl)-*N,N'*-diphenylbenzidine (TPD), a hole transport molecule luminescent in the blue spectral range. The film thickness was changed by acting on the solution concentration, realizing about 30 different samples with thickness between 80 nm and 1000 nm. For each sample, the spectra linewidth at high excitation density, the ASE (when present) threshold, and peak wavelength were measured. Moreover, the waveguiding properties were modeled by determining the cutoff thickness and the mode confinement for each sample, starting from the experimentally determined refractive index.

This large systematic investigation allowed the authors to quantitatively understand the role of waveguiding cutoff and of the mode confinement on both the ASE wavelength and threshold, making the first important step in the study of the ASE properties of organic films. First of all, the authors observe a progressive redshift of the ASE band from 404 nm to 417 nm as the film thickness increases from 105 nm to 200 nm and a thickness-independent peak wavelength of 417 nm for thickness above 200 nm, in qualitative agreement with the previous discussion on the thickness role in ASE tuning. However, a quantitative comparison between the thickness dependence of the minimum guided wavelength and of the ASE peak wavelength allows to observe clear differences in the slope

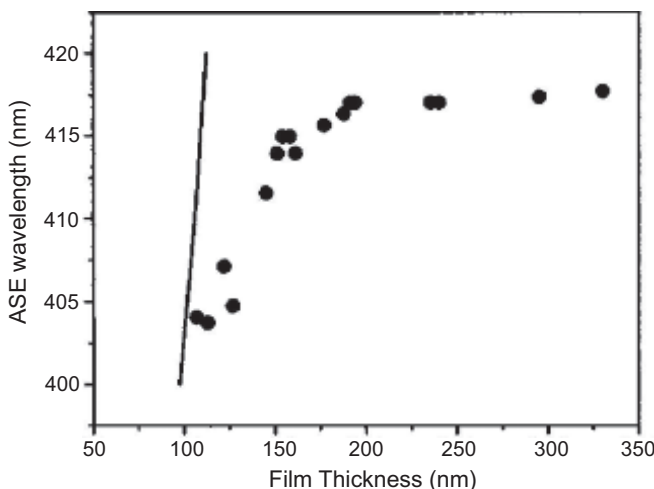


**Figure 2.10** Thickness dependence of the minimum guided wavelength (line) and of the ASE peak (dots). Reprinted from Ref. [16], with the permission of AIP Publishing.

(see Fig. 2.10). An ASE shift only due to the cutoff would result in a peak shift from about 400 nm to 417 nm in a thickness range from about 105 nm to about 110 nm, while the experiment evidences a much weaker thickness dependence, with a progressive ASE shift up to a thickness of 200 nm. This disagreement is particularly instructive as it clearly evidences how a data analysis based only on qualitative arguments can sometimes allow to reproduce experimental trends, without allowing to observe quantitative disagreements, which actually demonstrate the inadequacy of the proposed explanation.

In order to understand the origin of the observed differences, the authors considered first of all that the ASE wavelength depends on the PL spectrum of the active films, which is strongly affected by the film thickness (see Fig. 2.11). The PL spectrum of the 94 nm thick film is peaked at about 395 nm, while the peak wavelength progressively shifts to 417 nm as the thickness increases to 127 nm. This effect is due to the limitation of the wavelengths that can be guided in the films that, close to the cutoff thickness, increases the weight in the PL spectra of the light at lower wavelength (which

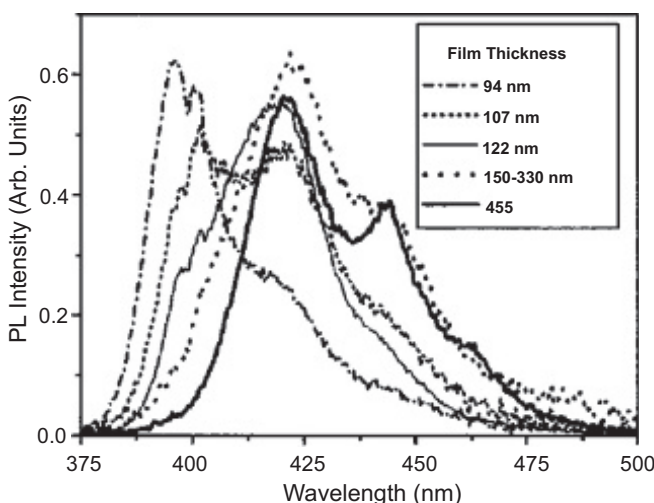


**Figure 2.11** Thickness dependence of the PL spectra evidencing a clear lineshape variation for thicknesses up to 127 nm. Reprinted from Ref. [16], with the permission of AIP Publishing.

can be guided) with respect to the unguided sample PL. As the thickness increases, the effect becomes progressively smaller, as all the wavelengths of the PL spectra can be efficiently guided, and for thick enough films, a thickness-independent spectrum is collected.

Again a quantitative comparison between the thickness range of PL spectrum variation and of ASE shift evidences an important disagreement, as the PL becomes thickness independent above 127 nm, while the ASE redshifts up to 200 nm, again evidencing that some other process, enhancing the ASE at low wavelength, has to be added in the modeling. As the last step, the authors considered that, for a given film thickness, the modes at lower wavelength are more confined in the active material, thus enhancing the ASE at low wavelength. A quantitative model including both the mode confinement and the spectra lineshape allowed to obtain a reasonable quantitative agreement between the experimental ASE position and the predicted ones.

Finally, the authors also investigated the thickness effect on the ASE threshold, observing a maximum threshold for the thinnest sample above the cutoff thickness of about  $125 \text{ kWcm}^{-2}$ , with a

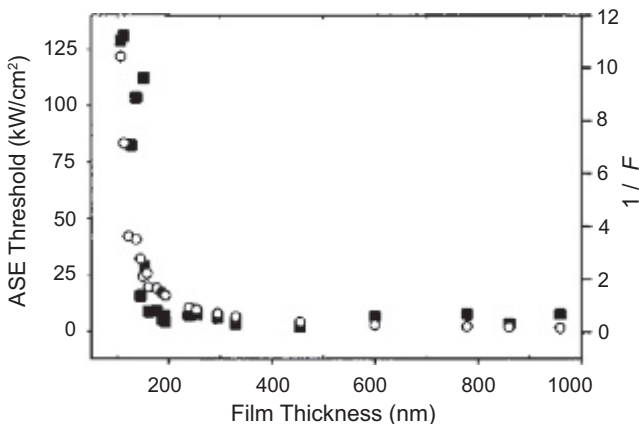


**Figure 2.12** Thickness dependence of the ASE threshold (left scale) and of the reciprocal of the mode confinement factor (right scale) evidencing a good agreement over all the explored thickness range. Reprinted from Ref. [16], with the permission of AIP Publishing.

systematic decrease down to about  $5 \text{ kWcm}^{-2}$  as the thickness increases (see Fig. 2.12). In this case, the result was ascribed to the thickness dependence of the mode confinement in the waveguide observing that highly confined modes can efficiently propagate in the film, thus being amplified in the optical gain spectral range. On the contrary, for poorly confined modes, a relevant fraction of light will radiate in the substrate, where no amplification takes place. Also in this case, a quantitative comparison was made, between the experimental thresholds and the reciprocal confinement factor, evidencing a convincing agreement and thus allowing to conclude that the ASE threshold is mainly determined by the confinement level of the first guided mode.

## 2.5.2 ASE Thickness Dependence in Poly(9,9-dioctylfluorene) Neat Films

The thickness role on the ASE properties of polymeric waveguides has also been investigated [19] in neat films of poly(9,9-dioctylfluorene)(PF8). PF8 can be considered a good prototype

active polymer for lasing application as it shows ASE [13, 20] and lasing [7] under strong enough optical pumping.

In this experiment, nine different samples were realized by spin coating from toluene solution, with a fixed rotation speed of 2500 rpm. In order to change the film thickness, solutions with concentration from about  $4 \times 10^{-5}$  M to about  $3 \times 10^{-4}$  M were used, leading to thickness from about 35 nm to about 660 nm. In order to avoid the formation of the PF8  $\beta$  phase [14, 21, 22], the solution was heated at about 50°C for a few minutes [23].

Particular care was taken to minimize the role of random fluctuations of the measured quantities. In particular, all the PL spectra have been acquired by accumulating the signal due to 10 laser pulses, in order to minimize the effects of potential laser instabilities. Moreover, the sample thickness and the ASE threshold were measured in six different positions on the films, by using the average value as best estimate and the standard deviation as error bar.

The emission spectra of all the investigated samples showed the typical features of the PF8 glassy phase PL [13], with a 0-0 line at about 429 nm, followed by vibronic replicas at about 450 nm and 480 nm, evidencing the absence of  $\beta$  phase in the samples. As the incident excitation density increased, ASE was observed in all the samples with thickness above 48 nm. A strong thickness dependence of the ASE threshold was observed (see Fig. 2.13) with an initial decrease from about  $2.8 \text{ mJcm}^{-2}$  in sample S1 to  $47 \mu\text{Jcm}^{-2}$  in sample S5, and then a progressive increase up to about  $100 \mu\text{Jcm}^{-2}$  for samples S6-S9. This first result is interesting, as it is only partially consistent with the results of [16], in which only the initial threshold decrease with thickness is observed, without any evidence of increase in the high thickness range.

The origin of this thickness dependence was investigated by analyzing the role of several film properties, starting from the surface roughness, affecting the waveguide propagation losses. A similar and very low roughness of about 2 nm over about 100  $\mu\text{m}$ , was observed in all the samples, thus allowing to exclude that the ASE threshold differences come from a different active layer quality.

As further step, the role of the PL spectra lineshape variation with thickness was investigated, observing that the ASE peak

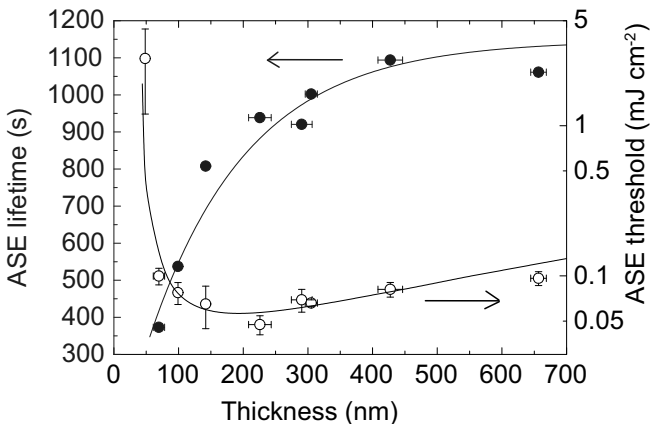


**Figure 2.13** Thickness dependence of the ASE lifetime (full dots) and of the ASE threshold (empty dots). The line across the lifetime data is a guide for the eyes, while the line across the threshold data is the best fit curves with Eq. 2.36. Reprinted from Ref. [19] with the permission of AIP Publishing.

wavelength shows a red-shift of about 5.5 nm from sample S1 to sample S3, followed by a weak peak wavelength thickness dependence. Actually, the ASE threshold is expected to decrease as the ASE wavelength approaches the 0-1 band peak wavelength. By using the PL intensity at the ASE wavelength, relative to the 0-1 peak one, in order to quantify the oscillator strength at the ASE wavelength (see Table 2.2), it was concluded that the observed ASE threshold variation with thickness cannot be ascribed to the different oscillator strength at the ASE wavelength. Actually, sample S1 had an oscillator strength comparable, within 1%, with samples S2–S4, but a much higher threshold. Moreover, samples S2–S4 and S5–S8 have comparable oscillator strength, within 1%, but clearly different thresholds.

The ASE threshold was then correlated to the active film waveguiding properties, quantitatively analyzed by numerically calculating the guided modes in all the samples, by using the experimental values of the PF8 and glass refractive index and of the film thickness. No guided modes were found at the ASE peak wavelength for PF8 thickness up to 43 nm, in agreement with the

**Table 2.2** Thickness of all the investigated samples, corresponding number of guided modes, ASE peak wavelength, and PL intensity at the ASE wavelength relative to the maximum 0-1 band one

Sample	Thick. (nm)	Modes	ASE peak (nm)	PL int.
S0	35 ± 7	0	-	-
S1	48 ± 3	1 (1 TE)	444.5	0.997
S2	70 ± 9	1 (1 TE)	449.2	0.988
S3	99 ± 5	2 (1 TE, 1 TM)	450.0	0.997
S4	142 ± 5	2 (1 TE, 1 TM)	451.4	0.997
S5	226 ± 17	2 (1 TE, 1 TM)	450.3	0.970
S6	290 ± 16	4 (2 TE, 2 TM)	450.5	0.974
S7	305 ± 9	4 (2 TE, 2 TM)	450.0	0.977
S8	427 ± 19	5 (3 TE, 2 TM)	450.8	0.967
S9	657 ± 12	8 (4 TE, 4 TM)	451.3	0.909

Source: Reprinted from Ref. [19] with the permission of AIP Publishing.

absence of ASE in sample S0, due to the absence of waveguiding in the active film.

Moreover, the further indication of the comparison between the simulation and the experimental results is that the apparently reasonable guess of threshold increase with the number of guided modes is instead not present. For example, samples S3–S5 (with two guided modes) show an ASE threshold lower than both samples S1 and S2 (with only one guided mode). Moreover, samples S3–S5 show different ASE threshold despite the same number and kind of guided modes.

These results then suggest that the ASE threshold is mainly dependent on the properties of the TE0 mode. The calculation of the mode profile allowed to determine the TE0 mode confinement [16] (MC) in the active layer as the ratio between the total electric field of the mode within the active films, relative to the total electric field of the mode, thus:

$$MC = \frac{\int_0^d E(z) dz}{\int_{-\infty}^{+\infty} E(z) dz} \quad (2.34)$$

where the z-axis is orthogonal to the air–PF8 film interface, with origin on the air–PF8 interface, and directed toward the PF8 layer (z is thus negative in the air layer),  $E(z)$  is the corresponding electric field of the TE0 mode, and  $d$  is the PF8 film thickness. The mode

confinement strongly and monotonically increases with the PF8 thickness (see Fig. 2.17), and this should lead to a corresponding continuous ASE threshold decrease, as observed by [16], again not explaining the increase in thick enough film. The main difference between these two similar experiments is the use of neat films instead of diluted binary blends between the active molecule and polystyrene. This results in a higher absorption coefficient at the pump wavelength, and then in a pronounced pump laser intensity decrease during the propagation in the active film. From the measurement of the absorbance thickness dependence, a PF8 absorption coefficient of  $\alpha = 6.5 \times 10^4 \text{ cm}^{-1}$  at  $\lambda = 337 \text{ nm}$  was estimated, corresponding to a pump laser penetration depth  $d_{\text{las}}$  in the PF8 film  $d_{\text{las}} \approx 155 \text{ nm}$ , which lies in the thickness range in which the ASE threshold was found to increase. This suggests that the observed ASE increase can be related to the transition between a situation in which the active waveguide is almost uniformly pumped (in section) and a situation in which only a region within 155 nm from the surface is strongly pumped, with the rest of the active film weakly excited. In other terms, the pump laser intensity exponentially decreases with the distance from the surface, due to the strong PF8 absorption. As the guided mode electric field maximum is closer to the PF8-glass surface than to the air-PF8 one (see Fig. 2.14), a PF8 layer thickness increase leads to a progressive decrease in the spatial overlap between the strongly pumped active layer region and the maximum electric field region. This was quantified by estimating the pump-mode overlap (PMO) as:

$$\text{PMO} = \frac{\int_0^d e^{-\alpha z} E(z) dz}{\int_0^d E(z) dz} \quad (2.35)$$

The PMO (see Fig. 2.17) is above 0.8 up to a PF8 thickness of about 70 nm, and it progressively decreases down to 0.2 as the thickness increases.

The ASE threshold can be correlated to the thickness dependence of both MC and PMO to the ASE threshold by simply observing that the ASE threshold is reduced both by an MC increase and by a PMO increase. Assuming the same functional dependence of the ASE threshold on both PMO and MC, the simplest decreasing function of

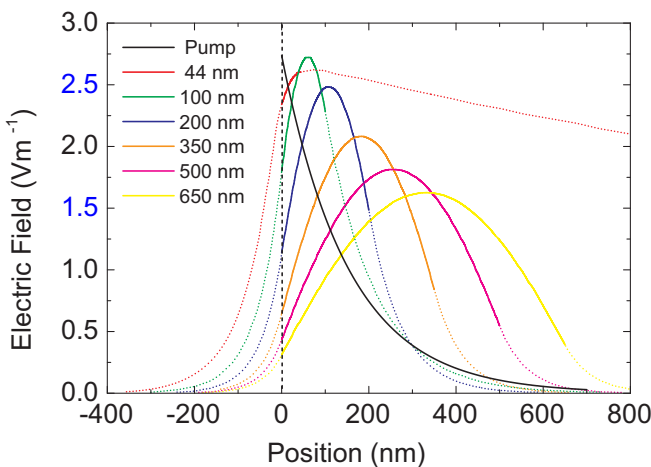


**Figure 2.14** TE0 mode electric field as a function of the position along the waveguide section. The dashed lines (for negative position) correspond to the air region, the thick continuous lines correspond to the active film, while the dash line on the right corresponds to the substrate region. The black curve represents the pump laser intensity decay due to PF8 absorption. Reprinted from Ref. [19] with the permission of AIP Publishing.

both PMO and MC is:

$$ASE_{th} = \frac{A}{PMO \cdot MC} \quad (2.36)$$

Excellent agreement between the experimental data and the simulated thickness dependence is obtained for  $A = 21.7 \mu\text{Jcm}^{-2}$  (see Fig. 2.13).

It can be then concluded that the observed ASE threshold thickness dependence has to be ascribed to the interplay between the increase in the mode confinement with the thickness, dominating at thicknesses below  $d_{\text{las}}$ , and the decrease in pump-mode overlap, dominating at higher thickness. This determines the presence of a minimum ASE threshold thickness and provides a first simple degree of freedom to maximize ASE in active films, by simply optimizing the waveguide thickness. From an applicative point of view, it is also important to underline that, as the thickness of minimum ASE threshold is determined by the pump laser penetration depth, the optimal thickness for low ASE threshold also

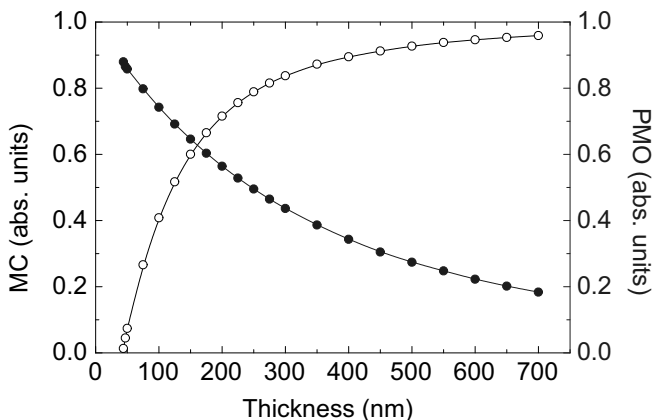


**Figure 2.15** Mode confinement (MC empty dots) and pump-mode overlap (PMO full dots) calculated from Eqs. 2.17 and 2.35 as a function of the waveguide thickness. The lines are guides for the eyes. Reprinted from Ref. [19] with the permission of AIP Publishing.

depends on the pump wavelength. In particular, the tuning of the pump laser close to the absorption maximum results in a lower penetration depth, and thus in a lower optimal thickness.

Similar experiments performed on neat films of spiro-quaterphenyl and its derivatives confirmed the existence of a thickness of minimum ASE threshold [24].

A further important operational aspect of the films showing ASE investigated by [19] is the ASE intensity stability during operation in air, which is clearly fundamental in order to candidate a material to real laser applications.

Rather surprisingly, the ASE operational stability received an extremely limited attention till relative recent times, with the only notable exception of the research group in Alicante, which often includes ASE stability measurements in the basic characterization of new materials for laser applications [25, 26].

In our experiment on PF8 waveguides, the ASE operational stability was investigated by measuring the sample emission spectrum every 5 s for 15 min, at an excitation density of  $2.2 \text{ mJcm}^{-2}$ . The ASE intensity showed (see Fig. 2.16) an exponential decrease with time in all the samples S2–S9 (sample S1 does not show

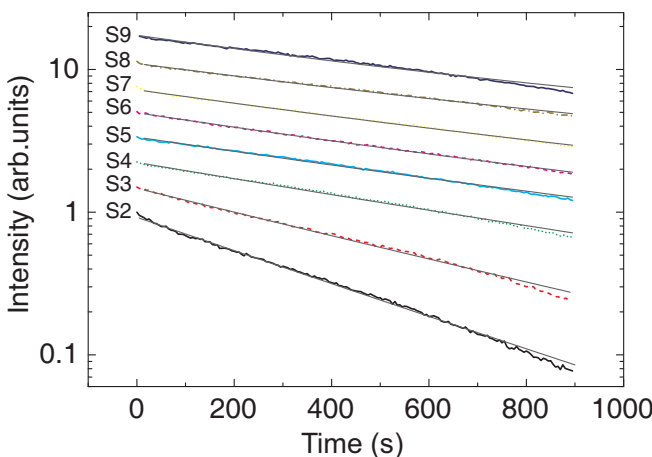


**Figure 2.16** Thickness dependence of the ASE intensity decay in time for an incident excitation density of  $2.2 \text{ mJcm}^{-2}$ , and best fit curves with Eq. 2.38 (gray lines) (the data are scaled for clarity). Reprinted from Ref. [19] with the permission of AIP Publishing.

ASE at  $2.2 \text{ mJcm}^{-2}$ ), with a decay time (see Fig. 2.13) (operational lifetime) increasing with the sample thickness up to the S7 sample, and similar for S7–S9 samples. This result is also not immediate to understand if one considers that the ASE intensity decrease should be caused by the PF8 photodegradation during the strong laser pumping. Actually the degradation rate is proportional to the incident pump photon flux, which is the same in all the measurements, and depends on the active molecule photostability (which is again identical for all the sample). Thus, no thickness dependence can be immediately guessed.

In order to explain the observed increase in the ASE operational lifetime  $\tau_{\text{ASE}}$  with thickness, it is useful to observe that the exponential decrease in the ASE intensity in time, together with the well-known almost exponential dependence of the ASE intensity on the net gain, indicates that each pump laser pulse induces the same active material net gain decrease. The ASE decay rate, which is directly proportional to the number of incoming pump laser photons per unit of time,  $I^p$ , can thus be written as:

$$k(z) = k_0 \cdot I^p(z) = k_0 \cdot I_0^p e^{-\alpha z} = k_{\max} e^{-\alpha z} \quad (2.37)$$

where the last two expressions consider the exponential decrease in the pump laser in the active film due to PF8 absorption. Considering the progressive pump laser intensity decrease with the depth in the active film, the superficial regions of PF8 will be more strongly pumped (thus more strongly emitting), but will also show a quicker ASE decay with time. As all the sample fraction with the same value of  $z$  will give ASE with the same decay rate, and as the exciton density (and thus the ASE intensity) also exponentially decreases with  $z$ , the ASE intensity of the whole film is given by:

$$I_{\text{ASE}}(t) = I_0 \frac{\int_0^d e^{-\alpha z} e^{-tk(z)} dz}{\int_0^{+\infty} e^{-\alpha z} dz} \propto \frac{1}{t} e^{-tk_{\max}} \left( e^{-tk_{\max}(e^{-\alpha d} - 1)} - 1 \right) \quad (2.38)$$

representing a weighted average of all the exponentially decaying ASE signals, weighted by the corresponding exciton density. Excellent agreement is found between the experimental decay dynamics and the best fit curves (see Fig. 2.16), obtained by fixing  $d$  and  $\alpha$  to the experimental values and by using only  $I_0$  and  $k_{\max}$  as free parameters. Similar values within the error bar of  $k_{\max}$  are found for PF8 thickness higher than 142 nm (samples S4–S9), with an average value of  $k_{\max} = (1.98 \pm 0.12) 10^{-3} \text{ s}^{-1}$ , while  $k_{\max}$  is found to increase for lower thickness to  $(2.54 \pm 0.07) 10^{-3} \text{ s}^{-1}$  in sample S3 and to  $(3.33 \pm 0.15) 10^{-3} \text{ s}^{-1}$  in sample S2. The stronger interaction rate in the thinnest samples suggests that the reactivity with oxygen is higher close to the sample surface than in the bulk of the film.

These results indicate that in thick samples, the possible light propagation in film regions far from the air surface, where optical losses are lower (due to lower photo-induced absorption and/or lower photodegradation), results in a slower ASE intensity decay.

Overall the obtained results indicate that a thickness increase of the active layer results in a desirable increase in the ASE operational lifetime, but also in an ASE threshold increase up to a factor of 2, which is evidently negative. The active layer thickness that allows the best compromise between high stability and low threshold can be determined by considering a waveguide quality factor defined as:

$$\text{QF} = \frac{\tau_{\text{ASE}}}{\text{ASE}_{\text{th}}} \quad (2.39)$$

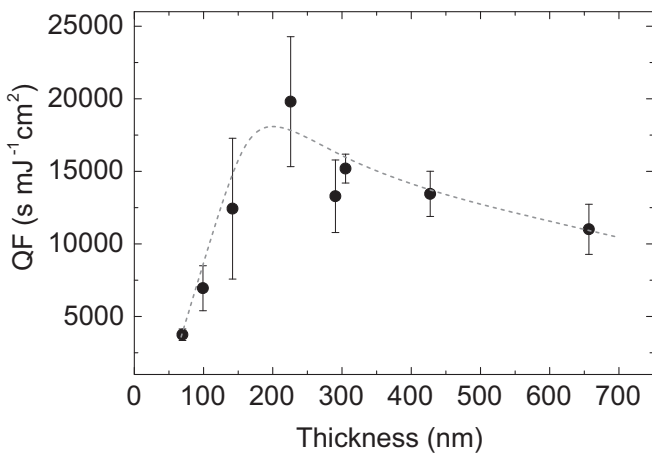


**Figure 2.17** Thickness dependence of the quality factor defined in Eq. 2.39 (the line is a guide for the eyes). Reprinted from Ref. [19] with the permission of AIP Publishing.

where  $\tau_{\text{ASE}}$  is the ASE intensity decay time obtained by a single exponential fit of the ASE decay dynamics. The experimental results (see Fig. 2.17) show that the quality factor increases up to four times from 50 nm to about 200 nm, and then decreases for higher thicknesses.

The demonstration of a film thickness that minimizes the ASE threshold and of a thickness dependence of the ASE operational stability can be extremely important in the field of organic lasers development, as the organic lasers with minimum threshold typically exploits distributed feedback (DFB) resonators in patterned waveguides. The DFBs lasing wavelength  $\lambda_{\text{las}}$  is determined by the Bragg resonance condition  $\lambda_{\text{las}} = 2n_{\text{eff}}\Lambda/m$ , where  $n_{\text{eff}}$  is the effective refractive index of the waveguide,  $\Lambda$  is the DFB pattern period, and  $m$  is the diffraction order. As the active material thickness increases,  $n_{\text{eff}}$  increases, thus resulting in a  $\lambda_{\text{las}}$  redshift (a similar effect is obtained increasing the pattern period  $\Lambda$ ). Most of the times, the DFB threshold is minimized only looking at the emission wavelength, in order to realize lasers emitting at the wavelength of maximum optical gain (coinciding with the ASE peak wavelength [27, 28]), acting on the active layer thickness and/or on the grating

period [27]. A recent systematic work, again from the Alicante group, investigated the lasing threshold dependence in organic DFBs on the grating depth and on the film thickness [29], obtaining evidences that the lasing threshold is affected by the TE0 mode confinement level. This result evidences how the lasing threshold can be optimized by first optimizing the waveguiding and ASE properties.

On the basis of our results on PF8 waveguides, we expect that the thickness-period combination resulting in minimum lasing threshold should be obtained in DFBs exploiting an active film with thickness leading to the minimum ASE threshold, and then by choosing the grating period that allows lasing at the maximum gain wavelength.

## 2.6 ASE Dependence on the Molecule Alignment

An interesting approach to minimize ASE threshold has been proposed some years ago by the R. Friend's group in Cambridge [30], with further works from the D. D. C. Bradley's group in London [31, 32], working on the active molecules alignment. The role of the molecule alignment direction on the ASE threshold can be understood considering that an elongated molecule interacts with external light basically as a linear antenna. The light absorption is then maximized when the incident light is linearly polarized along the molecule axis, and the single molecule PL is strongly linearly polarized along the same axis [33]. In an active film with randomly oriented molecules, as typically obtained by spin coating or drop casting, the total absorption of the pump laser light will be lower than the absorption of a film with the same number of molecules, in which the molecules are aligned along the pump laser polarization direction. For this reason, an active film with aligned molecules would allow to reach a given excitation regime with a lower laser pumping energy, with obvious advantages for eventual applications.

A further advantage of aligned films is related to the light emission properties. As in ASE experiments the sample is typically excited by a rectangular stripe pump laser, the stimulated emission would be maximized for directional spontaneous emission along the

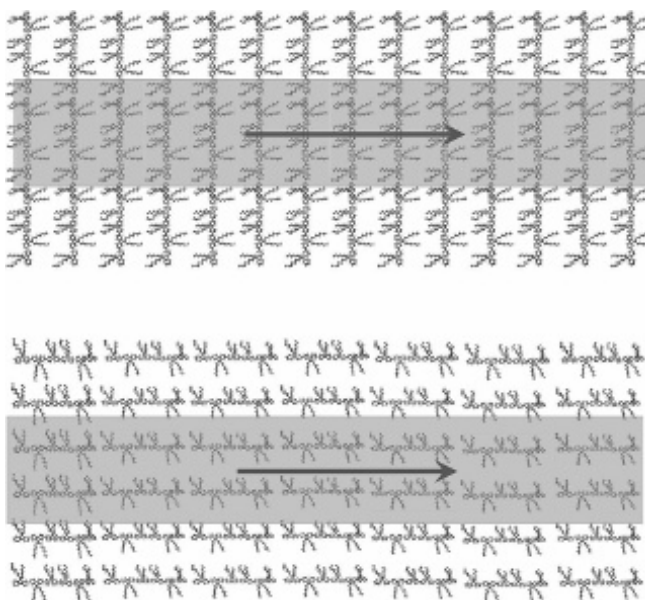


**Figure 2.18** Pictorial view of a film of PF8 with perfectly aligned molecules in vertical (top) and horizontal direction (bottom). The central rectangle represents the pumped stripe, while the arrow indicates the light amplification direction.

pump stripe. Actually a linear antenna does not radiate isotropically, but it mainly radiates in the plane perpendicular to the antenna axis. For this reason, a sample with molecules aligned perpendicularly to the pump stripe would have a larger fraction of spontaneous emission emitted along the pump stripe, and thus a stronger ASE than an isotropic sample. A practical demonstration of the role of alignment on the ASE properties of a polymeric thin films has been obtained both on poly-di-octyl-fluorene (PF8) films [31] and on poly(9,9-di-octylfluorene-co-benzothiadiazole) (F8BT) [32]. The aligned active films were obtained by spin coating on a spectrosil substrate, covered by a thin (about 30 nm) polyimide (PI) layer, mechanically rubbed to act as an alignment layer for the active polymer. Alignment was then achieved by annealing the samples in nitrogen atmosphere, followed by slow cooling and finally rapid quenching down to room temperature.

The ASE properties of the films were then investigated both with molecules aligned perpendicularly to the stripe and along the stripe, and for two different pump laser polarizations (perpendicular or parallel to the stripe) (see Fig. 2.18). The lowest threshold (about  $30 \mu\text{Jcm}^{-2}$ ) was obtained with PF8 molecules aligned perpendicularly to the stripe, and laser polarized along the alignment direction, as qualitatively expected. The polarization of the pump laser along the stripe resulted in less efficient absorption and thus in higher threshold (about  $73 \mu\text{Jcm}^{-2}$ ). When the molecules are aligned along the stripe, the ASE threshold continues to increase up to  $108 \mu\text{Jcm}^{-2}$  if the pump laser is polarized along the alignment direction and up to  $180 \mu\text{Jcm}^{-2}$  when the pump laser polarization direction is perpendicular to the molecule alignment direction. Overall the ASE threshold in the best configuration was found to be about six times lower than the one of the worst configuration. The molecule alignment resulted also in strong differences in the output intensity as well as in the slope efficiency, with a difference between the best and the worst case of about 14 times. The ASE properties were also investigated in standard spin-coated samples obtaining a threshold about two times larger than the best one, and a slope efficiency about two times lower. Overall, this experiment and the similar work on F8BT clearly show that the molecule alignment optimization is a powerful way to reduce the ASE threshold.

## 2.7 ASE Dependence on the Film Morphology

Among the interest reasons of organic active molecules, there is the possibility to deposit thin films of many materials starting from solutions, and using different techniques, such as spin coating, doctor blading, drop casting, spray coating, and screen printing. The final physical properties of the film is determined by the interplay of several factors, such as the molecule solubility in the used solvent, the solvent evaporation rate, the possibility to have aggregation, and so on. For these reasons, in many cases the use of different deposition conditions results in the realization of films with strongly different optical and/or electrical properties. A nice example of this aspect is again given by PF8, in which films with different

quantities of the glassy and  $\beta$  phases, and with completely different morphology can be obtained by simply changing the solvent used to prepare the solution to be spin coated [14]. Given the common chemistry aspects of the active molecule solubilization and of the film formation during the solvent evaporation, we can safely say that the variation of the deposition conditions typically leads to different morphology, aggregation, roughness, optical and electrical properties in any organic thin film (of course with quantitative variations depending on the specific investigated system).

The possibility to realize films with different properties starting from a given chemical structure of the active molecule can be considered a degree of freedom in the optimization of the specific properties of the film of interest but also, on the other side, an issue to address in order to really understand the intrinsic properties of the investigated system in a given experiment. The dependence on the morphology of the active properties of organic thin films, modified by changing the deposition conditions and eventually by performing some postdeposition sample processing, has been clearly demonstrated with regard to the photoluminescence efficiency [34], electroluminescence efficiency [35, 36], and photovoltaic efficiency [36, 37] of organic systems.

On the contrary, rather surprisingly, the morphology dependence of the optical gain of organic waveguides has received a very limited attention, despite the evidence that ASE depends on the solvent used for the spin coating already in the first paper demonstrating ASE from MeHPPV neat films [38]. Up to the end of 2015, the only exceptions, to the best of our knowledge, were a couple of studies on the morphology dependence of the ASE of MeHPPV, with the investigations of the thermal annealing effects [39, 40] indicating that, despite the morphology variation, the thermal annealing does not significantly affect the ASE properties up to about 80°C, while it drastically reduces the ASE at 120°C. A further experiment investigated the role of the solvent used for the deposition, suggesting that the solvent-dependent MeHPPV aggregation has marginal effects on the ASE properties [41].

In the next two subsections, we will present two clear examples on the importance of the local morphology in determining the ASE properties of active films based on polymer:polymer host:guest

systems. In the first experiment, we compared the ASE properties of four nominally identical films, with the same composition and the same thickness, deposited by spin coating from four different solvents [42]. In the second experiment, we correlated the ASE properties to the local morphology of eight host:guest blends with different relative composition [43].

### 2.7.1 Minimization of the Amplified Spontaneous Emission Threshold by Optimization of the Micromorphology

In the first experiment, we investigated the ASE properties of spin-coated film of regio regular-poly(3-hexylthiophene) (rrP3HT): poly(9,9-dioctylfluorene-co-benzothiadiazole) (F8BT) blends as a function of the film morphology, changed by using different solvent for the solution preparation [42]. The ASE and optically pumped lasing properties of this active blend have been recently deeply investigated [44] as a function of the F8BT:rrP3HT relative content, in films deposited by spin coating from toluene. The samples are mainly made by F8BT, which is thus the material mainly excited by the pump laser, while rrP3HT is efficiently excited by FRET from F8BT. This system is particularly relevant as it shows ASE close to 650 nm, which is a strategic wavelength for polymethylmethacrylate (PMMA)-based polymer optical fiber (POF) data-communications.

The samples were realized by spin coating of a F8BT:rrP3HT blend with a relative concentration of 80:20 in weight, which is the one of minimum ASE threshold [44], in four different solvents, namely chloroform, toluene, chlorobenzene, and xylene. All the samples have the same thickness, of about 130 nm (within more or less 10 nm).

All the samples show similar PL spectra at low excitation density, dominated by the rrP3HT PL. As the rrP3HT is the minority component of the blend, this is an indication that efficient FRET from F8BT to rrP3HT takes place. As the excitation density increases, a clear ASE band at about 662 nm is observed in the spectra of all the samples, progressively dominating the spectra (see Fig. 2.19 for the sample from toluene and Fig. 2.20 for the sample from xylene). Despite the qualitatively similar excitation density dependence of

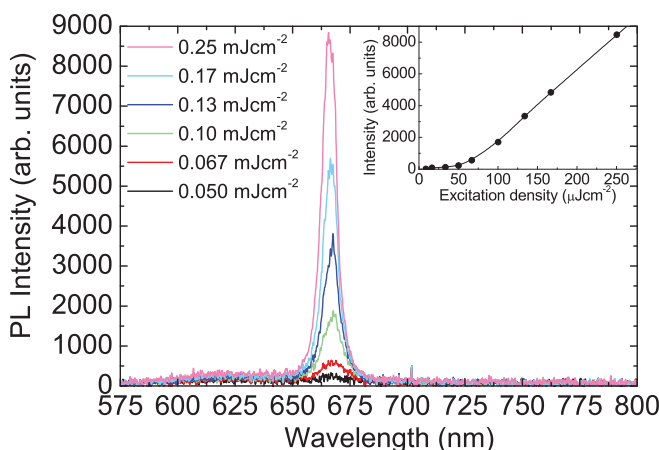


**Figure 2.19** Excitation density dependence of the PL spectra of the sample spin coated from toluene. Inset: Excitation density dependence of the intensity at the ASE band peak wavelength, evidencing the superlinear intensity increase above threshold (the line is a guide for the eyes). Reproduced with permission from Ref. [42], Copyright 2015 American Chemical Society.

the PL spectra in all the samples, clear differences are observed in the excitation density necessary to observe ASE in the spectra, evidencing differences in the ASE threshold.

The ASE threshold was estimated from the excitation density dependence of the PL spectra FWHM (see inset of Fig. 2.21), as the excitation density at which the linewidth decreases down to one half of the low excitation density value. The minimum ASE threshold, of about  $45 \mu\text{Jcm}^{-2}$ , is observed in the sample from toluene (see Fig. 2.21), followed by the samples from chlorobenzene ( $54 \mu\text{Jcm}^{-2}$ ), chloroform ( $116 \mu\text{Jcm}^{-2}$ ), and xylene ( $340 \mu\text{Jcm}^{-2}$ ). The huge difference between the highest and the lowest ASE threshold (about eight times), in samples with identical composition and thickness, clearly evidences that the solvent choice is critical in determining the ASE properties.

A first step, helpful to understand the origin of the ASE threshold behavior, is the separate measurement of the waveguide net gain  $g'$  and of the propagation losses  $\alpha$ . Remembering that the net gain  $g'$  is related to the waveguide gain  $g$  and to  $\alpha$  by the relation

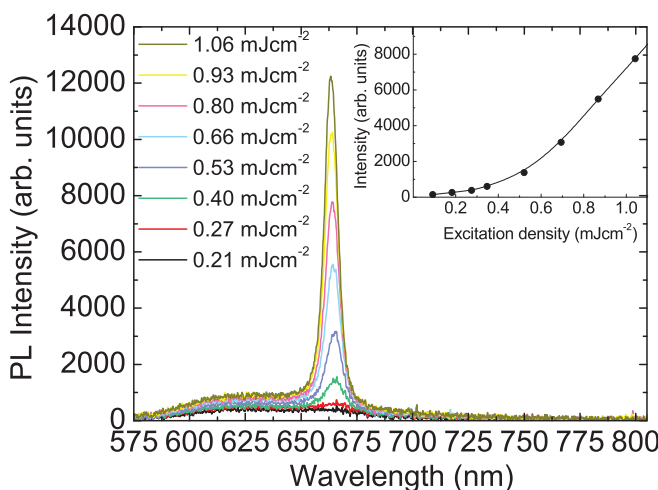


**Figure 2.20** Excitation density dependence of the PL spectra of the sample spin coated from xylene. Inset: Excitation density dependence of the intensity at the ASE band peak wavelength, evidencing the superlinear intensity increase above threshold (the line is a guide for the eyes). Reproduced with permission from Ref. [42], Copyright 2015 American Chemical Society.

$g' = g - \alpha$  and that  $g = \sigma N$ , where  $\sigma$  is the gain cross section and  $N$  the population inversion density, an ASE threshold variation can be due to a variation of the losses  $\alpha$ , or of the gain  $g$ , or to a combination of both. Moreover, an eventual variation of  $g$  can be also due to a variation of the active molecule gain cross section, or to a variation of the value of  $N$  for a given excitation density, reflecting for example a variation in the sample absorption or in the active molecule excitation process. Given the wide range of different situations leading to the same kind of variation of the ASE threshold, the possibility to separate the contribution of  $g$  and  $\alpha$  to  $g'$  is extremely useful.

In the present case, we measured a maximum net gain value  $g' = 21.4 \text{ cm}^{-1}$  in the sample form toluene (see Fig. 2.22), with a progressive decrease to  $17.4 \text{ cm}^{-1}$  in chlorobenzene,  $13.4 \text{ cm}^{-1}$  in chloroform, and  $7.6 \text{ cm}^{-1}$  in xylene. This trend is qualitatively consistent with the observed progressive ASE threshold increase in the same solvents order. By looking at the  $\alpha$  values, we observe a

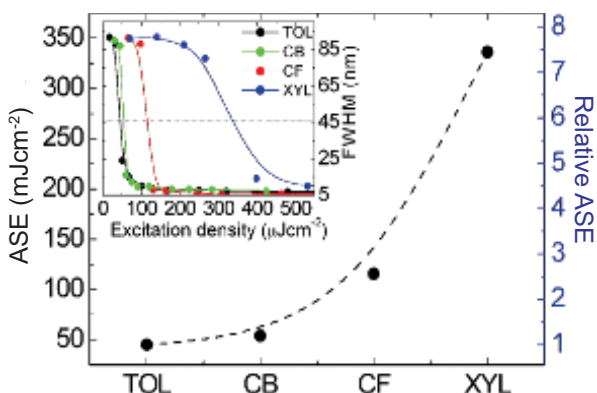


**Figure 2.21** ASE threshold of all the investigated samples. Inset: Excitation density dependence of the full width at half maximum (FWHM) of the PL spectra of the four samples. The continuous line indicates a linewidth of 50% of the low excitation density FWHM value. Reproduced with permission from Ref. [42], Copyright 2015 American Chemical Society.

minimum value of  $1.7 \text{ cm}^{-1}$  in the sample from toluene, followed by a remarkable increase to  $7.7 \text{ cm}^{-1}$  in chlorobenzene, and then a progressive decrease to  $5.3 \text{ cm}^{-1}$  in chloroform and  $2.4 \text{ cm}^{-1}$  in xylene. Concerning the  $g$  values obtained from the previous  $g'$  and  $\alpha$  values, we observe that the best sample for ASE (from toluene) does not show the maximum gain, showing a gain value of  $23.1 \text{ cm}^{-1}$ , which is lower than the one of the chlorobenzene sample of  $25.1 \text{ cm}^{-1}$ . Thus, the sample from toluene shows a lower ASE threshold than the chlorobenzene one, as it shows much lower losses, which compensate the lower gain. The further ASE threshold increase in chloroform and xylene is due to a progressive decrease in the gain to  $18.7 \text{ cm}^{-1}$  and  $10 \text{ cm}^{-1}$ , respectively, despite the progressive reduction in the propagation losses to  $5.3 \text{ cm}^{-1}$  and  $2.4 \text{ cm}^{-1}$ , respectively. We can thus conclude that the solvent strongly affects both the gain and the losses, thus determining the observed strong ASE threshold variations.

The further step in the sample characterization was based on confocal laser spectroscopy mapping of the F8BT and of the rrP3HT PL in all the samples, aiming to understand the microscopic origin of the observed gain and losses solvent dependence.

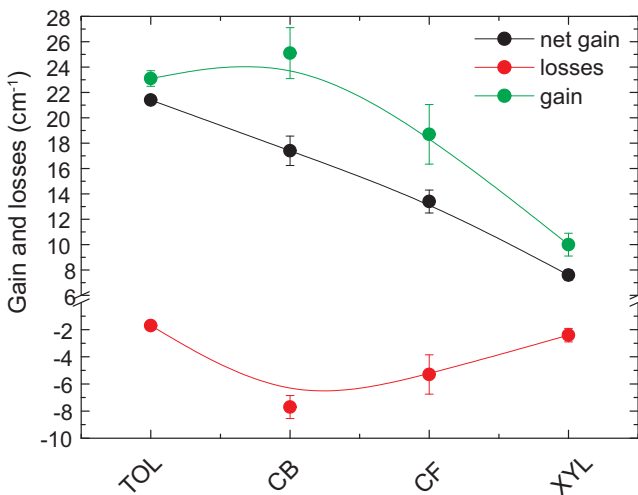


**Figure 2.22** Gain, loss, and net gain as a function of the solvent. Reproduced with permission from Ref. [42], Copyright 2015 American Chemical Society.

Going in order of increasing ASE threshold, we observed that the F8BT and rrP3HT PL maps of the film from toluene show uniform PL intensity (see Fig. 2.23), without relevant morphology and optical properties irregularities. A few bright spots are visible only in the rrP3HT map, and thus ascribed to rrP3HT clusters, with an average size of about  $9\text{ }\mu\text{m}$  and a surface density of about  $65\text{ clusters/mm}^2$ .

Very similar features are observed in the sample from chlorobenzene, with uniform F8BT and rrP3HT PL maps, and with an evidently higher (about five times) surface density of bright rrP3HT clusters.

The sample from chloroform shows instead a clearly non-uniform emission, with very evident dark and bright stripes, both in the F8BT and in the rrP3HT PL maps. These structures are also observed in standard transmission microscopy and are due to thickness ondulation (measured by profilometry). The characteristic lateral size of the stripes is about  $100\text{ }\mu\text{m}$  with a peak to valley height of about  $150\text{ nm}$ .

The stripes are mainly oriented along the radial direction, suggesting their formation during the spin coating, due to the fast chloroform evaporation.

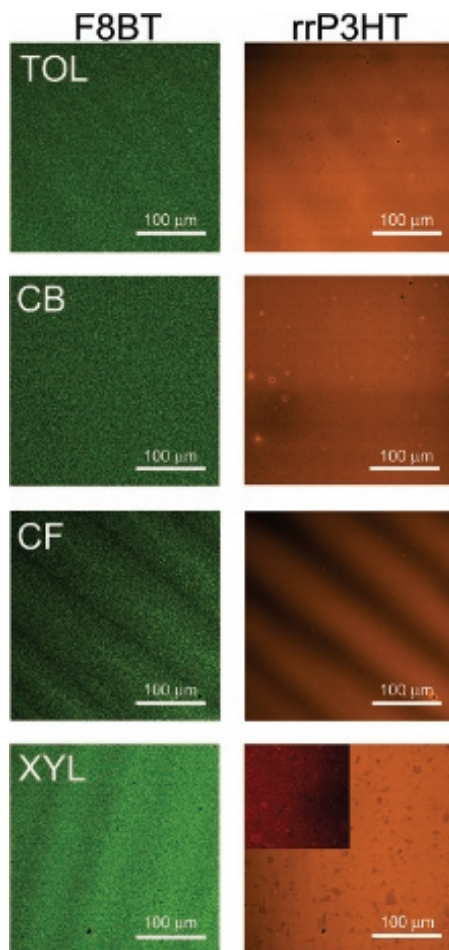


**Figure 2.23**  $300 \mu\text{m} \times 300 \mu\text{m}$  confocal PL maps at 530 nm (left) and 605 nm (right) for the different solvents. Reproduced with permission from Ref. [42], Copyright 2015 American Chemical Society.

A careful observation of the position of high PL intensity allows to observe that the F8BT and rrP3HT PL maps are almost complementary, with the regions of high F8BT PL coinciding with the low rrP3HT PL intensity regions (see Fig. 2.24). The different spatial dependence of the F8BT and rrP3HT demonstrates that the fast solvent evaporation during the film spin coating results

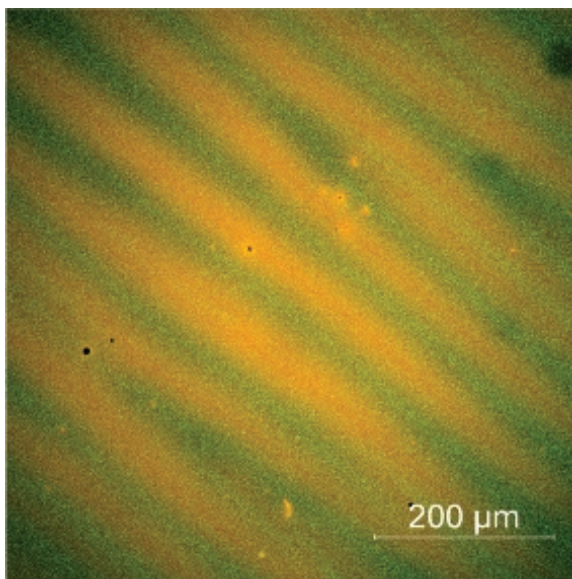


**Figure 2.24**  $650 \mu\text{m} \times 650 \mu\text{m}$  confocal PL maps of the film from chloroform showing the superposition of the green F8BT PL with the orange rrP3HT one. The local color variation, with almost fully green stripes alternated to almost completely orange stripes evidences the anticorrelation of the blend component PL in correspondence of the thickness fluctuations.

not only in thickness fluctuations, but also in a non-uniform local relative composition of the blend. This local composition variation leads to non-uniform FRET from F8BT to rrP3HT and thus to anticorrelated local PL intensity of the two materials. Moreover, a higher rrP3HT aggregation is expected in the rrP3HT richer zones, resulting in lower PL quantum yield and lower optical gain. Beyond the thickness fluctuation effects, some bright clusters of rrP3HT with a typical size of about  $8 \mu\text{m}$  are also observed, with a surface density of about  $80 \text{ clusters/mm}^2$ .

Concerning the sample from xylene, a uniform F8BT PL map is observed, while dark rounded islands are observed in the rrP3HT map, with an average diameter of about  $15 \mu\text{m}$  and a surface density of about  $900 \text{ islands/mm}^2$ . Starting from the observation that no visible F8BT PL variation is observed in correspondence of the dark

rrP3HT island, we can exclude that this effect is related to a locally smaller thickness. The origin of these features can be understood by mapping the PL at different wavelengths. In particular it is well known that rrP3HT shows a PL spectrum lineshape depending on its aggregation level, with aggregate PL redshifted with respect to the non-aggregated polymer one [45]. We thus measured the PL map at  $\lambda > 700$  nm (see inset of Fig. 2.23), observing that all the islands dark at 605 nm are instead bright above 700 nm, clearly evidencing that in these islands, rrP3HT is mainly in an aggregated phase.

The confocal mapping of the four investigated samples, which we remember once again have the same thickness, same components, and same relative composition in the blend, and which are nominally identical, allows to observe several kinds of local differences, both in the morphology and in the optical properties, which allows a microscopic understanding of the origin of the macroscopically different ASE, gain and losses behavior.

Concerning the gain value, we observe that the highest and very similar values are observed in the samples from toluene and from chlorobenzene, which are the only two samples showing uniform PL maps. This property evidences a generally uniform morphology and blend composition. As the relative composition of the blend is the one of maximum gain, in these samples the composition is locally uniformly coincident with the maximum gain one, and the best gain values are obtained.

When the solvent is chloroform, the film composition is non-uniform, resulting in a macroscopic ideal composition that microscopically comes from the combination of regions with more than 20% in weight of rrP3HT and with regions with local content lower than 20%. The first regions are not optimal for optical gain due to the rrP3HT aggregation, while the last ones are not optimal due to the not optimized FRET from F8BT. Thus, even if the total relative content of rrP3HT is the optimal one, the sample has overall a not optimized composition, resulting in a decreased value of the optical gain.

Finally, remembering that rrP3HT aggregation is known to be detrimental for ASE, resulting in the absence of ASE in rrP3HT neat films [44], the presence of the minimum gain in the sample

deposited from xylene can be easily understood. More clearly this sample shows a high density of aggregated rrP3HT not showing optical gain, which reduce the total gain of the film.

The solvent variation of the waveguide losses can be also explained again starting from the best sample. In the sample from toluene, the only evident local non-uniformity is the presence of the rrP3HT clusters, leading to light scattering during the propagation along the pumped stripe. The attribution of the losses to the scattering from the clusters is also confirmed by the very good agreement between the losses increase in chlorobenzene sample (about 4.5 times) and the cluster density increase (about five times). These two films thus show an optimized gain and an ASE threshold determined by the scattering rrP3HT cluster density.

The sample from chloroform instead shows a cluster density similar to the toluene one, but higher losses. Moreover, very evident thickness fluctuations are present in the sample, also leading to scattering due to the local variation of the waveguide refractive index at any fluctuation. Considering that the toluene sample shows losses of  $1.7 \text{ cm}^{-1}$ , a similar cluster contribution to the chloroform sample losses can be assumed. As the total losses of the CF sample are  $5.3 \text{ cm}^{-1}$ , the thickness irregularities contribution to the losses can be estimated in  $5.3 - 1.7 = 3.6 \text{ cm}^{-1}$ , thus indicating that the main channel of waveguide losses in the chloroform sample is given by the scattering from thickness non-uniformity.

Finally, the sample from xylene shows losses about 40% larger than the toluene sample, but a very large density of islands (about 14 times larger than the cluster density of the toluene sample). This result suggests a low scattering cross section from the aggregated rrP3HT islands, which is consistent with a low refractive index contrast due to the local variation of the aggregation state of the minority component of the blend.

This experiment allows to learn two main lessons. The first is again that the use of the ASE threshold value as an indicator of the intrinsic potential of a given molecule for lasers application is extremely dangerous, as very different threshold value can be obtained even in samples with the same composition but simply deposited from different solvent. From the applicative point of view, and reversing the perspective, the strong dependence of the ASE

threshold on the local morphology and composition of a film, and the possibility to strongly vary these aspects by simply changing the solvent used for the film deposition, provide a potentially extremely powerful degree of freedom for the ASE threshold minimization (and thus for the net gain maximization) in a given material of interest. According to our results, it is reasonable to guess that at least some of the materials to date considered *not interesting* for organic lasers due to the high value of the ASE threshold (or accordingly to the low value of the optical gain) are actually potentially good materials simply deposited from the wrong solvent. In a similar way, we cannot exclude that even some of the good and interesting materials could have further margins of gain optimization by performing the proper microscopic morphology, composition, and molecular arrangement optimization.

### **2.7.2 Unexpected Composition Dependence of the ASE Properties of Polymer:Polymer Blends—The Case of PF8:F8BT**

As last example of the physics of organic materials that can be described starting from the ASE properties investigation, in this subsection we present a recent study of our group on the ASE dependence of a polymer:polymer donor:acceptor blend on the relative composition [43]. The relative composition of host:guest blends typically modifies the ASE, gain, and lasing properties of the blend. As the guest concentration increases, the FRET efficiency increases, thus increasing the guest excitation level for a given pumping regime, and thus increasing the gain at a fixed pumping energy density. This effect thus leads to an ASE threshold reduction. On the other side, the guest concentration increase can result in aggregation and/or intermolecular energy migration, thus reducing the PLQY and the optical gain. The increase in the guest content in the blend thus results in an ASE threshold decrease, eventually followed by an increase due to the aggregation for high enough content values. In the first case, the ASE threshold decreases down to a saturation value [46], while in the last case, a minimum ASE threshold is obtained resulting from the interplay between the FRET increase and the aggregation increase effects, thus determining the

existence of an optimal concentration minimizing the acceptor ASE threshold [44].

However, the previous discussion is correct only under the implicit hypothesis of uniform films, concerning composition, intermolecular interaction, and component molecule optical properties. This is apparently reasonable in films deposited from a solution (very likely uniform) by using a dynamic and fast process such as spin coating. Anyway in the specific case of polymer:polymer blends, the film homogeneity hypothesis is an oversimplification of the system, violating the famous aphorism, sometimes ascribed to Albert Einstein, *everything should be made as simple as possible, but not simpler*, that basically reformulates the Occam's razor principle.

Actually the microscopic properties of fully polymeric blends are guided by thermodynamics and miscibility basic aspects, often resulting in micro/nano morphologies very far from uniformity, including for example phase-separation. This aspect is very well documented both regarding the theory of polymer blends film formation and the experimental characterization of the possible observable effects of non-uniform mixing, both in books and in research paper (see for example [47, 48]). Concerning applications, the knowledge and control of the phase separation at the nanoscale are, for example, fundamental for the realization and optimization of bulk heterojunction solar cells, and it has thus deeply investigated in the field of organic photovoltaics. On the contrary, the correlation between the ASE properties and the eventual phase separation in the active blend has not been investigated in detail, despite the clear evidence that phase separation leads to local variations of both the FRET rate [47] and the acceptor PLQY [49], thus likely modifying the final ASE properties of the film.

The investigated blend is based on two well-known and commercially available organic polymer, already used in other experiments described in this chapter, namely PF8 and F8BT.

Eight different samples have been realized with an F8BT relative content in weight of 5%, 10%, 25%, 50%, 75%, 90%, 95%, and 100% (the samples will be named  $x$ -F8BT in the following, where  $x$  is the F8BT percentage in the blend). In all the samples, the PL spectra are dominated by the F8BT luminescence, evidencing an overall high FRET from PF8 to F8BT. On the contrary, a strong

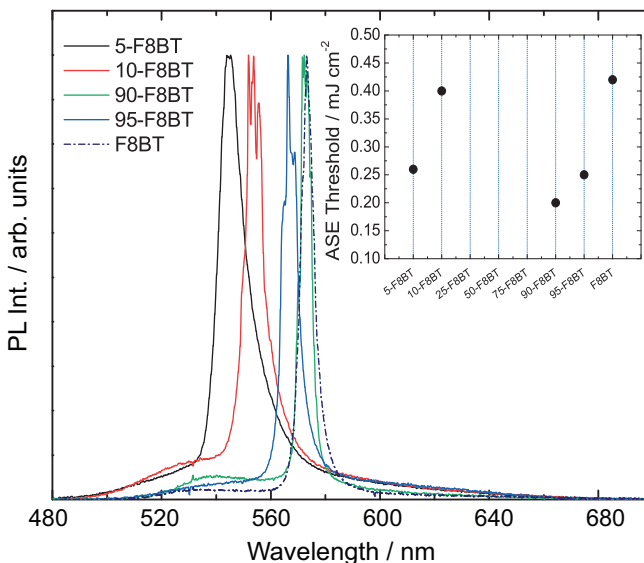


**Figure 2.25** PL spectra above the ASE threshold of the samples showing ASE. Inset: ASE threshold dependence on the F8BT content of the blend. Reproduced from Ref. [43] with permission from Elsevier.

dependence of the ASE properties on the F8BT content is observed. In particular, the 5-F8BT sample shows ASE (see Fig. 2.25), with a threshold of about  $0.26 \text{ mJcm}^{-2}$ . The F8BT increase to 10% still allows to have ASE, but with a threshold increase to  $0.39 \text{ mJcm}^{-2}$  (see inset of Fig. 2.25). When the F8BT content is further increased, the ASE disappears and no ASE is observed in the 25-F8BT, 50-F8BT, and 75-F8BT samples. For still higher F8BT content, ASE is recovered, with a threshold of about  $0.20 \text{ mJcm}^{-2}$  in the 90-F8BT sample increasing to  $0.25 \text{ mJcm}^{-2}$  in the 95-F8BT sample and to  $0.40 \text{ mJcm}^{-2}$  in the neat F8BT sample.

This ASE evolution is clearly different from the results expected for the interplay between the FRET and the aggregation concentration dependence, typically leading to an initial ASE threshold decrease, followed by an increase in the high acceptor content range.

We thus tried to understand the origin of our nonstandard results, starting from the investigation of the macroscopic properties

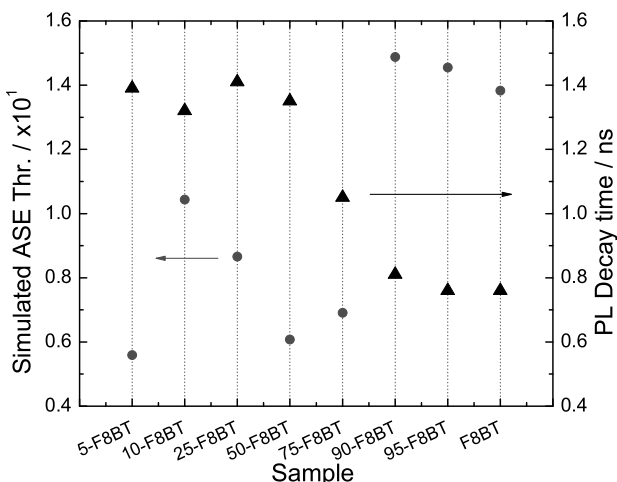


**Figure 2.26** Simulated ASE threshold (circles) and PL decay time (triangles) of the analyzed X-F8BT samples. Reproduced from Ref. [43] with permission from Elsevier.

of the samples, considering as first the waveguiding properties, with the same approach described in Section 2.5.1. The waveguiding properties have been modeled considering the experimental values of the film thickness and estimating the film refractive index as a weighted average of the component materials refractive indexes, using the relative content in the blend as weights. The F8BT content dependence of the simulated ASE threshold values (see Fig. 2.26) is very different from the experimental results, with the only exception of the threshold increase from 5% to 10% of F8BT. In particular, the films that do not show ASE have better waveguiding properties both than the 10-F8BT sample (between 20% and 40%) and the 90-F8BT sample (up to 2.5 times). This discrepancy clearly demonstrates that the ASE threshold content dependence is not mainly determined by the differences in the waveguiding properties of the films.

As a further step, we quantitatively investigated the intermolecular energy migration within F8BT molecules by time-resolved PL measurements. The F8BT relaxation dynamics is monoexponential, with an almost F8BT content independent decay time of about 1.35 ns up to the 50-F8BT (see Fig. 2.26), and a progressively

decreasing decay time for higher F8BT contents, down to 0.78 ns in the neat F8BT film. This behavior is consistent with the progressive increase in the intermolecular energy migration rate within the F8BT density of states, which allows exciton migration toward defect states and decreases the F8BT PLQY.

Again a comparison of the concentration dependence of the F8BT decay time and of the ASE threshold allows to observe the lack of clear correlation. In particular, the energy migration is basically absent up to at least 50% of F8BT in the blend, while the ASE disappears already for a content of 25%. Moreover, the samples with 90%, 95%, and 100% of F8BT show the shortest decay times, thus the maximum energy migration rate, but also show ASE. In other terms if the ASE was suppressed due to some concentration quenching effect, it should not be present in the three samples with the maximum F8BT content. Overall the macroscopic ASE properties of the film are thus neither mainly determined by the waveguiding properties, not by the total exciton relaxation dynamics.

We then explored the microscopic PL and morphology by confocal mapping, in order to correlate the measured ASE properties and the spatial features of the F8BT PL maps. The PL maps in the F8BT PL spectral region (see Fig. 2.27) show a uniform PL intensity, with a comparable density of micrometric F8BT clusters. On the contrary, a clear phase segregation of F8BT is observed in the samples without ASE, with evident rounded micro-islands with higher PL intensity, and a characteristic size spanning from about 1  $\mu\text{m}$  in the 75-F8BT sample down to about 0.5  $\mu\text{m}$  in the 25-F8BT sample (comparable to the confocal microscope lateral resolution, thus possibly resolution limited). The lack of uniformity is observed also in the PF8 PL spectral range, evidencing local differences in the blend composition, and thus in non-uniform FRET and F8BT aggregation (see Fig. 2.28). Moreover, the lack of thickness uniformity is also expected to lead to light scattering during the waveguide propagation, increasing the propagation losses, and thus further compromising the ASE properties.

In this last case, we could thus conclude that the macroscopic ASE properties of the blend samples are mainly determined by the microscale mixing properties of the component polymers, leading to overall ASE properties very different from the ones expected

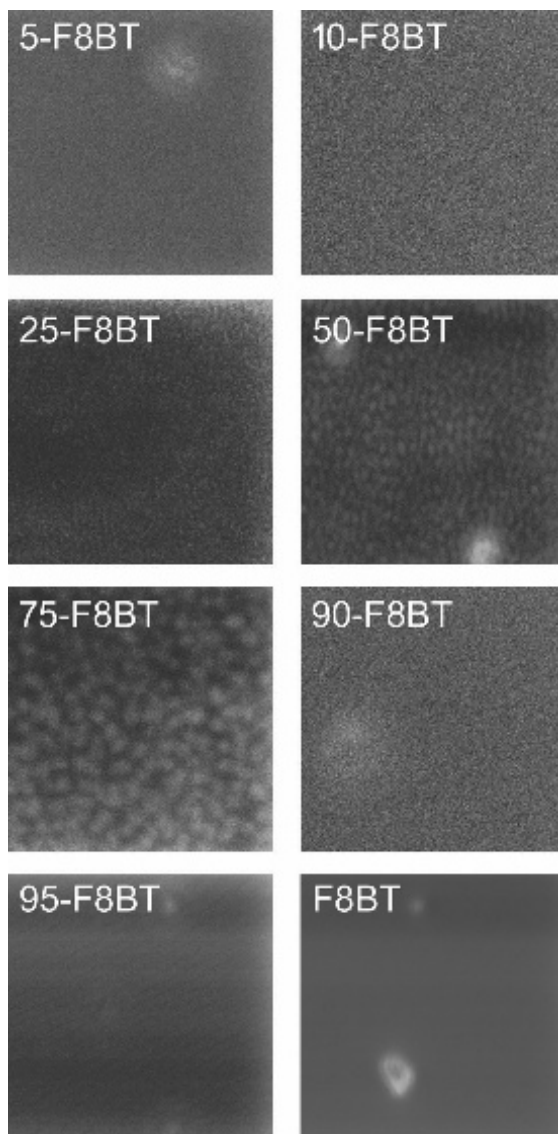


**Figure 2.27** 15  $\mu\text{m} \times 15 \mu\text{m}$  confocal PL maps in the F8BT PL spectral region. Uniform maps are observed in the samples 5-F8BT, 10-F8BT, 90-F8BT, 95-F8BT, and neat F8BT, all showing ASE. On the contrary, F8BT segregation is evident for samples 25-F8BT, 50-F8BT, and 75-F8BT, with progressively increasing segregation domains size, all not showing ASE.

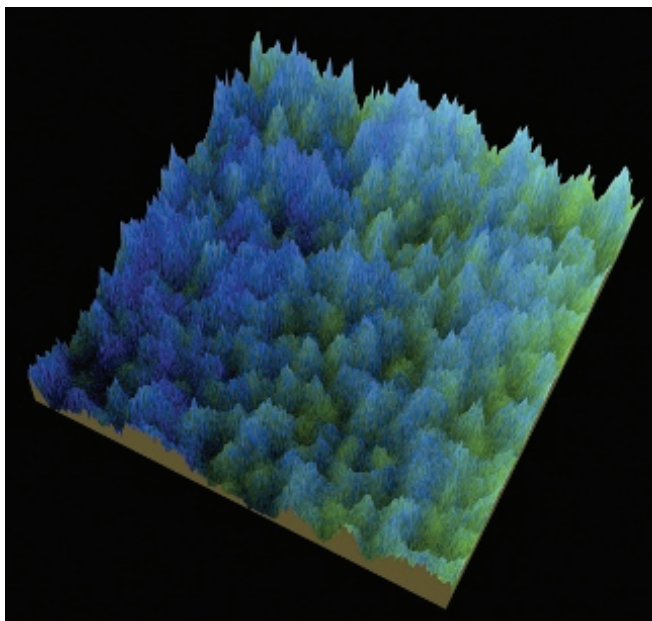


**Figure 2.28** Three-dimensional rendering of  $15 \mu\text{m} \times 15 \mu\text{m}$  confocal PL maps of the sample 75-F8BT showing the overlap of the blue PF8 PL and the green F8BT one. The micro-island segregation of the two materials and their different spatial distribution are evident.

for uniform active films. Once more this experiment evidences how the photophysics of conjugated molecule thin films can be strongly affected by fine properties, most of the time neglected in the qualitative description of the active films.

## References

1. Bernius, M. T., Inbasekaran, M., O'Brien, J., and Wu, W. S. (2000). Progress with light-emitting polymers, *Adv. Mater.* **12**, pp. 1737–1750.
2. Sirringhaus, H., Wilson, R. J., Friend, R. H., Inbasekaran, M., Wu, W., Woo, E. P., Grell, M., and Bradley, D. D. C. (2000). Mobility enhancement in conjugated polymer field-effect transistors through chain alignment in a liquid-crystalline phase, *Appl. Phys. Lett.* **77**, pp. 406–408.

3. Anni, M. and Rella, R. (2010). Oxygen optical gas sensing by reversible fluorescence quenching in photo-oxidized poly(9,9-dioctylfluorene) thin films, *J. Phys. Chem. B* **114**, pp. 1559–1561.
4. Halls, J. J. M., Arias, A. C., MacKenzie, J. D., Wu, W., Inbasekaran, M., Woo, E. P., and Friend, R. H. (2000). Photodiodes based on polyfluorene composites: Influence of morphology, *Adv. Mater.* **12**, pp. 498–502.
5. Cadby, A. J., Lane, P. A., Mellor, H., Martin, S. J., Grell, M., Giebelter, C., Bradley, D. D. C., Wohlgemant, M., An, C., and Vardeny, Z. V. (2000). Film morphology and photophysics of polyfluorene, *Phys. Rev. B* **62**, pp. 15604–15609.
6. Xia, R., Heliotis, G., and Bradley, D. D. C. (2003). Fluorene-based polymer gain media for solid-state laser emission across the full visible spectrum, *Appl. Phys. Lett.* **89**, pp. 3599–3601.
7. Heliotis, G., Xia, R., Bradley, D. D. C., Turnbull, G. A., Samuel, I. D. W., Andrew, P., and Barnes, W. L. (2003). Blue, surface-emitting, distributed feedback polyfluorene lasers, *Appl. Phys. Lett.* **83**, pp. 2118–2120.
8. Shkunov, M. N., Osterbacka, R., Fujii, A., Yoshino, K., and Vardeny, Z. V. (1999). Laser action in polydialkylfluorene films: Influence of low-temperature thermal treatment, *Appl. Phys. Lett.* **74**, 12, pp. 1648–1650.
9. Rabe, T., Hoping, M., Schneider, D., Becker, E., Johannes, H. H., Kowalsky, W., Weimann, T., Wang, J., Hinz, P., Nehls, B. S., Scherf, U., Farrell, T., and Riedl, T. (2005). Threshold reduction in polymer lasers based on poly(9,9-dioctylfluorene) with statistical binaphthyl units, *Adv. Funct. Mater.* **15**, pp. 1188–1192.
10. Ryu, G., Xia, R., and Bradley, D. D. C. (2007). Optical gain characteristics of  $\beta$ -phase poly(9,9-dioctylfluorene), *J. Phys. Condens. Matter.* **19**, p. 056205.
11. Azuma, H., Kobayashi, T., Shim, Y., Mamedov, N., and Naito, H. (2007). Amplified spontaneous emission in  $\alpha$ -phase and  $\beta$ -phase polyfluorene waveguides, *Org. Electron.* **8**, pp. 184–188.
12. Virgili, T., Marinotto, D., Manzoni, C., Cerullo, G., and Lanzani, G. (2005). Ultrafast intrachain photoexcitation of polymeric semiconductors, *Phys. Rev. Lett.* **94**, p. 117402.
13. Anni, M. (2008). The role of the  $\beta$ -phase content on the stimulated emission of poly(9,9-dioctylfluorene) thin films, *Appl. Phys. Lett.* **93**, p. 023308.
14. Caruso, M. E., Lattante, S., Cingolani, R., and Anni, M. (2006). Microscopic investigation of the poly(9,9-dioctylfluorene) photoluminescence

- dependence on the deposition conditions by confocal laser microscopy, *Appl. Phys. Lett.* **88**, p. 181906.
- 15. Anni, M., Caruso, M. E., and Lattante, S. (2008). Microscopic investigation of the excitons' intermolecular energy migration in the  $\beta$  phase of poly(9,9-dioctyl fluorene) by confocal laser spectroscopy, *J. Phys. Chem. C* **112**, pp. 2958–2963.
  - 16. Calzado, E. M., Villalvilla, J. M., Boj, P. G., Quintana, J. A., and Diaz-Garcia, M. A. (2005). Tuneability of amplified spontaneous emission through control of the thickness in organic-based waveguides, *J. Appl. Phys.* **97**, p. 093103.
  - 17. Sheridan, A. K., Turnbull, G. A., Safonov, A. N., and Samuel, I. D. W. (2000). Tuneability of amplified spontaneous emission through control of the waveguide-mode structure in conjugated polymer films, *Phys. Rev. B* **62**, p. 11929.
  - 18. Xia, R., Heliotis, G., Hou, Y., and Bradley, D. D. C. (2011). Fluorene-based conjugated polymer optical gain media, *Org. Electron.* **4**, pp. 165–177.
  - 19. Anni, M., Perulli, A., and Monti, G. (2012). Thickness dependence of the amplified spontaneous emission threshold and operational stability in poly(9,9-dioctylfluorene) active waveguides, *J. Appl. Phys.* **111**, pp. 093109-1, 093109-5.
  - 20. Heliotis, G., Bradley, D. D. C., Turnbull, G. A., and Samuel, I. D. W. (2002). Light amplification and gain in polyfluorene waveguides, *Appl. Phys. Lett.* **81**, pp. 415–417.
  - 21. Scherf, U. and List, E. J. W. (2002). Semiconducting polyfluorenes—towards reliable structure–property relationships, *Adv. Mater.* **14**, pp. 477–487.
  - 22. Winokur, M. J., Slinker, J., and Huber, D. L. (2003). Structure, photo-physics, and the order-disorder transition to the  $\beta$  phase in poly(9,9-(di-n,n-octyl)fluorene), *Phys. Rev. B* **67**, p. 188106.
  - 23. Kitts, C. C. and Bout, D. A. V. (2007). The effect of solvent quality on the chain morphology in solutions of poly(9,9-dioctylfluorene), *Polymer* **48**, pp. 2322–2330.
  - 24. Abdel-Awwada, M., Luana, H., Messowa, F., Kusserowa, T., Wiskec, A., Siebertc, A., Fuhrmann-Liekerc, T., Salbeck, J., and Hillme, H. (2015). Optical amplification and photodegradation in films of spiro-quaterphenyl and its derivatives, *J. Luminescence* **159**, pp. 47–54.
  - 25. Calzado, E. M., Villalvilla, J. M., Boj, P. G., Quintana, J. A., Gomez, R., Segura, J. L., and Diaz-Garcia, M. A. (2007). Amplified spontaneous emission in

- polymer films doped with a perylenediimide derivative, *Appl. Opt.* **46**, p. 3836.
26. Calzado, E. M., Villalvilla, J. M., Boj, P. G., Quintana, J. A., Gomez, R., Segura, J. L., and Diaz-Garcia, M. A. (2007). Effect of structural modifications in the spectral and laser properties of perylenediimide derivatives, *J. Phys. Chem. C* **111**, p. 13595.
  27. Karnutsch, C., Gyrtnerand, C., Haugand, V., Lemmer, U., Farrell, T., Nehlsand, B. S., Scherf, U., Wangand, J., Weimannand, T., Heliotis, G., Pflumm, C., deMello, J. C., and Bradley, D. D. C. (2006). Low threshold blue conjugated polymer lasers with first- and second-order distributed feedback, *Appl. Phys. Lett.* **89**, p. 201108.
  28. Karnutsch, C., Pflumm, C., Heliotis, G., deMello, J. C., Bradley, D. D. C., Wang, J., Weimann, T., Haug, V., Gärtner, C., and Lemmer, U. (2007). Improved organic semiconductor lasers based on a mixed-order distributed feedback resonator design, *Appl. Phys. Lett.* **90**, p. 131104.
  29. Navarro-Fuster, V., Vragovic, I., Calzado, E. M., Boj, P. G., Quintana, J. A., Villalvilla, J. M., Retolaza, A., Juarros, A., Otaduy, D., Merino, S., and Diaz-Garcia, M. A. (2012). Film thickness and grating depth variation in organic second-order distributed feedback lasers, *J. Appl. Phys.* **112**, 4, 043104.
  30. Song, M. H., Wenger, B., and Friend, R. H. (2008). Tuning the wavelength of lasing emission in organic semiconducting laser by the orientation of liquid crystalline conjugated polymer, *J. Appl. Phys.* **104**, 3, 033107.
  31. Heliotis, G., Xia, R., Whiehead, K. S., Turnbull, G. A., Samuel, I. D. W., and Bradley, D. D. C. (2003). Investigation of amplified spontaneous emission in oriented films of a liquid crystalline conjugated polymer, *Synth. Met.* **139**, p. 727.
  32. Xia, R., Campoy-Quiles, M., Heliotis, G., Stavrinou, P., Whitehead, K. S., and Bradley, D. D. C. (2005). Significant improvements in the optical gain properties of oriented liquid crystalline conjugated polymer films, *Synth. Met.* **155**, p. 274.
  33. Müller, J. G., Anni, M., Scherf, U., Lupton, J. M., and Feldmann, J. (2004). Vibrational fluorescence spectroscopy of single conjugated polymer molecules, *Phys. Rev. B* **70**, p. 035205.
  34. Ariu, M., Lidzey, D. G., Sims, M., Cadby, A. J., Lane, P. A., and Bradley, D. D. C. (2002). The effect of morphology on the temperature-dependent photoluminescence quantum efficiency of the conjugated polymer poly(9, 9-diethylfluorene), *J. Phys. Condens. Matter* **14**, pp. 9975–9986.

35. Moons, E. (2002). Conjugated polymer blends: Linking film morphology to performance of light-emitting diodes and photodiodes, *J. Phys. Condens. Matter* **14**, pp. 12235–12260.
36. Sekine, C., Tsubata, Y., Yamada, T., Kitano, M., and Doi, S. (2014). Recent progress of high performance polymer OLED and OPV materials for organic printed electronics, *Sci. Technol. Adv. Mater.* **15**, pp. 034203–1, 034203–15.
37. Bartelt, J. A., Beiley, Z. M., Hoke, E. T., Mateker, W. R., Douglas, J. D., Collins, B. A., Tumbleston, J. R., Graham, K. R., Amassian, A., Ade, H., Fréchet, J. M. J., Toney, M. F., and McGehee, M. D. (2013). The importance of fullerene percolation in the mixed regions of polymer–fullerene bulk heterojunction solar cells, *Adv. Energy Mater.* **3**, pp. 364–374.
38. Hide, F., Diaz-Garcia, M., Schwartz, B., Andersson, M., Pei, Q., and Heeger, A. (1996). Semiconducting polymers: A new class of solid-state laser materials, *Science* **273**, pp. 1833–1836.
39. Lampert, Z. E., Lappi, S. E., Papanikolas, J. M., Reynolds, C. L., and Aboelfotoh, M. O. (2015). Morphology and chain aggregation dependence of optical gain in thermally annealed films of the conjugated polymer poly[2-methoxy-5-(2'-ethylhexyloxy)-p-phenylene vinylene], *J. Appl. Phys.* **113**, pp. 233509–1, 233509–9.
40. Wang, Y., Yang, X., Wang, R., Li, L., and Li, H. (2015). Morphology dependent amplified spontaneous emission in p-conjugated polymer, *Opt. Laser Technol.* **71**, pp. 73–77.
41. Lampert, Z. E., Reynolds, C. L. Jr., Papanikolas, J. M., and Aboelfotoh, M. O. (2015). Controlling morphology and chain aggregation in semiconducting conjugated polymers: The role of solvent on optical gain in MEH-PPV, *J. Phys. Chem. B* **116**, pp. 12835–12841.
42. Anni, M. and Lattante, S. (2015). Amplified spontaneous emission optimization in region regular-poly(3-hexylthiophene) (rrP3HT):poly(9,9-dioctylfluorene-co-benzothiadiazole) (F8BT) thin films through control of the morphology, *J. Phys. Chem. C* **119**, p. 21620–21625.
43. Lattante, S., Creti, A., Lomascolo, M., and Anni, M. (2016). On the correlation between morphology and amplified spontaneous emission properties of a polymer: polymer blend, *Org. Electron.* **29**, pp. 44–49.
44. Xia, R., Stavrinou, P. N., Bradley, D. D. C., and Kim, Y. (2012). Efficient optical gain media comprising binary blends of poly(3-hexylthiophene) and poly(9,9-dioctylfluorene-co-benzothiadiazole), *J. Appl. Phys.* **111**, pp. 123107–1, 123107–8.

45. Samuel, I. D. W., Magnani, L., Rumbles, G., Murray, K., Stone, B. M., Moratti, S. C., and Holmes, A. B. (1997). Photoluminescence in poly(3-hexylthiophene), *Proc. SPIE Int. Soc. Opt. Eng.* **3145**, pp. 163–170.
46. Camposeo, A., Mele, E., Persano, L., Pisignano, D., and Cingolani, R. (2006). Role of doping concentration on the competition between amplified spontaneous emission and nonradiative energy transfer in blends of conjugated polymers, *Phys. Rev. B* **73**, p. 165201.
47. Chappell, J., Lidzey, D. G., Jukes, P. C., Higgins, A. M., Thompson, R. L., O'Connor, S., Grizzi, I., Fletcher, R., O'Brien, J., Geoghegan, M., and Jones, R. A. L. (2003). Correlating structure with fluorescence emission in phase-separated conjugated-polymer blends, *Nature Mater.* **2**, pp. 616–621.
48. Sabu, T., Grohens, Y., and Jyotishkumar, P. (2014). *Characterization of Polymer Blends: Miscibility, Morphology and Interfaces* (Wiley-Vch), ISBN 978-3527331536.
49. Cadby, A. J., Dean, R., Elliott, C., Jones, R. A. L., Fox, A. M., and Lidzey, D. G. (2006). Imaging the fluorescence decay lifetime of a conjugated-polymer blend by using a scanning near-field optical microscope, *Adv. Mater.* **19**, pp. 107–111.



Taylor & Francis  
Taylor & Francis Group  
<http://taylorandfrancis.com>

## Chapter 3

# State-of-the-Art Active Materials for Organic Lasers

Luis Cerdán

*Institute of Physical Chemistry “Rocasolano” (IQFR), Consejo Superior de Investigaciones Científicas (CSIC), Serrano 119, Madrid, 28006, Spain*  
[lcerdanphd@gmail.com](mailto:lcerdanphd@gmail.com)

This chapter is devoted to provide the widest perspective on the rich variety of materials that are available so far to develop organic lasers, revisiting the most iconic and well-established compounds but focusing on the newest developments. Along this chapter, we will go from dyes with stunning efficiencies or biological activity, to organic semiconductors approaching their ultimate goal—electrical pumping. For completeness, we will shine a light over “hybrid” compounds that, despite not being rigorously organic, deserve our attention due to their potential to outreach organic materials.

### 3.1 Introduction

In 1960, Theodor H. Maiman [1] brought to reality what others had predicted [2, 3] and dreamed about since 1917, when Albert Einstein proposed in a seminal work [4] that photons could

---

*Organic Lasers: Fundamentals, Developments, and Applications*

Edited by Marco Anni and Sandro Lattante

Copyright © 2018 Pan Stanford Publishing Pte. Ltd.

ISBN 978-981-4774-46-8 (Hardcover), 978-1-315-10233-7 (eBook)

[www.panstanford.com](http://www.panstanford.com)

stimulate emission of identical photons from excited atoms: the optical maser or, as coined by Gordon Gould, LASER, acronym for Light Amplification by Stimulated Emission of Radiation. The laser designed by Maiman was based on a rod of synthetic ruby crystal with reflecting coatings on the ends as feedback elements, surrounded by a helical flash lamp acting as pumping source. This demonstration opened the floodgates to the emergence of new laser materials and applications [5].

Maiman published his results in May 1960; by the end of that year, the first four-level solid-state laser (uranium in  $\text{CF}_2$ ) and the first continuous-wave (CW) laser (the well-known helium-neon), respectively, were already reported [6, 7]. In 1961, the first neodymium laser was announced and the second harmonic of the ruby laser radiation was generated [8], giving birth to the field of nonlinear optics. By 1964, the well-established semiconductor diode laser, the nitrogen laser, the argon ion laser, and the  $\text{CO}_2$  laser had been demonstrated [5]. Nevertheless, it was not until 1966 that the first organic lasers were reported independently by Sorokin and Lankard [9] and Schäfer, Schmidt, and Volze [10] using, respectively, phthalocyanine and carbocyanines (Fig. 3.1). Six years later, an anthracene-doped single crystal emitted stimulated emission [11], and already in the 1990s, the first conjugated polymer laser was demonstrated [12, 13].

Since the discovery of the first organic dyes emitting laser light, thousands of different organic systems have been shown to emit laser light in a rich variety of situations and conditions. The reason for this profusion lays in the easy modulation of the properties

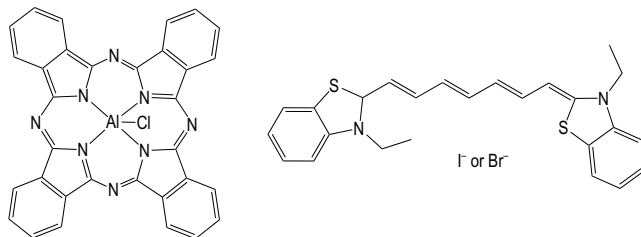


**Figure 3.1** The first organic molecules emitting laser light: chloro-aluminum phthalocyanine [9] and 3,3'-diethylthiatricarbocyanine iodide (or bromide) [10].

of organic compounds by straightforward and well-known functionalizations, in such a way that controlled modifications of the chromophore structure lead to completely new materials, with or without profound photophysical changes, and, when desired, with added functionalities (e.g., chemical or biological sensing [14]). The feverish pursuit of new organic laser materials was, and in fact is, heated up by a mix of several factors: the need of more efficient and photodegradation resistant materials in the whole visible spectrum, the inherent chemical and processing versatility enabled by organic chemistry (feasibility of new materials and devices), the operational versatility of the fabricated devices (pulsed and CW lasing upon optical or electrical excitation), and, more recently, the prospect of realizing low-cost, flexible, and/or integrated lasers [15].

Nevertheless, the achievement of these goals soon became a greater challenge. Most candidates for organic active materials present relatively high fluorescent quantum yields (approaching unity in some cases) in diluted solution, but this is reduced, or even nullified, at high concentrations due to excitation self-annihilation, thus increasing the laser threshold and reducing the conversion efficiency. On the other hand, the easy modification of the molecular structure by means of chemical reactions acts as a double-edged sword. Upon photoexcitation, the chromophores may interact with foreign species, such as oxygen, free radicals, or even with other chromophoric units, resulting in the formation of new species. They are non-fluorescent and, in the worst cases, absorbing, which, in turn, reduce the laser efficiency with time and hinder long-term operation. Hence, much of the efforts in the last decades of organic material development have been focused in overcoming these issues. In addition, since the discovery of organic semiconductor laser materials, a great deal of research has been directed toward the realization of electrically pumped devices, entailing the development of materials presenting simultaneously high carrier mobilities, low losses, and large quantum yields, a goal that, as will be shown along this chapter, has proved rather elusive.

In this sense, the quest for new materials was so enthusiastic that, nowadays, there is such a variety of organic laser media that this denomination is too generic, and different subclasses must be specified. Subdividing organic compounds in different

classes is a difficult task, as the frontiers separating them are diffused and sometimes intertwined. In this chapter, we will divide organic compounds into four major classes: dyes ([Section 3.2](#)), molecular crystals ([Section 3.3](#)), molecular glasses (oligomers and macromolecules) ([Section 3.4](#)), and conjugated polymers ([Section 3.5](#)). The last three classes have been commonly included into the broader class of organic semiconductors due to their charge transport and electroluminescence properties [16], and we will make use of this terminology along the chapter too. The present segregation is simply based on structural and processing differences of the given family in the final device. In other words, dyes are mostly used in solution (either a solvent or a matrix), and they completely lose their luminescent properties at high concentrations (undiluted form) due to fluorescence quenching. On the other hand, organic semiconductors are usually used in neat form (undiluted) and still keep fluorescence. With respect to organic semiconductors, molecular crystals are formed by relatively small molecules with long-range crystal-like order, whereas molecular glasses and conjugated polymers give place to amorphous solids (glasses). But again, there are particular cases where one subclass element could be included in another subclass.

## 3.2 Dyes

Dyes are the eldest and most mature compounds among all the available organic laser materials. Dye lasers have a deserved space in laser history, as they enabled two of the major achievements never realized before: ultranarrow linewidth (<1 kHz or  $\Delta\lambda \sim 1 \times 10^{-9}$  nm) CW laser emission across tens of nanometers with a single dye, and generation of ultrashort pulses (down to 6 fs after amplification and extracavity compression) in the visible spectrum without the need of using frequency conversion [[17](#), [18](#)]. In fact, until the advent of Ti:Sapphire lasers, dye lasers were the reference in labs and industry due to its unusual flexibility, spectral purity and tunability, and power scalability [[19](#)]. Not surprisingly, dye lasers are still profusely used in spectroscopy and material processing.

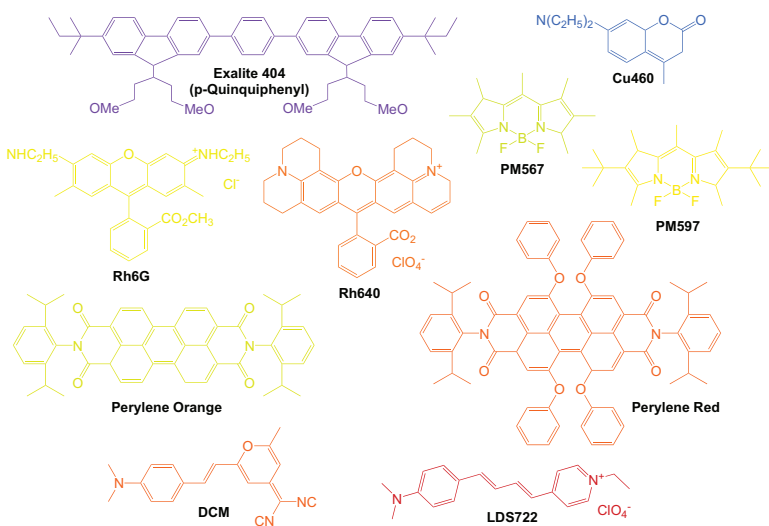


**Figure 3.2** Selection of well-established laser dyes. The structure color matches its laser emission wavelength.

Since the pioneering works by Sorokin and Schäfer (and colleagues), many dyes covering the UV to IR spectral region have reached the status of state-of-the-art commercial dyes (Fig. 3.2). To mention a few: polyconjugated hydrocarbons (Exalite 404), coumarins (Cu460), xanthenes (Rh6G, Rh640), pyrromethenes (PM567, PM597), perylenediimides (Perylene Orange, Perylene Red), and hemicyanines (DCM, LDS722). All of them are commonly used in solution but have lately received considerable attention due to the possibility of incorporating them into solids (polymers, silica, . . . ), as will be seen along the book.

In the following pages, we will review new developments in some of these families (Section 3.2.1) and will discover biologically produced dyes (Section 3.2.2).

### 3.2.1 Synthetic Molecules

#### 3.2.1.1 BODIPYs

Discovered by Treibs and Kreuzer [20], 4,4-difluoro-4-bora-3a,4a-diaza-s-indacenes (Fig. 3.3), commercially known as BODIPYs

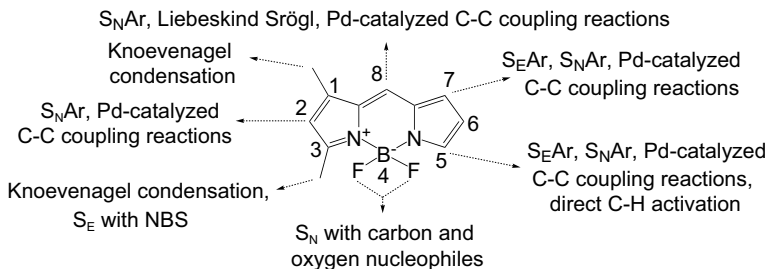


**Figure 3.3** The IUPAC numbering system and reactivity of BODIPY core [21].

(BORon DIPYrrromethenes), are considered today as one of the most useful and versatile organic chromophores [21, 22]. The interest in BODIPY dyes originates from their outstanding photophysical properties, such as high absorption coefficient, high fluorescence quantum yield, high photostability, and low sensitivity to medium effects. Currently, the development of new fluorescent BODIPYs has become a booming area of research due to their potential applications in biosciences and photonics, including lasers.

One of the main reasons for this huge development is, without any doubt, the chemical versatility of the BODIPY core, which allows its straightforward and almost infinite functionalization. These systems are extremely reactive and can undergo many types of reactions in every core site [21] (Fig. 3.3). Thanks to this versatility, just in the last 5 years a tremendous amount of BODIPY derivatives have been synthesized and many of them have demonstrated efficient laser emission across the whole visible spectrum (from 450 to 740 nm), as can be appreciated in the summarized selection presented in Fig. 3.4. There is no other known chromophore family with such an extended chromaticity, testifying the relevance of BODIPYs.

There is a range of commercial BODIPYs whose emission covers the green to red spectral region (e.g., PM546, PM567, PM597, or PM650).<sup>a</sup> In the last decade, different strategies have been followed to improve both the efficiency and photostability of these commercial dyes without modifying their emission wavelength. Two

<sup>a</sup> See catalog by Exciton Inc. for a list of commercial BODIPYs.

relevant examples are fluorination at position 2 (BODIPY **11** [23]) and (multi)chlorination at positions 1, 2, 3, 5, 6, and/or 7 (BODIPY **18** [24]) of the BODIPY core, which allows nearly doubling the laser efficiency and significantly boosting the irradiation resistance. The inclusion of halogen atoms, with its electron-withdrawing capability, induces a drastic reduction in nonradiative deactivation processes without modifying the  $\pi$  conjugation, thus improving the laser performance. The monofluorination has been revealed as a sort of general way to improve both the efficiency (nearly doubling it) and photostability not only of BODIPYs, but also in rhodamines, coumarins, and perylenediimides, as will be shown later [23]. With respect to chlorination, the more chlorine atoms in the core are included, the better the laser efficiency and photostability becomes [24].

There are many other examples of smart functionalizations at position 8 (Fig. 3.3) that improves the efficiencies or photostabilities of BODIPY dyes: Diiodination (BODIPY **20** [25]), functionalization with an octasilsesquioxane (BODIPY **15** [26]), and incorporation of triphenylamine (BODIPY **12** [27]), pyrane (BODIPY **9** [28]), acetylacetone [29], or carbazole units [30]. In this last case, the carbazol unit slightly reduces efficiency but boosts the photostability due to a decrease in the generation of singlet oxygen and a reduction in the electron donation capacity.

Most of the functionalizations in the BODIPY core (Fig. 3.4) are performed at positions 1 to 3 and 5 to 8 (Fig. 3.3), but recent reports have explored the substitution of the fluorine atoms at position 4 by other groups as an alternative route. For example, Duran-Sampedro et al. demonstrated for several commercial BODIPYs that the substitution of the fluorine atoms by electron-withdrawing groups (among others, trifluoroacetoxy substituted BODIPYs **16** and **19**, cyano-substituted BODIPYs **17** and **28**, or mono-TMS-protected 1,4-diethynylbenzene substituted BODIPY **21**) could lead to stunning laser performances in solution, doped into polymer rods, as well as in DFB lasers (thresholds of  $10 \text{ kWcm}^{-2}$ ) [31, 32]. Some of these cases almost reached the quantum defect limit (i.e., each pump photon is converted into a laser photon,  $\Phi = \lambda_{\text{pump}}/\lambda_{\text{laser}}$ ). Such is the case of the PM597 derivatives (e.g., BODIPY **19**), which quantum limit is  $\Phi = 90\%$  and its

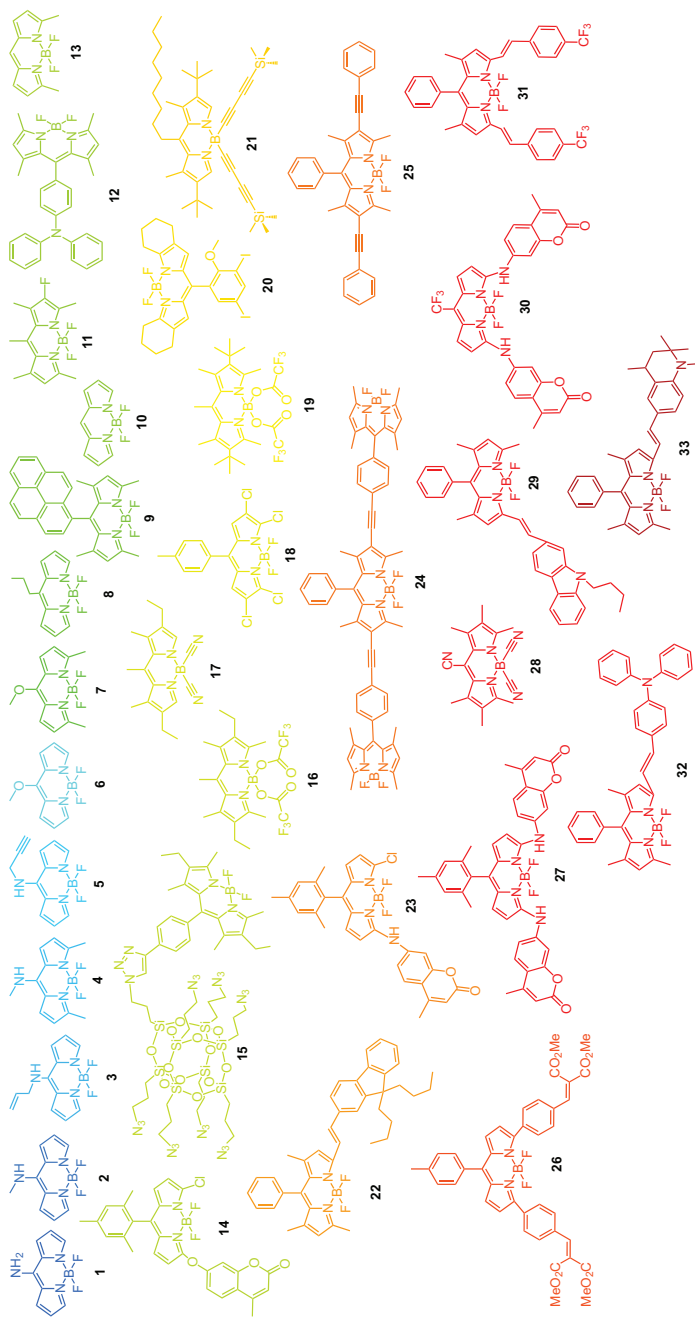


**Figure 3.4** Compendium of laser BODIPYs. The structure color matches its laser emission wavelength.

laser efficiency in solution (ratio of output and input energy) scaled up to a 73% in an unoptimized cavity, as compared to the 50% for the unsubstituted PM597. The incorporation of electron-withdrawing groups at position 4 removes charge density from the core, improving the chromophore aromaticity and planarity, reducing the nonradiative processes. In other words, the quantum yield is increased and the molecule becomes stronger, which is translated into higher efficiencies and photostabilities. Of course, the opposite is true, i.e., the incorporation of electron-donating groups (e.g., methoxy groups or phenyl rings) scrambles the laser emission. Prior to these works, Jagtap et al. reported an ethenyl-substituted BODIPY, which did not significantly improve the laser efficiency but did enhance the photostability due to a lower reaction rate with singlet oxygen [33].

Up to now we have analyzed functionalizations that improve the laser performance but keep the emission wavelength unchanged. But synthesizing BODIPYs whose emission expands toward the UV and the IR is of much interest; consequently, much efforts have been dedicated in this respect. To shift the emission wavelength to the red spectral edge (beyond 650 nm), one can extend the  $\pi$  conjugation by substitutions at positions 2, 3, 5, or 6 [34–36] (BODIPYs 25, 26, and 31) and/or forming intramolecular charge transfer (ICT) structures by inclusion of different groups at position 3 [37] (BODIPYs 29, 32, and 33). BODIPY 33, where a tetrahydroquinoline group is used as the ICT unit, is particularly interesting, as it renders laser emission at 740 nm, nearly reaching the IR range, with an efficiency of 26% and a decent photostability.

To shift the emission wavelength to the blue spectral edge (below 530 nm), a radically different approach must be used. One might think of decreasing the  $\pi$  conjugation by dispossessing the BODIPY core of functional groups as much as possible. Nevertheless, the fully unsubstituted BODIPY 10 [38], formed exclusively by the basic skeleton, shows laser emission in the green spectral range [39]. It was found that a moderate substitution is needed to achieve blue lasing. For example, the first BODIPY showing blue laser emission was that only substituted at position 8 with a propargylamino group (BODIPY 5 [40]). With a laser efficiency of 32% at 480 nm, it showed a modest photostability, although much better than coumarin 480

(Cu480) emitting in the same spectral region. Later, changing the functional groups at 8, and tailoring the substitution at positions 3 and 5, a range of blue to green laser BODIPYs (**1** to **8** and **13**) were synthesized [39, 41–44]. In particular, Bañuelos et al. reported that the BODIPY **1** showed laser emission at 456 nm, nearly reaching the UV range, with an efficiency of 40% when pumped at 355 nm. All of these compounds present a modest photostability, partially due to the reactivity associated with the low functionalization of the core.

An alternative strategy to obtaining laser BODIPYs at different wavelengths is the use of multichromophoric systems or cassettes. For example, Xiao et al. synthesized an efficient “through-bond energy transfer” multi-BODIPY cassette (BODIPY **24**) that spanned the absorption spectrum into a broader region, and exhibited higher molar extinction coefficients with enhanced fluorescence emission and increased Stokes shifts [45]. Later, Esnal et al. reported a series of coumarin-BODIPY cassettes (BODIPYs **14**, **23**, **27**, and **30**) that enabled efficient lasing from 540 to 680 nm pumping at 355 nm [46].

### 3.2.1.2 Perylenediimides

Perylenediimides (PDIs), with their bulky structure (Fig. 3.5), are chromophores that exhibit a great photochemical and thermal stability, being some of them excellent n type semiconductors [47]. PDIs were identified as promising laser materials in solution in the 1980s [48] and in solid matrices in the 1990s [49, 50]. Two of the more prominently used laser PDIs are Perylene Orange (BASF Lumogen F Orange 240) and Perylene Red (BASF Lumogen F Red 350) (Fig. 3.2). Since then, research in PDIs has regained momentum due to their prospects of being used in integrated lasers, as will be seen in the following pages.

We can distinguish between (a) PDI derivatives with substitutions at the *pery* position (imide nitrogen) with no substitutions at *bay* position (Perylene Orange, **PDIs 1** and **2**), and (b) PDI derivatives with functional groups at both *pery* and *bay* (Perylene Red, **PDIs 4** to **8**). In PDIs, the highest occupied molecular orbital (HOMO) and the lowest unoccupied molecular orbital (LUMO) are

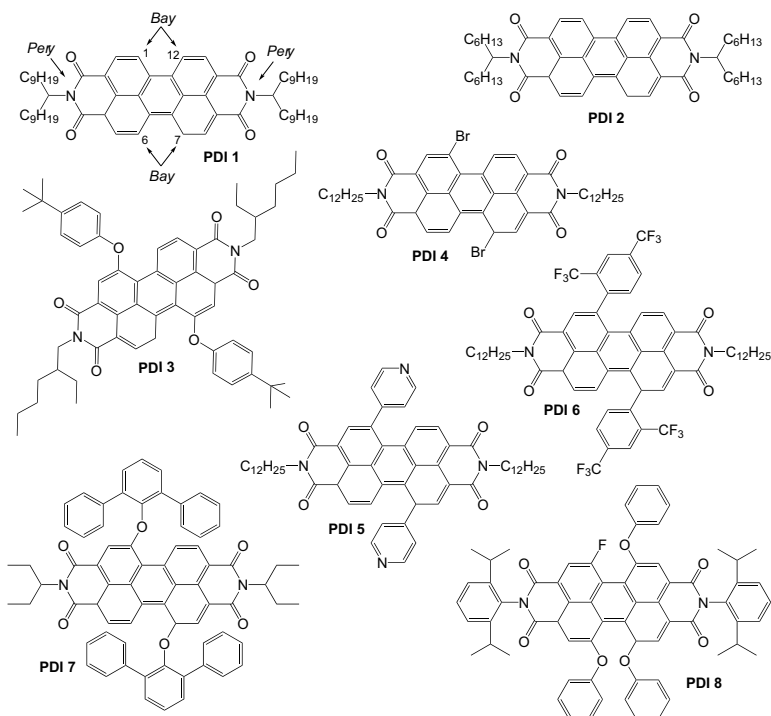


**Figure 3.5** PDI derivatives recently reported. In **PDI 1**, the relevant position numbering and the *pery* and *bay* positions are indicated.

distributed along the perylene core. Substitutions at *bay* affect the delocalized  $\pi$  system and hence modifies the spectral characteristics of the derivatives. On the contrary, substitutions at *pery* do not affect the chromophore photophysics, since there is an energy node in both the HOMO and LUMO at that position [51], minimizing the interaction chromophore/functional group at *pery*. Hence, substitutions at this position allows modulating the dye solubility and avoiding aggregation effects without modifying the emission properties. In this regard, due to steric hindrance, bulky groups at *pery* are oriented out of the plane containing the chromophoric unit, in such a way that they reduce the  $\pi-\pi$  stacking between neighbor molecules, thus alleviating quenching effects at the high concentrations required for DFB lasers ( $\sim 10^{-2}$  M).

With respect to PDIs without substitution at *bay*, Calzado et al. reported efficient and photostable amplified spontaneous emission (ASE) in polystyrene (PS) thin films doped with **PDI 1**, a derivative with nonadecyl groups attached to *pery* [52]. Later on, the same group performed a deep characterization of both ASE and DFB laser performance in **PDI 2**, a derivative with hexylheptyl groups when doped in PS [53–56]. As expected, both **PDI 1** and **2** absorb and emit at the same wavelength ( $\sim 575$  nm) and have very similar ASE behavior. Recently, these authors showed that Perylene Orange (Fig. 3.2), commercially sold by BASF and that had been previously tested as a DFB laser material [57], presents much better laser performance than **PDI 2**, with a DFB laser threshold an order of magnitude smaller, a three times larger photostability, and much less sensitivity to concentration quenching or aggregates formation [58]. This tremendous improvement comes from the bulky diisopropylphenyl groups attached to *pery* in Perylene Orange, that avoids  $\pi$ - $\pi$  stacking between neighbor molecules through steric hindrance much more efficiently than the nonadecyl (**PDI 1**) or hexylheptyl (**PDI 2**) groups.

Both Perylene Orange and **PDI 1** and **2** share the same chromophoric system and hence emit at the same spectral region ( $\sim 570$  nm). As said before, to obtain emission at different wavelengths, substitutions must be performed at *bay* position. Calzado et al. demonstrated ASE at 600 nm in PS films doped with **PDI 3**, a derivative with ethylhexyl groups at *pery* and butylphenoxy groups at *bay* positions 1 and 7 [59]. Unfortunately, this compound exhibited an ASE threshold two orders of magnitude higher than that of the parent compound **PDI 1**, probably due to the reduction in quantum yield induced by the introduction of butylphenoxy groups and a clear aggregation quenching effect. Recently, these authors smartly mitigated these problems by synthesizing a new 1,7-*bay* substituted derivative (**PDI 7**) emitting at 620 nm with an ASE threshold even lower than **PDI 1** [60]. Remarkably, these results were obtained pumping at 532 nm, in a condition at which Perylene Red, emitting at the same spectral region, showed no ASE emission [57]. 1,7-*bay* substituted **PDI 4** to **6** emitting around 600 nm had been synthesized earlier [61]. Although their ASE thresholds improved those of **PDI 3**, they were higher than those of **PDI 7**. In

contrast, the photostabilities were certainly higher, particularly in **PDI 4**.

As stated before in [Section 3.2.1.1](#), monofluorination is seemingly a general way of improving the laser performance of new chromophores. At least this is true for Perylene Red, in which the replacement of the phenoxy group at position 1 by a fluorine atom (**PDI 8**) doubles the laser efficiency in solution and improves the photostability [23].

### 3.2.1.3 Xhanthenes

Xhanthenes (Xhs), either rhodamines or fluoresceins, are one of the most relevant dyes in the history of lasers [17, 18]. In particular, Rhodamine 6G (Rh6G, [Fig. 3.2](#)) was, and is still today for some researchers, the reference dye for dye lasers, with its efficient and photostable laser emission. In fact, Rh6G is probably the most studied laser dye so far, with most of their photophysical, photochemical, and laser parameters evaluated and revealed. The main concern with Xhs is their pathological problem with aggregation beyond mM concentrations, both in aqueous and organic solutions [62].

Although the interest in laser dye synthesis has shifted in the last decades to other kind of dyes (BODIPYs or PDIs), some new Xhs have been developed and their laser performance characterized ([Fig. 3.6](#)). For example, we evaluated the laser properties of solutions of newly synthesized rosamines (**Xh 1**) [63]. Rosamines, which had never been used as laser materials before, presented efficient and photostable laser emission around 610 nm. More interestingly, some of them, such as **Xh 1**, presented bichromatic laser emission with

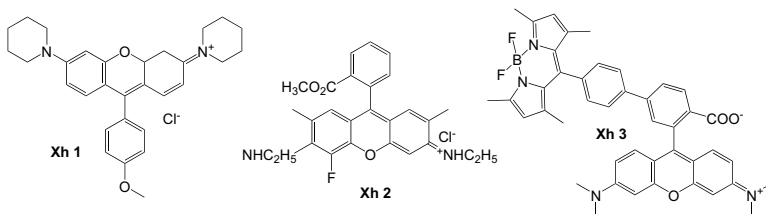


**Figure 3.6** Xhanthene (Xh) derivatives showing laser emission.

bands at 610 nm and 640 nm, allowing a wavelength tunability of at least 80 nm with a single dye. The authors ascribed the high energy band (610 nm) to a monomeric form of rosamine and the low-energy band (640 nm) to naturally assembled excimers (excited-state aggregate).

Another Xh derivative was obtained with the monofluorination of Rh6G (**Xh 2**) that, as was mentioned before, improved the laser performance with respect to the parent dye [23]. Some time before, Gartzia-Rivero et al. reported a BODIPY-Rh6G cassette (**Xh 3**), which lactone isomer emitted at 540 nm when pumped at 355 nm, and which zwitterion isomer emitted at 580 nm when pumped at 532 nm [64]. Finally, there have been reports on fluorescein derivatives that carry an acryloyloxy group that allows their covalent bonding to polymers [65, 66].

### 3.2.1.4 Miscellanea

To finish with synthetic dyes, we include in this subsection some developments that do not belong to the three families described previously but that do not deserve a whole subsection. For example, some coumarin derivatives, a family of dyes emitting in the blue and green spectral range, have been reported recently [23, 67], including a monofluorinated Cu460 with remarkable laser performance. Lahoz et al. demonstrated efficient ASE from solutions of a drug-dye complex formed by the covalent binding of an anticancer drug (tamoxifen), commonly applied in breast cancer therapy, and nitrobenzoxadiazolyl dye, commonly used as biomarker in lipid membranes [68]. Finally, some other blue-emitting dyes have been reported recently: a difluoro-boron-triaza-anthracene [69], a pyridylfluorene [70], or a triphenylamine benzothiazole [71].

## 3.2.2 Biomolecules

Organic laser materials started their journey the last century and, in just 50 years, have experienced an unprecedented development. Unlike scientists, who more often than not take shortcuts in synthetic issues, nature chooses the long road of evolutionary

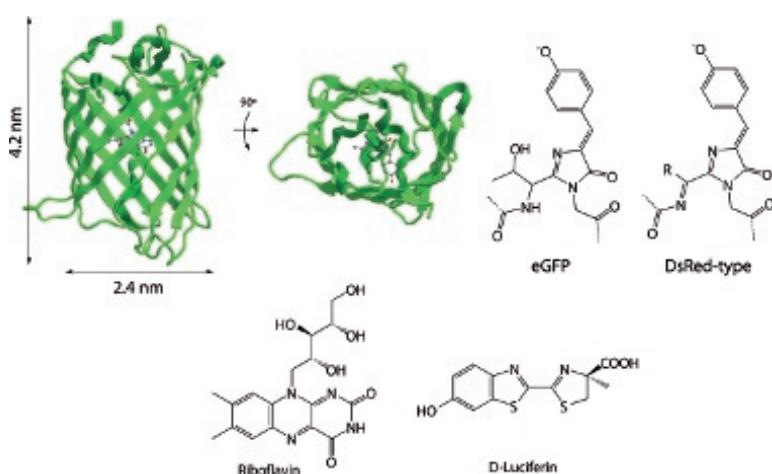


**Figure 3.7** (Top) Enhanced green fluorescent protein (**eGFP**) external barrel side and top view, and chromophoric units of different FPs. (Bottom) Laser molecules with biological activity.

optimization. Fluorescent compounds are not an exception, and nature has come up, through a multi-million year process, with biologically produced compounds with characteristics ameliorating, in some cases, synthetic compounds. This section will review some biomolecules that have shown laser emission.

Fluorescent proteins (FPs) have emerged as a powerful set of tools for live cell imaging [72]. FPs fold into a nano-cylinder (barrel) comprising 11  $\beta$ -sheets with a single  $\alpha$ -helix running through the center of the  $\beta$ -barrel (Fig. 3.7). It is along this central helix, deep within the hydrophobic core of the protein, that the actual chromophore lays. The  $\beta$ -barrel prevents close contact between neighbor FPs, and it has been recently suggested that evolution has optimized their size so that it limits intermolecular energy migration and quenching even at the highest possible concentration [73]. The most representative case is that of green fluorescent protein (GFP), isolated from the *Aequorea victoria* jellyfish, and which mutations afford emission from blue to yellow. Meanwhile, orange and red-emitting FPs have been obtained from the marine anemone *Discosoma striata* and several reef corals from the class Anthozoa [72].

Lasing has been obtained in some of these FPs. For example, Gather and collaborators have attained laser emission from **eGFP**—a GFP mutation with enhanced absorption and emission characteristics (Fig. 3.7)—in a variety of situations and cavity configurations: expressed into a single living cell [74], from solutions with colonies of *Escherichia coli* bacteria genetically programmed to synthesized **eGFP** [75], in dried **eGFP** either as VCSELs or ring resonators [73], and protein microcrystals [76]. The VCSEL based on solid-state FPs is particularly interesting, as it rendered one of the lowest thresholds ever reported for this type of organic devices [73]. This stunning figure of merit is a result of the huge “dye” concentrations achieved in the films of pure **eGFP**. As mentioned above, the concentration quenching is avoided thanks to the  $\beta$ -barrel. In addition, laser emission has also been obtained from ring resonators containing the red-emitting FPs mCherry [77] and tdTomato [73], two mutations of the FP isolated from the anemone *Discosoma striata*, **DsRed** (Fig. 3.7).

But FPs are not the only biomolecules that may achieve laser emission, and nature has developed, through evolutionary optimization, two other examples. **Riboflavin** or vitamin B<sub>2</sub> (Fig. 3.7), which is vital for the metabolism of animals, has been shown to lase in DFB lasers when doped into gelatine [78], although the laser threshold is high compared with synthetic dyes. On the other hand, **luciferine** (Fig. 3.7), responsible for the bioluminescence in fireflies, showed whispering gallery mode lasing around 550 nm [79].

### 3.3 Molecular Single Crystals

Molecular single crystals are a very distinctive class of organic materials where the constituent molecules are oriented in a well-defined crystal-type long-range order.<sup>b</sup> This ordered structure and their particular intermolecular couplings confer molecular crystals with very high carrier mobilities, highly polarized emission, and high refractive indices, all of these parameters being of utmost

<sup>b</sup>As we have just seen fluorescent proteins may as well lase in crystalline state [76], but do not evidence semiconducting properties.

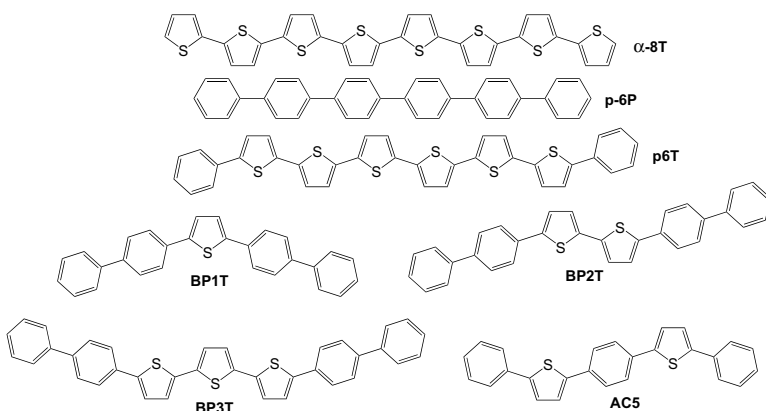


**Figure 3.8** Selection of oligomeric molecules forming single laser crystals. Oligothiophenes ( $\alpha\text{-}8\text{T}$ ), oligophenylenes ( $\mathbf{p}\text{-}6\mathbf{P}$ ), and thiophene/phenylene co-oligomers ( $\mathbf{p6T}$ ,  $\mathbf{BP1T}$ ,  $\mathbf{BP2T}$ ,  $\mathbf{BP3T}$ ,  $\mathbf{AC5}$ ).

importance to implement laser devices, overall if they are to be electrically driven. One of their main drawbacks is the growth and processing difficulties, as complex and time-consuming techniques are needed to achieve very high-quality large crystals. For this reason, many works only report ASE in nano-, micro-, or millimetre scale crystals, as implementing laser cavities (DFBs, VCSELs, Fabry–Pérot, ...) is not straightforward.

Stimulated emission from a molecular crystal was demonstrated in a fluorene crystal doped with anthracene [11], but it was not until 1997 that stimulated emission in an undoped (monolithic) single crystal of  $\alpha$ -octathiophene ( $\alpha\text{-}8\text{T}$ , Fig. 3.8) was reported [80]. After this report, many others followed in which the molecular constituents were based on different compounds, such as oligophenylenes, thiophene/phenylene co-oligomers (TPCO), phenylene vinylene oligomers, and non-oligomeric molecules. Recently, an excellent review on organic single crystals for laser applications, with a comprehensive compilation of molecular crystal compounds, has been published [81]. In the following pages, we will review some of these compounds as well as recent developments on oligomeric (Section 3.3.1) and non-oligomeric (Section 3.3.2) molecular crystals. The readers of this book are kindly referred

to the review by Fang et al. to have a flavor of other single-crystal compounds and to learn more about some other particulars related to them, such as crystal growth techniques, crystal structures and related optical properties, laser cavity configurations, and electrically pumped light-emitting devices [81].

### 3.3.1 Oligomeric Compounds

Alpha-linked oligothiophenes, such as  $\alpha$ -**8T** (Fig. 3.8), consist of linear chains of thiophene molecules. These materials have played an important role not only in organic laser crystals ( $\alpha$ -**8T** was the first monolithic crystal showing ASE) but on optoelectronic devices. A common problem with unsubstituted oligothiophenes is their low quantum yields due to strong intermolecular interactions. This quenching can be alleviated with smart substitutions, such as the inclusion of two oxygens into the thienyl sulfur atom, increasing the quantum yield to a 37% [82].

Historically, the next family of molecular crystals that was used was that of oligophenylenes, formed by linear chains of phenylene groups. The blue-emitting *p*-sexiphenyl or **p-6P** (Fig. 3.8), which was the first organic crystal of this family showing ASE [83], has been extensively studied, since it exhibits high optical gains ( $g > 100 \text{ cm}^{-1}$  [84]).

Another class of molecular crystals that have received intense attention are thiophene/phenylene co-oligomers (TPCOs), in which the thiophene and phenylene groups are hybridized at the molecular level. TPCOs crystals can be designed with various molecular shapes (Fig. 3.8), straight (**p6T**), bent (**BP1T**), or zigzag (**AC5**) [85, 86], which helps reducing deleterious intermolecular interactions and enhancing the quantum yields. With **p6T**, large crystals with high-quality and plane parallel facets with molecular-scale flatness can be obtained, which allow Fabry-Pérot type multimode laser oscillation at 680 nm [86]. In TPCOs, by extending the  $\pi$  conjugation (e.g., increasing the number of core thiophenes), the emission can be tuned across the visible spectrum, from 466 nm in **BP1T** [85], to 565 nm and 618 nm in **BP2T** [87] and **BP3T** [88], respectively (Fig. 3.8). In addition, **BP3T** has demonstrated rather high carrier mobility values for both holes ( $1 \text{ cm}^2 \text{ V}^{-1} \text{ s}^{-1}$ ) and electrons ( $0.2 \text{ cm}^2 \text{ V}^{-1} \text{ s}^{-1}$ )

in an ambipolar light-emitting transistor with strong electroluminescence and signatures of current density-dependent spectral narrowing [89]. In fact, this material is considered a good candidate to achieve electrically pumped lasing [90].

A particular problem with **BP1T** and **AC5** is that the transition dipole moment is normal to the crystal slab [91], which added to the difficulty in growing crystals having high flatness in their top and bottom surfaces, making it almost impossible to implement VCSELs. Quite recently, Yamashita et al. have demonstrated optically pumped VCSEL operation in a **BP1T** terminated with cyanophenyl groups [92]. The cyano groups not only oriented the transition dipole moment to the in-plane direction in its plate-like crystal, but allowed for the obtaining of optically flat top and bottom surfaces onto which grow Bragg mirrors. Fang et al. obtained Whispering Gallery Mode (WGM) lasing using microdisk (triangles, squares, pentagons, and hexagons) arrays of **BP1T** and **BP2T** crystals by means of photolithography and reactive-ion etching, testifying the versatility of these materials [93].

Oligo(phenylene vinylene) derivatives (Fig. 3.9) have been greatly studied in the last years due to their well-balanced photo-physical and semiconducting properties. For example, **CNDPDBS**, a cyano-substituted oligo(*p*-phenylene vinylene) (Fig. 3.9), has a very good combination of optical gain and semiconducting properties [94]. Emitting at 470 nm, it has a 95% quantum yield, an ASE gain of  $35\text{ cm}^{-1}$ , and highly balanced bipolar mobilities,  $\sim 10^{-2}\text{ cm}^2\text{ V}^{-1}\text{ s}^{-1}$

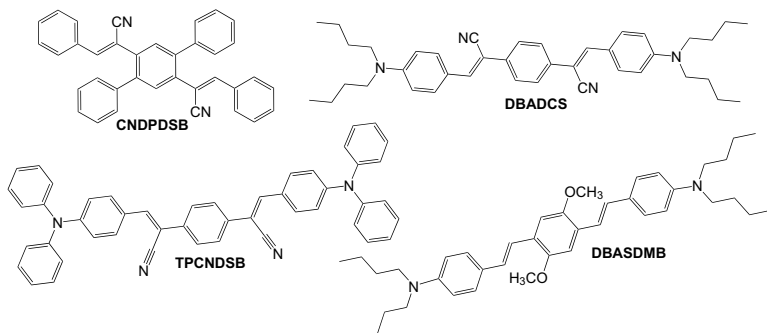


**Figure 3.9** Selection of phenylene vinylene (or distyryl-benzene).

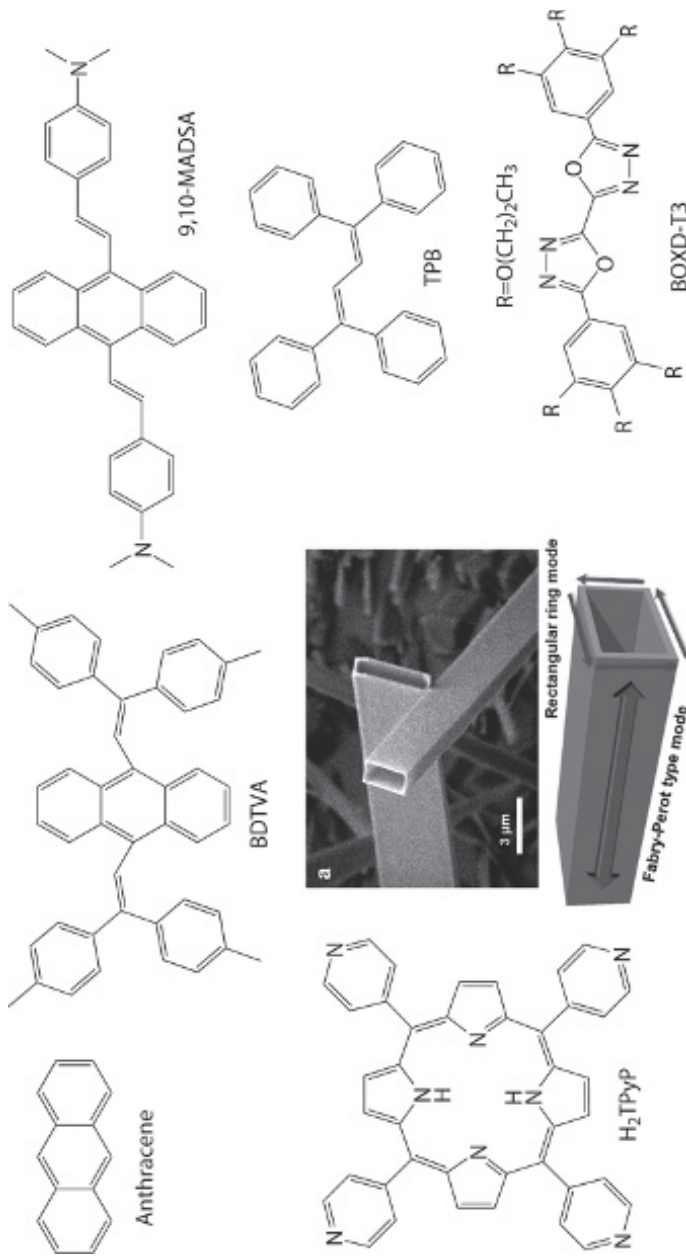


**Figure 3.10** Various non-oligomeric crystal constituents showing laser emission. **H<sub>2</sub>TPyP** images adapted with permission from Ref. [95]. Copyright 2011 American Chemical Society.

for both electrons and holes. In fact, this material is considered a good candidate to achieve electrically pumped lasing [90].

On the other hand, the molecular crystal obtained with **DBADCS** (Fig. 3.9) showed red laser emission through different mechanisms [96]. Upon laser pumping at the low-energy edge of the absorption band ( $\lambda_{\text{ex}} = 532$  nm), single-mode stimulated emission was found and ascribed to Stimulated Resonant Raman Scattering (SRRS), whereas at  $\lambda_{\text{ex}} = 355$  nm, Fabry-Pérot multimode lasing, as well as ASE, was observed. In the single crystalline state, the compound exhibits efficient red emission, which is not only due to the restricted environment, but clearly arises from synergetic molecular packing, leading to J-aggregation [96].

Finally, there are some oligo(phenylene vinylene)s that show efficient two-photon pumped ASE, a property that opens the door to pumping with red or near-IR wavelengths. Among other compounds, we could highlight **DBASDMB** [97] or **TPCNDSB** [98] (Fig. 3.9), but many more have been synthesized [81]. **TPCNDSB**, in particular, presents aggregation-induced emission enhancement, implying that the chromophore barely shows fluorescence in solution but strongly glows in the crystalline state.

### 3.3.2 Non-oligomeric Molecules

In the previous section, we have analyzed materials whose constituents are composed by a finite repetition of a given molecular entity. In this section, we will focus in “monomeric” molecular crystals that have shown ASE or laser emission.

Among this kind of compounds, we can highlight **anthracene** and its derivatives (Fig. 3.10). Anthracene was the first organic molecule emitting stimulated emission in the crystalline state. ASE was firstly demonstrated in an anthracene doped into a fluorene crystal [11] and much later in monolithic crystal [85]. These reports did not show lasing, but later a 120 nm thin anthracene film sandwiched between Bragg reflectors allowed for the excitation of coherent laser-like “polariton laser” emission [99]. Polariton lasers, in which there is a strong exciton–photon coupling, are known to present much lower threshold densities, whereupon could lead

to electrically pumped lasers in the near future. Recently, some anthracene derivatives in crystalline state have shown ASE emission (Fig. 3.10), like the green-emitting distyrylanthracene **BDTVA** [100] and the red-emitting dimethylaminostyrylanthracene **9,10-MADSA** [101]. **9,10-MADSA** is another system presenting aggregation-induced emission enhancement and, in addition, shows an unusual red-shifted emission compared with that in solution, being ascribed to the formation of J-aggregates.

Another family of compounds forming molecular crystals are oxadiazoles [102, 103], which “have enjoyed widespread use as electron-transporting/hole-blocking materials, emitting layers in electroluminescent diodes and non-linear optical materials, due to their electron-deficient nature of the heterocycle, high photoluminescence quantum yield and good thermal and chemical stabilities” [102]. An interesting case is that of **BOXD-T3** (Fig. 3.10), which shows a very low ASE threshold at 420 nm ( $40 \text{ Wcm}^{-2}$ ) when prepared in a slow solvent evaporation method but shows not ASE at all in vacuum-evaporated films. This is one of the lowest, if not the lowest, ASE thresholds ever reported.

A particularly interesting crystal structure is that obtained with tetrapyridyl-porphyrin ( $\text{H}_2\text{TPyP}$ , Fig. 3.10). Grown by means of a vaporization–condensation–recrystallization process, it renders hollow rectangular microtubes with sharp bends and subwavelength wall thicknesses (Fig. 3.10). These microcrystals may sustain laser emission around 720 nm by means of a combination of Fabry–Pérot type modes along the crystal axis and a sort of whispering gallery modes in the microtube walls [95]. Also, laser emission at 430 nm due to a combination of Fabry–Pérot and random resonances has been recently observed in tetraphenyl-butadiene (**TPB**) thin films [104].

### 3.3.2.1 Excited-state intramolecular proton transfer

A number of recently developed molecular crystals can undergo an excited-state intramolecular proton-transfer (ESIPT) reaction, a fast enol–keto (E–K) prototropy occurring in the excited states of intramolecularly H-bonded molecules (Fig. 3.11).

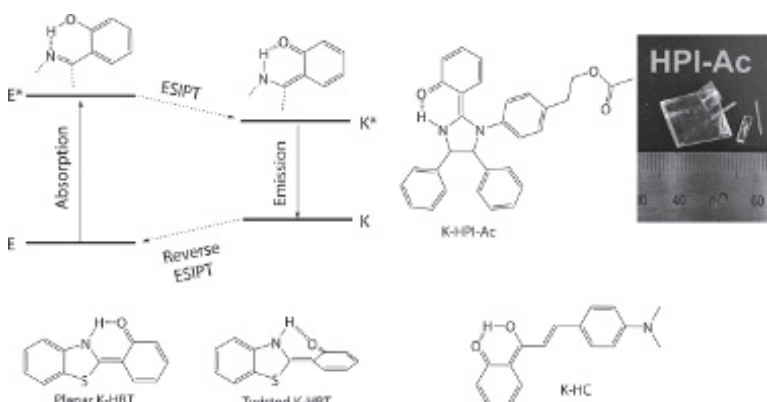


**Figure 3.11** Schematic representation of ESIPT four-level photocycle and enol (E) and keto (K) forms, and various ESIPT molecules in Keto form. HPI-Ac image adapted with permission from Ref. [105], Copyright 2005 American Chemical Society.

ESIPT molecules are more stable in E forms in the ground state but in K\* forms in the excited state. Thus, photoexcitation of the E form is immediately followed by a cyclic proton-transfer reaction  $E \rightarrow E^* \rightarrow K^* \rightarrow K \rightarrow E$  (scheme in Fig. 3.11), becoming nearly ideal four-level lasers. Their abnormally large Stokes shifts with virtually no self-absorption, in conjunction with the four-level scheme, makes them ideal for lasers.

The imidazole-based blue-emitting compound **HPI-Ac** [105] was the first ESIPT molecule showing laser emission in crystalline form, and single crystals as large as  $20\text{ mm} \times 25\text{ mm} \times 5\text{ mm}$  can be easily grown from its dilute solution (Fig. 3.11). More recently new examples have been reported: a green-emitting ( $\lambda = 514\text{ nm}$ ) (hydroxyphenyl)benzothiazole **HBT** [106] and several near-IR emitting ( $\lambda = 714\text{ nm}$ ) hydroxychalcone derivatives (e.g., **HC**) [107]. **HBT** shows pump power-dependent wavelength-switchable lasing as a consequence of a photoisomerization process in which the hydroxyphenyl and benzothiazole rings are found in a planar ( $\lambda = 514\text{ nm}$ ) or partially twisted ( $\lambda = 537\text{ nm}$ ) conformation (Fig. 3.11).

### 3.4 Molecular Glasses

Molecular glasses, where the constituent molecules are randomly oriented in the solid state, represent a structural bridge between molecular crystals and conjugated polymers. Unlike in molecular crystals, in molecular glasses, the fluorescence mechanism does not benefit from intermolecular interactions, and they are prone to quenching effects due to  $\pi-\pi$  interactions. Hence, to avoid this quenching and increasing the material solubility, the molecular constituents are provided with conjugated branches and surface groups. In this regard, the core defines the key electronic properties such as the color of light emission, while the surface groups confer solubility and steric hindrance. Hence, the glass maintains, mostly, the fluorescent properties of the constituent molecules.

It must be noted that an alternative way to overcome concentration quenching is to physically separate the emitting centers by diluting them into suitable semiconducting hosts. The most frequently used pair is the green-emitting aluminum tris-(8-hydroxyquinoline) (**Alq<sub>3</sub>**, Fig. 3.12) host, which is an electron-transporting material, doped with the red-emitting laser dyes **DCM** or **DCM2** (Fig. 3.12) in low concentrations [15]. In this case, the pump light is absorbed by **Alq<sub>3</sub>**, which very efficiently transfers its energy to **DCM** through Förster resonance energy transfer. The advantage of using guest–host systems is that they increase the separation between the spectral band of optical absorption and laser emission, thereby decreasing the reabsorption of the emitted light and reducing the laser threshold. Thanks to this reduction and the very wide emission spectrum of **DCM**, a DFB laser based on the blend **Alq<sub>3</sub>/DCM2** showed the broadest tuning range (115 nm, from 587 to 713 nm) reported to date [108].

Although the blends like **Alq<sub>3/DCM(2)</sub>** can be considered (binary) molecular glasses, we will focus in the following on molecular pure glasses, i.e., those with only one molecular compound. This kind of materials came later than dyes, molecular crystals, or conjugated polymers, but they have received considerable attention in the last decade, overall for the promising results obtained with oligofluorenes. Molecular glass constituents may be

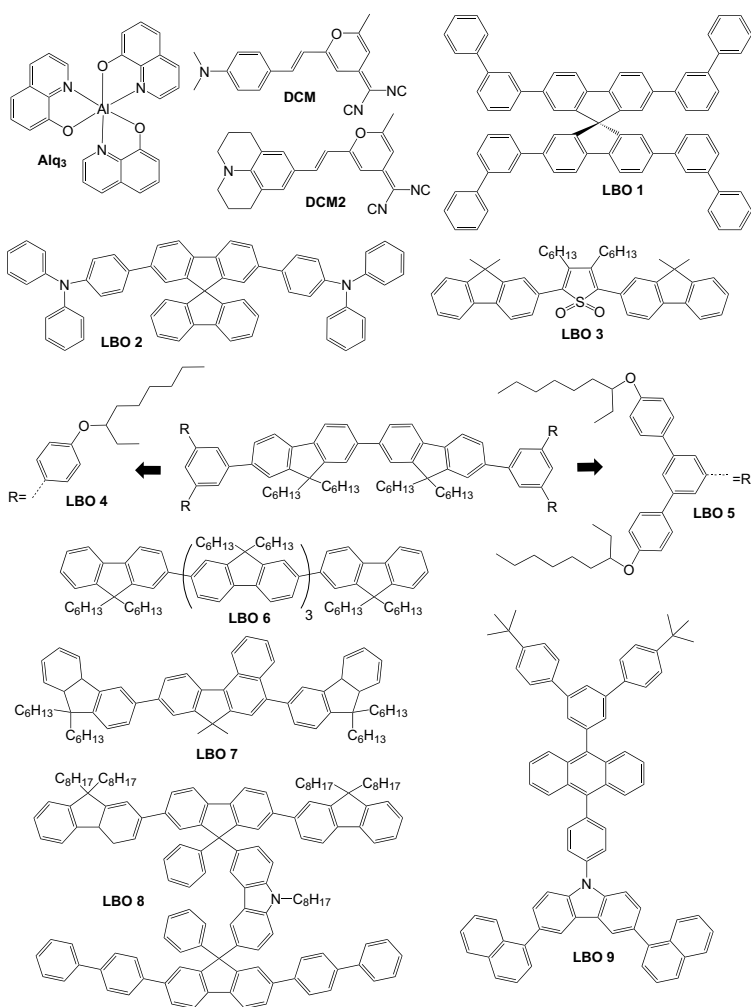


**Figure 3.12** Several linear, branched, and spiro compounds (LBO).

subdivided into two groups according to the molecule structure: linear, branched, and spiro compounds (Section 3.4.1), and star-shaped oligomers (Section 3.4.2). In particular, molecular glasses based on oligofluorenes are the most widely studied, but other molecular constituents have shown laser emission, as we will see in the following pages.

### 3.4.1 Linear, Branched, and Spiro Compounds

The first molecular glasses were based on spiro compounds, characterized by a spiro linkage of two chromophores (e.g., **LBO 1**, **2** in Fig. 3.12). ASE was demonstrated back in 1998 in a spirooligophenyl [109], and shortly after in a spirobifluorene [108]. Later, Komino et al. demonstrated ASE in thin films of vacuum-evaporated spirobifluorene **LBO 2** and assessed the effects of the substrate temperature during deposition on the emission thresholds and film morphology [110]. They found that the higher the temperature, the higher the threshold due to a randomization of the molecular orientation and an increase in surface roughness. Recently, a series of UV (<400 nm) emitting spiroquaterphenyls (**LBO 1**) with gains above 100 cm<sup>-1</sup> have been systematically evaluated [111].

On the other hand, linear molecular glasses are formed by molecules with a linear repetition of one or more chromophores. Laser emission was firstly demonstrated in a quinquethiophene-S,S-dioxide (a fivefold repetition of the central unit in **LBO 3**) [112]. Latter, some of these authors extended this work to a fluorenyl-thiophene co-oligomer (**LBO 3**), which showed a moderately efficient ASE in the green [113].

The real explosion of molecular glasses came with the first demonstration of laser emission in linear oligofluorenes [114]. This first report was based, in particular, on a bisfluorene core terminated with first-generation dendrimers (**LBO 4**). Dendritic compounds have a modular molecular architecture consisting of a conjugated core and dendrons, and solubility conferring surface groups, each of which contains conjugated units. The first-generation compounds showed efficient DFB emission around 400 nm, but much lower thresholds (down to 50 nJ/pulse, 240 kWcm<sup>-2</sup>) and higher efficiencies (14%) were obtained using second-generation dendrimers (**LBO 5**), in which the dendrons had two levels of branching [115]. In addition, two-photon pumped laser emission can be obtained in these compounds pumping both at fs and ns regimes [116].

Some other examples of linear oligofluorenes came later. Choi et al. synthesized and studied the effect of thermal annealing on both the emission and charge transport properties of films of a series

of linear oligofluorenes with three, five (**LBO 6**), seven, and eight fluorene units with hexyl chains at position 9 [117]. In particular, pentafluorene (**LBO 6**) films demonstrated low ASE thresholds and the highest photostability of all the synthesized compounds (half-lifetime of 1.2 and  $6 \times 10^6$  pulses in ambient and N<sub>2</sub> atmosphere with energy twice the threshold), and an increase in hole mobility after annealing due to an increase in crystallinity. Nevertheless, the hole mobility was still orders of magnitude smaller than those shown by molecular crystals or some conjugated polymers. More recently, the blue-emitting ( $\lambda = 420$  nm) benzofluorene-cored **LBO 7**, featuring twisted peripheral moieties to alleviate concentration quenching effects, has shown ASE with low threshold and moderate photostability [118]. These authors have later studied the ASE and charge transport properties of different fluorene–carbazole triads [119], and found that the all-fluorene containing triad presented the best compromise between ASE threshold and hole mobility values ( $\sim 10^{-2}$  cm<sup>2</sup> V<sup>-1</sup> s<sup>-1</sup>). Unfortunately, the electron mobilities could not be determined due to the presence of oxygen–water complexes that act as efficient electron traps.

Finally, Qian et al. have recently synthesized a range of branched (H-shaped) trifluorene–carbazole–diarylfluorene based hybrid oligomers [120]. For example, **LBO 8** presents a quantum yield of 77% in solid state with lifetimes around 0.6 ns, which guarantees high radiative decay rates. This is translated into rather low DFB threshold 1.6 kWcm<sup>-2</sup> and 4% efficiencies in the spectral range from 411 to 441 nm. This threshold is smaller than those obtained with polymers doped with Perylene Orange or BODIPY **19**, or the bisfluorene-core dendrimer **LBO 5**.

Although most of linear or branched oligomers or macromolecules are based on fluorene units, there are some developments on different compounds (apart from the spiro compounds mentioned above). For example, Niu et al. showed efficient blue DFB laser emission (threshold of 1.8 kWcm<sup>-2</sup> and efficiencies of 4%) from a molecular glass based on an anthracene derivative (**LBO 9**) with a solubilizing dendron at position 9 and a hole injection and transport promoter group at the opposite position 10 [121]. On the other extreme of the spectral range, Huang et al.

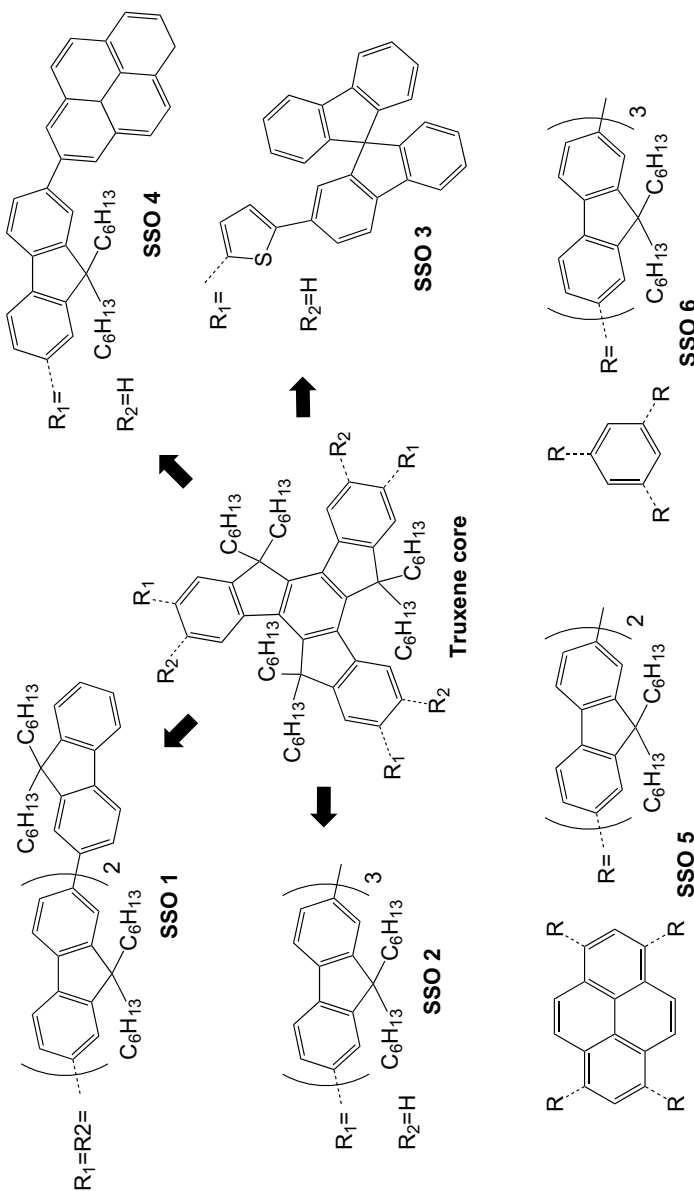


Figure 3.13 Selection of different star-shaped oligofluorenes (SSO).

demonstrated laser emission at 650 nm with a molecular glass containing dithienylbenzothiadiazole [122].

Along this section, we have only focused on oligomers that have been tested in neat films. Nevertheless, there are some reports in which different macromolecules are characterized as laser materials diluted in polymer films to avoid quenching effects. Such is the case of pyrenyl- fluorene and carbazoles [123], oligothienoacene [124], multiphenyl-diamine derivatives [125], dimethyloxysilane-fluorene [126], or fluorene- and benzofluorene-core oligomers [127].

### 3.4.2 Star-Shaped Oligomers

Oligofluorenes have benefited from a rather different oligomeric structure, that of star-shaped or starburst macromolecules. These dendritic molecular glasses consist of (oligo)fluorene branches “growing”, in a radial fashion, from a conjugated core (Fig. 3.13).

In the last years, several examples have been reported in which different core and dendrons have been used. The first and most studied core unit is the so-called truxene (10,15-dihydro-5H-diindeno[1,2-*a*;10,20-*c*]fluorene), a planar heptacyclic polyarene structure that can be considered three annulated fluorene moieties (Fig. 3.13). These polycyclic aromatic hydrocarbons have received considerable attention in the last decade due to their prospects of being used in organic photonics and electronics [128].

Stimulated emission (ASE) was first obtained in a series of truxenes with three or six bi- or tri-fluorene branches [129]. Later, these same authors analyzed the effect of the dendrimer lengths (one to four fluorenes) on the photophysical properties of six-branched truxenes, and found that the trifluorene-branched derivative (**SSO 1**) rendered excellent lasing characteristics (threshold of  $110 \text{ Wcm}^{-2}$  and slope efficiency of 5.3% at 437 nm) in 1D-DFB lasers [130]. Note that this threshold is two orders of magnitude smaller than that of the H-shaped oligofluorene **LBO 8** [120].

Later, a different group reported laser emission in a series of truxene derivatives with three mono-to-tetrafluorene branches [131, 132]. Whereas the tetrafluorene-branched derivative showed the lowest DFB threshold of them ( $270 \text{ Wcm}^{-2}$ ) [131], the trifluorene-branched truxene (**SSO 2**) rendered one of the broadest

tuning ranges (51 nm, from 422 to 473 nm) reported for organic blue lasing materials with just twice the threshold ( $515 \text{ Wcm}^{-2}$ ) [132]. Herrnsdorf et al. used **SSO 2** to implement mechanically flexible DFB lasers [133].

More recently, other lasing truxene derivatives have been synthesized and studied, such as a series of spirobifluorene-branched truxenes (**SSO 3**, [134]) or pyrane-capped oligofluorene-branched truxenes (**SSO 4**, [135]). Nevertheless, the ASE and laser performance of these new compounds is somewhat worse than that observed for the star-shaped compounds **SSO 1** and **2**.

Apart from truxene, different chromophoric units have been used as core in starburst molecules. For example, Xia et al. characterized the ASE and DFB performance of pyrane-cored oligofluorenes with 1 to 3 fluorene units in each of the four arms [136]. The compound with two fluorene units (**SSO 5**) showed the best laser performance not only of this family, but of all the molecular glasses described so far, with an extraordinarily low DFB threshold of  $40 \text{ Wcm}^{-2}$ , a 4% slope efficiency and 40 nm tuning (from 471 to 512 nm). Recently, some of these authors showed that the inclusion of terminal electron-withdrawing cyanophenyl groups in each arm did not influence the optical gain properties but leads to a reduction in the LUMO level, hence improving the electron affinity [137]. This could be beneficial to the electron injection and transport, without harming the hole affinity and injection of these pyrene-cored starbursts.

Benzene has also been used as a core unit in lasing star-shaped oligofluorenes [138]. These authors demonstrated that the trifluorene branched benzene derivative (**SSO 6**) presents a DFB laser performance comparable, but slightly worse, than truxenes with the same arm lengths (**SSO 2**), probably due to a higher level of intermolecular interactions in the benzene-core compound. In this regard, the solid-state quantum yield of the truxene-cored molecules change very little from their solution values ( $\sim 0.85$ ), in strong contrast to the drop in quantum yields of the benzene-cored molecules when in the solid state (from  $\sim 0.85$  to  $\sim 0.55$ ) [138].

TD-DFT calculations have shown that in both truxene- and benzene-cored compounds (**SSO 1-2** and **6**), the HOMO is distributed along the whole molecule, whereas the LUMO is

concentrated in one of the multiple branches [139]. In other words, the absorption takes place across the entire molecule and, after excited-state relaxation, the emission results from a single arm. Nevertheless, truxene-cored compounds **SSO 3** and **4** delocalize both the HOMO and the LUMO along two arms, but not necessarily the same [134, 135]. Quite differently, in pyrene-core compounds (e.g., **SSO 5**) both the HOMO and the LUMO are almost concentrated on the pyrene backbone, which implies that its emission and absorption are mostly controlled by the pyrene unit [136].

The results provided in this section illustrate the great potential of starburst macromolecular materials for use in laser applications. Nevertheless, there are almost no reports on the charge transport properties, and those works in which this property has been measured report mobilities for non-lasing truxene compounds of just  $10^{-3} \text{ cm}^2 \text{ V}^{-1} \text{ s}^{-1}$  [140], reducing the present prospects of using these materials for organic laser diodes.

### 3.5 Conjugated Polymers

Conjugated polymers are long chain-like molecules that consist, at least, of one backbone of alternating double and single bonds. Due to the particular distribution of the carbon  $p_z$ -orbitals in the chain, the single and double bonds mesomerize and become similar, i.e., there is electron delocalization along the chain. Hence, the  $\pi$ -electrons can “easily” move from one bond to other, making conjugated polymers resemble one-dimensional semiconductors. Poly(2-methoxy-5-(2-ethylhexyloxy)-1,4-phenylenevinylene) (**MEH-PPV**, Fig. 3.14) was the first conjugated polymer to show laser emission, first in solution [12], and later in thin films [141]. Albeit the first optically pumped organic solid-state laser was demonstrated in poly(*para*-phenylene vinylene) (**PPV**, Fig. 3.14) [13]. Since then, many other reports on laser emission from conjugated polymer have been published [15, 142, 143]. Two families of conjugated polymers have been studied particularly extensively for lasers: poly(phenylene vinylene)s (e.g., **MEH-PPV**, Fig. 3.14) and polyfluorenes (e.g., **PFO**, Fig. 3.14).

In these gain media, both the processes of excitation generation, transfer, and annihilation occur between neighboring chains

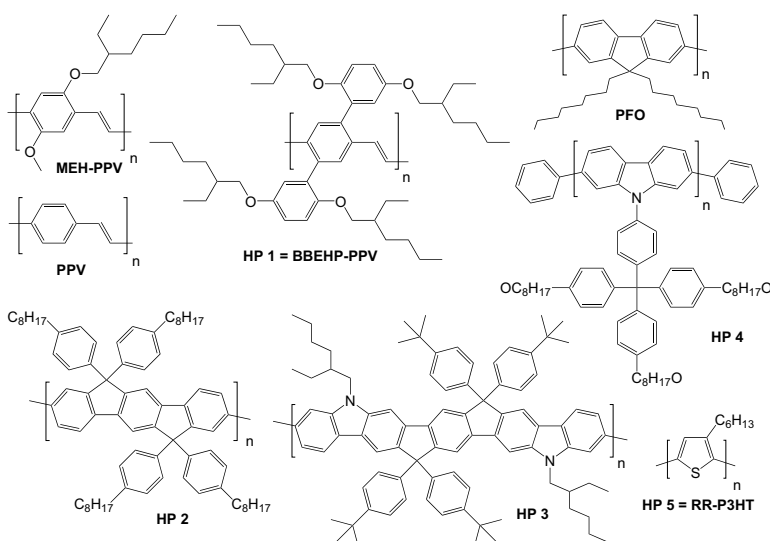


**Figure 3.14** Selection of laser conjugated homopolymers (HP).

(intermolecular interaction). Hence, most of the efforts on material developments have been focused on mitigating the effects of chain-chain interactions on the optical gain properties while trying to improve the charge transport properties. The most general strategy has consisted of tailoring the distance between chains through the inclusions of side-chains or spacers. In this regard, the main backbone defines the key electronic properties such as the emission wavelength and charge mobility, while the side groups confer solubility and control the chain-chain distances.

For convenience, we will classify conjugated polymers in homopolymers (Section 3.5.1), formed by a single monomeric unit, and copolymers (Section 3.5.2), in which the chain contains two or more chromophoric units with variable stoichiometry.

### 3.5.1 Homopolymers

At the dawn of laser conjugated polymer research, most reports dealt with homopolymers (HP), specially those based on poly(para-phenylene vinylene) derivatives [144–146]. Among them,

**MEH-PPV** (Fig. 3.14) has stood the test of time and is one of the most widely used and studied conjugated polymers so far [15, 142, 143]. Although the interest in conjugated polymer synthesis has shifted in the last decades to other kinds of polymers (such as polyfluorenes), some new phenylene vinylene HPs have been developed and their laser performance characterized (Fig. 3.14). Such is the case of the green-emitting **HP 1** (also known as **BBEHP-PPV** [147]), which has been recently used to fabricate very low threshold ( $\sim 210 \text{ Wcm}^{-2}$ ) nanoimprinted lasers pumped by InGaN LEDs [148, 149], as well as flexible devices [150].

HP-containing fluorene units have received a great deal of attention, overall poly(9,9-dioctylfluorene) (**PFO**), a blue-emitting polymer. Heliotis et al. first reported ASE with gains above  $70 \text{ cm}^{-1}$ , and subsequently DFB emission with thresholds of  $3 \text{ kWcm}^{-2}$  and efficiencies as high as 8% [151–153]. It must be noted that later reports showed thresholds down to  $100 \text{ Wcm}^{-2}$  [154]. **PFO** is known to exhibit amorphous ( $\alpha$ ) and crystalline ( $\beta$ ) phases in thin films [155], each with its photophysical properties, and the relative quantity of each phase depends on the sample deposition conditions, but it can be modified by postdeposition processing. Although the  $\beta$  phase shows improved quantum yield [156], enhanced charge-carrier transport [157], and superior optical gain properties [158], it is usually avoided for laser devices [154, 159], since any postdeposition solvent or heat treatment would destroy its fragile morphology. In the next section, we will see that its copolymerization with different units may tame this behavior. Besides, **PFO** can be pumped by means of a two-photon absorption process [160] and has been used for explosive vapor detection [161].

HPs with different chromophoric families have been studied. For example, Laquai et al. reported ASE in thin films of a series of blue-emitting ladder-type poly(phenylenes)s consisting of an increasing number of bridged phenylene rings per monomer unit starting from fully arylated poly(ladder-type indenofluorene) (**HP 2**) up to poly(ladder-type pentaphenylene) with carbazole units (**HP 3**) [162]. Among them, **HP 2** rendered the best performance, with a threshold down to  $375 \text{ Wcm}^{-2}$ . **HP 3**, on the contrary, demonstrated the worst performance, with a threshold 50 times higher. These results suggest that carbazoles are not as good as fluorenes for active

materials, something that we had already seen for molecular glasses ([Section 3.4.1](#)). Nevertheless, the figure of merits of polycarbazoles has been slightly improved in the recently reported derivative **HP 4** [[163](#)].

Finally, polythiophenes remain as one of the most promising building blocks for polymer semiconductors [[164](#)]. The red-emitting regio-regular poly(3-hexylthiophene) (**HP 5** or **RR-P3HT**), in particular, presents one of the highest hole mobilities among conjugated polymers ( $\sim 0.1 \text{ cm}^2 \text{ V}^{-1} \text{ s}^{-1}$ ), three orders of magnitude stronger than that of **PFO**. Unfortunately, the cofacial lamellar  $\pi$ -stacking that favors its charge transport is detrimental to photoluminescence efficiency, and hence it does not present laser emission in neat films. Nevertheless, it has been recently shown that blending **RR-P3HT** with the semiconducting copolymer **F8BT** ([Fig. 3.15](#)) allows for obtaining modest DFB thresholds ( $2.2 \text{ kWcm}^{-2}$ ) and efficiencies above 2% [[165](#)]. Later, the editors of this book have shown that the ASE properties of this blend can be optimized through changes in the film morphology, controlled by changing the solvent used for deposition [[166](#)].

### 3.5.2 Copolymers

The use of copolymers enables a higher synthetic flexibility to tailor the emission, morphological and charge transport properties independently. Research on the effect of copolymerization has been particularly fruitful in polyfluorenes ([Fig. 3.15](#)). In this regard, fluorenes have been copolymerized, among others, with dimethoxyphenylfluorene [[167](#)], benzothiadiazole (**F8BT**) [[167](#)], octyloxy-binaphthyl (**CP 3**) [[168](#)], dimethylbutyl fluorene (**CP 1**) [[154](#)], phenylene sulfonate [[169](#)], spirobifluorenes [[170](#)], vinyl-ether functionalized fluorene (**CP 2**) [[171](#)], dibenzothiophene-s,s-dioxide [[172](#)], or diarylfluorene [[173](#)].

**F8BT**, together with poly(dioctylfluorene-co-dimethoxyphenyl fluorene) (**F8DP**), and **Red F**, a Dow Chemical proprietary red-emitting copolymer, were the first fluorene copolymers to show lasing [[167, 174, 175](#)]. Changing the group(s) copolymerizing with **PFO**, the emission wavelength could be changed, with **F8BT** emitting around 570 nm and **Red F** around 680 nm. In fact, **Red F** is not

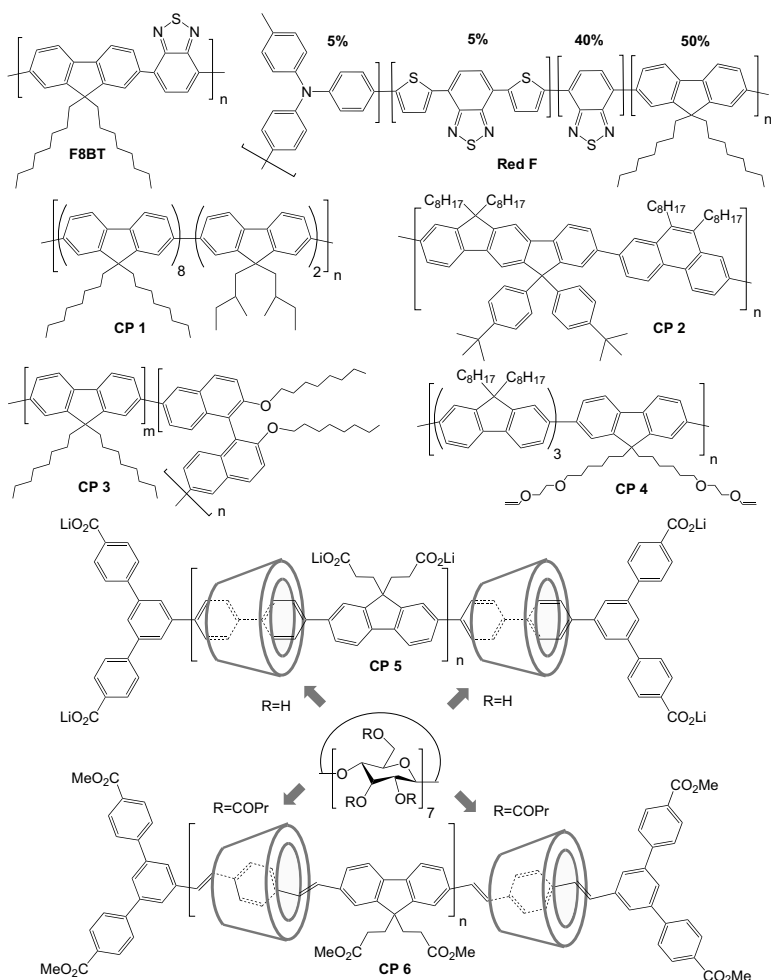


**Figure 3.15** Recently synthesized conjugated copolymers (CP).

only one of the reddest emitting conjugated polymers, but it has demonstrated stunning photostabilities, with operational half-times reaching  $2 \times 10^7$  pulses [174]. **F8BT** and its statistical derivatives (fluorene:benzothiadiazole ratios different from 1:1) have received considerable attention. Amarasinghe et al. demonstrated pulse amplification in thin films of both **F8BT** and ADS233YE (statistical

ratio 9:1) with gains greater than 10 dB [176, 177]. A **F8BT** DFB laser encapsulated in a PDMS matrix rendered a tunability of 20 nm by stretching the sample up to a 7% of its initial size [178]. Later, a highly sensitive reversible photo-quenching of ASE and photocurrent in **F8BT** blended with a photochromic material was reported [179]. Finally, the first electrically driven organic laser was demonstrated on a ADS233YE DFB laser pumped with an InGaN LED [180].

The inclusion of the benzothiadiazole group in **F8BT** increased the charge mobilities of **PFO** by an order of magnitude [181], but much higher mobilities have been obtained with smarter substitutions. For example, the copolymerization of **PFO** with small ratios of 9,9-di(2-methyl)butyl substituted fluorene (**CP 1**) has rendered one of the better, if not the best, combinations of efficient laser emission and high charge-carrier mobilities in organic compounds to date [154]. In particular, **CP 1** showed DFB thresholds as low as  $30 \text{ Wcm}^{-2}$ , efficiencies around 4%, and a tuning range of 45 nm, thus benchmarking the pyrane-cored oligofluorene **SSO 5** (Fig. 3.13), and with hole mobilities  $\sim 3\text{--}6 \times 10^{-2} \text{ cm}^2 \text{ V}^{-1} \text{ s}^{-1}$ , 100 to 200 higher than that of **PFO**. This balanced combination of lasing and charge mobility is possible because the long alkyl-substituted fluorene units retain the emission properties of **PFO** by preventing close contact between neighboring backbones, whereas the short alkyl-substituted fluorene units create charge-carrier hoping sites by allowing the backbones to approach sufficiently at those sites.

Another example of well-balanced combination of gain and charge transport properties was demonstrated in indenofluorene-phenanthracene copolymers (**CP 2**) [182]. Like in **CP 1**, blue ASE was obtained from **CP 2**, rendering gains of up to  $154 \text{ cm}^{-1}$ —one of the highest among conjugated polymers—and propagation losses of just  $1 \text{ cm}^{-1}$ . On top of these gain parameters, **CP 2** is characterized by hole mobilities of  $10^{-2} \text{ cm}^2 \text{ V}^{-1} \text{ s}^{-1}$ , slightly below that of **CP 1**. In this case, the origin of the balanced laser and transport properties is the planarized structure of the bridged phenylene units in the indenofluorene comonomer, which enhances the interchain interactions and thus facilitates charge-

carrier hopping and transport. This, in combination with the rather narrow density of states and the absence of deep traps, appears to be the main origin of the high hole mobility.

The use of copolymers not only enables tuning the emission and charge transport properties of the final material, but allows controlling the morphology of the solid samples. For example, the copolymerization of dioctylfluorene monomers with appropriate proportions of octyloxy-binaphthyl spacer groups (**CP 3**) hinders the formation of the highly ordered  $\beta$  phase and leads to a fourfold reduction in laser threshold with respect to that of neat **PFO** without modifying the emission range [168]. On the contrary, the copolymerization of dioctylfluorene monomers with fluorene monomers functionalized with crosslinkable vinyl-ether side groups (**CP 4**) allows freezing either the  $\alpha$  or  $\beta$  phases upon crosslinking, thus enabling postdeposition processing without morphology changes [171]. These authors demonstrated low laser thresholds of  $65 \text{ Wcm}^{-2}$  in the  $\beta$  phase, nine times lower than those in the  $\alpha$  phase.

All of the previous examples, either homopolymers or copolymers, control the interchain interactions with the introduction of bulky side groups or spacers in the backbone. An alternative solution to avoid aggregate formation between neighbor chains is the use of supramolecular structures encapsulating the conjugated polymer backbone, thus giving place to what has been coined as “insulated molecular wires” [183]. One strategy for insulating a molecular wire is to thread it through a series of insulating macrocycles to form a polyrotaxane. Laser materials have benefited from this approach. For example, Mroz et al. obtained pulsed DFB laser emission from the blue-emitting polyrotaxane **CP 5**, consisting of a conjugated polymer polyfluorene-*alt*-biphenylene threaded through  $\beta$ -cyclodextrins, a naturally occurring molecular tube [184]. Recently, these authors reported quasi-CW ASE ( $\sim 1 \text{ ms}$  pulses) from the green-emitting polyrotaxane **CP 6**, based on polyfluorene-*alt*-bisvinylphenylene copolymer threaded through modified  $\beta$ -cyclodextrins [185].

## 3.6 Hybrid Compounds

In the previous sections, we have revisited a great variety of organic active materials. In these compounds, the emitting center, i.e., the chromophore part responsible for the emission, is organic (mainly C, and H, with traces of other elements such as O, N, S, Br). In this section, we will shine a light over some organic/inorganic “hybrid” compounds whose emitting center is not purely organic. These materials, which can be processed from solution, deserve our attention due to their potential to outreach, or at least compete with, organic counterparts.

Most organic compounds usually suffer from absorption by vibrations of the C-H bond in the NIR wavelength region, and thus most laser chromophores emit at wavelengths well below 1  $\mu\text{m}$ . In fact, all of the molecules described in this chapter emit below 740 nm. Hence, the second (1330 nm) and third (1550 nm) communication windows will be almost impossibly covered by devices based on dye-doped polymers or organic semiconductors. On the other hand, trivalent lanthanide laser crystals have demonstrated their tremendous value in this spectral range [186]. For example, lasers based on the trivalent neodymium ion ( $\text{Nd}^{3+}$ ), like the Nd:YAG crystal, are by far the most important solid-state laser for scientific, medical, industrial, and military applications. Although the technology to grow bulk high-quality crystals is very mature and controlled, it cannot comply with the requirements that make organic photonics so appealing (integrable, easy and cheap to implement, flexible, disposable, biocompatible). A way to develop devices featuring the best of both worlds (operating in the IR spectral region and being solution-processable) is by doping polymer hosts with lanthanide complexes that encapsulate rare-earth ions (Fig. 3.16a). This approach has been successfully implemented with a number of rare-earth ions, and optical gain has been demonstrated in polymer waveguides doped with  $\text{Eu}^{3+}$  [187],  $\text{Sm}^{3+}$  [188],  $\text{Er}^{3+}$  [189], and  $\text{Nd}^{3+}$  [190, 191]. The  $\text{Nd}^{3+}$  complex neodymium(thenoyltrifluoroacetone)<sub>3</sub> 1,10-phenanthroline (**Nd(TTA)<sub>3</sub>phen**, Fig. 3.16a) is particularly relevant [191]. With this complex, CW laser operation at 1060 nm (transition  $^4F_{3/2} \rightarrow ^4I_{11/2}$ ) was demonstrated in polymer

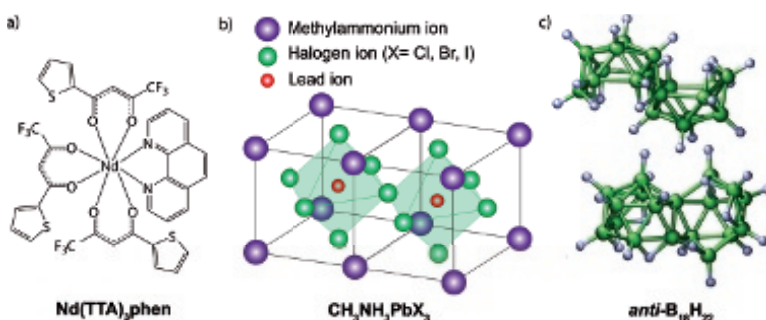


**Figure 3.16** Organic/inorganic hybrid compounds: (a)  $\text{Nd}^{3+}$  ion complex, (b) Halide perovskite (two cubic unit cells), and (c) borane *anti*- $\text{B}_{18}\text{H}_{22}$  (side and top view).

channel waveguides, with a slope efficiency of  $\sim 2\%$  and a maximum output power of  $\sim 1$  mW [192, 193]. In addition, lasing was also achieved from the quasi-three-level 878 nm transition  ${}^4F_{3/2} \rightarrow {}^4I_{9/2}$ , but with a lower efficiency. More relevantly, over 2 h long-term, stable CW laser operation was demonstrated, indicating the durability of the polymer gain medium. These results are particularly relevant, as they supposed the first demonstration of CW emission in an static organic solid-state medium.<sup>c</sup> Recently, an excellent review on organic solid-state integrated amplifiers and lasers, with a comprehensive compilation of lanthanide complexes used for organic photonics, has been published [15]. The readers of this book are kindly referred to this review to have a flavor on rare-earth-ion activated polymer photonic devices (laser and amplifiers), as well as much information about gain materials, fabrication, and applications for integrated devices.

Perovskite materials, which may crystallize in cubic, tetrahedral, or orthorhombic structures, adopt the chemical formula  $\text{ABX}_3$ , where A and B are cations of dissimilar sizes, and X are anions, typically oxygen, halogens, or alkali metals. In the particular case of hybrid organic/inorganic halide perovskites (halide perovskite in short), A is usually a methylammonium ion ( $\text{CH}_3\text{NH}_3$ ), B is a

<sup>c</sup>CW laser emission had been previously achieved in a rotating dye-doped polymer disc [194].

lead ion, and X are halogen ions (iodine, bromine, or chlorine), affording the chemical formula  $\text{CH}_3\text{NH}_3\text{PbX}_3$  (Fig. 3.16b). Thanks to their exceptional attributes (high fluorescence quantum yields, high carrier mobility, adjustable spectral absorption and emission ranges, long diffusion lengths, easiness of fabrication), halide perovskites have recently emerged as promising materials for low-cost and highly efficient optoelectronic devices [195]. In fact, just in a few years, perovskite solar cells have reached 20% power conversion efficiencies.<sup>d</sup> With these merits, it was just a matter of time that halide perovskites reached the status of laser materials. This happened in 2014, when Xing et al. reported efficient, tunable, and strikingly photostable ASE from thin films deposited from solution [196]. By simply changing the stoichiometry of halogen ions in the sample ( $X = \text{Cl}_x\text{Br}_{3-x}$  or  $\text{Br}_x\text{I}_{3-x}$ ), the emission could be tuned from 390 nm ( $X = \text{Cl}_3$ ) to 790 nm ( $X = \text{I}_3$ ). More impressively, after  $9 \times 10^7$  pulses ( $\sim 25$  h of operation), the samples did not show any traces of photodegradation. After this report, others have followed in which halide perovskites showed laser emission in VCSELs [197], coated onto silica microspheres [198], in single-crystal nanowires [199], as well as in flexible devices [200]. In summary, the processing versatility of these materials makes them highly compatible with unconventional substrates, printing technologies, and monolithic integration with silicon-based electronics. If we add the long-range balanced electron and hole mobilities ( $5\text{--}10 \text{ cm}^2 \text{ V}^{-1} \text{ s}^{-1}$  and  $1\text{--}5 \text{ cm}^2 \text{ V}^{-1} \text{ s}^{-1}$ , respectively) [201], the low bi-molecular charge-recombination rates [202], and large wavelength range tunability [196], it can be said that  $\text{CH}_3\text{NH}_3\text{PbX}_3$  has injected itself in the race toward the first realization of electrically pumped solution-processed on-chip lasers.

The last hybrid compounds that we will deal with are boron hydrides or boranes, inorganic cluster compounds whose main constituents are boron and hydrogen. Boron has one valence electron fewer than its number of valence orbitals. This ostensible electron deficiency forces boranes to share electron density in a sort

---

<sup>d</sup>Research Cell Efficiency Records, NREL (2015). [http://www.nrel.gov/ncpv/images/efficiency chart.jpg](http://www.nrel.gov/ncpv/images/efficiency%20chart.jpg)

of quasi-aromatic delocalization [203], resulting in the formation of molecules with polyhedral cluster geometries (Fig. 3.16c). Boranes and carboranes (boron hydrides including carbon atoms in their skeleton) have found a place in material science [204]. Nevertheless, only a handful of them present luminescence and in none of them was ever evidenced the existence of stimulated emission. This held true until recently, when we demonstrated that, at least one borane, was indeed capable of generating laser light in organic solutions [205]. This borane, *anti*-B<sub>18</sub>H<sub>22</sub> (Fig. 3.16c), is formed by 18 boron atoms and 22 hydrogen atoms that render a polyhedral structure resembling a split soccer ball. This compound was already synthesized in the 1960s, but it was not until recently that its fluorescence properties were comprehensively described [206]. Photophysically speaking, *anti*-B<sub>18</sub>H<sub>22</sub> is analogous to common dyes. With a quantum yield approaching unity (0.97), it has broad absorption and emission bands peaked at 330 nm and 410 nm, respectively, and a lifetime of 11 ns. With these properties, we demonstrated that solutions of *anti*-B<sub>18</sub>H<sub>22</sub> show, under pulsed excitation, blue laser emission at 406 nm with an efficiency of 9.5%, and a photostability superior to many of the commercially available state-of-the-art blue laser dyes [205]. What makes boranes photophysically different from dyes is that the latter have  $\pi$  bonds while the former have  $\sigma$  bonds. This results in a rather weak oscillator strength and hence a low absorption probability. In fact, the peak molar extinction coefficient of *anti*-B<sub>18</sub>H<sub>22</sub> is 10 times smaller than that of blue dyes. Thus, to achieve the needed optical densities for the pump radiation, one must use high concentrations ( $\sim 10^{-2}$  M) that lead to: (a) reduction in the fluorescence quantum yield due to self-quenching, (b) formation of microcrystallites due to solvent problems that cause optical scattering, and (c) feasibility of excited-state absorption at the pump and laser wavelengths. All these processes contribute to the reduction in the laser efficiencies. Nevertheless, these results are encouraging, as the very first organic dyes (Fig. 3.1) rendered efficiencies of  $\sim 4\%$ , whereas in Section 3.2.1 we have seen current dyes with efficiencies above 70%.

### 3.7 Final Remarks

The aim of this chapter was to provide the widest perspective on the rich variety of materials that are available so far to develop organic lasers, and such goal has been accomplished. Along these pages, and categorized into five well-defined families (dyes, molecular crystals, molecular glasses, conjugated polymers, and hybrid compounds), more than a hundred different compounds synthesized and characterized in the last 10–15 years have been selected and described, a number that could have grown to more than 400 if all the compounds studied in the cited references would have been included.<sup>e</sup> Among them, two chromophoric units shine with their own light, BODIPY and fluorene (oligomeric or polymeric), each in its plot. Inexorably, some compounds have stayed out of this chapter, partly because of lack of space, partly because they have escaped the bibliographic search. As was stated at the beginning of the chapter, the reason for this profusion lays in one of the wonders of organic chemistry: the “easy” modulation of structural and photophysical properties by straightforward and well-known functionalizations.

Despite being the eldest and most mature compounds among all the available organic laser materials, dyes are still alive and kicking. Among them, BODIPYs have shown a tremendous advancement in terms of efficiency, photostability, and spectral coverage (from 450 to 740 nm, [Fig. 3.4](#)), not only in solution, where they have few rivals, but on polymeric rods and thin films. Nevertheless, the photostability in thin films is still reduced. In this regard, perylenediimides (PDIs, [Fig. 3.5](#)) are much more robust and withstand stronger pumping conditions than BODIPYs with just a little less efficiency, and thus have received much attention due to their prospects of being used in integrated lasers. But truth be told, for the time being PDIs are by far outperformed by organic semiconductors in this ground. On the other hand, fluorescent proteins ([Fig. 3.7](#)) have surprisingly emerged as a promising active media for solid-state lasers, as the external barrel encapsulating

<sup>e</sup>Many other compounds that have been synthesized could exhibit laser emission, but their ASE or laser properties have not been studied.

the chromophores limits intermolecular energy migration and quenching even at pure solid-state form. For sure we will hear more about these compounds in the future.

In spite of the difficulties associated with the growth and processing of high-quality large samples, molecular crystals keep a good pace in the development of new materials with high quantum yields and increasing values of charge-carrier mobilities. In this sense, thiophene/phenylene co-oligomers (TPCOs, Fig. 3.8) and oligo(phenylene vinylene)s (Fig. 3.9) stand out for their well-balanced combination of lasing and transport properties. Nevertheless, the non-oligomeric compounds (Figs. 3.10 and 3.11) are not far behind as they are demonstrating remarkably low laser thresholds as well as added functionalities and capabilities, such as optical switching or polaritonic lasing.

Molecular glasses have held promise for the realization of electrically pumped organic lasers during the last decade. Being a structural bridge between molecular crystals and conjugated polymers, they have benefited from the processing simplicity and flexibility of polymers, while avoiding their synthetic difficulties. Oligofluorenes have demonstrated very low laser thresholds (specially star-shaped oligofluorenes, Fig. 3.13), and moderate mobilities. Unfortunately, simplicity comes at a price: the absence of molecular glasses with a well-balanced combination of lasing and transport properties as up to date. But future developments could revert this reality. Following the path of conjugated polymers, molecular “binary” glasses with adequate blends of molecules with high mobilities and molecules with high quantum yields could render the desire balance.

Conjugated polymers have been on the run toward electrically pumped lasers for 20 years, but it has been in the last decade when the major milestones have been achieved. Although several conjugated homopolymers (Fig. 3.14) have demonstrated remarkably low laser thresholds and have stood the test of time due to their exceptional photophysical properties, it has proved difficult to attain higher charge-carrier mobilities without scrambling the emission properties. On the contrary, the use of copolymers (Fig. 3.15) has enabled a higher synthetic flexibility to tailor the emission, morphological and charge-transport properties independently. By

smart combinations of appropriate monomers, tremendous advancements have been achieved in terms of well-balanced lasing and charge transport properties, two properties that, for many years, were thought to be mutually exclusive in organic semiconductors [207]. On a parallel path, conjugated polymers have stood up as particularly suitable materials for sensing tasks, including explosive [208] or biomolecule [209] detection.

A typical problem associated with organic gain media is their limited operational lifetime, shortened due to thermal and/or chemical (mainly oxidative) degradation upon intense photoexcitation. As we have seen, this degradation can be partially mitigated by smart functionalizations, but it entails complex, and not always successful, protocols. An alternative route is the physical encapsulation of the gain medium into other materials to protect the active layer from oxidation. The biggest benefit of this approach is that it is independent on the nature of the medium, as has been demonstrated in dyes [210], molecular glasses [133], and conjugated polymers [150, 159, 211]. In particular, the device based on encapsulated **MEH-PPV** demonstrated a 2500-fold improvement in operational lifetime [211].

Organic/inorganic hybrid compounds (Fig. 3.16) are pushing hard to earn their place among solution-processed materials. Rare-earth complexes, with their photophysical properties optimized for the IR and its straightforward consecution of CW operation, have few rivals in this ground. Halide perovskites, on the contrary, compete with all organic semiconductors, but thanks to their exceptional attributes, success is certainly granted. Boranes, on the other hand, have recently taken their first steps, and it is still uncertain where these steps will lead them.

In the last two decades, the field of organic laser materials has experienced an unprecedented development, pushing the limits of what was thought to be physically and chemically possible. Today, we are living an exciting era in organic photonics, in general, and in organic lasers, in particular, with many fundamental challenges being solved and an ever-growing number of fascinating new developments on materials, devices, and applications being demonstrated. In the near future, organic laser materials have

several challenges to face. It would be a tremendous technological advancement to develop new dyes from the UV ( $<400$  nm) to the IR ( $>800$  nm) that could be pumped at a single wavelength (e.g., 355 nm), with efficiencies reaching the quantum defect limit (each pump photon is converted into a laser photon) and record-breaking photostabilities. Some steps have been given in this direction by using coumarin-BODIPY cassettes (**BODIPY 30**, Fig. 3.4) [46]. In addition, efforts should be directed to enable the maturity of solid-state dye lasers. On the other hand, organic semiconductors, either molecular crystals and glasses or conjugated polymers, face common challenges of utmost importance to implement organic laser diodes: develop new materials with (a) much higher and well-balanced hole and electron mobilities (ambipolar transport), and (b) higher quantum yields to reduce the laser threshold, as it would not only reduce the needed injection current densities but would increase the final device operational lifetime. From the processing point of view, molecular crystals, in particular, should improve their mechanical performance and stability, as they are brittle materials difficult to post-process (cutting or polishing). Finally, and independently on the organic semiconductor, new cavity configurations with extremely reduced laser thresholds, even in the presence of electrodes, should be designed. In this regard, plasmonics is a path that could be explored [212, 213].

## References

1. Maiman, T. H. (1960). Stimulated optical radiation in ruby, *Nature* **187**, pp. 493–494
2. Fabrikant, V. A. (1940). Emission mechanism of a gas discharge, *Trudy VEI* **41**, p. 236.
3. Schawlow, A. L. and Townes, C. H. (1958). Infrared and optical masers, *Phys. Rev.* **112**, pp. 1940–1949
4. Einstein, A. (1917). Zur Quantentheorie der Strahlung, *Physika Zeitschrift* **18**, pp. 121–128.
5. Hetch, J. (2010). A short history of laser development, *Opt. Eng.* **49**, 091002, pp. 1–23.

6. Javan, A., Bennett, W. R., and Herriott, D. R. (1961). Population inversion and continuous optical maser oscillation in a gas discharge containing He-Ne mixture, *Phys. Rev. Lett.* **6**, 3, pp. 106–110.
7. Sorokin, P. P. and Stevenson, M. J. (1960). Stimulated infrared emission from trivalent uranium, *Phys. Rev. Lett.* **5**, pp. 557–559.
8. Franken, P. A., Hill, A. E., Peters, C. W., and Weinreich, G. (1961). Generation of optical harmonics, *Phys. Rev. Lett.* **7**, 4, pp. 118–119.
9. Sorokin, P. P. and Lankard, J. R. (1966). Stimulated emission observed from an organic dye, chloro-aluminum phthalocyanine, *IBM J. Res. Dev.* **10**, 3, pp. 162–163.
10. Schäfer, F. P., Schmidt, W., and Volze, J. (1966). Organic dye solution laser, *Appl. Phys. Lett.* **9**, 8, pp. 306–309.
11. Karl, N. (1972). Laser emission from an organic molecular crystal, *Phys. Status Solidi A* **13**, pp. 651–655.
12. Moses, D. (1992). High quantum efficiency luminescence from a conducting polymer in solution: A novel polymer laser dye, *Appl. Phys. Lett.* **60**, 3215, pp. 1–3.
13. Tessler, N., Denton, G. J., and Friend, R. H. (1996). Lasing from conjugated-polymer microcavities, *Nature* **382**, pp. 695–697.
14. Bogue, R. (2011). Developments in organic lasers and their role in sensing, *Sensor Rev.* **31**, pp. 13–17.
15. Grivas, C. and Pollnau, M. (2012). Organic solid-state integrated amplifiers and lasers, *Laser Photon. Rev.* **4**, pp. 419–462.
16. Brutting, W. and Adachi, C. (eds.) (2012). *Physics of Organic Semiconductors* (Wiley).
17. Duarte, F. J. and Hillman, L. W. (1990). *Dye Laser Principles* (Academic Press, San Diego, CA).
18. Schäfer, F. P. (1990). *Dye Lasers* (Springer-Verlag, Berlin, Germany).
19. Duarte, F. J. (1991). *High-Power Dye Laser* (Springer-Verlag, Berlin, Germany).
20. Treibs, A. and Kreuzer, F. H. (1968). *Difluoroboryl-komplexe von di- und tripyrrylmethenen*, *Liebigs Ann. Chem.* **718**, pp. 208–223.
21. Loudet, A. and Burgess, K. (2007). BODIPY dyes and their derivatives: Syntheses and spectroscopic properties, *Chem. Rev.* **107**, pp. 4891–4932.
22. Bensted, M., Mehl, G. H., and Boyle, R. W. (2011). 4,4'-difluoro-4-bora-3a,4a-diaza-s-indacenes (BODIPYs) as components of novel light active materials, *Tetrahedron* **67**, pp. 3573–3601.

23. Durán-Sampedro, G., Agarrabeitia, A. R., Arbeloa, T., Bañuelos, J., López-Arbeloa, I., Chiara, J. L., García-Moreno, I., and Ortiz, M. J. (2014). Increased laser action in commercial dyes from fluorination regardless of their skeleton, *Laser Phys. Lett.* **11**, 115818, pp. 1–7.
24. Durán-Sampedro, G., Agarrabeitia, A. R., García-Moreno, I., Costela, A., Bañuelos, J., Arbeloa, T., López-Arbeloa, I., Chiara, J. L., and Ortiz, M. J. (2012). Chlorinated BODIPYS: Surprisingly efficient and highly photostable laser dyes, *Eur. J. Org. Chem.*, pp. 6335–6350.
25. Pérez-Ojeda, M. E., Thivierge, C., Martín, V., Costela, A., Burgess, K., and García-Moreno, I. (2011). Highly efficient and photostable photonic materials from diiodinated BODIPY laser dyes, *Opt. Mat. Express* **1**, 2, pp. 243–251.
26. Pérez-Ojeda, M. E., Trastoy, B., López-Arbeloa, I., Bañuelos, J., Costela, A., García-Moreno, I., and Chiara, J. L. (2011). Click assembly of dye-functionalized octasilsesquioxanes for highly efficient and photostable photonic systems, *Chem. Eur. J.* **17**, pp. 13258–13268.
27. Yang, Y., Zhang, L., Li, B., Zhang, L., and Liu, X. (2013). Triphenylamine-cored tetramethyl-BODIPY dyes: Synthesis, photophysics and lasing properties in organic media, *RSC Adv.* **3**, pp. 14993–14996.
28. Yang, Y., Zhang, L., Gao, C., Xu, L., Bai, S., and Liu, X. (2014). Pyrene-based BODIPY: Synthesis, photophysics and lasing properties under UV-pumping radiation, *RSC Adv.* **4**, pp. 38119–38123.
29. Gutiérrez-Ramos, B. D., Bañuelos, J., Arbeloa, T., López-Arbeloa, I., González-Navarro, P. E., Wrobel, K., Cerdán, L., García-Moreno, I., Costela, A., and Peña-Cabrera, E. (2015). Straightforward synthetic protocol for the introduction of stabilized C nucleophiles in the BODIPY core for advance sensing and photonic applications, *Chem. Eur. J.* **21**, pp. 1755–1764.
30. Thorat, K. G., Kamble, P., Ray, A. K., and Sekar, N. (2015). Novel pyrromethene dyes with N-ethyl carbazole at the meso position: A comprehensive photophysical, lasing, photostability and TD-DFT study, *Phys. Chem. Chem. Phys.* **17**, pp. 17221–17236.
31. Durán-Sampedro, G., Agarrabeitia, A. R., Cerdán, L., Pérez-Ojeda, M. E., Costela, A., García-Moreno, I., Esnal, I., Bañuelos, J., López-Arbeloa, I., and Ortiz, M. J. (2013). Carboxylates versus fluorines: Boosting the emission properties of commercial BODIPYs in liquid and solid media, *Adv. Funct. Mater.* **23**, pp. 4195–4205.
32. Durán-Sampedro, G., Esnal, I., Agarrabeitia, A. R., Bañuelos, J., Cerdán, L., García-Moreno, I., Costela, A., López-Arbeloa, I., and Ortiz, M. J.

- (2014). First highly efficient and photostable E and C derivatives of 4,4-difluoro-4-bora-3a,4a-diaza-s-indacene (BODIPY) as dye lasers in the liquid phase, thin films and solid-state rods, *Chem. Eur. J.* **20**, pp. 2646–2653.
33. Jagtap, K. K., Shivran, N., Mula, S., Naik, D. B., Sarkar, S. K., Mukherjee, T., Maity, D. K., and Ray, A. K. (2013). Change of boron substitution improves the lasing performance of bodipy dyes: A mechanistic rationalisation, *Chem. Eur. J.* **19**, pp. 702–708.
34. García-Moreno, I., Wang, L., Costela, A., Bañuelos, J., López-Arbeloa, I., and Xiao, Y. (2013). Synthesis and optical and redox properties of symmetric and asymmetric BODIPYs, *ChemPhysChem* **13**, pp. 3923–3931.
35. García-Moreno, I., Zhang, D., Costela, A., Martín, V., Sastre, R., and Xiao, Y. (2010). Red-edge laser action from borondipyrromethene dyes, *J. Appl. Phys.* **107**, 073105, pp. 1–7.
36. Ortiz, M. J., García-Moreno, I., Agarrabeitia, A. R., Duran-Sampedro, G., Costela, A., Sastre, R., López-Arbeloa, F., Bañuelos, J., and López-Arbeloa, I. (2010). Red-edge-wavelength finely-tunable laser action from new BODIPY dyes, *Phys. Chem. Chem. Phys.* **12**, pp. 7804–7811.
37. Zhang, D., Martín, V., García-Moreno, I., Costela, A., Pérez-Ojeda, M. E., and Xiao, Y. (2011). Development of excellent long-wavelength BODIPY laser dyes with a strategy that combines extending  $\pi$ -conjugation and tuning ICT effect, *Phys. Chem. Chem. Phys.* **13**, pp. 13026–13033.
38. Holzwarth, A. R., Lehner, H., Braslavsky, S. E., and Schaffner, K. (1978). Phytochrome models, II. The fluorescence of biliverdin dimethyl ester, *Liebigs Ann. Chem.* **12**, pp. 2002–2017.
39. Bañuelos, J., Martín, V., Gómez-Durán, C. F. A., Arroyo-Córdoba, I. J., Peña-Cabrera, E., García-Moreno, I., Costela, A., Pérez-Ojeda, M. E., López-Arbeloa, T., and López-Arbeloa, I. (2011). New 8-amino-BODIPY derivatives: Surpassing laser dyes at blue-edge wavelengths, *Chem. Eur. J.* **17**, pp. 7261–7270.
40. Gómez-Durán, C. F. A., García-Moreno, I., Costela, A., Martín, V., Sastre, R., Bañuelos, J., López-Arbeloa, F., López-Arbeloa, I., and Peña-Cabrera, E. (2010). 8-propargylaminoBODIPY: Unprecedented blue-emitting pyrromethene dye. Synthesis, photophysics and laser properties, *Chem. Comm.* **46**, pp. 5103–5105.
41. Esnal, I., Bañuelos, J., López-Arbeloa, I., Costela, A., García-Moreno, I., Garzón, M., Agarrabeitia, A. R., and Ortiz, M. J. (2013). Nitro and amino

- BODIPYs: Crucial substituents to modulate their photonic behavior, *RSC Adv.* **3**, pp. 1547–1556.
- 42. Esnal, I., Urías-Benavides, A., Gómez-Durán, C. F. A., Osorio-Martínez, C. A., García-Moreno, I., Costela, A., Bañuelos, J., Epelde, N., López-Arbeloa, I., Hu, R., Tang, B. Z., and Peña-Cabrera, E. (2013). Reaction of amines with 8-methylthioBODIPY: Dramatic optical and laser response to amine substitution, *Chem. Asian J.* **8**, pp. 2691–2700.
  - 43. Esnal, I., Valois-Escamilla, I., Gómez-Durán, C. F. A., Urías-Benavides, A., Betancourt-Mendiola, M. L., López-Arbeloa, I., Bañuelos, J., García-Moreno, I., Costela, A., and Peña-Cabrera, E. (2013). Blue-to-orange color-tunable laser emission from tailored boron-dipyrromethene dyes, *ChemPhysChem* **14**, pp. 4134–4142.
  - 44. Pérez-Ojeda, M. E., Martín, V., Costela, A., García-Moreno, I., Arroyo-Córdoba, I. J., and Peña-Cabrera, E. (2012). Unprecedented solid-state laser action from BODIPY dyes under UV-pumping radiation, *Appl. Phys. B* **106**, pp. 911–914.
  - 45. Xiao, Y., Zhang, D., X. Qian, Costela, A., García-Moreno, I., Martín, V., Pérez-Ojeda, M. E., Bañuelos, J., Gartzia, L., and López-Arbeloa, I. (2011). Unprecedented laser action from energy transfer in multichromophoric BODIPY cassettes, *Chem. Commun.* **47**, pp. 11513–11515.
  - 46. Esnal, I., Duran-Sampedro, G., Agarrabeitia, A. R., Bañuelos, J., García-Moreno, I., Macías, M. A., Peña-Cabrera, E., López-Arbeloa, I., de la Moya, S., and Ortiz, M. J. (2015). Coumarin-BODIPY hybrids by heteroatom linkage: Versatile, tunable and photostable dye lasers for UV irradiation, *Phys. Chem. Chem. Phys.* **17**, pp. 8239–8247.
  - 47. Dimitrakopoulos, C. D. and Malenfant, P. R. L. (2002). Organic thin film transistors for large area electronics, *Adv. Mater.* **14**, pp. 99–117.
  - 48. Sadrai, M. and Bird, G. R. (1984). A new laser dye with potential for high stability and a broad band of lasing action: Perylene-3,4,9,10-tetracarboxylic acid-bis-n,n'(2',6' xylidyl)diimide, *Opt. Commun.* **51**, pp. 62–64.
  - 49. Canva, M., Georges, P., Perelgritz, J.-F., Brum, A., Chaput, F., and Boilot, J.-P. (1995). Perylene- and pyrromethene-doped xerogel for a pulsed laser, *Appl. Opt.* **34**, pp. 428–431.
  - 50. Rahn, M. D. and King, T. A. (1995). Comparison of laser performance of dye molecules in sol-gel, polycom, ormosil, and poly(methyl methacrylate) host media, *Appl. Opt.* **34**, pp. 8260–8271.

51. Würthner (2004). Perylene bisimide dyes as versatile building blocks for functional supramolecular architectures, *Chem. Commun.*, pp. 1564–1579.
52. Calzado, E. M., Villalvilla, J. M., Boj, P. G., Quintana, J. A., Gómez, R., Segura, J. L., and Díaz-García, M. A. (2007). Amplified spontaneous emission in polymer films doped with a perylenediimide derivative, *Appl. Opt.* **46**, pp. 3836–3842.
53. Calzado, E. M., Ramírez, M. G., Boj, P. G., and Díaz-García, M. A. (2012). Thickness dependence of amplified spontaneous emission in low-absorbing organic waveguides, *Appl. Opt.* **51**, pp. 3287–3293.
54. Calzado, E. M., Villalvilla, J. M., Boj, P. G., Quintana, J. A., Navarro-Fuster, V., Retolaza, A., Merino, S., and Díaz-García, M. A. (2012). Influence of the excitation area on the thresholds of organic second-order distributed feedback lasers, *Appl. Phys. Lett.* **101**, 223303, pp. 1–5.
55. Navarro-Fuster, V., Calzado, E. M., Boj, P. G., Quintana, J. A., Villalvilla, J. M., Díaz-García, M. A., Trabadelo, V., Juarros, A., Retolaza, A., and Merino, S. (2010). Highly photostable organic distributed feedback laser emitting at 573 nm, *Appl. Phys. Lett.* **97**, 171104, pp. 1–3.
56. Ramírez, M. G., Quintana, J. A., Villalvilla, J. M., Boj, P. G., Retolaza, A., Merino, S., and Díaz-García, M. A. (2013). Perylenediimide-based distributed feedback lasers with holographic relief gratings on dichromated gelatine, *J. Appl. Phys.* **114**, 033107, pp. 1–5.
57. Cerdán, L., Costela, A., Durán-Sampedro, G., García-Moreno, I., Calle, M., y Seva, M. J., de Abajo, J., and Turnbull, G. A. (2012). New perylene-doped polymeric thin films for efficient and long-lasting lasers, *J. Mater. Chem.* **22**, pp. 8938–8947.
58. Ramírez, M. G., Morales-Vidal, M., Navarro-Fuster, V., Quintana, P. G. B. J. A., Villalvilla, J. M., Retolaza, A., Merino, S., and Díaz-García, M. A. (2013). Improved performance of perylenediimide-based lasers, *J. Mater. Chem. C* **1**, pp. 1182–1191.
59. Calzado, E. M., Villalvilla, J. M., Boj, P. G., Quintana, J. A., Gómez, R., Segura, J. L., and Díaz-García, M. A. (2007). Effect of structural modifications in the spectral and laser properties of perylenediimide derivatives, *J. Phys. Chem. C* **111**, pp. 13595–13605.
60. Ramírez, M. G., Pla, S., Boj, P. G., Villalvilla, J. M., Quintana, J. A., Díaz-García, M. A., Ferández-Lázaro, F., and Sastre-Santos, A. (2013). 1,7-bay-substituted perylenediimide derivative with outstanding laser performance, *Adv. Opt. Mater.* **1**, pp. 933–938.

61. Miasojedovas, A., Kazlauskas, K., Armonaitė, G., Sivamurugan, V., Valiyaveettil, S., Grazulevicius, J. V., and Jursenas, S. (2012). Concentration effects on emission of bay-substituted perylene diimide derivatives in a polymer matrix, *Dyes Pigments* **92**, pp. 1285–1291.
62. López Arbeloa, F., Rodrígues Liébana, Y., Cordero Fernández, E., and López Arbeloa, I. (1989). Self-association of the molecular forms of rhodamine 19: Solvent effect, *Spectrochim. Acta Part A* **45**, pp. 1201–1206.
63. Cerdán, L., Martínez-Martínez, V., García-Moreno, I., Costela, A., Pérez-Ojeda, M. E., López-Arbeloa, I., Wu, L., and Burgess, K. (2013). Naturally assembled excimers in xanthenes as singular and highly efficient laser dyes in liquid and solid media, *Adv. Optical Mater.* **1**, pp. 984–990.
64. Gartzia-Rivero, L., Yu, H., Bañuelos, J., López-Arbeloa, I., Costela, A., García-Moreno, I., and Xiao, Y. (2013). Photophysical and laser properties of cassettes based on a BODIPY and rhodamine pair, *Chem. Asian J.* **8**, pp. 3133–3141.
65. Abou Kana, M. T. H., Al-Shamiri, H. A. S., Azzouz, I. M., and Elwahy, A. H. M. (2007). Spectroscopic properties and amplified spontaneous emission of a new derivative of fluorescein, *Appl. Phys. B* **88**, pp. 575–580.
66. Al-Shamiri, H. A. S., Abou Kana, M. T. H., Azzouz, I. M., and Elwahy, A. H. M. (2010). Photo-physical properties and amplified spontaneous emission of a new derivative of fluorescein, *Opt. Commun.* **283**, pp. 1438–1444.
67. Anufrik, S. S., Tarkovsky, V. V., Sazonko, G. G., and Asimov, M. M. (2012). New laser dyes based on 3-imidazopyridylcoumarin derivatives, *J. Appl. Spectrosc.* **79**, pp. 46–52.
68. Lahoz, F., Oton, C. J., López, D., Marrero-Alonso, J., Boto, A., and Díaz, M. (2013). High efficiency amplified spontaneous emission from a fluorescent anticancer drug-dye complex, *Org. Electron.* **14**, pp. 1225–1230.
69. Bañuelos, J., López-Arbeloa, F., Martínez, V., Liras, M., Costela, A., García-Moreno, I., and López-Arbeloa, I. (2011). Difluoro-boron-triaza-anthracene: A laser dye in the blue region. Theoretical simulation of alternative difluoro-boron-diaza-aromatic systems, *Phys. Chem. Chem. Phys.* **13**, pp. 3437–3445.
70. Zhao, X., Li, X., Zhao, Y., Zhang, J., Pan, J., and Zhou, J. (2013). Amplified spontaneous emission from 2,7-bis(4-pyridyl) fluorene-doped DNA-acetyltrimethyl ammonium, *Opt. Eng.* **52**, 106109, pp. 1–6.

71. Yang, Y., Li, B., Zhang, L., and Guan, Y. (2014). Triphenylamine based benzimidazole and benzothiazole: Synthesis and applications in fluorescent chemosensors and laser dyes, *J. Lumin.* **145**, pp. 895–898.
72. Sample, V., Newman, R. H., and Zhang, J. (2009). The structure and function of fluorescent proteins, *Chem. Soc. Rev.* **38**, pp. 2852–2864.
73. Gather, M. C. and Yun, S. H. (2014). Bio-optimized energy transfer in densely packed fluorescent protein enables near-maximal luminescence and solid-state lasers, *Nat. Commun.* **5**, pp. 406–410.
74. Gather, M. C. and Yun, S. H. (2011). Single-cell biological lasers, *Nat. Photonics* **5**, 5722, pp. 1–8.
75. Gather, M. C. and Yun, S. H. (2011). Lasing from *Escherichia coli* bacteria genetically programmed to express green fluorescent protein, *Opt. Lett.* **36**, pp. 3299–3301.
76. Oh, H. J., Gather, M. C., Song, J.-J., and Yun, S. H. (2014). Lasing from fluorescent protein crystals, *Opt. Express* **22**, pp. 31411–31416.
77. Chen, Q., Zhang, X., Sun, Y., Ritt, M., Sivaramakrishnan, S., and Fan, X. (2013). Highly sensitive fluorescent protein FRET detection using optofluidic lasers, *Lab Chip.* **13**, pp. 2679–2681.
78. Vannahme, C., Maier-Flaig, F., Lemmer, U., and Kristensen, A. (2013). Single-mode biological distributed feedback laser, *Lab Chip.* **13**, pp. 2675–2678.
79. Wu, X., Chen, Q., Sun, Y., and Fan, X. (2013). Bio-inspired optofluidic lasers with luciferin, *Appl. Phys. Lett.* **102**, 203706, pp. 1–3.
80. Fichou, D., Delysse, S., and Nunzi, J.-M. (1997). First evidence of stimulated emission from a monolithic organic single crystal:  $\alpha$ -octithiophene, *Adv. Mater.* **5**, pp. 1178–1181.
81. Fang, H. H., Yang, J., Yamao, T., Hotta, S., and Sun, H. B. (2014). Functional organic single crystals for solid-state laser applications, *Laser Photon. Rev.* **8**, pp. 687–715.
82. Fichou, D. (2000). Structural order in conjugated oligothiophenes and its implications on opto-electronic devices, *J. Mater. Chem.* **10**, pp. 571–588.
83. Yanagi, H., Ohara, T., and Morikawa, T. (2001). Self-waveguided gain-narrowing of blue light emission from epitaxially oriented *p*-sexiphenyl crystals, *Adv. Mater.* **13**, pp. 1452–1455.
84. Quochi, F., Cordella, F., Mura, A., Bongiovanni, G., Balzer, F., and Rubahn, H. G. (2006). Gain amplification and lasing properties of individual organic nanofibers, *Appl. Phys. Lett.* **88**, 041106, pp. 1–3.

85. Hibino, R., Nagawa, M., Hotta, S., Ichikawa, M., Koyama, T., and Taniguchi, Y. (2002). Emission gain-narrowing from melt-recrystallized organic semiconductors, *Adv. Mater.* **14**, pp. 119–122.
86. Ichikawa, M., Hibino, R., Inoue, M., Haritani, T., Hotta, S., Araki, K., Koyama, T., and Taniguchi, Y. (2005). Laser oscillation in monolithic molecular single crystals, *Adv. Mater.* **17**, pp. 2073–2077.
87. Fang, H. H., Ding, R., Lu, S.-Y., Yang, J., Zhang, X.-L., Yang, R., Feng, J., Chen, Q.-D., Song, J.-F., and Sun, H.-B. (2012). Distributed feedback lasers based on thiophene/phenylene co-oligomer single crystals, *Adv. Funct. Mater.* **22**, pp. 33–38.
88. Ichikawa, M., Nakamura, K., Inoue, M., Mishima, H., Haritani, T., Hibino, R., Koyama, T., and Taniguchi, Y. (2005). Photopumped laser oscillation and charge-injected luminescence from organic semiconductor single crystals of thiophene/phenylene co-oligomer, *Appl. Phys. Lett.* **87**, 221113, pp. 1–3.
89. Bisri, S. Z., Takenobu, T., Yomogida, Y., Shimotani, H., Yamao, T., Hotta, S., and Iwasa, Y. (2009). High mobility and luminescent efficiency in organic single-crystal light-emitting transistors, *Adv. Mater.* **19**, pp. 1728–1735.
90. Bisri, S. Z., Takenobu, T., and Iwasa, Y. (2014). The pursuit of electrically-driven organic semiconductor lasers, *J. Mater. Chem. C* **2**, pp. 2827–2836.
91. Yamao, T., Taniguchi, Y., Yamamoto, K., Miki, T., Ohira, T., and Hotta, S. (2008). Polarized emission from single crystals of thiophene/phenylene cooligomers measured by microspectroscopy, *Jpn. J. Appl. Phys., Part 1* **47**, p. 4719.
92. Yamashita, K., Nakahata, T., Hayakawa, T., Sakurai, Y., Yamao, T., Yanagi, H., and Hotta, S. (2014). Vertical cavity surface emitting lasing from cyano-substituted thiophene/phenylene co-oligomer single crystals, *Appl. Phys. Lett.* **104**, 253301, pp. 1–4.
93. Fang, H. H., Ding, R., Lu, S.-Y., Yang, Y. D., Chen, Q. D., Feng, J., Huang, Y. Z., and Sun, H. B. (2013). Whispering-gallery mode lasing from patterned molecular single-crystalline microcavity array, *Laser Photon. Rev.* **7**, pp. 281–288.
94. Wang, H., Li, F., Ravia, I., Gao, B., Li, Y., Medvedev, V., Sun, H., Tessler, N., and Ma, Y. (2011). Cyano-substituted oligo(*p*-phenylene vinylene) single crystals: A promising laser material, *Adv. Mater.* **21**, pp. 3770–3777.

95. Yoon, S. M., Lee, J., Je, J. H., Choi, H. C., and Yoon, M. (2011). Optical waveguiding and lasing action in porphyrin rectangular microtube with subwavelength wall thicknesses, *ACS Nano* **5**, pp. 2923–2929.
96. Varghese, S., Yoon, S.-J., Calzado, E. M., Casado, S., Boj, P. G., Díaz-García, M. A., Resel, R., Fischer, R., Milián-Medina, B., Wannemacher, R., Park, S. Y., and Gierschner, J. (2012). Stimulated resonance Raman scattering and laser oscillation in highly emissive distyrylbenzene-based molecular crystals, *Adv. Mater.* **24**, pp. 6473–6478.
97. Xia, H., Yang, J., Fang, H.-H., Chen, Q.-D., Wang, H.-Y., Yu, X.-Q., Ma, Y.-G., Jiang, M.-H., and Sun, H.-B. (2010). Efficient two-photon excited amplified spontaneous emission from organic single crystals, *ChemPhysChem* **11**, pp. 1871–1875.
98. Fang, H. H., Chen, Q.-D., Yang, J., Xia, H., Gao, B.-R., Feng, J., Ma, Y.-G., and Sun, H.-B. (2010). Two-photon pumped amplified spontaneous emission from cyano-substituted oligo(*p*-phenylenevinylene) crystals with aggregation-induced emisssion enhancement, *J. Phys. Chem. C* **114**, pp. 11958–11961.
99. Kéna-Cohen, S. and Forrest, S. R. (2010). Room-temperature polariton lasing in an organic single-crystal microcavity, *Nat. Photonics* **4**, pp. 371–375.
100. Chen, J., Ma, S., Zhang, J., Li, B., Xu, B., and Tian, W. (2015). Low-loss optical waveguide and highly polarized emission in a uniaxially oriented molecular crystal based on 9,10-distyrylanthracene derivatives, *ACS Photonics* **2**, pp. 313–318.
101. Wang, Y., Liu, T., Bu, L., Li, J., Yang, C., Li, X., Tao, Y., and Yang, W. (2012). Aqueous nanoaggregation-enhanced one- and two-photon fluorescence, crystalline J-aggregation-induced red shift, and amplified spontaneous emission of 9,10-bis(*p*-dimethylaminostyryl)anthracene, *J. Phys. Chem. C* **116**, pp. 15576–15583.
102. Qu, S., Li, Y., Wang, L., Lu, Q., and Liu, X. (2011). Waveguide and ultralow-threshold amplified spontaneous emission in an aligned ordered solid state based on a highly fluorescent twin-tapered bi-1,3,4-oxadiazole derivative, *Chem. Commun.* **47**, pp. 4207–4209.
103. Qu, S., Lu, Q., Wu, S., Wang, L., and Liu, X. (2012). Two dimensional directed  $\pi$ - $\pi$  interactions in a linear shaped bi-1,3,4-oxadiazole derivative to achieve organic single crystal with highly polarized fluorescence and amplified spontaneous emissions, *J. Mater. Chem.* **22**, pp. 24605–24609.

104. Camposeo, A., Polo, M., Del Carro, P., Silvestri, L., Tavazzi, S., and Pisignano, D. (2015). Random lasing in an organic light-emitting crystal and its interplay with vertical cavity feedback, *Laser Photonics Rev.* **8**, pp. 785–791.
105. Park, S., Kwon, O.-H., Kim, S., Park, S., Choi, M.-G., Cha, M., Park, S. Y., and Jang, D.-J. (2005). Imidazole-based excited-state intermolecular proton-transfer materials: Synthesis and amplified spontaneous emission from a large single crystal, *J. Am. Chem. Soc.* **127**, pp. 10070–10074.
106. Zhang, W., Yan, Y., Gu, J., Yao, J., and Zhao, Y. S. (2015). Low-threshold wavelength-switchable organic nanowire lasers based on excited-state intramolecular proton transfer, *Angew. Chem. Int. Ed.* **54**, pp. 7125–7129.
107. Cheng, X., Wang, K., Huang, S., Zhang, H., Zhang, H., and Wang, Y. (2015). Organic crystals with near-infrared amplified spontaneous emissions based on 2'-hydroxychalcone derivatives: Subtle structure modification but great property change, *Angew. Chem. Int. Ed.* **54**, pp. 8369–8373.
108. Schneider, D., Rabe, T., Riedl, T., Dobbertin, T., Werner, O., Kröger, M., Becker, E., Johannes, H.-H., Kowalsky, W., Weimann, T., Wang, J., Hinze, P., Gerhard, A., Stössel, P., and Vestweber, H. (2004). Deep-blue widely tunable organic solid-state laser based on a spirobifluorene derivative, *Appl. Phys. Lett.* **84**, pp. 4693–4695.
109. Johansson, N., Salbeck, J., Bauer, J., Weissörtel, F., Bröms, P., Andersson, A., and Salaneck, W. R. (1998). Solid-state amplified spontaneous emission in some spiro-type molecules: A new concept for the design of solid-state lasing materials, *Adv. Mater.* **10**, pp. 1136–1141.
110. Komino, T., Nomura, H., Yahiro, M., Endo, K., and Adachi, C. (2011). Dependence of the amplified spontaneous emission threshold in spirofluorene thin films on molecular orientation, *J. Phys. Chem. C* **115**, pp. 19890–19896.
111. Fuhrmann-Lieker, T., Lambrecht, J., Hoinka, N., Kiurski, M., Wiske, A., Hagelstein, G., Yurttagül, N., Abdel-Awwad, M., Wilke, H., Messow, F., Hillmer, H., and Salbeck, J. (2015). Optical amplification and stability of spiroquaterphenyl compounds and blends, *J. Eur. Opt. Soc.-Rapid* **10**, 15007, pp. 1–7.
112. Zavelani-Rossi, M., Lanzani, G., De Silvestri, S., Anni, M., Gigli, G., Cingolani, R., Barbarella, G., and Favaretto, L. (2001). Single-mode

- tunable organic laser based on an electroluminescent oligothiophene, *Appl. Phys. Lett.* **79**, pp. 4082–4084.
- 113. Lattante, S., Anni, M., Salerno, M., Lagonigro, L., Cingolani, R., Gigli, G., Pasini, M., Destri, S., and Porzio, W. (2006). Optical gain in fluorenyl-thiophene co-oligomer thin films, *Opt. Mater.* **28**, pp. 1072–1075.
  - 114. Lawrence, J. R., Turnbull, G. A., Samuel, I. D. W., Richards, G. J., and Burn, P. L. (2004). Optical amplification in a first-generation dendritic organic semiconductor, *Opt. Lett.* **29**, pp. 869–871.
  - 115. Lawrence, J. R., Namdas, E. B., Richards, G. J., Burn, P. L., and Samuel, I. D. W. (2007). Effect of generation and soft lithography on semiconducting dendrimer lasers, *Adv. Mater.* **19**, pp. 3000–3003.
  - 116. Tsiminis, G., Ribierre, J.-C., Ruseckas, A., Barcena, H. S., Richards, G. J., Turnbull, G. A., Burn, P. L., and Samuel, I. D. W. (2008). Two-photon absorption and lasing in first-generation bisfluorene dendrimers, *Adv. Mater.* **20**, pp. 1940–1944.
  - 117. Choi, E. Y., Mazur, L., Mager, L., Gwon, M., Pitrat, D., Mulatier, J. C., Monnereau, C., Fort, A., Attias, A. J., Dorkenoo, K., Kwon, J. E., Xiao, Y., Matczyszyn, K., Samoc, M., Kim, D.-W., Nakao, A., Heinrich, B., Hashizume, D., Uchiyama, M., Park, S. Y., Mathevet, F., Aoyama, T., Andraud, C., Wu, J. W., Barsella, A., and Ribierre, J. C. (2014). Photophysical, amplified spontaneous emission and charge transport properties of oligofluorene derivatives in thin films, *Phys. Chem. Chem. Phys.* **16**, pp. 16941–16956.
  - 118. Kazlauskas, K., Kreiza, G., Radiunas, E., Adomėnas, P., Adomėnienė, O., Karpavičius, K., Bucevičius, J., Jankauskas, V., and Juršėnas, S. (2015). Concentration effects on spontaneous and amplified emission in benzo[c]fluorenes, *Phys. Chem. Chem. Phys.* **17**, pp. 12935–12948.
  - 119. Baronas, P., Kazlauskas, K., Kreiza, G., Jankauskas, V., Tomkeviciene, A., Simokaitiene, J., Grigalevicius, S., Grazulevicius, J. V., and Jursenas, S. (2015). Differently linked fluorene-carbazole triads for light amplification, *Dyes Pigments* **123**, pp. 370–379.
  - 120. Qian, Y., Wei, Q., Pozo, G. D., Mróz, M. M., Lüer, L., Casado, S., Cabanillas-Gonzalez, J., Zhang, Q., Xie, L., Xia, R., and Huang, W. (2014). H-shaped oligofluorenes for highly air-stable and low-threshold non-doped deep-blue lasing, *Adv. Mater.* **26**, pp. 2937–2942.
  - 121. Niu, Q., Zhang, Q., Xu, W., Jiang, Y., Xia, R., Bradley, D. D. C., Li, D., and Wen, X. (2015). Solution-processed anthracene-based molecular glasses as stable blue-light-emission laser gain media, *Org. Electron.* **18**, pp. 95–100.

122. Huang, J., Liu, Q., Zou, J.-H., Zhu, X.-H., Li, A.-Y., Li, J.-W., Wu, S., Peng, J., Cao, Y., Xia, R., Bradley, D. D. C., and Roncali, J. (2009). Electroluminescence and laser emission of soluble pure red fluorescent molecular glasses based on dithienylbenzothiadiazole, *Adv. Funct. Mater.* **18**, pp. 2978–2986.
123. Krotkus, S., Kazlauskas, K., Miasojedovas, A., Groudis, A., tomkeviciene, A., Grazulevicius, J. V., and Jursenas, S. (2012). Pyrenyl-functionalized fluorene and carbazole derivatives as blue light emitters, *J. Phys. Chem. C* **116**, pp. 7561–7572.
124. Casado, J., Hernández, V., López Navarrete, J. T., Algarra, M., Filho, D. A. S., Yamaguchi, S., Ao, R. R., de Melo, J. S. S., Navarro-Fuster, V., Boj, P. G., and Díaz-García, M. A. (2013). Amplified spontaneous emission in pentathienoacene dioxides by direct optical pump and by energy transfer: Correlation with photophysical parameters, *Adv. Optical Mater.* **1**, pp. 588–599.
125. Ma, L., Wu, Z., Lei, T., Yu, Y., Yuan, F., Ning, S., Jiao, B., and Hou, X. (2014). Theoretical insight into the deep-blue amplified spontaneous emission of new organic semiconductor molecules, *Org. Electron.* **15**, pp. 3144–3153.
126. Yoshioka, H., Itoh, Y., Kiyomori, A., Era, M., and Oki, Y. (2013). Fluorene-based chromophore for degradation-recoverable solid-state dye laser, *Opt. Mater. Express* **3**, pp. 176–183.
127. Kazlauskas, K., Kreiza, G., Bobrovas, O., Adoménienė, O., Adomėnės, P., Jankauskas, V., and Juršėnas, S. (2015). Fluorene- and benzofluorene-cored oligomers as low threshold and high gain amplifying media, *Appl. Phys. Lett.* **107**, 043301, pp. 1–5.
128. Goubard, F. and Dumur, F. (2015). Truxene: A promising scaffold for future materials, *RSC Adv.* **5**, pp. 3521–3551.
129. Levermore, P. A., Xia, R., Lai, W., Wang, X. H., and Bradley, D. D. C. (2007). Deep-blue light-emitting triazatruxene core/oligo-fluorene branch dendrimers for electroluminescence and optical gain applications, *J. Phys. D Appl. Phys.* **40**, pp. 1896–1901.
130. Lai, W.-Y., Xia, R., He, Q.-Y., Levermore, P. A., Huang, W., and Bradley, D. D. C. (2009). Enhanced solid-state luminescence and low-threshold lasing from starburst macromolecular materials, *Adv. Mater.* **21**, pp. 355–360.
131. Tsiminis, G., Wang, Y., Shaw, P. E., Kanibolotsky, A. L., Perepichka, I. F., Dawson, M. D., Skabara, P. J., Turnbull, G. A., and Samuel, I. D. W. (2009).

- Low-threshold organic laser based on an oligofluorene truxene with low optical losses, *Appl. Phys. Lett.* **94**, 243304, pp. 1–3.
- 132. Wang, Y., Tsiminis, G., Yang, Y., Ruseckas, A., Kanibolotsky, A. L., Perepichka, I. F., Skabara, P. J., Turnbull, G. A., and Samuel, I. D. W. (2010). Broadly tunable deep-blue laser based on a star-shaped oligofluorene truxene, *Synthetic Met.* **160**, pp. 1397–1400.
  - 133. Herrnsdorf, J., Guilhabert, B., Chen, Y., Kanibolotsky, A. L., Mackintosh, A. R., Petrick, R. A., Skabara, P. J., Gu, E., Laurand, N., and Dawson, M. D. (2010). Flexible blue-emitting encapsulated organic semiconductor DFB laser, *Opt. Express* **18**, pp. 25535–25545.
  - 134. Ma, L., Wu, Z., Zhou, G., Yuan, F., Yu, Y., Yao, C., Ning, S., Hou, X., Li, Y., Wang, S., and Gong, Q. (2015). The molecular picture of amplified spontaneous emission of star-shaped functionalized-truxene derivatives, *J. Mater. Chem. C* **3**, pp. 7004–7013.
  - 135. Xu, W., Yi, J., Lai, W.-Y., Zhao, L., Zhang, Q., Hu, W., Zhang, X.-W., Jiang, Y., Liu, L., and Huang, W. (2015). Pyrene-capped conjugated amorphous starbursts: Synthesis, characterization, and stable lasing properties in ambient atmosphere, *Adv. Funct. Mater.* **25**, pp. 4617–4625.
  - 136. Xia, R., Lai, W.-Y., Levermore, P. A., Huang, W., and Bradley, D. D. C. (2009). Low-threshold distributed-feedback lasers based on pyrene-cored starburst molecules with 1,3,6,8-attached oligo(9,9-dialkylfluorene) arms, *Adv. Funct. Mater.* **19**, pp. 2844–2850.
  - 137. Zhang, Q., Zhang, Y., Xu, W., Li, X., Liu, J., Guo, X., Xia, R., and Huang, W. (2015). Efficient amplified spontaneous emission from oligofluorene-pyrene starburst with improved electron affinity property, *Opt. Express* **23**, pp. A465–A470.
  - 138. Tsiminis, G., Montgomery, N. A., Kanibolotsky, A. L., Ruseckas, A., Perepichka, I. F., Skabara, P. J., Turnbull, G. A., and Samuel, I. D. W. (2012). Laser characteristics of a family of benzene-cored star-shaped oligofluorenes, *Semicond. Sci. Technol.* **27**, 094005, pp. 1–6.
  - 139. Montgomery, N. A., Denis, J.-C., Schumacher, S., Ruseckas, A., Skabara, P. J., Kanibolotsky, A., Paterson, M. J., Galbraith, I., Turnbull, G. A., and Samuel, I. D. W. (2011). Optical excitations in star-shaped fluorene molecules, *J. Phys. Chem. A* **115**, pp. 2913–2919.
  - 140. Sun, Y. M., Xiao, K., Liu, Y. Q., Wang, J. L., Pei, J., Yu, G., and Zhu, B. D. (2005). Oligothiphene-functionalized truxene: Star-shaped compounds for organic field-effect transistors, *Adv. Funct. Mater.* **5**, pp. 818–822.

141. Hide, F., Schwartz, B. J., Díaz-García, M. A., and Heeger, A. J. (1996). Laser emission from solutions and films containing semiconducting polymer and titanium dioxide nanocrystals, *Chem. Phys. Lett.* **256**, pp. 424–430.
142. Chénais, S. and Forget, S. (2012). Recent advances in solid-state organic lasers, *Polym. Int.* **61**, pp. 390–406.
143. Samuel, I. D. W. and Turnbull, G. A. (2007). Organic semiconductor lasers, *Chem. Rev.* **107**, pp. 1272–1295.
144. Kranelbinder, G. and Leising, G. (1999). Organic solid-state lasers, *Rep. Prog. Phys.* **63**, pp. 729–762.
145. McGehee, M. D. and Heeger, A. J. (2000). Semiconducting (conjugated) polymers as materials for solid-state lasers, *Adv. Mater.* **12**, pp. 1655–1668.
146. Tessler, N. (1999). Lasers based on semiconducting organic materials, *Adv. Mater.* **11**, pp. 363–370.
147. Rose, A., Zhu, Z., Madigan, C. F., Swager, T. M., and Bulović, V. (2005). Sensitivity gains in chemosensing by lasing action in organic polymers, *Nature* **434**, pp. 876–879.
148. Tsiminis, G., Wang, Y., Kanibolotsky, A. L., Inigo, A. R., Skabara, P. J., Samuel, I. D. W., and Turnbull, G. A. (2013). Nanoimprinted organic semiconductor laser pumped by a light-emitting diode, *Adv. Mater.* **25**, pp. 2826–2830.
149. Wang, Y., Tsiminis, G., Kanibolotsky, A. L., Samuel, I. D. W., Skabara, P. J. S., and Turnbull, G. A. (2013). Nanoimprinted polymer lasers with threshold below 100 W/cm<sup>2</sup> using mixed-order distributed feedback resonators, *Opt. Express* **21**, pp. 14362–14367.
150. Foucher, C., Guilhabert, B., Herrnsdorf, J., Laurand, N., and Dawson, M. D. (2014). Diode-pumped, mechanically-flexible polymer DFB laser encapsulated by glass membranes, *Opt. Express* **22**, pp. 24160–24168.
151. Heliotis, G., Bradley, D. D. C., Turnbull, G. A., and Samuel, I. D. W. (2002). Light amplification and gain in polyfluorene waveguides, *Appl. Phys. Lett.* **81**, 3, pp. 415–417.
152. Heliotis, G., Xia, R., Bradley, D. D. C., Turnbull, G. A., Samuel, I. D. W., Andrew, P., and Barnes, W. L. (2003). Blue, surface-emitting, distributed feedback polyfluorene lasers, *Appl. Phys. Lett.* **83**, pp. 2118–2120.
153. Heliotis, G., Xia, R., Turnbull, G. A., Andrew, P., Barnes, W. L., Samuel, I. D. W., and Bradley, D. D. C. (2004). Emission characteristics and

- performance comparison of polyfluorene lasers with one- and two-dimensional distributed feedback, *Adv. Funct. Mater.* **14**, pp. 91–97.
- 154. Yap, B. K., Xia, R., Campoy-Quiles, M., Stavrinou, P. N., and Bradley, D. C. (2008). Simultaneous optimization of charge-carrier mobility and optical gain in semiconducting polymer films, *Nat. Mater.* **7**, pp. 376–380.
  - 155. Scherf, U. and List, E. J. W. (2002). Semiconducting polyfluorenes: Towards reliable structure-property relationships, *Adv. Mater.* **14**, pp. 477–487.
  - 156. Cadby, A. J., Lane, P. A., Mellor, H., Martin, S. J., Grell, M., Giebelser, C., Bradley, D. D. C., Wohlgemant, M., An, C., and Vardeny, Z. V. (2000). Film morphology and photophysics of polyfluorene, *Phys. Rev. B* **62**, pp. 15604–15609.
  - 157. Redecker, M., Bradley, D. D. C., Inbasekaran, M., and Woo, E. P. (1999). Mobility enhancement through homogeneous nematic alignment of a liquid-crystalline polyfluorene, *Appl. Phys. Lett.* **74**, pp. 1400–1402.
  - 158. Anni, M. (2008). The role of the  $\beta$ -phase content on the stimulated emission of poly(9,9-diptylfluorene) thin films, *Appl. Phys. Lett.* **93**, 023308, pp. 1–3.
  - 159. Anni, M. (2012). Operational lifetime improvement of poly(9,9-diptylfluorene) active waveguides by thermal lamination, *Appl. Phys. Lett.* **101**, 013303, pp. 1–3.
  - 160. Tsiminis, G., Ruseckas, A., Samuel, I. D. W., and Turnbull, G. A. (2009). A two-photon pumped polyfluorene laser, *Appl. Phys. Lett.* **94**, 253304, pp. 1–3.
  - 161. Yang, Y., Turnbull, G. A., and Samuel, I. D. W. (2010). Sensitive explosive vapor detection with polyfluorene lasers, *Adv. Funct. Mater.* **20**, pp. 2093–2097.
  - 162. Laquai, F., Mishra, A. K., Müllen, K., and Friend, R. H. (2008). Amplified spontaneous emission of poly(ladder-type phenylene)s: The influence of photophysical properties on ASE thresholds, *Adv. Funct. Mater.* **18**, pp. 3265–3275.
  - 163. Li, X., Li, M., Gao, N., Li, F., Zhang, M., and Baumgarten, M. (2013). A new blue-emitting conjugated polycarbazoles: Low threshold of amplified spontaneous emission and charge-transporting properties, *Synthetic Metals* **176**, pp. 51–54.
  - 164. Zaumseil, J. and Sirringhaus, H. (2007). Electron and ambipolar transport in organic field-effect transistors, *Chem. Rev.* **107**, pp. 1296–1323.

165. Xia, R., Stavrinou, P. N., Bradley, D. D. C., and Kim, Y. (2012). Efficient optical gain media comprising binary blends of poly(3-hexylthiophene) and poly(9,9-dioctylfluorene-co-benzothiadiazole), *J. Appl. Phys.* **111**, 123107, pp. 1–8.
166. Anni, M. and Lattante, S. (2015). Amplified spontaneous emission optimization in regioregular poly(3-hexylthiophene) (rrP3HT):poly(9,9-dioctylfluorene-*co*-benzothiadiazole) (F8BT) thin films through control of the morphology, *J. Phys. Chem. C* doi:10.1021/acs.jpcc.5b05008.
167. Xia, R., Heliotis, G., Hou, Y., and Bradley, D. D. C. (2003). Fluorene-based conjugated polymer optical gain media, *Org. Electron.* **4**, pp. 165–177.
168. Rabe, T., Hoping, M., Schneider, D., Becker, E., Johannes, H.-H., Kowalsky, W., Weimann, T., Wang, J., Hinze, P., Nehls, B. S., Scherf, U., Farrel, T., and Riedl, T. (2005). Threshold reduction in polymer lasers based on poly(9,9-dioctylfluorene) with statistical binaphthyl units, *Adv. Funct. Mater.* **15**, pp. 1188–1192.
169. Li, J. Y., Laquai, F., and Wegner, G. (2009). Amplified spontaneous emission in optically pumped neat films of a polyfluorene derivative, *Chem. Phys. Lett.* **478**, pp. 37–41.
170. Wallikewitz, B. H., Hertel, D., and Meerholz, K. (2009). Cross-linkable polyspirobiifluorene: A material class featuring good OLED performance and low amplified spontaneous emission thresholds, *Chem. Mater.* **21**, pp. 2912–2919.
171. Kuehne, A. J. C., Kaiser, M., Mackintosh, A. R., Wallikewitz, B. H., Hertel, D., Pethrick, R. A., and Meerholz, K. (2011). Sub-micrometer patterning of amorphous- and  $\beta$ -phase in a crosslinkable poly(9,9-dioctylfluorene): Dual-wavelength lasing from a mixed-morphology device, *Adv. Funct. Mater.* **21**, pp. 2564–2570.
172. Chowdury, M. A. H., Monkman, A. P., and Chawdhury, N. (2011). Spectral investigation and laser action in solid films of fluorene-dibenzothiophene-s,s-dioxide co-polymers, *J. Polym. Res.* **18**, pp. 1379–1384.
173. Lin, J. Y., Zhu, W. S., Liu, F., Xie, L. H., Zhang, L., Xia, R., Xing, G. C., and Huang, W. (2014). A rational molecular design of  $\beta$ -phase poly diarylfuorenes: Synthesis, morphology and organic lasers, *Macromolecules* **47**, pp. 1001–1007.
174. Heliotis, G., Xia, R., Bradley, D. D. C., Turnbull, G. A., Samuel, I. D. W., Andrew, P., and Barnes, W. L. (2004). Two-dimensional distributed feedback lasers using broadband, red polyfluorene gain medium, *J. Appl. Phys.* **96**, pp. 6959–6965.

175. Xia, R., Heliotis, G., Stavrinou, P. N., and Bradley, D. D. C. (2005). Polyfluorene distributed feedback lasers operating in the green-yellow spectral region, *Appl. Phys. Lett.* **87**, 031104, pp. 1–3.
176. Amarasinghe, D., Ruseckas, A., Vasdekis, A. E., Turnbull, G. A., and Samuel, I. D. W. (2008). High-gain broadband solid-state optical amplifier using a semiconducting copolymer, *Adv. Mater.* **21**, pp. 107–110.
177. Amarasinghe, D., Ruseckas, A., Vasdekis, A. E., Turnbull, G. A., and Samuel, I. D. W. (2007). Amplification of optical pulse sequences at a high repetition rate in a polymer slab waveguide, *Appl. Phys. Lett.* **91**, 011105, pp. 1–3.
178. Wenger, B., Tétreault, N., Welland, M. E., and Friend, R. H. (2010). Mechanically tunable conjugated polymer distributed feedback lasers, *Appl. Phys. Lett.* **97**, 193303, pp. 1–3.
179. Perissinotto, S., Garbugli, M., Fazzi, D., Bartarelli, C., Carvelli, M., Kandada, A. R. S., Yue, Z., Wong, K. S., and Lanzani, G. (2011). Optical modulation of amplified emission in a polyfluorene-diarylethene blend, *ChemPhysChem* **12**, pp. 3619–3623.
180. Yang, Y., Turnbull, G. A., and Samuel, I. D. W. (2008). Hybrid optoelectronics: A polymer laser pumped by a nitride light-emitting diode, *Appl. Phys. Lett.* **92**, 163306, pp. 1–3.
181. Zhang, Y. and Blom, P. W. M. (2011). Electron and hole transport in poly(fluorene-benzothiadiazole), *Appl. Phys. Lett.* **98**, 143504, pp. 1–3.
182. Kim, H., Schulte, N., Zhou, G., Müllen, K., and Laquai, F. (2011). A high gain and high charge carrier mobility indenofluorene-phenanthracene copolymer for light amplification and organic lasing, *Adv. Mater.* **23**, pp. 894–897.
183. Frampton, M. J. and Anderson, H. L. (2007). Insulated molecular wires, *Angew. Chem. Int. Ed.* **46**, pp. 1028–1064.
184. Mróz, M. M., Perissinoto, S., Virgili, T., Gigli, G., Salerno, M., Frampton, M. J., Sforazzini, G., Anderson, H. L., and Lanzani, G. (2009). Laser action from a sugar-threaded polyrotaxane, *Appl. Phys. Lett.* **95**, 031108, pp. 1–3.
185. Mróz, M. M., Sforazzini, G., Zhong, Y., Wong, K. S., Anderson, H. L., Lanzani, G., and Cabanillas-Gonzalez, J. (2013). Amplified spontaneous emission in conjugated polyrotaxanes under quasi-cw pumping, *Adv. Mater.* **25**, pp. 4347–4351.

186. Koechner, W. (2006). *Solid-State Laser Engineering* (Springer Science+ Business Media, Inc., New York, USA).
187. Tsan, K. C., Wong, C.-Y., and Pun, E. Y. B. (2010). High-gain optical amplification in Eu<sup>3+</sup>-doped polymer, *Opt. Lett.* **35**, pp. 520–522.
188. Huang, L., Tsang, K. C., Pun, E. Y. B., and Xu, S. (2010). Sm<sup>3+</sup>-doped polymer optical waveguide amplifiers, *Opt. Commun.* **283**, pp. 1363–1365.
189. Le Quang, A. Q., Hierle, R., Zyss, J., Ledoux, I., Cusmai, G., Costa, R., Barberis, A., and Pietralunga, S. M. (2006). Demonstration of net gain at 1550 nm in an erbium-doped polymer single mode rib waveguide, *Appl. Phys. Lett.* **89**, 141124, pp. 1–3.
190. Dekker, R., Klunder, D. J. W., Borreman, A., Diemeer, M. B. J., Wörhoff, K., Driessens, A., Stouwdam, J. W., and van Veggel, F. C. J. M. (2004). Stimulated emission and optical gain in LaF<sub>3</sub>:Nd nanoparticle-doped polymer-based waveguides, *Appl. Phys. Lett.* **85**, pp. 6104–6106.
191. Yang, J., Diemeer, M. B. J., Geskus, D., Sengo, G., Pollnau, M., and Driessens, A. (2009). Neodymium-complex-doped photodefined polymer channel waveguide amplifiers, *Opt. Lett.* **34**, pp. 473–475.
192. Grivas, C., Yang, J., Diemeer, M. B. J., Driessens, A., and Pollnau, M. (2010). Continuous-wave Nd-doped polymer lasers, *Opt. Lett.* **35**, pp. 1983–1985.
193. Yang, J., Diemeer, M. B. J., Grivas, C., Sengo, G., Driessens, A., and Pollnau, M. (2010). Steady-state lasing in a solid polymer, *Laser Phys. Lett.* **9**, pp. 650–656.
194. Bornemann, R., Lemmer, U., and Thiel, E. (2006). Continuous-wave solid-state dye laser, *Opt. Lett.* **31**, pp. 1669–1671.
195. Chen, Q., De Marco, N., Yang, Y., Song, T.-B., Chen, C.-C., Zhao, H., Hong, Z., Zhou, H., and Yang, Y. (2015). Under the spotlight: The organic-inorganic hybrid halide perovskite for optoelectronic applications, *Nano Today* **10**, pp. 355–396.
196. Xing, G., Mathews, N., Lim, S. S., Yantara, N., Liu, X., Sabba, D., Grätzel, M., Mhaisalkar, S., and Sum, T. C. (2014). Low-temperature solution-processed wavelength-tunable perovskites for lasing, *Nature Mater.* **13**, pp. 476–480.
197. Deschler, F., Price, M., Pathak, S., Klintberg, L. E., Jarausch, D.-D., Higler, R., Hüttner, S., Leijtens, T., Stranks, S. D., Snaith, H. J., Atatüre, M., Phillips, R. T., and Friend, R. H. (2014). High photoluminescence efficiency and optical pumped lasing in solution-processed mixed

- halide perovskite semiconductors, *J. Phys. Chem. Lett.* **85**, pp. 1421–1426.
198. Sutherland, B. R., Hoogland, S., Adn C. T. O., Wong, M. M. A., and Sargent, E. H. (2014). Conformal organohalide perovskites enable lasing on spherical resonators, *ACS Nano* **8**, pp. 10947–10952.
199. Zhu, H., Fu, Y., Meng, F., Wu, X., Gong, Z., Ding, Q., Gustafsson, M., Tuan Trinh, M., and Zhu, X.-Y. (2015). Lead halide perovskite nanowire lasers with low lasing thresholds and high quality factors, *Nature Mater.* **14**, pp. 636–643.
200. Stranks, S. D., Wood, S. M., Wojciechowski, K., Deschler, F., Saliba, M., Khandelwal, H., Patel, J. B., Elston, S. J., Herz, L. M., Johnston, M. B., Schenning, A. P. H. J., Debjie, M. G., Riede, M. K., Morris, S. M., and Snaith, H. J. (2015). Enhanced amplified spontaneous emission in perovskites using a flexible cholesteric liquid crystal reflector, *Nano Lett.* **15**, pp. 4935–4941.
201. Motta, C., El-Mellouhi, F., and Sanvito, S. (2015). Charge carrier mobility in hybrid halide perovskites, *Sci. Rep.* **5**, pp. 1–8.
202. Wehrenfennig, C., Eperon, G. E., Johnston, M., Snaith, H. J., and Herz, L. M. (2013). High charge carrier mobilities and lifetimes in organolead trihalide perovskites, *Adv. Mater.* **26**, pp. 1584–1589.
203. King, R. B. (2001). Three-dimensional aromaticity in polyhedral boranes and related molecules, *Chem. Rev.* **101**, pp. 1119–1152.
204. Dash, B. P., Satapathy, R., Maguire, J. A., and Hosmane, N. S. (2011). Polyhedral boron clusters in materials science, *New J. Chem.* **35**, pp. 1955–1972.
205. Cerdán, L., Braborec, J., García-Moreno, I., Costela, A., and Londesborough, M. G. S. (2015). A borane laser, *Nat. Commun.* **6**, 5958, pp. 1–7.
206. Londesborough, M. G. S., Hnyk, D., Bould, J., Serrano-Andrés, L., Sauri, V., Oliva, J. M., Kubát, P., Polívka, T., and Lang, K. (2012). Distinct photophysics of the isomers of  $B_{18}H_{22}$  explained, *Inorg. Chem.* **51**, pp. 1471–1479.
207. Bradley, D. D. C. (2014). Organic electronics and photonics: Concluding remarks, *Faraday Discuss.* **174**, pp. 429–438.
208. Wang, Y., Yang, Y., Turnbull, G. A., and Samuel, I. D. W. (2012). Explosive sensing using polymer lasers, *Mol. Cryst. Liq. Cryst.* **554**, pp. 103–110.
209. Rochat, S. and Swager, T. M. (2013). Conjugated amplifying polymers for optical sensing applications, *ACS Appl. Mater. Interfaces* **434**, pp. 4488–4502.

210. Vannahme, C., Klinkhammer, S., Christiansen, M. B., Kolew, A., Kristensen, A., Lemmer, U., and Mappes, T. (2010). All-polymer organic semiconductor laser chips: Parallel fabrication and encapsulation, *Opt. Express* **18**, pp. 24881–24887.
211. Richardson, S., Gaudin, O. P. M., Turnbull, G. A., and Samuel, I. D. W. (2007). Improved operational lifetime of semiconducting polymer lasers by encapsulation, *Appl. Phys. Lett.* **91**, 261104, pp. 1–3.
212. Cuerda, J., Ruting, F., García-Vidal, J. F., and Bravo-Abad, J. (2015). Theory of lasing action in plasmonic crystals, *Phys. Rev. B Rapid Comm.* **91**, 041118(R).
213. Ruting, F., Cuerda, J., Bravo-Abad, J., and García-Vidal, F. J. (2014). Lasing action assisted by long-range surface plasmons, *Laser Photon. Rev.* **8**, pp. L65–L70.



Taylor & Francis  
Taylor & Francis Group  
<http://taylorandfrancis.com>

## Chapter 4

# Basic Physics and Recent Developments of Organic Random Lasers

Ilenia Viola,<sup>a</sup> Luca Leuzzi,<sup>a</sup> Claudio Conti,<sup>b</sup>  
and Neda Ghoфraniha<sup>b</sup>

<sup>a</sup>*Istituto di Nanotecnologia (CNR-NANOTEC), Dipartimento di Fisica-Università La Sapienza, Piazzale A. Moro 2, 00185 Roma, Italy*

<sup>b</sup>*Istituto dei Sistemi Complessi (CNR-ISC), Dipartimento di Fisica-Università La Sapienza, Piazzale A. Moro 2, 00185 Roma, Italy*  
[ilenia.viola@nanotec.cnr.it](mailto:ilenia.viola@nanotec.cnr.it), [neda.ghofraniha@cnr.it](mailto:neda.ghofraniha@cnr.it)

### 4.1 Introduction

In this chapter, we discuss “random laser” devices based on organic materials. After a brief introduction about the history and physics of random lasers (Section 4.2), we describe the use of semiconductor materials for optoelectronics and photonics devices in terms of physical-chemical properties, characteristics, and advantages (Section 4.3). In Section 4.4, self-organization and lithographic processes are described for the realization of nanoscale organic random lasers. A selection of recent results are reported in Sections 4.5 and 4.6.

---

*Organic Lasers: Fundamentals, Developments, and Applications*

Edited by Marco Anni and Sandro Lattante

Copyright © 2018 Pan Stanford Publishing Pte. Ltd.

ISBN 978-981-4774-46-8 (Hardcover), 978-1-315-10233-7 (eBook)

[www.panstanford.com](http://www.panstanford.com)

## 4.2 Random Laser

A laser is made of three basic elements: a pump source, a material that provides optical gain, and an optical cavity, e.g., two mirrors in the most simple configuration, which trap the light. Light from a pump source induces spontaneous emission of radiation within the gain medium, and these spontaneously emitted photons will then stimulate other radiative transitions in the gain medium to take place, unleashing yet more photons. Such process has been considered analogous to the chain reaction in the fission of neutrons in a nuclear reactor and has been referred to by R. H. Dicke as an “optical bomb.” When the total gain in the cavity is larger than the losses, the system reaches a threshold and lases. The directionality and the frequency of the output, namely traversal and longitudinal modes, are determined by the geometry of the cavity. In random lasers, the feedback mechanism is, instead, provided by multiple scattering, a well-known phenomenon that occurs in materials that appear opaque, such as white paint, human tissue, and clouds. Light rays that penetrate these materials are scattered often thousands of times in a random fashion before they exit again. This type of propagation is that of a random walk, just as in the Brownian motion of particles suspended in a liquid (Fig. 4.1).

The fundamental parameters describing this process are the mean free path (the average step size in the random walk) and

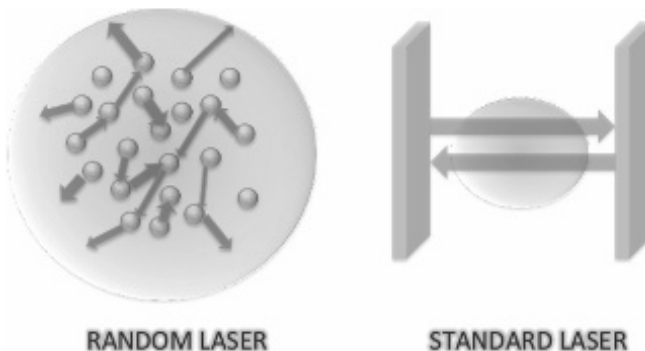


**Figure 4.1** Schematics of feedback mechanism in standard and random lasers.

the diffusion constant. Scattering in disordered optical materials is complex and coherent. This means that the phase of each of the optical wavelengths undergoing a random walk is well defined and interference effects can occur, even if a material is strongly disordered.

In the 1960s, light diffusion with gain was already discussed theoretically by Letokhov [1]. He argued that for a diffusion process with amplification, a situation where the total gain is proportional to the volume is obtained, whereas the losses will be proportional to the total surface. It is then easy to see that there exists a critical volume above which gain becomes larger than loss, and the intensity diverges. This model also predicts that the emission spectrum narrows down above threshold with a maximum intensity at the wavelength of maximum gain.

Later some authors made a disordered amplifying material by grinding laser crystal into a fine powder and they excited this powder optically and achieved optical gain through stimulated emission together with multiple scattering [2]. Above a certain threshold gain level, the emission spectrum was observed to narrow down and the peak intensity increased. A different strategy to achieve multiple scattering with gain was followed by Lawandy et al., who suspended microparticles in laser dye liquid. Lawandy called this material “laser paint,” as it constitutes a laser that can be painted directly on a surface [3]. Only later in 1995, the term random laser was introduced. The advantage of such a fluid material is that the amount of scattering can be easily varied by changing the particle concentration and thus the scattering strength and the laser efficiency.

Although a simplified model of diffusion with gain, as originally discussed by Letokhov, is very powerful in predicting certain emission properties of a random laser, it neglects interference effects of the light rays, being the interference in the multiple scattering responsible of the mode structure of a random laser.

Modes in a regular laser are determined by the laser cavity and usually consist of standing-wave patterns. In a random laser, the multiple scattering process defines optical modes with a certain central frequency and bandwidth, lifetime, and a rich spatial profile. The spatial profile of the modes is dominated by a speckle pattern

with variable intensity. In most random materials, high-intensity regions of modes, at given wavelengths, are spread throughout the sample and the modes are termed “extended.” In certain random materials, interference is constructive only in limited connected regions. This feature is commonly referred to light localization [4, 5], which has been supposed by some authors as the optical counterpart of Anderson localization of electrons [6]. In this case, the free propagation of waves is stopped and the radiation is completely entrapped inside the material. However, whereas Anderson localization is relatively easy to obtain in lower dimensions, it is still a debated issue whether it can occur in three-dimensional (3D) systems. Anderson localization might only take place in optical materials that are extremely strongly scattering, the requirement being that the mean free path  $l$  becomes smaller than the reciprocal wavevector  $k$ . The limit  $kl \leq 1$ , known as Ioffe-Regel criterion, is very difficult to fulfill in optics because most random optical materials have  $kl$  values much larger than 1. In a series of experiments, it was found that the narrow emission lines of a random laser can be observed in materials with a broad range of scattering strengths, much too weak to produce Anderson localization effects.

Several alternative mechanisms have been theoretically proposed to explain the existence of narrow resonances: (i) random variation of refractive index [7]; (ii) lifetime of the passive (without gain) modes, those with the longest lifetime have the lowest lasing threshold intensity in presence of a gain, even though extended in space [8–10]; (iii) mode locking and Hauss equation [11, 12]. Both extended and localized modes in random systems can lase and lead to spectrally narrow and coherent output [13–16]. Depending on the experimental geometry, this can be observed as narrow peaks, or as global narrowing of the spectrum if the narrow peaks are averaged out. All depends on the number of activated modes. If the system has many passive modes, it is possible to excite a few of them by shaping the pumping beam. This leads to a few distinguishable, and in some cases single, lasing resonant modes [17–19]. If many passive modes are present and they are all activated, the total energy is spread among all of them and the lasing modes will not be separated and shrink in a broad peak over the gain emission.

A third possibility is to obtain narrow resonances by manipulating the material to have a few passive modes. This is possible in systems with low dimensions and/or with very high scattering strength [20].

In this context, the relation between random laser and amplified spontaneous emission (ASE) can also be understood [21]. ASE is light that originates from spontaneous emission and that is subsequently amplified by stimulated emission. This process takes place without an optical cavity, and the emission spectrum is characterized by the narrowing of the gain curve of the active material with increasing pumping energy. In ASE, there are no modes and the main difference with single peak random lasers is the absence of an energy threshold.

A random laser that sustains a large number of modes that are strongly coupled and compete for the available gain can show a fluctuating behavior in its temporal and spectral response: A random laser can have a different spectrum each time it is excited [22]. Mode coupling is particularly strong for extended modes, and it takes place through the gain mechanism, which means that modes of different wavelengths can still be coupled, even if they are not spectrally overlapping. It was found that in these situations, the emission spectra are then completely uncorrelated from shot to shot and being sure that the scattering particles are not moving and all other conditions are kept perfectly constant. The fluctuations have been described by means of mode repulsion [23], Levy statistics [24–27], and the first explanation has been given by replica symmetry breaking theory [28–30].

### 4.2.1 Random-Laser Materials

To build random lasers, it is important to create strong enough scattering for the material to become optically thick. That is, the mean free path  $l$  should become at least smaller than the sample thickness. Strong enough scattering can be achieved by grinding a material into a powder, by suspending scattering elements in solution, or, by etching a porous network of air into a solid glass or semiconductor crystal [31, 32]. The last of these has the advantage that it can lead to very strong scattering, while the

pore size and thereby the scattering strength can be controlled in the etching process. A different approach to achieve strong and controllable scattering is to assemble monodisperse spheres in a random fashion. In analogy to photonic crystals, which consist of an ordered assembly of microspheres, researchers have dubbed this new random material a photonic glass [33]. By using monodisperse spheres, a material in which the scattering at certain wavelengths is resonant with the sphere diameter can be obtained. This leads to strong resonant Mie scattering, which favors random laser modes at the specific wavelengths of the resonances [34]. In the last years, many other materials have been proposed for their variable scattering capacity. Dilute opaque colloidal suspensions, plasmonic waveguides [35], quantum dots [36], organic conjugated polymers (see following section), disordered fibers [37, 38], polymeric micro-channels [39], microdroplets [40], granulars [41], paper [42, 43] and bio-inspired materials [44] have been designed and successfully used as disordered matrices for random laser.

Essential in the realization of a random laser is to obtain enough gain to reach the laser threshold. Powders of laser crystals are good candidates: titanium-doped sapphire emits at visible and near-infrared wavelengths, and zinc oxide is very suitable for random lasing in the near-ultraviolet region, owing to its high gain and strong potential for scattering. For visible wavelengths, gain can be obtained by incorporating laser dyes, either in solution or incorporated into the scattering elements or the solid surrounding them. Very recently, organic semiconductors, used for LEDs and as gain in lasers, have shown random-laser behavior, as detailed in the next section.

The gain material has to be excited to reach a population inversion, achieved through optical pumping. Nearly all random lasers are excited by a high-power pulsed pump laser. Although it is relatively easy to synthesize a random-laser material that supports extended modes, it is extremely difficult to realize one in which the modes are localized. This requires very strong scattering and, therefore, scattering elements with a size comparable to the wavelength and very high refractive index. At the same time, absorption has to be avoided because it would be counterproductive for lasing. One possible approach is to try to induce a population

inversion in disordered gallium arsenide or other semiconductor structures, which has a refractive index as high as 3.5 [5, 45]. For visible light, signatures of localized modes with long lifetime have been found in titanium dioxide powders, which have a refractive index of about 2.7 [46–48].

#### 4.2.2 Applications

Random lasers are cheap and require simple technology, contrary to high precision microcavities. In addition, the materials can be produced on a large scale and have a high and controllable emission efficiency. The properties that make a random laser special with respect to regular lasers are its color and angular dependence, as well as its complex features in emission spectra. The angular distribution of the emission of a random laser can be distributed over the complete solid angle. Such a property is, in principle, ideal for display applications, as recently proposed for random laser from a new type of active polymer-dispersed liquid crystal, using liquid crystal droplets in a polymer matrix with added laser dye. The liquid crystal droplets are optically birefringent and, therefore, give rise to an extremely anisotropic, quasi-2D diffusion process, when all aligned in the same direction by an electric field. The result is a random laser that emits mainly in a plane and of which the output is polarized with controllable polarization [49].

A particular advantage of random-laser materials is that they can be prepared in the form of suspensions of particles that can be applied as coatings on surfaces of arbitrary shape. For the control over random-laser emission, temperature tuning has been demonstrated as well. In this case, the random-laser spectrum depends strongly on environment temperature and the random laser can even be brought above and below threshold by temperature changes [50].

An application for random lasers in a very different area was proposed in medical diagnostics. It has been found that the emission spectrum of cancerous human tissue, when doped with laser dye, could be distinguished from healthy tissue [51]. Such alternative strategy for tumor diagnostics links to the very active field of biomedical imaging with diffuse light and makes use of the fact that different tissue and bone types have different optical structures

and mean free paths [52]. Very recently, random-laser emission has been used as illumination for the imaging of turbid samples [53, 54].

### 4.3 Organic Semiconductor Materials in Random Lasers

In the last few years, advances in the field of organic optoelectronics concern materials development, device design, film-deposition procedures, understanding of assembly and growth processes, device lifetime, performance, and stability [55–58]. The opportunities for the use of organic materials in modern optoelectronics are rapidly expanding, based on novel optoelectronic properties, unique functionalities, and very high performances offered principally by carbon-containing semiconductors. Polymeric and low-molecular weight organic compounds are considered innovative and promising materials because they could be efficient light emitters in a wide spectral range, biodegradable, chemically stable, low cost and easily usable for deposition on rigid and flexible substrates.

Therefore, the successful application of organic semiconductor platforms will depend on capturing its low-cost potential through the innovative and simple fabrication of devices on inexpensive, large-area substrates. However, their real practical implementation in optoelectronic applications depends on the ability to produce devices at a cost that is significantly below that required for the production of conventional devices [59]. Interest in organic optoelectronics stems from the ability to deposit organic films on a variety of very low-cost substrates such as glass, plastic, metal foils, paper or fabric, and the relative ease of processing of the organic compounds that are usually ad hoc engineered. The organic light-emitting devices (OLEDs) are currently the most advanced organic electronic systems already in commercial production and they are mostly in high efficiency and very bright thin color displays [60, 61]. Significant progress is also being made in the realization of thin-film transistors (TFTs) and field-effect transistors (FETs) [62] as well as thin-film organic photovoltaic cells for low-cost solar energy generation [63–65].

The recent and significant development of organic semiconductor materials has played a crucial role also in the development of innovative organic lasers [66]. The first demonstration of lasing from an organic compound has been described in the early 1990s and was based on conjugated polymers in solution [67]. After this, other researchers observed lasing and stimulated emission also from conjugated polymers in the solid state [68–71]. These observations showed for the first time that polymer films, which were capable of conducting current, could amplify light, thus opening the way to the realization of organic diode lasers.

In the photo-physics of organic semiconductors, there are some aspects that make them attractive for application in lasers. First of all, it is desirable for the material to have the electronic structure of a four-level system so that the stimulated emission spectrum does not overlap with the ground-state absorption spectrum. This is true for most of the conjugated materials, which naturally form a four-level system because structural and vibronic relaxation in the excited state shifts the energy levels [21, 72]. Another advantage is that organic materials can absorb light very strongly. As an example, a thin film of a conjugated polymer can absorb 90% of the light incident on it at the peak of absorption spectrum [71]. This means that light can be absorbed in very short distances and, since stimulated emission is closely related to absorption, also means that very strong gain is also possible [66]. Besides, the photoluminescence spectra of organic semiconductors are broad and can be tuned over a significant spectral range by changing the chemical structure and the supramolecular organization. Organic materials have also a large stimulated cross section [73–77]. Finally, the photoluminescence efficiency of thin films of organic materials can be increased by acting on the control of intermolecular interactions [78–80].

From an experimental point of view, different types of organic semiconductors are suitable for lasing. They are characterized by innovative optoelectronic properties, tunable with the chemical-physical structure, and are suitable both for nonconventional manufacturing procedures and substrates. Organic semiconductors, like all organic materials, are carbon-rich compounds with a structure tailored to optimize a particular function, such as luminescent

properties or charge mobility. Usually the semiconducting properties arise from the overlap of molecular orbitals of these conjugated molecules. Organic semiconductors are conventionally classified in small molecules, oligomers, and polymers. Small molecules refer to those compounds with a well-defined molecular weight. Oligomers are molecular complexes that consist of a few monomer units, while polymers are long-chain molecules consisting of an indeterminate number of molecular repeat units.

In this chapter, we will focus only on the specific category of random lasers. In addition to the inorganic material listed in [Section 4.2](#), random lasing has been demonstrated in different organic materials and compounds including blend of laser dyes (Rhodamine 6G) and nanoparticles or powders ( $\text{TiO}_2$ ,  $\text{ZnO}$ ,  $\text{GaN}$ ) [[19](#), [23](#), [81](#), [82](#)];  $\pi$ -conjugated polymers, such as (poly(phenylene vinylene) (PPV), poly(2-methoxy-5-(2-ethylhexyloxy)-1, 4-phenylene vinylene) (MEH-PPV), poly-(dioctyloxy) phenylene vinylene (DOO-PPV), or the polyfluorene (PF)) [[67–71](#), [82](#), [83](#)]; organic-inorganic nanocomposites [[84](#)]; organic nanofibers [[85–87](#)]; thiophene-based oligomers [[55](#), [88–91](#)]. Deep understanding and control of the self-aggregation processes of organic molecules yielding efficient optical emission, nonlinear activity, and high optical gain are strategic for the realization of nano-scaled photonic and optoelectronic devices. Among the challenges of today's nanotechnologies, including molecular self-assembly techniques, is the realization of nanoaggregates having well-controlled morphological, photonic, and electronic properties and their large-scale integration in arrays and circuits with broad application capabilities [[73](#), [92](#), [93](#)]. In this regard, the properties of  $\pi$ -conjugated molecules and polymer films are quite sensitive to chain packing morphology, which can vary dramatically depending on the preparation conditions and greatly affect the photophysical properties. Morphology of organic materials can be finely tuned by selectively modifying the assembly and supramolecular packing of molecules with low-cost and unconventional techniques (spin casting, photolithography, ink-jet printing, micromolding, etc.) onto almost any type of substrates in order to finely target the performances of laser devices [[74](#), [94–97](#)]. We analyze below a selection of the main methods of patterning used in organic random lasers.

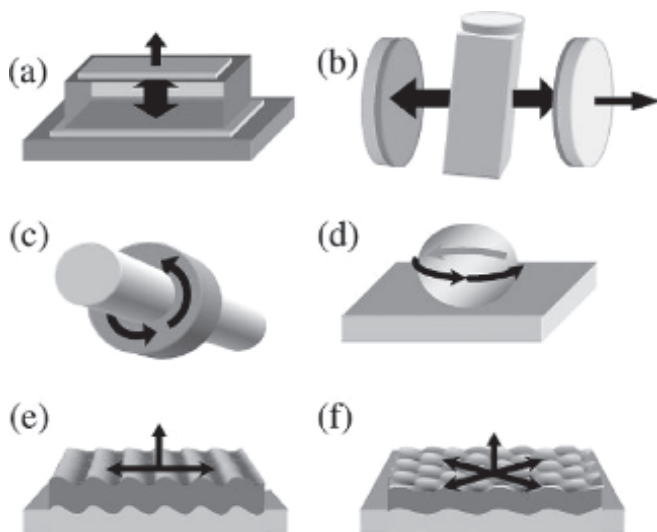


**Figure 4.2** Schematic resonators used for organic semiconductor lasers showing propagation directions of the resonant laser field: (a) planar microcavity; (b) Fabry-Pérot dye laser cavity; (c) microring resonator, coated around an optical fiber; (d) spherical microcavity; (e) distributed feedback resonator; (f) 2D DFB/ photonic crystal resonator. Reproduced with permission from Ref. [66], Copyright 2007 American Chemical Society.

#### 4.4 Patterning Organic Compounds for Random Lasing

Tessler and co-workers were first to demonstrate, in 1996, an optically pumped organic microcavity laser [71]. Over the years, different types of geometries have been realized for organic semiconductor lasers, some of which are represented in Fig. 4.2 [66].

Recently, both amplified spontaneous emission and lasing properties have been demonstrated directly from single crystals of thiophene oligomers, showing that crystalline materials can act as gain medium in itself and the resonators are a pair of facets of the crystal [98, 99], or microcavities of different shapes fabricated by electron beam lithography and dye etching [100, 101], or distributed feedback cavities [102]. These approaches allow

for remarkable device performances, even if they require complex technological steps and device architectures, which are not suitable for all the organic compounds and not easily integrable in practical applications.

Therefore, for this type of innovative applications with organic materials, it is more suitable to refer to random lasers, a class of devices that do not involve any additional external feedback structures, thus are simple to fabricate and low cost. In this regard, in recent years many researchers have reported promising evidence of random lasing from planar devices, based on an active layer of organic molecule in which defects, aggregates, or external beads behave as scattering centers [88, 103–106]. For random lasers, for which the modes are determined by multiple scattering without any laser cavity, the design and control of the supramolecular organization of active material as well as of the device geometry are particularly important. In fact, when realizing a random laser, it is important to achieve a strong and controllable scattering within the active material so as to make it opaque and to reduce the mean free path [106]. Therefore, due to the intrinsic randomness of the scattering centers, conventional methods for the fabrication of random lasers do not allow for a careful control of the device geometrical parameters, and in turn of the lasing properties. More importantly, it is clear how the peculiar properties of materials, optimization of the deposition procedures, and kinetics of the manufacturing process lead to tailor the coherent emission properties of a random laser by controlling the distribution and the size of randomly distributed scatterers. All this is particularly true in the case of organic materials. The interest on organic materials as active compounds stems not only from the possibility to design new and enhanced properties, but also to combine different properties within the same material, else to integrate functionalities from libraries of materials that can be processed or fabricated on the same technology. First, chemical design can additionally impart noncovalent interactions (sterical, dispersion forces, hydrogen bonding, competing interactions) that give rise to supramolecular architectures. Besides, the experimental control of architectures plays an important role in tailoring properties, since it is recognized that many relevant properties depend on size and dimensionality

of the suitably organized material [107]. However, despite the potential offered by chemical design, it could be extremely difficult to control the effects of designed interactions across spatial length scales, as the emerging architecture depends on the interplay of thermodynamic and kinetics factors [108]. More importantly, the realization of integrated devices with (sub)micrometer sizes requires the development of advanced lithography techniques suitable for soft materials; the lack of which is often a strong limitation to the use of such materials in practical applications [109–111]. Up to now, much work has been done on the manipulation of organic materials and the ability to fine-tune the desired functional properties by minor structural modifications or conformational changes [55, 112, 113]. It is possible to envision different schemes for additive manufacturing guided by concepts such as multi-scale control of self-organization through confinement, minimization of the amount of functional materials, enhancement of functionality. Several methods for controlled molecular patterning in functional devices are currently under investigation, based on either top-down (spin-coating, soft-embossing, and nano-imprinting [114]) or bottom-up lithography (spinodal dewetting [115], micro-contact printing [116], and surface tension-driven (STD) techniques [109, 110, 117]). The common goal of these approaches is to dynamically adjust the behavior of molecular solutions at the solid–liquid interface. Therefore, functional patterning of the organic material in well-defined features is obtained by exploiting and controlling the instability phenomena affecting a liquid thin film on a non-wetting surface and the intrinsic self-organization of  $\pi$ -conjugated molecules in spatially restricted environments [55, 109, 110, 117]. Such a bottom-up approach allows for both the modulation of the single-molecule conformation and the supramolecular organization, thus permitting to finely control a range of physical parameters typical of confined systems, without any conventional, complex, and expensive lithographic steps [107]. Quasi-equilibrium conditions in which self-organization evolves are, in fact, strongly affected by dimensionality and energetic parameters at the solid–liquid interface. Therefore, by modulating specific process parameters, it is possible to succeed in finely tuning dimensions and spatial distribution of the functional nanostructures that, in turn, affect the

emission properties, as the lasing threshold. From the point of view of fabrication, different types of approaches have been used for this purpose. Literature reports random lasing from weakly scattering polymeric neat films, despite the absence of intentionally introduced scattering centers [104, 105]. In the case of a substituted thiophene-based molecular film, the feedback for lasing is provided both by sequential scattering from holes formed in the spin-coated film [88, 103] or from randomly distributed aggregates, obtained by finely addressed molecular self-assembly of the organic molecules [90]. Self-assembly mechanisms of nanoaggregates, driven by molecular epitaxial growth, are the basis for the realization of random lasers with organic para-sexiphenyl nanofibers. The lasing processes are due, in this case, to the strong optical confinement realized during the supramolecular organization of the building blocks of organic material [85–87].

## 4.5 Thiophene-Based Compounds: Engineered Random Lasers and Replica Symmetry Breaking

### 4.5.1 Lithographed Random Lasers

In a recent publication, we investigated the random-laser emission from scattering nanoaggregates of a thiophene-based molecule, obtained in a controlled way by a simple soft-lithography technique.

We used a functionalized thienyl-S,S-dioxide quinque thiophene (T5OCx), which has been deeply investigated as active material for lasing applications. Amplified spontaneous emission (ASE) from spin-coated thin films, [88] as well as coherent lasing in external mirrors [91] or distributed feedback (DFB) based architectures [118], has been demonstrated for T5OCx. In our case, no external cavity or conventional DFB structures are exploited, being the feedback provided by the random distribution of highly scattering centers. The difference with standard random lasers [12, 20, 119] is that in the latter the scattering centers are usually high refractive index colloidal particles or powders dispersed in the active dye matrix. Differently, our systems consist of scattering

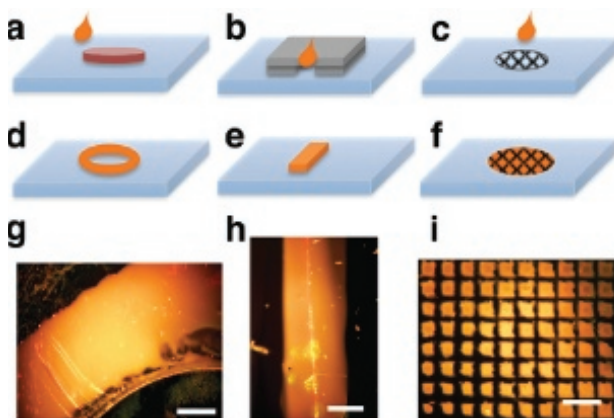


**Figure 4.3** Schematic illustration of the molecular material used and the STD patterning procedures. (a-c) Sketches of the different bottom-up lithographic techniques adopted to pattern the thiophene dye: ring (a), stripe (b), and squared pixels (c). (d-f) The corresponding illustrations of the realized patterns and (g-i) optical images in true color of the fabricated samples. A drop of T50Cx solution in  $\text{CH}_2\text{Cl}_2$  is poured at the center of the related template placed on a glass substrate. The average thickness of all samples is about 1  $\mu\text{m}$ . Scale bars: 100  $\mu\text{m}$  (g,i) and 50  $\mu\text{m}$  (h). Reproduced from Ref. [90] with permission from John Wiley and sons.

centers obtained by the accurate control of active molecules self-assembly.

For the preparation of T50Cx used in this study, an improved procedure was employed taking advantage of ultrasounds for the bromination reactions and microwaves for coupling reactions, using the typical conditions described in Ref. [90, 120].

The molecular patterns are obtained by exploiting surface tension-driven (STD) deposition under the effect of both energetic and geometric constraints, in which the amplification of the surface instabilities at the liquid interface, driven by an external template, realizes a controlled pattern of T50Cx. Figures 4.3a–c give schematic illustration of three different bottom-up lithographic techniques to obtain ring, stripe, and pixel microarrays.

Illustrations of the correspondent patterns are shown in Figs. 4.3d–f, and the optical images in true colors in Figs. 4.3g–i show the final structures.

A fine modulation of the shape and distribution of the scattering centers is obtained for each pattern also by acting on the process kinetics. It is known, in fact, that differences in supramolecular packing due to self-organization of molecular material occurring during nucleation phenomena can be selectively addressed by controlling different types of energetic parameters (i.e., surface energy at interface, geometric confinement, process temperature, etc.) [110, 111].

The optical properties of the STD micro-patterns are investigated by confocal microscope, as shown in Figs. 4.4 for stripe-shaped (see Figs. 4.4a,c,e,g) and micropixels (see Figs. 4.4b,d,f,h). Confocal  $x$ - $z$  optical section (see Figs. 4.4c and d), 3D reconstruction of the organic active layers (see Figs. 4.4e and f), and the spatially resolved photoluminescence spectra (SR-PL) (see Figs. 4.4g and h) show that the STD lithographic process does not affect the optical properties of T50Cx.

For the investigation of the lasing properties, the patterned samples are pumped by a frequency doubled Q-switched frequency doubled Nd:YAG pulsed laser emitting at  $\lambda = 532$  nm, with 10 Hz repetition rate, 8 ns pulse duration, and with 8 mm beam diameter. For each sample, the laser spot is tuned by using an iris at the exit and the emitted radiation is collected from the input face of the sample at an angle of about  $40^\circ$  from the beam direction after focalization into an optic fiber connected to a spectrograph equipped with electrically cooled CCD array detector. A sketch of the experimental setup is reported in Fig. 4.5a. We probe different emission directions in the angular range  $25^\circ$ – $65^\circ$  from the incident beam direction, and we do not observe any significative variation in the emission profiles. The exposure time was set to 1 s and each spectrum results from the average of 10 pump shots.

In Fig. 4.5, the emission spectra from stripe (b) and ring (c) confinement geometries are reported. The amplified stimulated emission from both systems is clearly evidenced by the appearance over the broad gain band of a peak at 610 nm with a linewidth narrowing down to an order of magnitude as the pump energy is increased. In these experiments, the spot size of the incident beam is about 8 mm for the stripe and 2 mm for the ring, meaning that only a portion of the ring is illuminated. In order to improve the

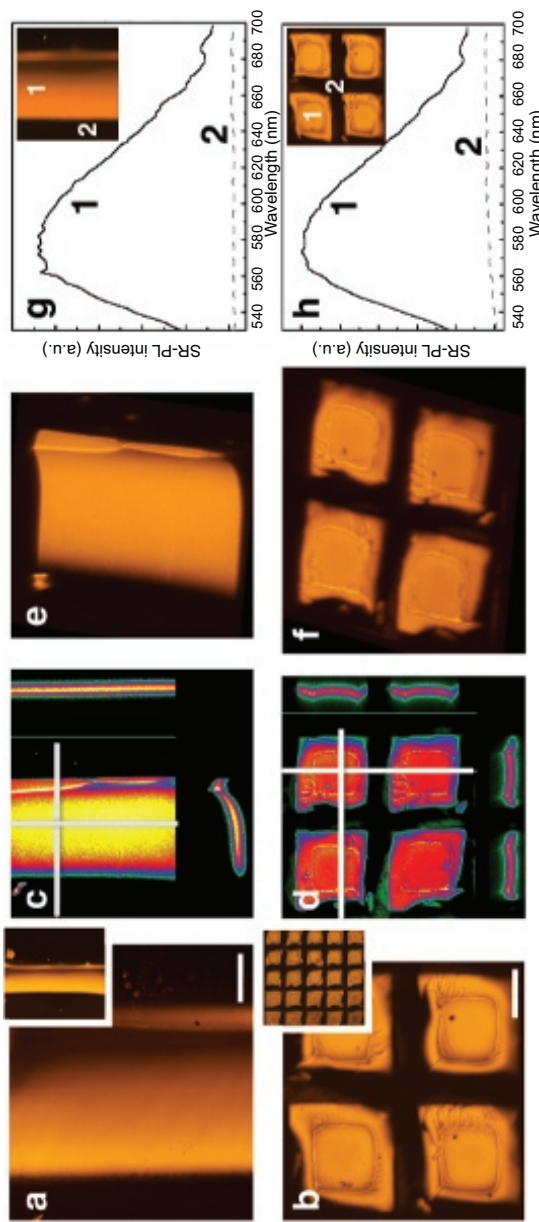


**Figure 4.4** (a,b) Laser scanning confocal microscopy images of the T50Cx stripe-shaped (a) and micropixels array (b) patterned by STD technique. Scale bars: 20  $\mu\text{m}$ ; (c,d) z-projection in false color of confocal scanning in depth of stripe (c) and pixels (d) patterns with a resolution step of 200 nm for each slice. The x-z and y-z optical sections are reported in the image sides; (e, f) 3D reconstruction of the spatial resolved photoluminescence emission, obtained by x-z optical sections of confocal scans; (g, h) spatially resolved photoluminescence spectra (SR-PL) of stripe-shaped (g) and micropixels array (h) acquired inside (1) and outside (2) the molecular pattern. Reproduced from Ref. [90] with permission from John Wiley and sons.

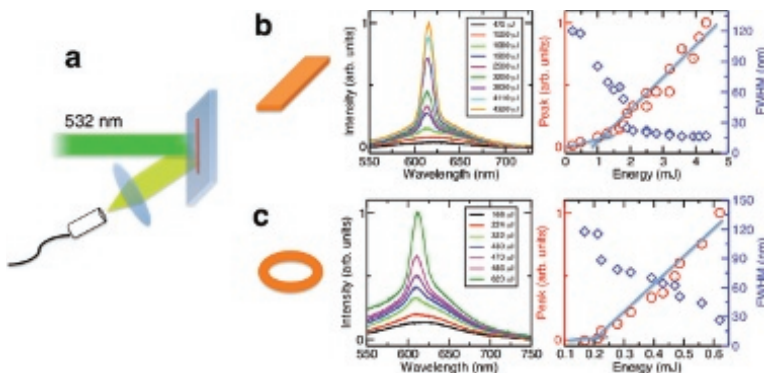


**Figure 4.5** (a) A sketch of the random-laser setup. (b, c) Emission spectra and corresponding spectral analyses of a portion of the stripe-shaped (b) and ring-shaped (c) dye self-assemblies at variance with the injected pump energy. In the right panels, the peak intensities (red) and the full width at half maximum (blue) are reported. Reproduced from Ref. [90] with permission from John Wiley and sons.

lasing properties of the fabricated random lasers, we prepare two different samples of the ring laser, with initial better performances with respect to the stripe one, at different process temperatures,  $T_{\text{slow}} = 24^\circ\text{C}$  and  $T_{\text{fast}} = 50^\circ\text{C}$ , corresponding to slow and fast molecular assembly kinetics, respectively.

In Fig. 4.6, atomic force microscopy characterization of the ring laser is reported, showing the conformational structure of the patterned organic dye at the nanoscale. In particular, an amorphous and quite homogeneous arrangement (dark part) of T5OCx with the presence of randomly distributed disk-shaped nanostructures (bright spots) is evident in both samples. Size and distribution density of the aggregates instead strongly depend on the process temperature, with smaller aggregates and larger relative distances in the case of fast kinetics (see Figs. 4.6c and f). The formation of these well-defined self-assembled nanostructures, dispersed across the amorphous bulk, is induced in both samples by the quasi-equilibrium self-assembling dynamics under energetic confinements of the STD lithography. In particular, it is known that the modulation of molecular arrangement in the solid state of a thiophene-based molecule, driven by an STD process, is due to a

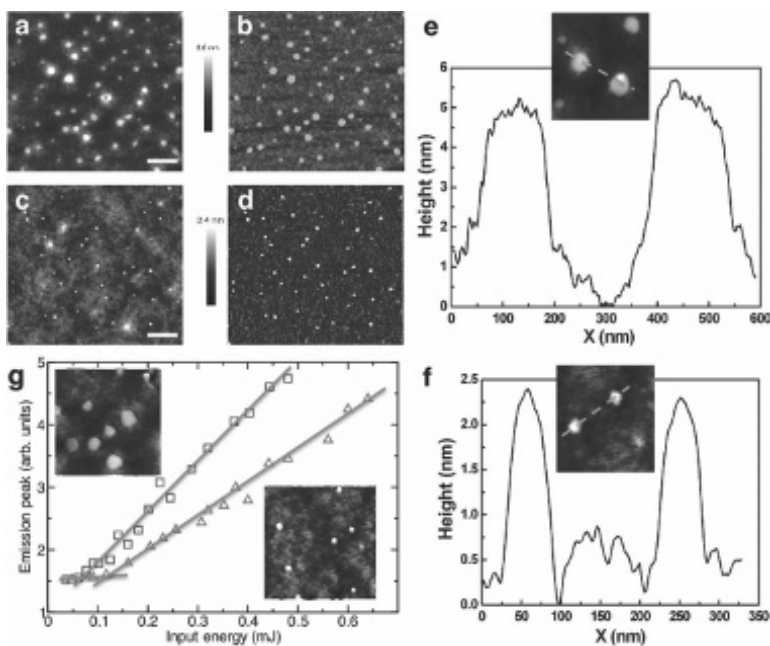


**Figure 4.6** (a-c) AFM topography (a) and phase (b) images of the ring-shaped thiophene sample prepared at room temperature ( $T_{\text{slow}} = 24^\circ\text{C}$ ) and section profile along the dashed lines of representative portions (in the insets) (c); (d-f) AFM topography (d), phase (e) images and section profile (f) of the ring-shaped thiophene sample prepared at temperature of  $T_{\text{fast}} = 50^\circ\text{C}$ . Scale bars: 500 nm. The bright spots indicate the T50Cx self-assembled nanostructures that act as scattering centers. (g) Peak emission intensities of samples prepared at  $T_{\text{slow}} = 24^\circ\text{C}$  (squares) and  $T_{\text{fast}} = 50^\circ\text{C}$  (triangles); insets: correspondent AFM zooms. Reproduced from Ref. [90] with permission from John Wiley and sons.

balance of polar and apolar contributes to surface energy [111]. Conversely, the conventional spin-coating deposition of T50Cx is exclusively characterized by an amorphous arrangement without any supramolecular structure [88]. The different dimension and distribution of the aggregates can be explained by considering that a slow kinetics, nearest to the quasi-equilibrium regime, makes easier the molecules to arrange in a crystalline packing [55]. Conversely, a fast dynamics enhances the propagation of instabilities at the liquid interface during the STD process, thus favoring

the formation of more distorted amorphous phase. Interestingly, in Figs. 4.6b and e, the correspondent phase images exhibit additional spots, not visible from the height signal, showing that such observed aggregates are present even in the space below the observable amorphous bulk and thus they are 3D spatially distributed.

The emission from the two ring-shaped lasers taken in the same experimental conditions is investigated and the relating lasing peak intensities reported in Fig. 4.6g, where clear lasing thresholds of 70  $\mu\text{J}$  and 130  $\mu\text{J}$  are evident for  $T_{\text{slow}}$  and  $T_{\text{fast}}$  devices, respectively. Better lasing properties are obtained in  $T_{\text{slow}}$  device where more packed and bigger supramolecular nanostructures (bright spots) provide better feedback conditions.

In this way, we realized a random laser with desired shape, where the scattering centers are thiophene aggregates formed by spontaneous molecular self-assembly guided by STD lithography. The optimization of the deposition procedure and process kinetics leads to tailor the coherent emission properties by controlling the distribution and the size of the random scatterers.

#### 4.5.2 Intensity Fluctuations in Random Lasers

For the study of fluctuations in random lasers, we used the T50Cx dye treated in order to have a thick disordered solid material (Fig. 4.7a) that shows evident and strong shot-to-shot fluctuations in the intensity emission.

A sketch of the pumping and collecting geometry is given in the inset of Fig. 4.7b.

In Fig. 4.7b, single-shot high-resolution (0.07 nm) emission spectra, taken at identical experimental conditions, are illustrated. Input energy is 10 mJ. The presence of random-laser modes with configuration variable from pulse to pulse is evident: each time the system is pumped, the numerous passive modes randomly compete for the available gain, giving rise to several different compositions of the activated spectral peaks [25]. Such behavior is also evidenced by the direct visualization of the sample during pumping, as reported in Fig. 4.8, where four different fluorescence images taken at four

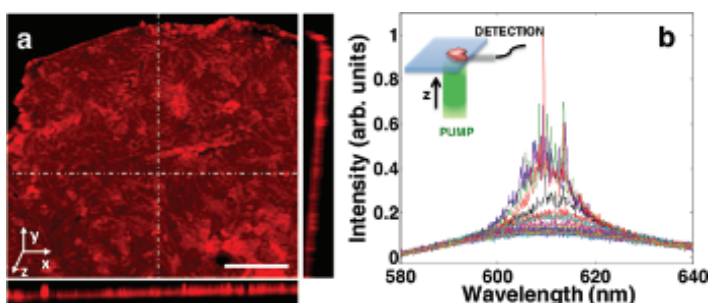


**Figure 4.7** Sample image and emission spectra showing random lasing. (a) 3D reconstruction of confocal microscopy Z-stack images of the supramolecular laminar packing in a T50Cx solid sample. The right and the bottom panels report the yz and xz sections, respectively. Scale bar: 20  $\mu\text{m}$ . (b) High-resolution single-shot spectra taken in the same conditions, 10 mJ pump energy. Inset: sketch of the experiment. Reproduced from Ref. [30] with permission from Nature Publishing Group.

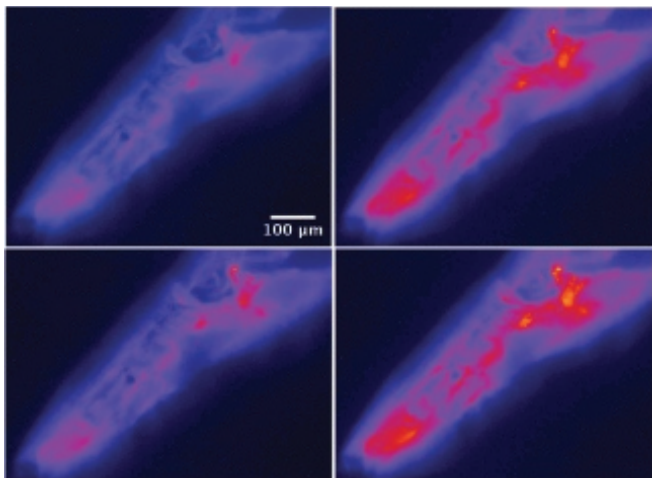


**Figure 4.8** Snapshots of random-laser emissions. Single-shot optical images during the pumping of the sample in the same experimental conditions. The input energy is 10 mJ. Reproduced from Ref. [30] with permission from Nature Publishing Group.

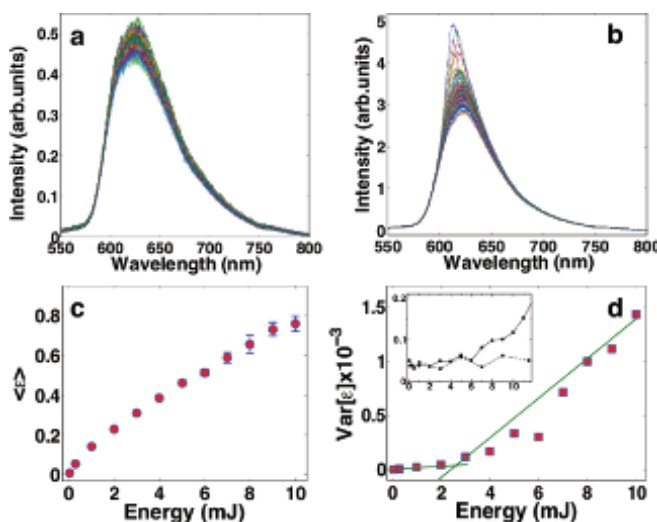


**Figure 4.9** Fluctuations in the random-laser emission. (a,b) Emission spectra at low energy 1 mJ (a) and high energy 12 mJ (b). (c) Mean emission intensity  $\epsilon$  versus pump energy, error bars are standard deviation. (d) Variance of  $\epsilon$  versus pump energy. Inset: peak standard deviation divided by mean peak intensity from the sample (solid line) and the pump laser (dashed line) emission spectra. Reproduced from Ref. [30] with permission from Nature Publishing Group.

single shots exhibit different emission patterns. The spatial intensity profile of the lasing modes changes from shot to shot.

In Figs. 4.9a,b, we show emissions of subsequent 100 shots with lower spectral resolution (0.3 nm), at two different pump energies. There is no time periodicity in the spectral fluctuations: their sequence is random. At low energy, the noisy variations of the spontaneous emission are negligible if compared to the pronounced fluctuations observed at high energy.

We analyzed the experimental results by means of the replica theory. Replica theory was originally introduced to solve the prototype model for spin-glasses [121]. It was readily recognized as one of the fundamental paradigms of statistical mechanics and found applications in a huge variety of different fields of research. Spin-glass theory gives a rigorous settlement to the physical meaning of “complexity” and describes a number of phenomena (e.g.,

glass transition) [121, 122]. More recently this theory has found application in the field of random photonics [123], as specifically for random lasers and nonlinear waves in disordered systems [28, 124]. However, notwithstanding the theoretical relevance, an experimental demonstration of the most important effect, the so-called “replica symmetry breaking,” is still missing. Spin-glass theory predicts that the statistical distribution of an order parameter, the “Parisi overlap,” changes shape when a large number of competing equilibrium states emerges in the energetic landscape [125]. When this happens, “replicas of the system,” i.e., identical copies under the same experimental conditions, may furnish different values of their mutual correlations, called “overlap,” depending on whether or not their equilibrium dynamics thermalize in the same ergodic components or in separate ones. In the spin-glass approach, the random-laser modes are treated as continuous complex spin variables with a global (power) constraint and whose coupling is governed by the interplay between frustration-inducing disorder and nonlinearity. In our experiments, the disorder is fixed and the nonlinearity increases with the pumping energy, which acts as the inverse of temperature in statistical mechanics [126, 127]: at low energy (high temperature), there is no gain competition [128, 129] between the modes and they oscillate independently in a continuous wave “paramagnetic regime”; while at high energy (low temperature), the coupling frustration, due to disorder, induces a nontrivial gain competition giving rise to a “glassy regime.” In this regime, a large number of electromagnetic modes is activated. The set of the activated mode configurations is found to change from pulse to pulse.

Details of our statistical analysis are reported in [30], and here we show the final results in Figs. 4.9c,d where the growth of the mean intensity and the variance of the intensity versus pump energy is evident.

A parameter relevant to quantify the fluctuations is the overlap between intensity fluctuations in different experimental replicas [29]. From the measured spectra, we calculate the set of all values of the overlap  $q$  for each different input energy, determining their distribution  $P(q)$  depicted in Fig. 4.10.

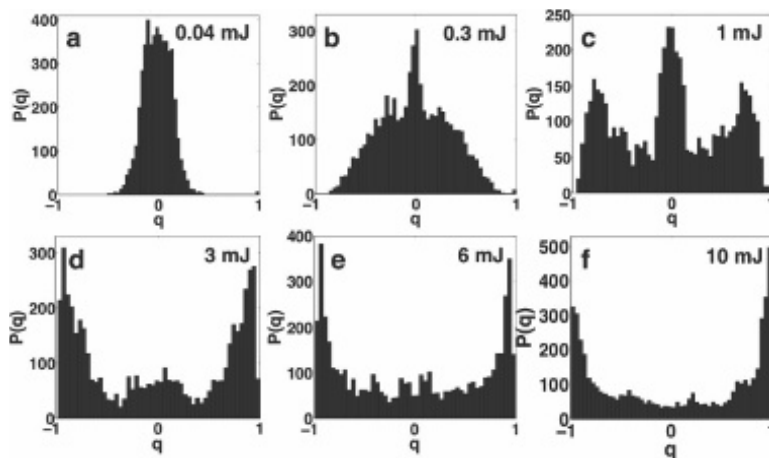


**Figure 4.10** Distribution function of the overlap showing replica symmetry breaking by increasing pump energy. Reproduced from Ref. [30] with permission from Nature Publishing Group.

Such behavior of the  $P(q)$  evidences the fact that the correlation between intensity fluctuations in any two replicas depends on the replicas selected. The variety of possible correlations extends to the whole range of values. This is a manifestation of the breaking of the replica symmetry.

## 4.6 Biocompatible and Biologically Inspired Random Lasers

The growing demand for innovative organic optical and photonic applications is also motivating research toward the realization of biodegradable, biocompatible, and implantable photonic components that offer smart, low-cost, and scalable interfaces that can be easily integrated on flexible substrates. Developments in novel and smart micro- and nano-photonics have shown that it is possible to make use of the intrinsic disorder in photonic materials to create useful optical structures. This is particularly true in the case of random laser, in which laser action is obtained in completely disordered and random structures. Up to now,

as we have shown, promising answers in this direction have been given from organic materials and devices. Compared to the interaction with solid interfaces and substrates, organic compounds can be multifunctional, chemically stable, mechanically flexible, compatible with large-area substrates, and require simple soft-lithography techniques and low-temperature processes for their patterning and assembly. In general, organics are compatible also with arbitrary nonconventional natural substrates, allowing the possibility of replacing conventional inorganic and glass substrates, normally used for optoelectronic and sensing applications, with biocompatible environmentally friendly materials. Furthermore, random lasers made with organics and natural biomaterials allow to develop biodegradable and biocompatible devices and have practical potential applications in sensing or diagnostic imaging, thus paving the way for smart coding of objects, remote sensing, or the implementation of low-cost targeted therapy [51, 106]. Among the most promising alternatives to conventional materials, recently, novel random-laser platforms based on paper sheets [42, 43], polymer channel-networks [39], diatomite [130], silk fibroin [131], cellulose nanofiber networks [132], DNA [133], as well as human tissue [51] have been proposed. With this in mind, we will choose to focus mainly on the results involving random lasers on flexible substrates, particularly paper sheets and polymer plastics.

Paper is a ubiquitous and low-cost material in everyday life, attracting now growing interest for applications in flexible electronics, as well as biological processing. In the last years, microfluidic devices for use in healthcare and electronic devices (i.e., transistors, capacitors, sensors, touchpads, etc.) have been realized on commercial papers [134–136]. These devices are characterized by enormous potentialities in terms of novel design architectures and use in low-cost applications.

In a recent publication, we reported on the first realization of lasing devices from paper flexible sheets without the presence of any optical cavity and by creating on the cellulose fibers microfluidic porous channels in which a lasing dye can flow by capillarity (Fig. 4.11) [42, 43]. The device used was a random laser in order to avoid any additional external feedback structures and better study the scattering properties of paper. Common paper has

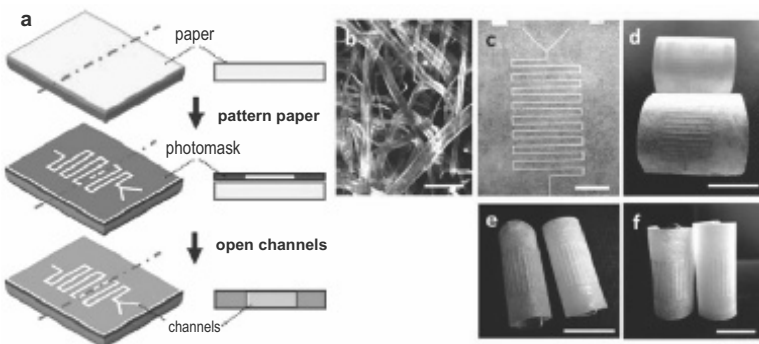


**Figure 4.11** Preparation of a microfluidic paper-based photonic device. (a) Fabrication process. (b) Confocal microscopy of the structure of native paper. (c–f) Photographs of one of the microfluidic circuits realized on paper after adding a fluorescent dye to the sample reservoirs. The images show a reference empty device (c) and different images of devices partially filled with a lasing dye demonstrating the high flexibility of integration of the lasing paper that can be bent (d), rolled (e), and vertically aligned (f). Scale bars: 100  $\mu\text{m}$  (b); 5 mm (c); 1 cm (d–f). Reproduced from Ref. [43] with permission from The Royal Society of Chemistry.

a hierarchical structure characterized by a randomly distributed network of different cellulose fibers and thus by an intrinsic randomly distributed refraction index (Fig. 4.11b), with an average value of  $n = 1.5$  for cellulose [137]. This porous structure can be imbibed with a lasing dye, acting as gain medium, thus resulting in stimulated photon scattering at the cellulose network or at each channel wall and, in turn, in a random-laser action when the losses are overcome by amplification.

The paper-based patterned random laser was realized from paper microchannels imbibed with Rhodamine B (RhB) solution, and by modulating the emission properties with an accurate control over the engineered fractal heterogeneity of the disordered cellulose network. The paper-based device is obtained by using commercially available biodegradable paper sheets and simple and low-cost soft-lithographic steps (Fig. 4.11). The devices refer to a microfluidic network with manifold degrees of confinement that are difficult to achieve using conventional open-channel microsystems for

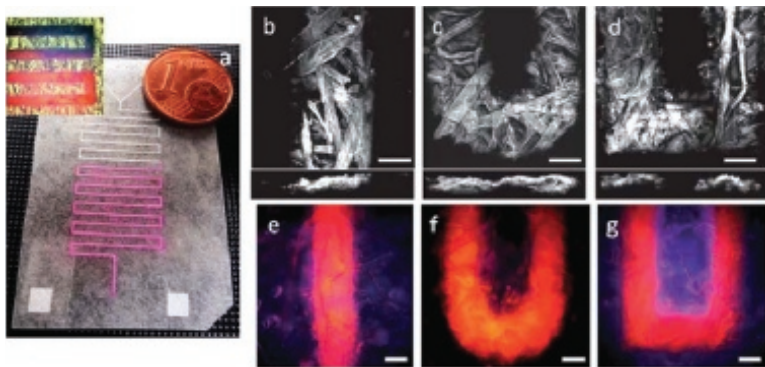


**Figure 4.12** Examples of paper-based photonic devices. (a) Photograph of one of the paper-based microfluidic devices. The microfluidic circuits are realized by soft-lithography on a single layer of a chromatography paper and fulfilled by capillarity with a laser dye. The left inset shows an optical image in true colors of the channel's imbibition (b-d) Z-stack confocal images of different features realized in the paper sheet. The *xz*-sections, in the bottom of the corresponding images, clearly show the active channels constituted by a network of cellulose micro-fibers, acting as randomly distributed hierarchical subchannels. (e-g) Optical images on true colors of the corresponding channels filled with the laser dye, Rhodamine B (RhB). Scale bars: 100 µm (b-g). Reproduced from Ref. [43] with permission from The Royal Society of Chemistry.

optofluidics [39]. The patterning process defines the width, length, and shape of paper-based microfluidic channels, while the thickness of paper defines the height of the open porous channels (Fig. 4.12).

Hence, this type of device allows to study how different levels of confinement for a lasing dye (shown in Fig. 4.12) can affect the emission properties of the paper-based random-laser device. The random lasing characteristics were monitored under varying channel dimensions and compared with the behavior in the native non-lithographed paper (Fig. 4.13). Trend of the peak intensity, taken under the same experimental conditions for different and independent devices, clearly shows a meaningful modulation of the lasing thresholds with the confinement induced by the lithographic process.

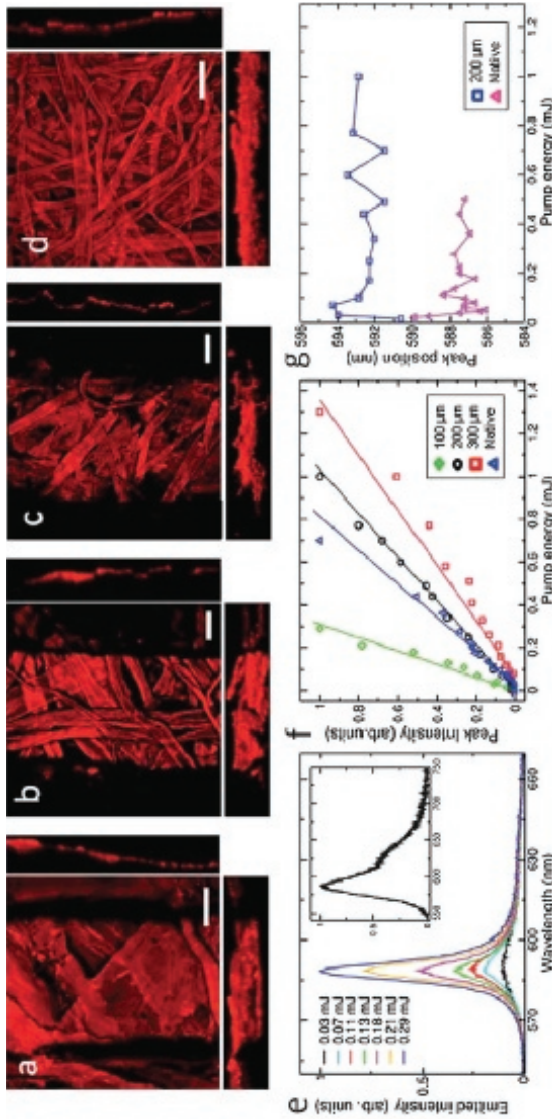


**Figure 4.13** Random-laser emission versus channel confinement. (a-d) Z-stack and 3D reconstruction of confocal microscopy images of paper-based microfluidic devices with different channels widths imbibed with RhB: (a) 100  $\mu\text{m}$ ; (b) 200  $\mu\text{m}$ ; (c) 300  $\mu\text{m}$ ; (d) native paper. The right and the bottom sides of each image report the  $yz$  single-slide section and the cumulative sum of  $xz$ -sections, respectively. Scale bars: 30  $\mu\text{m}$  (a); 50  $\mu\text{m}$  (b,c); 100  $\mu\text{m}$  (d). (e) Random-laser emission spectra of the 100  $\mu\text{m}$  wide channel and (f) the emission peak intensities of different paper-based channels at change of the injected pump energy. (g) Position of lasing peaks of two different devices (200  $\mu\text{m}$  wide channels and native paper) as function of the pump energy. Reproduced from Ref. [43] with permission from The Royal Society of Chemistry.

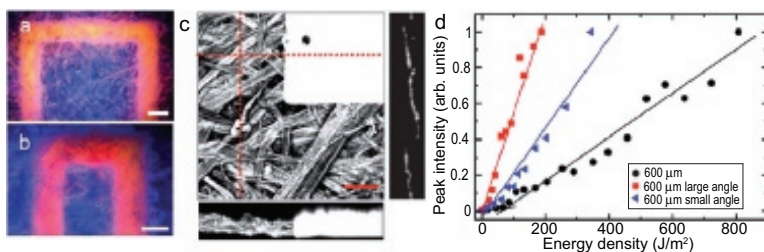


**Figure 4.14** Edge effects on random laser emission. (a,b) Optical images in true colors of differently spaced-edges filled with RhB. (c) Confocal image of a particular of the edge structure. The right and the bottom sides of the image report the  $yz$  single-slide section and the cumulative sum of  $xz$ -sections, respectively, with a resolution in  $z$  of about  $1\ \mu m$ . (d) Emission peak intensities of different edge-spaced channels are compared with a corresponding  $600\ \mu m$  wide linear one. Scale bars:  $500\ \mu m$  (a,b);  $100\ \mu m$  (c). Reproduced from Ref. [43] with permission from The Royal Society of Chemistry.

In particular, we observe that as the geometrical confinement increases, light goes through more scattering events, which amplify the photon generation and turn down the threshold [90, 138]. Moreover, the different levels of geometrical confinement, determined by the patterning of the intrinsically scattering paper (Fig. 4.13), operate a modulation of the wavelength in the emission peak. A red-shift in the random lasing peak is also detected as the geometrical confinement and the filling fraction of the paper increase. Finally, we have also highlighted the ability to modulate finely the emission characteristics by varying the shape of the lithographic channels (Fig. 4.14).

In summary, such a paper-based random-laser device attests a geometry-induced transition in random lasers: from random laser where the feedback mechanism is solely given by the scattering effect when it is not confined and in this sense called nonresonant, to random laser where the same material, constrained in microchannels with defined walls acting as cavity, shows a laser-like behavior because a secondary geometric feedback effect dominates, and for this reason named resonant random laser. In the presence of boundaries on the transverse direction, the scattering is strong since the waves cannot escape from the sides of the sample;

therefore, it is easy to achieve wave localization. In other words, the paper channels enhance the scattering effect and the light has a greater probability of returning to the coherence volume and interferes with itself and this gives the resonant behavior. All in all, the possibility of fabricating random laser on flexible, biodegradable, and low-cost substrates, such as paper, is a key issue for a successful integration in several systems and structures for a new-generation technology (such as sensing chips, coding documents or banknotes, intelligent packages). Importantly, the emission characteristics of random lasers, e.g., the lasing threshold reached when the optical gain of the laser medium is exactly balanced by the sum of all the losses experienced by light in the optical cavity, can be easily modulated by changing the geometry and the scattering strength of the random cavity and by tuning the gain distribution, for example, by acting on the shape of the pumping beam [12, 23, 123]. This is difficult to obtain in standard lasers where the cavity is rigid and well defined as well as the gain volume.

As a last application, we want to focus on the optimization of random-laser devices on polymeric interfaces. Promising results have been recently reported in the field of optofluidics. Combining optical devices with microfluidics, the properties of a random laser can be dynamically controlled with a microfluidic system, a versatility which is not readily available with solid-state optical components. Bhaktha et al. reported random lasing in a microfluidic device when filled with a Rhodamine 6G dye solution and pumped by a laser stripe (Fig. 4.15a). In this mirrorless optofluidic laser, the structural disorder is the result from limited accuracy of photolithographic process [39]. The authors demonstrated the spectral sensitivity of the laser emission on the pumped region inside the microchannel by changing the stripe position and length, and probe different parts of the random system (Fig. 4.15). Such a spatial dependence of the emission spectrum would not be seen in a single-mode distributed feedback laser based on multiple Bragg scattering. Besides, the sensing capability of such a device has been demonstrated by detecting the presence of different modes in the emission spectrum. The probed sensitivity of the spectrum to

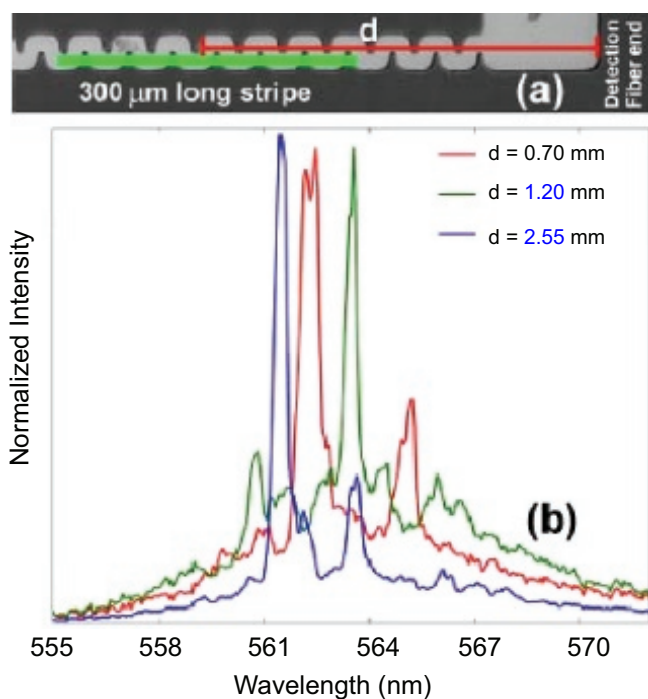


**Figure 4.15** Optofluidic random laser. (a) A  $300\text{ }\mu\text{m}$  long pump stripe is translated along the length of the channel, varying  $d$ , to study the spectral sensitivity of the random lasing modes to the pumped region. The spectra recorded for three different values of  $d$  are plotted in (b). Reproduced from Ref. [39] with permission from AIP Publishing.

local perturbation could have potential applications in multichannel sensing.

In conclusion, the microfluidic devices are conventionally used for flowing solutions of organic material [114]. Here, light has been manipulated at the microscale, forming attractive systems for lab-on-a-chip applications and opening avenues for smart sensing applications [139]. Finally, the infinite possibility of designs associated with the ease of fabrication makes the concept of optofluidic random laser attractive for optofluidic applications as well as a unique platform for investigating laser physics.

## References

1. Letokhov, V. S. (1968). Generation of light by a scattering medium with negative resonance absorption, *Sov. Phys. JETP* **26**, p. 835.
2. Gouédard, C., Husson, D., Sauteret, C., Auzel, F., and Migus, A. (1993). Generation of spatially incoherent short pulses in laser-pumped neodymium stoichiometric crystals and powders, *J. Opt. Soc. Am. B* **10**, p. 2358.
3. Lawandy, N. M., Balachandran, R. M., Gomes, A. S. L., and Sauvain, E. (1994). Laser action in strongly scattering media, *Nature* **368**, p. 436.
4. Anderson, P. W. (1985). The question of classical localization a theory of white paint? *Phil. Mag. B* **52**, 3, pp. 505–509.
5. Wiersma, D. S., Bartolini, P., Lagendijk, A., and Righini, R. (1997). Localization of light in a disordered medium, *Nature* **390**, 6661, pp. 671–673.
6. Abrahams, E., Anderson, P. W., Licciardello, D. C., and Ramakrishnan, T. V. (1979). Scaling theory of localization: Absence of quantum diffusion in two dimensions, *Phys. Rev. Lett.* **42**, pp. 673–676.
7. Apalkov, V. M., Raikh, M. E., and Shapiro, B. (2002). Random resonators and prelocalized modes in disordered dielectric films, *Phys. Rev. Lett.* **89**, p. 016802.
8. Chabanov, A. A., Zhang, Z. Q., and Genack, A. Z. (2003). Breakdown of diffusion in dynamics of extended waves in mesoscopic media, *Phys. Rev. Lett.* **90**, p. 203903.
9. Patra, M. (2003). Decay rate distributions of disordered slabs and application to random lasers, *Phys. Rev. E* **67**, p. 016603.
10. Skipetrov, S. E. and van Tiggelen, B. A. (2004). Dynamics of weakly localized waves, *Phys. Rev. Lett.* **92**, p. 113901.
11. Conti, C., Leonetti, M., Fratalocchi, A., Angelani, L., and Ruocco, G. (2008). Condensation in disordered lasers: Theory, 3D+1 simulations, and experiments, *Phys. Rev. Lett.* **101**, p. 143901.
12. Leonetti, M., Conti, C., and Lopez, C. (2011). The mode-locking transition of random lasers, *Nat. Photon.* **5**, 10, pp. 615–617.
13. Andreasen, J., Asatryan, A., Botten, L., Byrne, M., Cao, H., Ge, L., Labonté, L., Sebbah, P., Stone, A. D., Türeci, H., and Vanneste, C. (2011). Modes of random lasers, *Adv. Opt. Phot.* **3**, p. 88.
14. Fallert, J., Dietz, R. J. B., Sartor, J., Schneider, D., Klingshirn, C., and Kalt, H. (2009). Co-existence of strongly and weakly localized random laser modes, *Nat. Photon.* **3**, p. 279.

15. Sebbah, P. and Vanneste, C. (2002). Random laser in the localized regime, *Phys. Rev. B* **66**, p. 144202.
16. van der Molen, K. L., Tjerkstra, R. W., Mosk, A. P., and Lagendijk, A. (2007). Spatial extent of random laser modes, *Phys. Rev. Lett.* **98**, p. 143901.
17. Vanneste, C. and Sebbah, P. (2001). Selective excitation of localized modes in active random media, *Phys. Rev. Lett.* **87**, p. 183903.
18. Vanneste, C., Sebbah, P., and Cao, H. (2007). Lasing with resonant feedback in weakly scattering random systems, *Phys. Rev. Lett.* **98**, p. 143902.
19. Wu, X., Fang, W., Yamilov, A., Chabanov, A. A., Asatryan, A. A., Botten, L. C., and Cao, H. (2006). Random lasing in weakly scattering systems, *Phys. Rev. A* **74**, p. 053812.
20. Cao, H. (2003). Lasing in random media, *Wave Random Complex Media* **13**, 3, pp. R1–R39.
21. Siegman, A. E. (1987). *Lasers* (University Science Books, Oxford).
22. van der Molen, K. L., Mosk, A. P., and Lagendijk, A. (2006). Intrinsic intensity fluctuations in random lasers, *Phys. Rev. A* **74**, p. 053808.
23. Cao, H., Jiang, X., Ling, Y., Xu, J. Y., and Soukoulis, C. M. (2003). Mode repulsion and mode coupling in random lasers, *Phys. Rev. B* **67**, p. 161101.
24. Lepri, S. (2013). Fluctuations in a diffusive medium with gain, *Phys. Rev. Lett.* **110**, p. 230603.
25. Mujumdar, S., Türk, V., Torre, R., and Wiersma, D. S. (2007). Chaotic behavior of a random laser with static disorder, *Phys. Rev. A* **76**, p. 033807.
26. Raposo, E. P. and Gomes, A. S. L. (2015). Analytical solution for the Lévy-like steady-state distribution of intensities in random lasers, *Phys. Rev. A* **91**, 4, p. 043827.
27. Uppu, R. and Mujumdar, S. (2010). Statistical fluctuations of coherent and incoherent intensity in random lasers with nonresonant feedback, *Opt. Lett.* **35**, 17, pp. 2831–2833.
28. Antenucci, F., Conti, C., Crisanti, A., and Leuzzi, L. (2015). General phase diagram of multimodal ordered and disordered lasers in closed and open cavities, *Phys. Rev. Lett.* **114**, p. 043901.
29. Antenucci, F., Crisanti, A., and Leuzzi, L. (2015). The glassy random laser: Replica symmetry breaking in the intensity fluctuations of emission spectra, *Sci. Rep.* **5**, p. 16792.

30. Ghofraniha, N., Viola, I., Dimaria, F., Barbarella, G., Gigli, G., Leuzzi, L., and Conti, C. (2015). Experimental evidence of replica symmetry breaking in random lasers, *Nat. Comm.* **6**, p. 6058.
31. Noginov, M. A., Caulfield, H. J., Noginova, N. E., and Venkateswarlu, P. (1995). Line narrowing in the dye solution with scattering centers, *Opt. Commun.* **118**, p. 430.
32. Schuurmans, F. J., Vanmaekelbergh, D., van de Lagemaat, J., and Langendijk, A. (1999). Strongly photonic macroporous gallium phosphide networks, *Science* **284**, 5411, pp. 141–143.
33. Galisteo-López, J. F., Ibáñez, M., Sapienza, R., Froufe-Pérez, L., Blanco, A., and López, C. (2011). Self-assembled photonic structures, *Adv. Mater.* **23**, 1, pp. 30–69.
34. Gottardo, S., Sapienza, R., García, P. D., Blanco, A., Wiersma, D. S., and Lopez, C. (2008). Resonance-driven random lasing, *Nat. Phot.* **2**, pp. 429–432.
35. Zhai, T., Zhang, X., Pang, Z., Su, X., Liu, H., Feng, S., and Wang, L. (2011). Random laser based on waveguided plasmonic gain channels, *Nano Lett.* **11**, 10, pp. 4295–4298.
36. Chen, Y., Herrnsdorf, J., Guilhabert, B., Zhang, Y., Watson, I. M., Gu, E., Laurand, N., and Dawson, M. D. (2011). Colloidal quantum dot random laser, *Opt. Express* **19**, 4, pp. 2996–3003.
37. De Matos, C. J. S., de S. Menezes, L., Brito-Silva, A. M., Martínez Gámez, M. A., Gomes, A. S. L., and de Araújo, C. B. (2007). Random fiber laser, *Phys. Rev. Lett.* **99**, p. 153903.
38. Turitsyn, S. K., Babin, S. A., El-Taher, A. E., Harper, P., Churkin, D. V., Kablukov, S. I., Ania-Castanon, J. D., Karalekas, V., and Podivilov, E. V. (2010). Random distributed feedback fibre laser, *Nat. Photon.* **4**, pp. 231–235.
39. Bhaktha, B. N. S., Bachelard, N., Noblin, X., and Sebbah, P. (2012). Optofluidic random laser, *Appl. Phys. Lett.* **101**, 15, p. 151101.
40. Tiwari, A. K., Uppu, R., and Mujumdar, S. (2012). Aerosol-based coherent random laser, *Opt. Lett.* **37**, 6, pp. 1053–1055.
41. Folli, V., Ghofraniha, N., Puglisi, A., Leuzzi, L., and Conti, C. (2013). Time-resolved dynamics of granular matter by random laser emission, *Sci. Rep.* **3**, p. 2251.
42. Ghofraniha, N., Viola, I., Zacheo, A., Arima, V., Gigli, G., and Conti, C. (2013). Transition from nonresonant to resonant random lasers by the geometrical confinement of disorder, *Opt. Lett.* **38**, 23, pp. 5043–5046.

43. Viola, I., Ghofraniha, N., Zacheo, A., Arima, V., Conti, C., and Gigli, G. (2013). Random laser emission from a paper-based device, *J. Mater. Chem. C* **1**, pp. 8128–8133.
44. Wang, C.-S., Chang, T.-Y., Lin, T.-Y., and Chen, Y.-F. (2014). Biologically inspired flexible quasi-single-mode random laser: An integration of Pieris canidia butterfly wing and semiconductors, *Sci. Rep.* **4**, p. 6736.
45. Cao, H., Zhao, Y. G., Ho, S. T., Seelig, E. W., Wang, Q. H., and Chang, R. P. H. (1999). Random laser action in semiconductor powder, *Phys. Rev. Lett.* **82**, pp. 2278–2281.
46. Leonetti, M., Conti, C., and López, C. (2013). Dynamics of phase-locking random lasers, *Phys. Rev. A* **88**, p. 043834.
47. Störzer, M., Gross, P., Aegeerter, C. M., and Maret, G. (2006). Observation of the critical regime near Anderson localization of light, *Phys. Rev. Lett.* **96**, p. 063904.
48. Wiersma, D. S., van Albada, M. P., van Tiggelen, B. A., and Lagendijk, A. (1995). Experimental evidence for recurrent multiple scattering events of light in disordered media, *Phys. Rev. Lett.* **74**, pp. 4193–4196.
49. Gottardo, S., Cavalieri, S., Yaroshchuk, O., and Wiersma, D. S. (2004). Quasi-two-dimensional diffusive random laser action, *Phys. Rev. Lett.* **93**, p. 263901.
50. Wiersma, D. S. and Cavalieri, S. (2011). Light emission: A temperature-tunable random laser, *Nature* **414**, pp. 708–709.
51. Polson, R. C. and Vardeny, Z. V. (2004). Random lasing in human tissues, *Appl. Phys. Lett.* **85**, 7, pp. 1289–1291.
52. Song, Q., Xiao, S., Xu, Z., Liu, J., Sun, X., Drachev, V., Shalaev, V. M., Akkus, O., and Kim, Y. L. (2010). Random lasing in bone tissue, *Opt. Lett.* **35**, 9, pp. 1425–1427.
53. Redding, B., Ahmadi, P., Mokan, V., Seifert, M., Choma, M. A., and Cao, H. (2015). Low-spatial-coherence high-radiance broadband fiber source for speckle free imaging, *Opt. Lett.* **40**, 20, pp. 4607–4610.
54. Redding, B., Choma, M. A., and Cao, H. (2012). Speckle-free laser imaging using random laser illumination, *Nat. Phot.* **6**, p. 355.
55. Barbarella, G., Melucci, M., and Sotgiu, G. (2005). The versatile thiophene: An overview of recent research on thiophene-based materials, *Adv. Mater.* **17**, p. 1581.
56. Horowitz, G. (2004). Organic thin film transistors: From theory to real devices, *J. Mater. Res.* **19**, pp. 1946–1962.

57. Kelley, T. W., Baude, P. F., Gerlach, C., Ender, D. E., Muyres, D., Haase, M. A., Vogel, D. E., and Theiss, S. D. (2004). Recent progress in organic electronics: Materials, devices, and processes, *Chem. Mater.* **16**, pp. 4413–4422.
58. Sheats, J. (2004). Manufacturing and commercialization issues in organic electronics, *J. Mater. Res.* **19**, pp. 1974–1989.
59. Forrest, S. (2004). The path to ubiquitous and low-cost organic electronic appliances on plastic, *Nature* **428**, p. 911.
60. Kitamura, M., Imada, T., and Arakawa, Y. (2003). Organic light-emitting diodes driven by pentacene-based thin-film transistors, *Appl. Phys. Lett.* **83**, p. 3410.
61. Vaeth, K. M. (2003). Organic light-emitting diode display technology, *Inform. Display* **19**, pp. 12–17.
62. Shtein, M., Mapel, J., Benziger, J. B., and Forrest, S. R. (2002). Effects of film morphology and gate dielectric surface preparation on the electrical characteristics of organic-vapor-phase-deposited pentacene thin-film transistors, *Appl. Phys. Lett.* **81**, pp. 268–270.
63. Granström, M., Petritsch, K., Arias, A. C., Lux, A., Andersson, M. R., and Friend, R. H. (1998). Laminated fabrication of polymeric photovoltaic diodes, *Nature* **395**, pp. 257–260.
64. Peumans, P. and Forrest, S. R. (2001). Very-high-efficiency double-heterostructure copper phthalocyanine/C<sub>60</sub> photovoltaic cells, *Appl. Phys. Lett.* **79**, p. 126–128.
65. Peumans, P., Uchida, S., and Forrest, S. R. (2003). Efficient bulk heterojunction photovoltaic cells using small-molecular-weight organic thin films, *Nature* **425**, pp. 158–162.
66. Samuel, I. and Turnbull, G. (2007). Organic semiconductor lasers, *Chem. Rev.* **107**, p. 1272.
67. Moses, D. (1992). High quantum efficiency luminescence from a conducting polymer in solution: A novel polymer laser dye, *Appl. Phys. Lett.* **60**, p. 3215.
68. Frolov, S. V., Ozaki, M., Gellermann, W., Vardeny, Z. V., and Yoshino, K. (1996). Mirrorless lasing in conducting polymer poly(2,5-dioctyloxy-p-phenylenevinylene) films, *Jpn. J. Appl. Phys.* **35**, p. L1371.
69. Hide, F., Diaz-Garcia, M. A., Schwartz, B. J., Andersson, M. R., Pei, Q., and Heeger, A. J. (1996). Semiconducting polymers: A new class of solid state laser materials, *Science* **273**, p. 1833.

70. Holzer, W., Penzkofer, A., Gong, S. H., Bleyer, A., and Bradley, D. (1996). Laser action in poly (*m*-phenylenevinylene-co-2, 5-dioctoxy-*p*-phenylenevinylene), *Adv. Mater.* **8**, pp. 974–978.
71. Tessler, N., Denton, G. J., and Friend, R. H. (1996). Lasing from conjugated-polymer microcavities, *Nature* **382**, pp. 695–697.
72. Schweitzer, B., Wegmann, G., Giessen, H., Hertel, D., Bassler, H., Mahrt, R. F., Scherf, U., and Mullen, K. (1998). The optical gain mechanism in solid conjugated polymers, *Appl. Phys. Lett.* **72**, 23, pp. 2933–2935.
73. Hoeben, F. J., Jonkheijm, P., Meijer, E. W., and Schenning, A. P. (2005). About supramolecular assemblies of pi-conjugated systems, *Chem. Rev.* **105**, p. 1491.
74. McGehee, M. D. and Heeger, A. J. (2000). Semiconducting (conjugated) polymers as materials for solid-state lasers, *Adv. Mater.* **22**, p. 1655–1668.
75. Riedl, T., Rabe, T., Johannes, H., Kowalsky, W., Wang, J., Weimann, T., Hinze, P., Nehls, B., Farrell, T., and Scherf, U. (2006). Tunable organic thin-film laser pumped by an inorganic violet diode laser, *Appl. Phys. Lett.* **88**, p. 241116.
76. Sheridan, A. K., Turnbull, G. A., Safonov, A. N., and Samuel, I. D. W. (2000). Tuneability of amplified spontaneous emission through control of the waveguide-mode structure in conjugated polymer films, *Phys. Rev. B* **62**, p. 11929.
77. Xia, R. D., Heliotis, G., and Bradley, D. D. C. (2003). Fluorene-based polymer gain media for solid-state laser emission across the full visible spectrum, *Appl. Phys. Lett.* **82**, pp. 3599–3601.
78. Inganäs, O., Granlund, T., Theander, M., Berggren, M., Andersson, M. R., Ruseekas, A., and Sundström, V. (1998). Optical emission from confined poly(thiophene) chains, *Opt. Mater.* **9**, pp. 104–108.
79. Pope, M. and Swenberg, C. E. (1999). *Electronic Processes in Organic Crystals and Polymers* (Oxford University Press, New York).
80. Tang, C. W., VanSlyke, S. A. and Chen, C. H. (1989). Electroluminescence of doped organic thin films, *J. Appl. Phys.* **65**, pp. 3610–3616.
81. Mujumdar, S., Ricci, M., Torre, R., and Wiersma, D. S. (2004). Amplified extended modes in random lasers, *Phys. Rev. Lett.* **93**, p. 053903.
82. Polson, R. C. and Vardeny, Z. V. (2005). Organic random lasers in the weak-scattering regime, *Phys. Rev. B* **71**, p. 045205.
83. Tulek, A. and Vardeny, Z. V. (2010). Studies of random laser action in p-conjugated polymers, *J. Optics* **12**, 2, p. 024008.

84. Anglos, D., Stassinopoulos, A., Das, R. N., Zacharakis, G., Psyllaki, M., Jakubiak, R., Vaia, R. A., Giannelis, E. P., and Anastasiadis, S. H. (2004). Random laser action in organic-inorganic nanocomposites, *J. Opt. Soc. Am. B* **21**, pp. 208–213.
85. Andreev, A., Quochi, F., Cordella, F., Mura, A., Bongiovanni, G., Sitter, H., Hlawacek, G., Teichert, C., and Sariciftci, N. S. (2006). Coherent random lasing in the deep-blue from self-assembled organic nanofibers, *J. Appl. Phys.* **99**, 3, p. 034305.
86. Quochi, F., Cordella, F., Orrù, R., Communal, J. E., Verzeroli, P., Mura, A., Bongiovanni, G., Andreev, A., Sitter, H., and Sariciftci, N. S. (2004). Random laser action in self-organized para-sexiphenyl nanofibers grown by hot-wall epitaxy, *Appl. Phys. Lett.* **84**, pp. 4454–4456.
87. Quochi, F., Cordella, F., Mura, A., Bongiovanni, G., Balzer, F., and Rubahn, H.-G. (2006). Gain amplification and lasing properties of individual organic nanofibers, *Appl. Phys. Lett.* **88**, 4, p. 041106.
88. Anni, M., Lattante, S., Stomeo, T., Cingolani, R., Gigli, G., Barbarella, G., and Favaretto, L. (2004). Modes interaction and light transport in bidimensional organic random lasers in the weak scattering limit, *Phys. Rev. B* **70**, p. 195216.
89. Barbarella, G., Zambianchi, M., Antolini, L., Ostoja, P., Maccagnani, P., Bongini, A., Marseglia, E., Tedesco, E., Gigli, G., and Cingolani, R. (1999). Solid-state conformation, molecular packing, and electrical and optical properties of processable beta-methylated sexithiophenes, *J. Am. Chem. Soc.* **121**, pp. 8920–8926.
90. Ghofraniha, N., Viola, I., Maria, F. D., Barbarella, G., Gigli, G., and Conti, C. (2013). Random laser from engineered nanostructures obtained by surface tension driven lithography, *Laser Photon. Rev.* **7**, 3, pp. 432–438.
91. Pisignano, D., Anni, M., Gigli, G., Cingolani, R., Zavelani-Rossi, M., Lanzani, G., Barbarella, G., and Favaretto, L. (2002). Amplified spontaneous emission and efficient tunable laser emission from a substituted thiophene-based oligomer, *Appl. Phys. Lett.* **81**, 19, pp. 3534–3536.
92. Ciesielski, A., Palma, C., Bonini, M., and Samorì, P. (2010). Towards supramolecular engineering of functional nanomaterials: Pre-programming multi-component 2d self-assembly at solid-liquid interfaces, *Adv. Mater.* **22**, 32, pp. 3506–3520.
93. De Wild, M., Berner, S., Suzuki, H., Ramoino, L., Baratoff, A., and Junga, T. A. (2003). Molecular assembly and self-assembly: Molecular

- nanoscience for future technologies, *Ann. N Y Acad. Sci.* **1006**, 1, pp. 291–305.
- 94. Chang, S., Liu, J., Bharathan, J., Yang, Y., Onohara, J., and Kido, J. (1999). Multicolor organic light-emitting diodes processed by hybrid inkjet printing, *Adv. Mater.* **11**, pp. 734–737.
  - 95. Hebner, T. R., Wu, C. C., Marcy, D., Lu, M. H., and Sturm, J. C. (1998). Inkjet printing of doped polymers for organic light-emitting devices, *Appl. Phys. Lett.* **72**, pp. 519–521.
  - 96. Renak, M. L., Bazan, G. C., and Roitman, D. (1997). Microlithographic process for patterning conjugated emissive polymers, *Adv. Mater.* **9**, pp. 392–395.
  - 97. Rogers, J. A., Bao, Z., and Dhar, L. (1998). Fabrication of patterned electroluminescent polymers that emit in geometries with feature sizes into the submicron range, *Appl. Phys. Lett.* **73**, p. 294.
  - 98. Ichikawa, M., Hibino, R., Inoue, M., Haritani, T., Hotta, S., Araki, K., Koyama, T., and Taniguchi, Y. (2005). Laser oscillation in monolithic molecular single crystals, *Adv. Mater.* **17**, 17, pp. 2073–2077.
  - 99. Mizuno, H., Ohnishi, I., Yanagi, H., Sasaki, F., and Hotta, S. (2012). Lasing from epitaxially oriented needle crystals of a thiophene/phenylene co-oligomer, *Adv. Mater.* **24**, 18, pp. 2404–2408.
  - 100. Fujiwara, S., Bando, K., Masumoto, Y., Sasaki, F., Kobayashi, S., Haraichi, S., and Hotta, S. (2007). Laser oscillations of whispering gallery modes in thiophene/phenylene co-oligomer microrings, *Appl. Phys. Lett.* **91**, 2, p. 021104.
  - 101. Sasaki, F., Kobayashi, S., Haraichi, S., Fujiwara, S., Bando, K., Masumoto, Y., and Hotta, S. (2007). Microdisk and microring lasers of thiophene-phenylene co-oligomers embedded in Si/SiO<sub>2</sub> substrates, *Adv. Mater.* **19**, 21, pp. 3653–3655.
  - 102. Fang, H.-H., Ding, R., Lu, S.-Y., Yang, J., Zhang, X.-L., Yang, R., Feng, J., Chen, Q.-D., Song, J.-F., and Sun, H.-B. (2012). Distributed feedback lasers based on thiophene/phenylene co-oligomer single crystals, *Adv. Func. Mater.* **22**, 1, pp. 33–38.
  - 103. Anni, M., Lattante, S., Cingolani, R., Gigli, G., Barbarella, G., and Favaretto, L. (2003). Far-field emission and feedback origin of random lasing in oligothiopene dioxide neat films, *Appl. Phys. Lett.* **83**, p. 2754.
  - 104. Frolov, S. V., Vardeny, Z., Yoshino, K., Zakhidov, A., and Baugman, R. (1999). Stimulated emission in high-gain organic media, *Phys. Rev. B* **59**, p. R5284.

105. Polson, R., Raikh, M., and Vardeny, Z. (2002). Random lasing from weakly scattering media; spectrum universality in D0O-PPV polymer films, *Physica E* **12**, p. 1240.
106. Wiersma, D. S. (2008). The physics and applications of random lasers, *Nature Phys.* **4**, p. 359.
107. Cavallini, M., Albonetti, C., and Biscarini, F. (2009). Nanopatterning soluble multifunctional materials by unconventional wet lithography, *Adv. Mater.* **21**, pp. 1043–1053.
108. Ballardini, R., Balzani, V., Credi, A., Gandolfi, M., and Venturi, M. (2001). Artificial molecular-level machines: Which energy to make them work? *Acc. Chem. Res.* **34**, 6, pp. 445–455.
109. Viola, I., Della Sala, F., Piacenza, M., Favaretto, L., Gazzano, M., Anni, M., Barbarella, G., Cingolani, R., and Gigli, G. (2007). Bicolor pixels from a single active molecular material by surface tension-driven deposition, *Adv. Mater.* **19**, pp. 1597–1602.
110. Viola, I., Mazzeo, M., Passabí, A., D'Amone, S., Cingolani, R., and Gigli, G. (2005). Positive/negative arrays of organic light-emitting diodes by a surface tension-driven approach, *Adv. Mater.* **17**, 24, pp. 2935–2939.
111. Viola, I., Piliego, C., Favaretto, L., Barbarella, G., Cingolani, R., and Gigli, G. (2010). Bicolor electroluminescent pixels from single active molecular material, *ACS Appl. Mater. Inter.* **2**, pp. 484–490.
112. Cavallini, M., Lazzaroni, R., Zamboni, R., Biscarini, F., Timpel, D., Zerbetto, F., Clarkson, G., and Leigh, D. (2001). Conformational self-recognition as the origin of dewetting in bistable molecular surfaces, *J. Phys. Chem. B* **105**, 44, p. 10826.
113. Karthaus, O., Adachi, C., Kurimura, S., and Oyamada, T. (2004). Electroluminescence from self-organized microdomes, *Appl. Phys. Lett.* **84**, 23, pp. 4696–4698.
114. Xia, Y. and Whitesides, G. M. (1998). Soft lithography, *Angew. Chem. Int. Ed.* **37**, pp. 550–575.
115. Sharma, A. (1993). Relationship of thin film stability and morphology to macroscopic parameters of wetting in the apolar and polar systems, *Langmuir* **9**, pp. 861–869.
116. Zhao, X. M., Xia, Y., and Whitesides, G. M. (1997). Soft lithographic methods for nano-fabrication, *J. Mater. Chem.* **7**, pp. 1069–1074.
117. Cavallini, M., Biscarini, F., Massi, M., Farran-Morales, A., Leigh, D. A., and Zerbetto, F. (2002). Spontaneous fabrication of microscopic arrays of molecular structures with submicron length scales, *Nano Lett.* **2**, p. 635.

118. Pisignano, D., Mele, E., Persano, L., Gigli, G., Visconti, P., Cingolani, R., Barbarella, G., and Favaretto, L. (2004). Full organic distributed feedback cavities based on a soluble electroluminescent oligothiophene, *Phys. Rev. B* **70**, p. 205206.
119. Wiersma, D. S., van Albada, M. P., and Lagendijk, A. (1995). Random laser, *Nature* **373**, p. 203.
120. Bongini, A., Barbarella, G., Favaretto, L., Sotgiu, G., Zambianchi, M., and Casarini, D. (2011). Tuning solid-state photoluminescence frequencies and efficiencies of oligomers containing one central thiophene-s,s-dioxide unit, *Tetrahedron* **58**, p. 10151.
121. Mézard, M., Parisi, G., and Virasoro, M. (1987). *Spin Glass Theory and Beyond* (World Scientific, Singapore).
122. Young, A. P. (1997). *Spin Glasses and Random Fields* (University of California, Santa Cruz World Scientific).
123. Wiersma, D. S. (2013). Disordered photonics, *Nat. Photon.* **7**, 3, pp. 188–196.
124. Conti, C. and Leuzzi, L. (2011). Complexity of waves in nonlinear disordered media, *Phys. Rev. B* **83**, p. 134204.
125. Debenedetti, P. G. and Stillinger, F. H. (2013). Supercooled liquids and the glass transition, *Nature* **410**, p. 259.
126. Gordon, A. and Fischer, B. (2002). Phase transition theory of many-mode ordering and pulse formation in lasers, *Phys. Rev. Lett.* **89**, 10, p. 103901.
127. Klaers, J., Schmitt J., Vewinger, F., and Weitz, M. (2010). Bose–Einstein condensation of photons in an optical microcavity, *Nature* **468**, 7323, pp. 545–548.
128. El-Dardiry, R. G. S., Mooiweer, R., and Lagendijk, A. (2012). Experimental phase diagram for random laser spectra, *New J. Phys.* **14**, 11, p. 113031.
129. Türeci, H. E., Li, G., Rotter, S., and Stone, A. D. (2008). Strong interactions in multimode random lasers, *Science* **320**, 5876, pp. 643–646.
130. Chen, Y.-C., Wang, C.-S., Chang, T.-Y., Lin, T.-Y., Lin, H.-M., and Chen, Y.-F. (2015). Ultraviolet and visible random lasers assisted by diatom frustules, *Opt. Express* **23**, 12, pp. 16224–16231.
131. Da Silva, R. R., Dominguez, C. T., dos Santos, M. V., Barbosa-Silva, R., Cavicchioli, M., Christovan, L. M., de Melo, L. S. A., Gomes, A. S. L., de Araujo, C. B., and Ribeiro, S. J. L. (2013). Silk fibroin biopolymer films

- as efficient hosts for DFB laser operation, *J. Mater. Chem. C* **1**, 43, pp. 7181–7190.
- 132. Zhang, R., Knitter, S., Liew, S. F., Omenetto, F. G., Reinhard, B. M., Cao, H., and Dal Negro, L. (2016). Plasmon-enhanced random lasing in biocompatible networks of cellulose nanofibers, *Appl. Phys. Lett.* **108**, 1, p. 011103.
  - 133. Camposeo, A., Del Carro, P., Persano, L., Cyprych, K., Szukalski, A., Sznitko, L., Mysliwiec, J., and Pisignano, D. (2014). Physically transient photonics: Random versus distributed feedback lasing based on nanoimprinted DNA, *ACS Nano* **8**, 10, pp. 10893–10898.
  - 134. Martinez, A. W., Phillips, S. T., and Whitesides, G. M. (2008). Three-dimensional microfluidic devices fabricated in layered paper and tape, *Proc. Natl. Acad. Sci. U. S. A.* **105**, 50, p. 19606.
  - 135. Mazzeo, A., Kalb, W., Chan, L., Killian, M., Bloch, J.-F., Mazzeo, B., and Whitesides, G. (2012). Paper-based, capacitive touch pads, *Adv. Mater.* **24**, 21, pp. 2850–2856.
  - 136. Tobjörk, D. and Österbacka, R. (2011). Paper electronics, *Adv. Mater.* **23**, 17, pp. 1935–1961.
  - 137. Määttänen, A., Fors, D., Wang, S., Valtakari, D., Ihlainen, P., and Peltonen, J. (2011). Paper-based planar reaction arrays for printed diagnostics, *Sensors Actuat. B Chem.* **160**, 1, pp. 1404–1412.
  - 138. Wu, X., Yamilov, A., Noh, H., Cao, H., Seelig, E. W., and Chang, R. P. H. (2004). Random lasing in closely packed resonant scatterers, *J. Opt. Soc. Am. B* **21**, 1, p. 159.
  - 139. Monat, C., Domachuk, P., and Eggleton, B. J. (2007). Integrated optofluidics: A new river of light, *Nature Photon.* **1**, p. 106.

## Chapter 5

# Cavity–Matter Interaction in Weak- and Strong-Coupling Regime: From White OLEDs to Organic Polariton Lasers

Marco Mazzeo,<sup>a,b</sup> Fabrizio Mariano,<sup>a</sup> Armando Genco,<sup>a,c</sup>  
Claudia Triolo,<sup>d</sup> and Salvatore Patanè<sup>d</sup>

<sup>a</sup>*Dipartimento di Matematica e Fisica “Ennio De Giorgi”, Università del Salento,  
Via per Arnesano, 73100 Lecce, Italy*

<sup>b</sup>*Istituto di Nanotecnologia, CNR-Nanotec, Via Arnesano 16, 73100 Lecce, Italy*

<sup>c</sup>*Center for Bio-Molecular Nanotechnology, Fondazione Istituto Italiano di Tecnologia,  
Via Barsanti, 73010 Arnesano (Lecce), Italy*

<sup>d</sup>*Dipartimento di Fisica e Scienze della Terra, Università di Messina, Viale F. Stagno  
d’Alcontres 31, 98166 Messina, Italy*

[marco.mazzeo@unisalento.it](mailto:marco.mazzeo@unisalento.it)

The interaction between quantum coupled systems is ubiquitous in physics and is becoming an interesting tool in several applications where the coupling takes place between light and matter. Light-matter interaction can be managed, for example, by coupling an emitting dipole with an optical resonator such as a Fabry-Pérot microcavity made by metallic or dielectric mirrors. According to the coupling level, several phenomena take place, such as a modification of the radiative rate emission from the dipole (Purcell effect) or the generation of new quantum states called polaritons (strong-coupling interaction). In this chapter, we will discuss the

---

*Organic Lasers: Fundamentals, Developments, and Applications*

Edited by Marco Anni and Sandro Lattante

Copyright © 2018 Pan Stanford Publishing Pte. Ltd.

ISBN 978-981-4774-46-8 (Hardcover), 978-1-315-10233-7 (eBook)

[www.panstanford.com](http://www.panstanford.com)

physics of weak- and strong-coupling light–matter regimes between light and organic molecules with a special focus on organic electroluminescent device applications.

In the weak-coupling regime, the Purcell effect may allow for the management of light distribution and the increase in overall efficiency. The microcavities can be integrated in an electrical architecture that simultaneously would allow for light confinement and charge carrier injection. As we will show, microcavity resonators can be theoretically exploited to realize electrically injected organic lasers. Nevertheless, despite the Purcell effect, the amount of current density that must be employed to reach the lasing threshold is behind the thermal capacity of organic lasers. For this reason, organic lasers by electrical injection are still a dream. The strong-coupling regime may help to reach this technological target. Organic polaritons, the hybrid particles between photons and excitons emerging from the strong-coupling interaction, are able to undergo the quantum phase transition of Bose–Einstein condensation (BEC) at room temperature. From this state, they can emit light coherently, like a standard laser, but from spontaneous emission decay. Therefore, organic microcavities in the strong-coupling regime are very promising for the realization of low-threshold electrically injected organic polariton lasers.

In Fig. 5.1, a schematic representation of the devices is reported according to the amount of external pumping power of the organic material (by optical or electrical generation of excitons) and to the strength of the light–matter coupling  $g$ . In weak-coupling regime (when  $g$  is negligible) and at low power density, we find standard light-emitting diodes, which emit incoherent photons owing to electroluminescence process; then increasing the power population inversion and stimulated emission can be reached (organic solid-state laser devices). In strong-coupling regime, LEDs operate emitting photons from polariton states, which in principle could be driven with higher powers to reach the BEC quantum phase transition at lower threshold levels compared to standard lasers operating in the weak-coupling regime. Improving the light–matter coupling further on, new quantum electro-dynamical effects, due to virtual photons, can take place even in electroluminescence [ultrastrong-coupling (USC) regime]. After an introduction on the

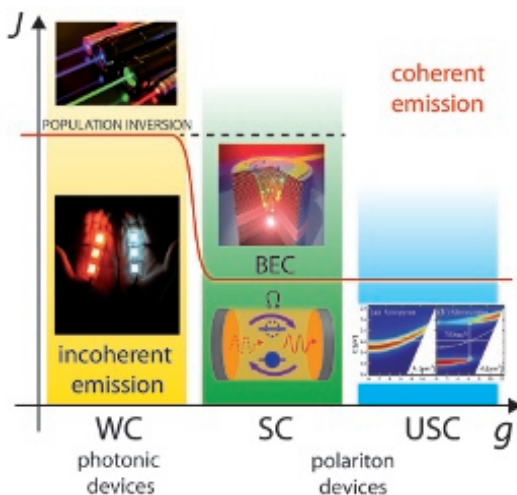


**Figure 5.1** Summary graph of the optoelectronic devices that work at different excitation power  $J$  (optical or electrical) and varying the light–matter coupling  $g$  from weak to ultrastrong coupling. The red line is the excitation power threshold for coherent emission: Exploiting polaritons in the BEC phase, it can be sensitively reduced.

classical and quantum theory about light–matter interactions, we will discuss three kinds of devices and related applications: white OLEDs in weak coupling for lighting, polariton light-emitting diodes under strong and USC regime, and organic polariton lasers.

## 5.1 Light–Matter Coupling: Classical and Quantum Theory

### 5.1.1 A Classical Toy Model

From a general point of view, the interaction between light (cavity) and matter (molecules or atoms) can be thought as two harmonic oscillators, coupled by a spring (the coupling term), which exchange energy with each other at a frequency  $\Omega$  [1]. The following discussion can be applied as a general tool for all the physical coupled systems, that is from coupled oscillators

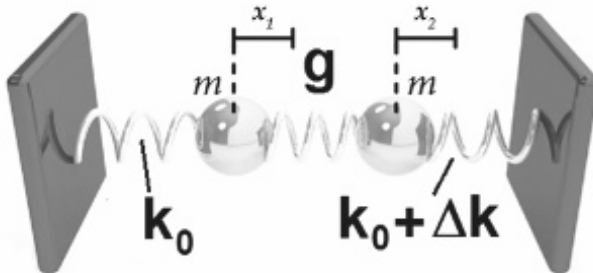


**Figure 5.2** Toy mode for light-matter coupling viewed as two coupled mechanical oscillators.

(mechanical coupled systems) to coupled atoms forming molecules with bonding and antibonding levels (orbital hybridization), from the coupling between molecular excited states and light (exciton–photon polaritons) to coupling between light and mechanical oscillations (optomechanics). In this model, each oscillator is also coupled to the environment, which causes the damping of the oscillations. If the damping rates  $\gamma_1$  and  $\gamma_2$  of the two oscillators are larger than the exchange energy rate  $\Omega$ , the system works in the weak-coupling regime; otherwise, it goes into the strong-coupling regime. In the former case, the oscillation frequencies are only slightly perturbed. On the contrary, in the strong-coupling regime, there is a perturbation of frequencies, proportional to the coupling, thus forming new eigenmodes that can be described as a mix of the uncoupled states. The coupled oscillators have a mass  $m$  and an elastic constant  $k_0$  and  $k_0 + \Delta k$ , respectively, and they are coupled by a spring with an elastic constant  $g$  (Fig. 5.2) [1].

In the absence of coupling ( $g = 0$ ), the two oscillators shown in Fig. 5.2 have the following eigen-frequencies

$$\omega_A = \sqrt{k_0/m} \quad (5.1)$$

and

$$\omega_B = \sqrt{(k_0 + \Delta k)/m} \quad (5.2)$$

When the systems are coupled by a spring ( $g > 0$ ), the eigen-frequencies change into the following values:

$$\omega_{\pm}^2 = \frac{1}{2} \left[ \omega_A^2 + \omega_B^2 \pm \sqrt{(\omega_A^2 - \omega_B^2)^2 + 4\Gamma^2\omega_A\omega_B} \right] \quad (5.3)$$

where  $\omega_A = \sqrt{(k_0 + g)/m}$  and  $\omega_B = \sqrt{(k_0 + \Delta k + g)/m}$ . Here the parameter  $\Gamma$  is related to the Rabi frequency and the uncoupled oscillator frequency by:

$$\Gamma = \frac{\Omega}{\sqrt{\omega_A \omega_B}} \quad (5.4)$$

Here  $\Omega = g/m$  represents the rate of energy exchange between the two oscillators, and it is called Rabi frequency. If the values of  $g$  are negligible (weak-coupling perturbative regime),  $\Gamma$  is zero and the frequency of each oscillator is not influenced by the other (Fig. 5.3a); as a consequence, each oscillator will have unperturbed frequency dispersion. When  $g$  is increased, a frequency gap is opened at the intersection point between the frequency dispersion curves (namely the anticrossing point where  $\omega_A = \omega_B$ ), the amount of the gap being equal to  $\Gamma$

$$\omega_+ - \omega_- = \Gamma \quad (5.5)$$

In other words, the splitting between the eigenmodes increases with the coupling  $g$ . The introduction of damping, which in the previous discussion has been neglected, gives rise to complex frequency eigenvalues in which the imaginary part represents the losses of the oscillations. If the damping of the two oscillators exceeds the critical value, the dispersion curves in Fig. 5.3b become broader and the visibility of the splitting smaller. The critical value useful to see the new dispersion branches is given by the following relationship:

$$\frac{\Gamma}{\gamma_1/m + \gamma_2/m} > 1 \quad (5.6)$$

This relationship indicates that the damping rates over mass must be smaller than the Rabi frequency to reach the visibility of the splitting. We can fit this classical model to any coupled oscillator (cavity-exciton, cavity-mechanical vibration, etc.), once all the parameters are redefined according to the type of oscillators involved in the coupling. In particular, for a radiative dipole coupled to a cavity resonator, the damping rates are the dephasing rate  $\gamma_{\text{exc}}$  of the excited states of molecular excitons, and the photon escape rate  $\gamma_{\text{cav}}$  of the resonator.

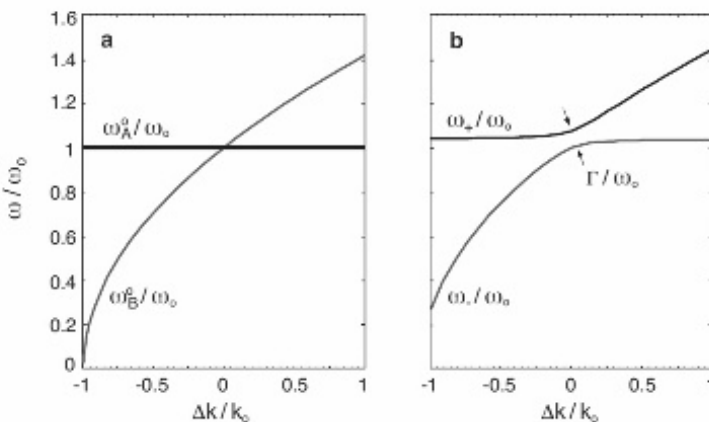


**Figure 5.3** (a) Eigen-frequencies of two uncoupled oscillators with coupling elastic constant  $g = 0$  (see the text) and constant  $k_0$  and  $k_0 + \Delta k$ . (b) The effect of strong coupling ( $g \neq 0$ ) on the separation of the frequencies dispersion. Reproduced from Ref. [1] with the permission of the American Association of Physics Teachers.

### 5.1.2 Optical Resonators: The Case of Optical Microcavity

A typical example of an optical resonator is the planar microcavity (or Fabry-Pérot structure). It consists (Fig. 5.4) of a vertical architecture containing a dielectric material placed between two highly reflective mirrors. Mirrors may consist of metallic films or a succession of  $\lambda/4$  layers of dielectric materials with different refractive index, which form a distributed Bragg reflector (DBR) and confine the electromagnetic (EM) waves owing to multiple reflections inside the optical structure. The advantages of the DBR compared to a metal mirror are: (i) lower absorption losses; (ii) variable reflectivity window according to the design; and (iii) very high reflectivity leading to high cavity finesse. The resonant optical modes within an optical cavity have characteristic lineshapes and wavelength spacing. Moreover, the optical response of the microcavity depends on the distance  $L_{\text{cav}}$  between the mirrors. If  $L_{\text{cav}}$  is only a few wavelengths of the incident light, the resulting cavity modes are equally spaced in frequency, apart from the shifts due to the phase variation arising from the reflection on each mirror.

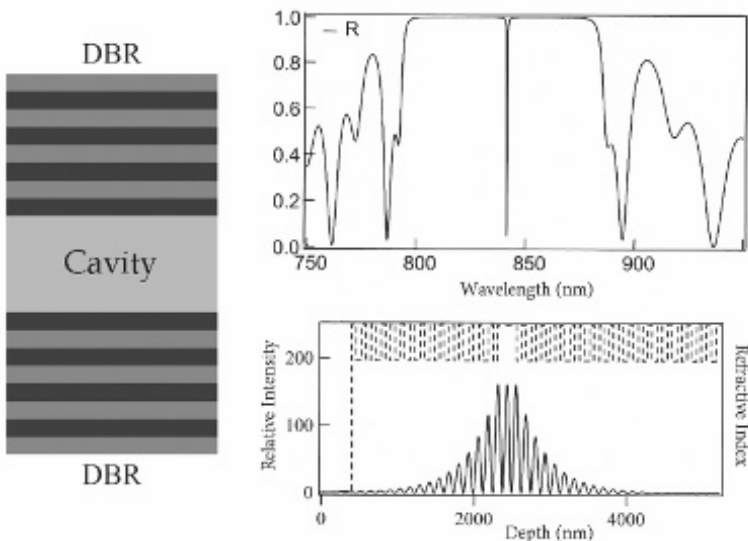


**Figure 5.4** Refractive index profile and EM field penetration (bottom) and reflectivity spectrum (top) of a  $\lambda$ -cavity (left). Figure adapted from Ref. [2].

Figure 5.4 shows the refractive index profile of the DBR layers and the reflectivity spectrum of an optical microcavity. The area of maximum reflectivity is called stopband.

A microcavity made by DBR mirrors can also be viewed as a 1D photonic crystal that, owing to the periodic refractive index, opens a gap in the allowed photon frequency. The buffer thickness ( $L_{\text{buf}}$ ) plays the role of a defect in the periodic structure, thus forming a defect state in the stopband, as well as in the periodic atomic crystal where different atomic species have been introduced in the lattice.

For a large number of pairs,  $N$ , the DBR reflectivity  $R$  at the center of the stopband can be approximated by [3]

$$R = 1 - 4 \frac{n_{\text{ext}}}{n_{\text{cav}}} \left( \frac{n_1}{n_2} \right)^{2N} \quad (5.7)$$

where  $n_L$ ,  $n_H$ ,  $n_{\text{ext}}$ , and  $n_{\text{cav}}$  are the refractive indices of the low (1) and high (2) index components of the DBR at forward direction, of the medium outside of the cavity (i.e., air or glass), and of the material placed between the mirrors, respectively. At the center, wavelength of the stopband  $L_{\text{cav}}$  is the effective cavity length,

given by

$$L_{\text{cav}} = L_{\text{buf}} + \frac{\lambda_s}{2n_{\text{cav}}} \left( \frac{n_1 n_2}{n_2 - n_1} \right) \quad (5.8)$$

In a perfectly reflecting planar microcavity, strong light confinement forces the axial wavevector to be  $k_z = \pi/L_{\text{cav}}$ , such that the dispersion of the cavity mode energy,  $E_{\text{cav}}(k)$ , is

$$E_{\text{cav}}(k) = \frac{\hbar c}{n_{\text{cav}}} \sqrt{\left( \frac{\pi}{L_{\text{cav}}} \right)^2 + k_{||}^2} \quad (5.9)$$

where  $k_{||}$  is the in-plane component of the photon wavevector [3], namely

$$k_{||} = E_{\text{cav}}(k) \sin \theta / \hbar c \quad (5.10)$$

Combining the last two equations, we obtain the energy dispersion against the photon angle of incidence

$$E_{\text{cav}}(\theta) = E_0 \left( 1 - \frac{\sin^2 \theta}{n_{\text{cav}}^2} \right)^{-1/2} \quad (5.11)$$

where  $E_0$  is the cutoff energy,  $\theta$  is the photon angle of incidence.

The eigen-frequencies sustained by the cavity are separated by the so-called free spectral range (FSR), defined as ratio of the velocity of light to twice the length  $L_{\text{cav}}$ . If the cavity is changed by  $dL$ , the corresponding change in the peak transmission frequency is given by [4]

$$d\nu = FSR \frac{dL}{\lambda/2} \quad (5.12)$$

According to this equation, the peak transmission frequency of a Fabry-Pérot cavity changes by one FSR if the cavity length is modified of half a wavelength. Another parameter that defines the working performances of an optical cavity is the quality factor (Q-factor). It parameterizes the frequency width of the resonant enhancement, and it is simply defined as the ratio of a resonant cavity frequency,  $\nu_c$ , to the linewidth (FWHM) of the cavity mode,  $\delta\nu_c$ :

$$Q = \frac{\nu_c}{\delta\nu_c} \quad (5.13)$$

The Q-factor is a measure of the rate at which the optical energy decays within the cavity (from absorption, scattering, or

leakage through the imperfect mirrors). Likewise, the exponentially decaying photon number has a lifetime given by

$$\tau = \frac{Q}{\nu_c} \quad (5.14)$$

The finesse is defined as the ratio of the separation between two successive longitudinal cavity modes to their linewidth (FWHM):

$$F = \frac{FSR}{\delta\nu_c} = \frac{\pi\sqrt{R}}{1-R} \quad (5.15)$$

This parameter is related to the spectral resolution of the cavity, and it depends on the mirrors reflectance  $R$ . In a microcavity, the emission from the dipole is beamed into particular directions. Owing to the control of the emission direction of the intensity of EM waves and the selection of emitted optical frequencies, microcavities provide a way to engineer the optical mode spectrum of a light-emitting dipole.

### 5.1.3 Cavity–Exciton Interaction in Weak-Coupling Regime

In the weak-coupling interaction (when  $g$  is small), the two oscillators (light and matter) interact in a perturbative regime. Nevertheless, the emission direction of light and the decay rate of spontaneous emission, such as fluorescence, can be strongly modified. Indeed the probability of spontaneous emission follows the Fermi golden rule:

$$P_{ij} \propto |M_{ij}|^2 \rho(\nu_{ij}) \quad (5.16)$$

where  $P_{ij}$  is the transition from an excited ( $i$ ) to a lower energy state ( $j$ ) of the matter state (atom, molecule, or a thin semiconductor film);  $M_{ij}$  is the transition matrix element of the emitter;  $\rho(\nu_{ij})$  is the optical density at transition frequency, namely the photonic mode density (PMD). Once PMD is modified, the probability of photon emission is modified as well. A way to manage the PMDs is by means of cavity resonators that confine the EM mode in a small volume  $V$ . If the PMD is higher in the cavity compared to vacuum, a phenomenon called Purcell effect takes place, observed for the first time by Edward Mills Purcell in 1946 [5]. The Purcell effect

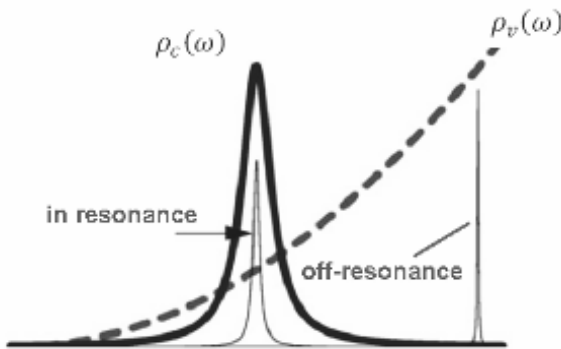


**Figure 5.5** Density of states of the vacuum,  $\rho_v(\omega)$  (thick dashed line), and of a cavity single mode (thick solid),  $\rho_c(\omega)$ , as a function of the frequency  $\omega$ . The lines of two emitters, e.g., quantum dots, are sketched in a configuration where the emitter is in resonance with the cavity (A) with an enhanced probability of emission into the cavity mode, or strongly detuned (B) with no final state to decay, resulting in an increase in its lifetime. Figure adapted from Ref. [2].

perfectly illustrates the role played by an optical cavity that locally modifies the photon density of states. In order to briefly describe this effect, we consider a dipole placed in a cavity. Intuitively, if the dipole is resonant with the cavity mode, the PMD seen by the dipole is increased with respect to the vacuum density of states. The spontaneous emission rate is, therefore, enhanced: The dipole decays radiatively faster than in vacuum, and the photons are emitted in the cavity mode. Both inhibition and enhancement of the spontaneous emission are essentially related to Fermi's golden rule. For the case of an electric dipole  $d$  interacting at point  $\mathbf{r}$  and time  $t$  with the light field  $\mathbf{E}(\mathbf{r}, t)$ , Eq. 5.16 becomes [2]:

$$\frac{1}{\tau} = \frac{2\pi}{\hbar^2} |\mathbf{d} \cdot \mathbf{E}(\mathbf{r}, t)|^2 \rho(\omega_e) \quad (5.17)$$

with  $\rho(\omega_e)$  the photon density of states at the energy  $\hbar\omega_e$  of the emitter. In the vacuum, it is given by

$$\rho_v(\omega) = \frac{\omega^2 V n^3}{\pi^2 c^3} \quad (5.18)$$

This becomes a Lorentzian in a cavity mode (see Fig. 5.5):

$$\rho_c(\omega) = \frac{2}{\pi} \frac{\Delta\omega_c}{4(\omega - \omega_c)^2 + \Delta\omega_c^2} \quad (5.19)$$

The localization of modes available for the final state (decay) of the emitter around the cavity mode allows us to enhance (inhibit) spontaneous emission by tuning (detuning) the emitter with the cavity mode. As a result of its reduced (increased) lifetime, the line gets correspondingly broadened (sharpened). If we compare the characteristic emission rate for dipole in the vacuum and in the cavity case [2]:

$$\frac{\Gamma_c}{\Gamma_v} = \frac{3Q(\lambda_c/n)^3}{4\pi^2 V_{\text{eff}}} \frac{\Delta\omega_c^2}{4(\omega_e - \omega_c)^2 + \Delta\omega_c^2} \frac{|\mathbf{E}(\mathbf{r})|^2}{|\mathbf{E}_{\text{max}}|^2} \left( \frac{\mathbf{d} \cdot \mathbf{E}(\mathbf{r})}{dE} \right)^2 \quad (5.20)$$

The first factor depends only on the parameters of the cavity, i.e., the quality factor  $Q$ , wavelength  $\lambda_c$ , refractive index  $n$ , and effective volume  $V_{\text{eff}}$ . As such, it quantifies the efficiency of Purcell enhancement for an ideal emitter coupled in an ideal way to the cavity. It is called Purcell factor  $F_p$ . The second factor comes from the density of states of a single mode in Fermi's golden rule formula. It shows the effect of the detuning on the efficiency of the coupling, on which it acts through a phase-space-filling effect. As this quantity is smaller than one, it contributes always toward inhibition of emission. The last two factors are related to the EM mode and its interaction with the dipole  $d$ . The orientation of the dipoles is really important as for dipoles perpendicular to the electric field, Purcell effect is null, as no coupling is possible at all. The previous relationship, at resonance and with the dipoles completely aligned to the electric field, becomes simply

$$F_p = \frac{3}{4\pi^2} \left( \frac{\lambda}{n} \right)^3 \frac{Q}{V} \quad (5.21)$$

#### 5.1.4 Quantum Description of Strong Coupling

A clear description of strong-coupling phenomena between light and matter is shown by a full quantum picture [6]. The confined photon will be described by the Fock space. To simplify the theory, we consider only the Fock states  $|0\rangle$  and  $|1\rangle$ , which describe the absence of any photon in the cavity or the presence of solely one photon, respectively. The material inside the cavity is schematized by an atomic two-level system. This last approximation is valid for atoms but also for molecular compounds in solid state (provided

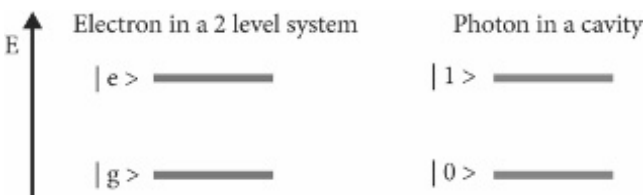


**Figure 5.6** Energy states of an electron in a two-level system and Fock states of a microcavity photon.

that intermolecular interactions are minimized) and for inorganic electron confinement structures (quantum wells). In a simple quantum picture, the electron of the atomic system can live in two states: the ground state  $|g\rangle$  or the excited state  $|e\rangle$ , which can be used as the basis of atomic Hilbert space.

The full atom-photon Hamiltonian is described by the following equation:

$$\mathcal{H} = \frac{1}{2m}(p - e\mathbf{A})^2 + V(r) + H_{\text{cav}} \quad (5.22)$$

The first term of the second member stands for the modified kinetic energy of an electron within an EM potential vector operator  $\mathbf{A}$ , where  $p$  is the momentum operator,  $e$  is the electron charge, and  $m$  is the electron mass. The second term is the atomic nuclear potential, and the third term is the Hamiltonian of the quantized EM field. We can collect the terms referred to the electron ( $H_e$ ) and those referred only to the light-matter interactions ( $H_{\text{int}}$ ) as follows

$$H_e = \frac{p^2}{2m} + V(r), \quad H_{\text{int}} = \frac{e^2 A^2}{2m} - \frac{epA}{m} \quad (5.23)$$

Therefore, the Hamiltonian operator can be rewritten as

$$\mathcal{H} = H_{\text{cav}} + H_e + H_{\text{int}} \quad (5.24)$$

Creation and destruction operators,  $b^\dagger$  and  $b$ , respectively, can be introduced for the “matter” Hamiltonian, considering the two-level atomic system as a quantum harmonic oscillator. Electronic transitions between ground and excited states can be approximated as a forced-damped electrical dipole oscillating at a frequency  $\omega_{\text{exc}}$ . The meaning of the operators  $b$  and  $b^\dagger$  is that when  $b^\dagger$  is applied to the state  $|g\rangle$ , it generates the state  $|e\rangle$ : In other words, the electron

performs a transition from the ground to the excited state. On the other hand, on applying  $b$  to the state  $|e\rangle$ , the electron decays from the excited state to the ground one  $|0\rangle$ . Using these operators, the electron Hamiltonian becomes:

$$H_e = \hbar\omega_{\text{exc}} b^\dagger b \quad (5.25)$$

It is also useful to define the momentum operator  $\mathbf{p}$  in terms of  $b^\dagger$  and  $b$ :

$$\mathbf{p} = -\frac{m\omega_{\text{exc}} d}{e} (b + b^\dagger) \quad (5.26)$$

where  $d$  is the electric dipole momentum. We can apply the approach of second quantization even to the cavity with the operator  $a$  and  $a^\dagger$ . In the second quantization approach, the EM field is a sum of harmonic oscillator with different frequencies  $\omega_k$ . Starting from Maxwell's solutions for an EM wave in the free space and applying a Fourier transformation in the reciprocal space, the EM field is expanded in plane waves, which represent a single harmonic oscillator. The number of quantized oscillations (photons) at each frequency depends on the amplitude of the field. As well as for "matter" where creation and destruction operators create or destruct excited states,  $a$  and  $a^\dagger$  have a similar meaning, that is they increase or decrease the photon number in the cavity. The resulting Hamiltonian of quantized EM radiation propagating in free space is

$$H_{\text{Field}} = \sum_{k,j} \hbar\omega_k a_{kj}^\dagger a_{kj} \quad (5.27)$$

where  $k$  is an index related to different frequencies  $\omega_k$  and  $j$  indicates one of the two wave polarizations. For the following quantum description of light-matter interaction, it is useful also to express the vector potential in terms of creation and destruction operators:

$$A_k(r) \sum_{k,j} \lambda_{kj} (a_{kj} e^{ikr} + a_{kj}^\dagger e^{-ikr}), \quad \lambda_{kj} = \sqrt{\frac{\hbar}{2\epsilon_0 V_{\omega_k}}} \mathbf{e}_j \quad (5.28)$$

where  $k$  is the wavevector,  $\mathbf{r}$  is the position,  $\mathbf{e}_j$  is the unitary polarization vector,  $\epsilon_0$  is the vacuum dielectric constant, and  $V$  is the mode volume. At this point, some approximations will be done, considering the peculiar photonic system of a microcavity. First of all in this structure, only resonant standing waves with

frequency  $\omega_{\text{cav}}$  are allowed, thus only the terms related to the resonance frequencies survive in the sum. For simplicity, we take only the first resonance mode and solely one polarization. Moreover, electronic transitions and light interactions occur in relatively small systems (atoms, molecules, or just a few lattice sites in inorganic semiconductors) and usually the working frequencies are in the visible range. Therefore, the product  $\mathbf{kr}$  is very small; thus the potential vector may be considered position independent (electric dipole approximation). Employing all these approximations, the previous equations can be simplified, resulting in:

$$H_{\text{cav}} = \hbar\omega_{\text{cav}}a^\dagger a \quad (5.29)$$

$$A_{\text{cav}}(r) = A_{\text{cav}}(0) = \sqrt{\frac{\hbar}{2\varepsilon_0 V \omega_{\text{cav}}}} e_1(a + a^\dagger) \quad (5.30)$$

Substituting the new expressions to  $H_{\text{cav}}$ , the full photon-atom Hamiltonian becomes simply:

$$\mathcal{H} = \hbar\omega_{\text{cav}}a^\dagger a + \hbar\omega_{\text{exc}}b^\dagger b + \hbar\Omega(a + a^\dagger)(b + b^\dagger) + \hbar\frac{\Omega^2}{\omega_{\text{cav}}}(a + a^\dagger)^2 \quad (5.31)$$

where  $\Omega$  is the Rabi frequency. At the anticrossing condition, ( $\omega_{\text{exc}} = \omega_{\text{cav}} = \omega$ ), in the case of electric dipoles  $d$  perfectly aligned to radiation polarization, Rabi frequency is

$$\Omega = d\sqrt{\frac{\hbar\omega}{2\varepsilon_0 V}} \quad (5.32)$$

This physical quantity is related to the photon-exciton energy exchange rate and is a measure of the coupling strength of the system. At this stage of the description, we should introduce the so-called *rotating wave approximation* (RWA) [7].

In this approximation, the last term in the sum of Eq. 5.31 is negligible because in real experiments, Rabi frequency is typically much lower than the exciton and cavity frequencies. Therefore, the interaction Hamiltonian may be written as:

$$H_{\text{int}} = \hbar\Omega(ab + ab^\dagger + a^\dagger b + a^\dagger b^\dagger) \quad (5.33)$$

In the last expression, we have to distinguish the resonant terms  $ab^\dagger$  and  $a^\dagger b$  from the antiresonant terms  $a^\dagger b^\dagger$  and  $ab$ . The resonant terms simultaneously create **and** destruct an excitation, thus

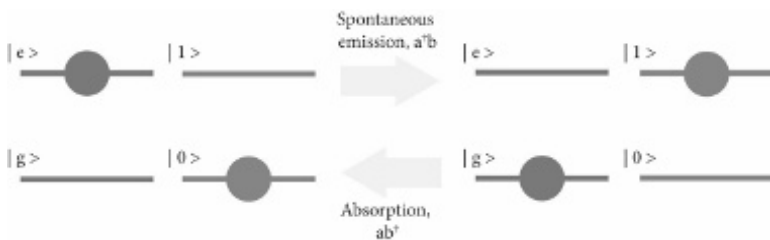


**Figure 5.7** Toy model for the quantum processes of absorption and spontaneous emission in the frame of the electron and photon states. The situation on the left describes one electronic excitation and no photon in the cavity, while that on the right refers to no electronic excitation and one photon. The transitions between these two states (absorption and emission) follow the resonant interaction terms  $ab^\dagger$ ,  $a^\dagger b$ .

describing real transitions that fulfilled the energy conservation (for example in spontaneous emission, a photon is created after an exciton decay). [Figure 5.7](#) shows the effects of the resonant terms on the actual state of the system.

On the other hand, antiresonant terms are energy non-conservative because they create or destruct simultaneously two excitations and describes *virtual transitions*. In RWA, these antiresonant terms are neglected because virtual transitions have a negligible probability compared to *real transitions*. With all these approximations, we can write the Hamiltonian of the coupled systems in a final compact form:

$$\mathcal{H} = \hbar\Omega_{\text{cav}}a^\dagger a + \hbar\omega_{\text{exc}}b^\dagger b + \hbar\omega(a^\dagger b + ab^\dagger) \quad (5.34)$$

This expression is called *Jaynes–Cummings Hamiltonian* in honor of the two scientists who first developed this model [7]. Because of the light–matter interaction terms, the Jaynes–Cummings Hamiltonian eigenstates are not the pristine states of photon and electron. The correct basis that makes the Hamiltonian diagonalizable is constituted by a linear combination of the basis  $|g, 1\rangle$  and  $|e, 0\rangle$ , that is,

$$|UP\rangle = \alpha|g, 1\rangle - \beta|e, 0\rangle, |LP\rangle = \alpha'|g, 1\rangle + \beta'|e, 0\rangle \quad (5.35)$$

The resulting mixed states are called upper and lower polariton, while the coefficients  $\alpha$  and  $\beta$ , which multiply the uncoupled states,

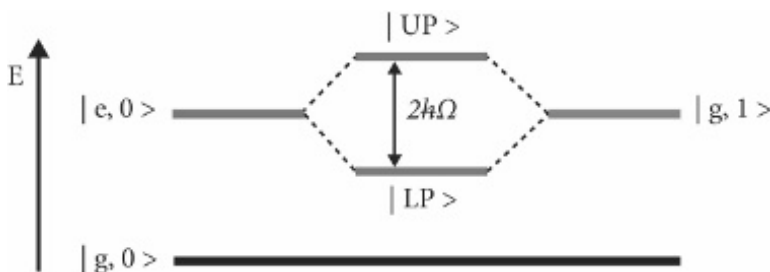


**Figure 5.8** Emerging upper polariton (UP) and lower polariton (LP) states from the uncoupled states  $|e, 0\rangle$  and  $|g, 1\rangle$ . The energy difference  $2\hbar\Omega$  between the UP and LP is proportional to the coupling strength of the system.

are called Hopfield coefficient and estimate the matter-like or light-like character of a polariton state. We can also identify an effective mass for polaritons: It is a function of the uncoupled particles masses weighted by the Hopfield coefficients. Usually, the polariton mass is dominated by the photon effective mass (which is not null in a cavity due to radiation confinement), which is much lower than the exciton one. Polariton eigenstates, at the anticrossing, have the following energy eigenvalues:

$$E_{\text{UP,LP}} = \hbar(\omega \pm \Omega) \quad (5.36)$$

As previously shown, in opposition to weak-coupling regime, the strong light–matter interaction mixes the two original degenerate states in two new states whose energy difference is equal to twice the Rabi energy ( $2\hbar\Omega$ ). The electron and the photon are entangled when they strongly interact because polariton states cannot be written as a simple product of the uncoupled systems basis.

The quantum picture gives a simple and elegant result, but it is valid only for ideal systems without losses. The polariton states angular dispersion follows those of the uncoupled systems weighted by the Hopfield coefficients (Fig. 5.9). The uncoupled cavity dispersion has a semi-parabolic trend (see Eq. 5.11), while for amorphous organic thin films, the exciton transition is independent of the angle. When the cavity and exciton modes are tuned to match the anticrossing condition at zero angle, the system is at *zero detuning*. If at the same angle the cavity mode energy is lower than

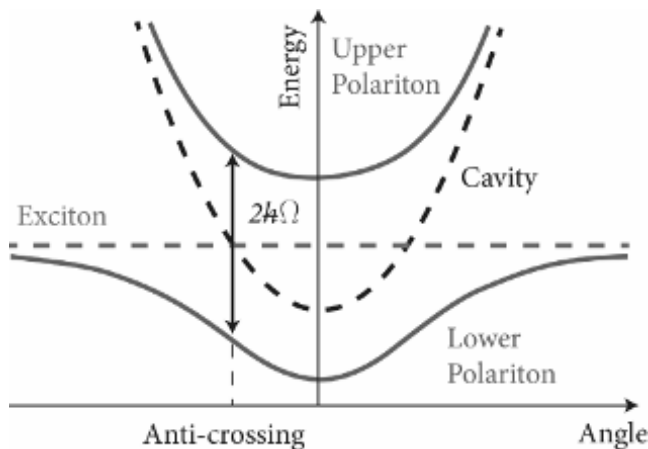


**Figure 5.9** Diagram of polariton energy dispersion against the angle. When cavity and exciton energies are the same, namely at anticrossing point, the Rabi energy splitting can be measured. The trend of polariton energies resembles that of the photon or the exciton depending on the Hopfield coefficients of the polariton states.

the exciton one and there is still strong coupling, the system is in the range of *negative detuning*. In the opposite case, the system is in *positive detuning*.

### 5.1.5 Strong Coupling with Damping

In order to take into account the possible losses, the excitonic transition and the cavity mode frequencies should be regarded as complex numbers. The imaginary parts are related to the exciton dephasing rate  $\gamma_{\text{exc}}$  and to the photon escape rate  $\gamma_{\text{cav}}$ , respectively. These parameters can be related to the linewidths of the experimentally measured reflectance spectra (see Fig. 5.10).

Higher the linewidths, higher the losses. The time-independent Schrödinger equation then will be

$$\hbar \begin{bmatrix} \omega_{\text{exc}} - i\gamma_{\text{exc}} & V \\ V & \omega_{\text{cav}} - i\gamma_{\text{cav}} \end{bmatrix} \begin{pmatrix} |Exc\rangle \\ |Cav\rangle \end{pmatrix} = \hbar\omega \begin{pmatrix} |Exc\rangle \\ |Cav\rangle \end{pmatrix} \quad (5.37)$$

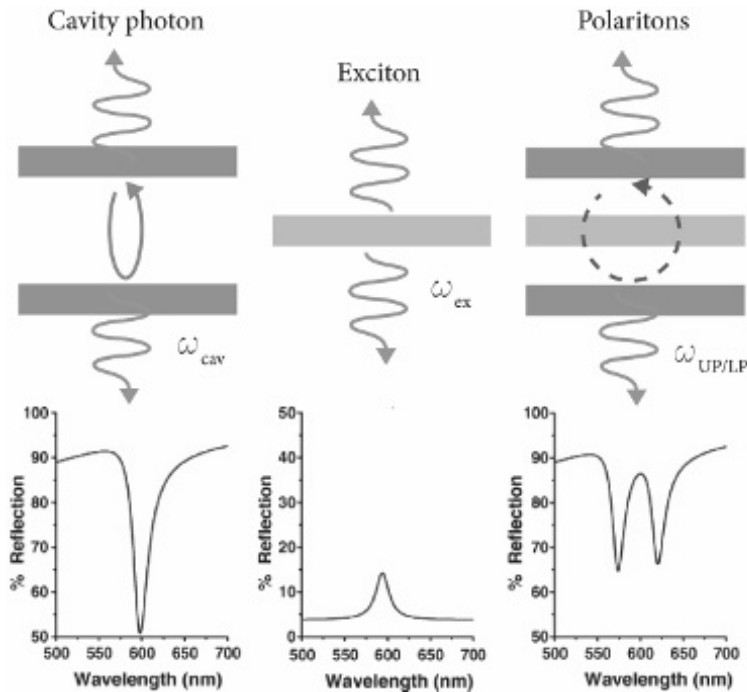


**Figure 5.10** Reflectance spectra of a bare cavity, an absorbing semiconductor layer and a coupled system, measured as a lack of transmittance  $T$ :  $R = 1 - T$ . The second spectrum identifies the absorption band of the material, thus the excitonic transitions. If we consider these systems like harmonic oscillators, the linewidth of the spectra is a measure of dephasing rate. Figure adapted from Ref. [8].

where  $V$  is the interaction coupling term. The polariton eigenvalues can be obtained after a diagonalization of the matrix:

$$\omega_{\text{UP/LP}} = \frac{\omega_{\text{exc}} + \omega_{\text{cav}} - i(\gamma_{\text{exc}} + \gamma_{\text{cav}})}{2} \pm \sqrt{V^2 + \frac{1}{4} [\omega_{\text{exc}} - \omega_{\text{cav}} - i(\gamma_{\text{exc}} - \gamma_{\text{cav}})]^2} \quad (5.38)$$

When  $\omega_{\text{exc}}$  and  $\omega_{\text{cav}}$  match (anticrossing), the energy difference between the upper and lower polariton frequencies is minimized and it is called Rabi splitting, equal to  $2\hbar\Omega$ , where

$$\Omega = \sqrt{V^2 - \frac{1}{4}(\gamma_{\text{cav}} - \gamma_{\text{exc}})^2} \quad (5.39)$$

is the Rabi frequency. Without losses, Rabi frequency is equal to the interacting term in the Hamiltonian. The square root of the previous equation is real only when  $V > \gamma_{\text{cav}} - \gamma_{\text{exc}}$ , i.e., when the interaction term is stronger than the difference between photon and exciton dissipation terms. At the anticrossing condition, the weights between exciton and photon in the polariton state are equal; thus, the polariton is a perfect hybridization of light and matter. The term  $V$  can be expressed in terms of experimental parameters of cavity–semiconductor system [3]:

$$V = \sqrt{\frac{4}{\pi} (Ad\gamma_{\text{exc}})(F\gamma_{\text{cav}})} \quad (5.40)$$

where  $A$  is the material absorption coefficient,  $d$  is the semiconductor layer thickness, and  $F$  is the cavity finesse (proportional to the quality factor  $Q$ ). From the last expression, we find that, in order to increase the coupling strength, a semiconductor film with high absorbance/thickness and a high-finesse cavity have to be employed. The last expression offers a direct link between the coupling strength and the material experimental properties.

## 5.2 Organic Light-Emitting Diodes: From Weak- to Strong-Coupling Regime

### 5.2.1 OLED in a Cavity

We shall now discuss several applications of cavity–matter interaction in organic light-emitting diodes (OLEDs), showing both the physics of weak- and strong-coupling electroluminescence and their applications on different fields from lighting to lasers. OLEDs are becoming a reality in several practical applications, from display to new lighting sources [9]. A typical OLED is made by several thin organic layers (namely “organic stack”) deposited by solution or thermal evaporation processes, embedded between two electrodes: a high work function anode, typically indium tin oxide (ITO), and a low work function metallic layer, such as Ag or Al. The organic stack is realized by depositing sequentially, onto the ITO anode, a hole-transporting layer (HTL), an emitting layer (EML), and an electron-transporting layer (ETL). Sometimes very thin organic buffer layers

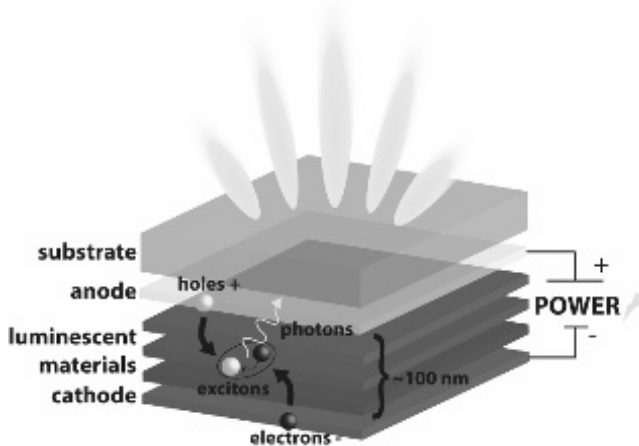


**Figure 5.11** Schematic representation of the OLED architecture and the related electroluminescence process.

are deposited between HTL or ETL and EML, to avoid quenching phenomena between the excitons and the free carriers transported by organic transport layers. Once powered by an external positive voltage, the electrons and the holes are injected, respectively, from the cathode/ETL and the anode/HTL into the EML, where they form excitons, which finally emit light (Fig. 5.11). This process is called electroluminescence.

As the total thickness of an OLED (hundreds of nanometers) is comparable to the wavelength of the emitted light, this class of devices can be integrated in an optical cavity made by two metallic or dielectric mirrors (DBR). It is not worth to note that owing to the very well-known large Stokes shift between emission and absorption spectra, a change from weak to strong coupling can be obtained by simply detuning the cavity from the absorption to the emission frequency, providing that all the conditions previously discussed are fulfilled (see Eq. 5.40), such as large molecular absorption coefficient and high-quality factor. Now we will discuss the weak-coupling regime in white OLEDs for lighting applications.

### 5.2.2 Weak-Coupling Interaction for Lighting Applications

White OLEDs are becoming an emerging technology, which could be competitive with the commercial light sources such as bulbs or fluorescent lamps. They are fabricated following the structure presented above where the active layer is made of two complementary color emitters (cyan and yellow light-emitting molecules) or three RGB primary colors. Despite their high performances compared to incandescence bulbs, still some efforts are required to improve their electroluminescence efficiency. So far a lot of efforts have been devoted to increase the quantum radiative efficiency of the luminescent materials employed as well as to reduce the working applied voltage [10–14]. Once the molecules are selected, is there a way to improve simultaneously their radiative efficiency by Purcell effect? Microcavities are affected by high-frequency selective effect due to the resonance of EM waves between the mirrors, determining the emission of just a monochromatic resonant light. Therefore, this can be useful to fabricate devices for displays and signaling applications, where color purity is important, but inapplicable for lighting, where different color emissions are needed to achieve the white color. Reducing metal reflectivity allows for a spectrum broadening, but the efficiency of the devices will be unavoidably low due to a less effective cavity resonant effect [15]. Therefore, it seems that high efficiency and good whiteness are almost two contradictory parameters. Recently, coupling between two and three microcavities, which determines an improvement in the overall

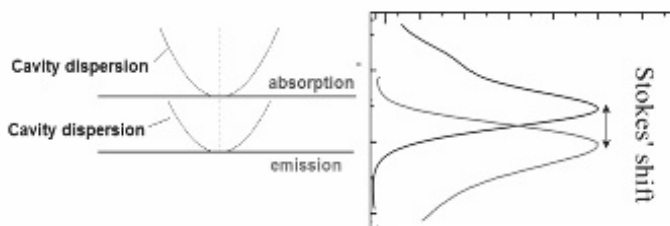


**Figure 5.12** Schematic representation of the detuning from weak- to strong-coupling regime by coupling the cavity to the emission and to the absorption transition, respectively.

performances of white OLEDs, has been demonstrated [16, 17]. The developed approach, named multicavity architecture, is based on the coupling of two or more metal/organic/metal single cavities. The coupling between the cavities splits the fundamental resonant mode frequency of the uncoupled resonators into a number of modes equal to the number of the coupled cavities, following the same physics reported in the first paragraph of this chapter. If two complementary-color fluorescent molecules or three primary phosphorescent RGB emitters are placed into the antinodes of the internal optical field, the coupling with the cavities results in an amplification of the white emission owing to the Purcell effect working on more resonant electronic transitions. This determines a lot of benefits in the device performances.

In Fig. 5.13, we show schematically three types of devices, which have been compared to study the effectiveness of Purcell effect in multicavity applications. We underline that the organic active stack is based on a p-i-n doped structure, discussed in the label of Fig. 5.13. P-i-n technology is developed by an electrical doping of organic transport layers, with the aim of improving their conductivity. Another important advantage for our purpose is the decoupling of the optical properties from the electrical characteristics, thus making the device structure optimization much easier. Indeed the doping of transport layers allows to make them almost independent of the electrodes work function. This means that Ag thin layers on top and at the bottom of the structure may be employed as both electrodes and cavity mirrors, allowing for a monolithic growth of the microcavity electroluminescent device. The materials selected as light-emitting layers change according to the fabrication of the double- or triple-cavity architecture. In the double cavity, two complementary cyan and yellow light-emitting materials (see Fig. 5.13b) have been employed, while for the triple cavity, the active layer consists of a red, green, and blue phosphorescent light emitters (see Fig. 5.13c). These two devices have been compared with a standard ITO-based structure having the same organic stack in both complementary and RGB configurations. To demonstrate the wavelength split of the resonance modes in a multicavity device, Fig. 5.14 reports a theoretical simulation of the reflected light intensity from devices with two and three microcavities,

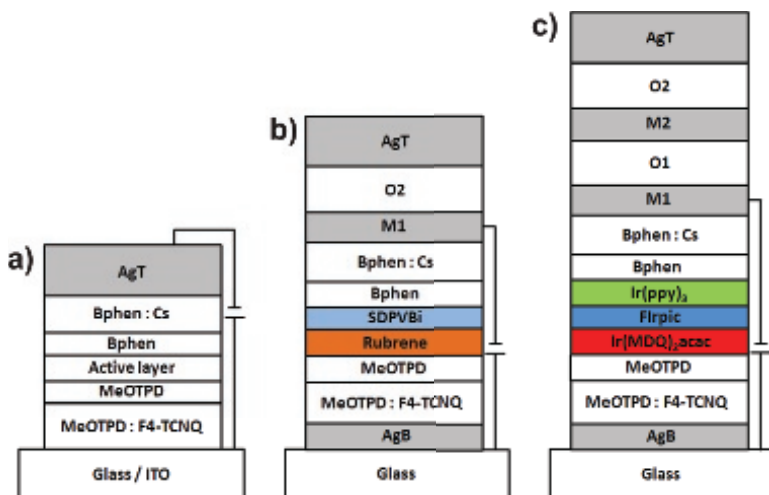


**Figure 5.13** Devices structure of the fabricated OLEDs: (a) standard ITO-based (b) double-cavity and (c) triple-cavity architecture. The p-doped layer consists of *N,N,N',N'*-tetrakis(4-methoxyphenyl) benzidine (MeO-TPD) doped with 2,3,5,6-tetrafluoro-7,7,8,8-tetracyanoquinodimethane (F4TCNQ), while the n-doped layer consists of 4,7-diphenyl-1,10-phenanthroline (Bphen) doped with Cesium atoms. Ten-nanometer-thick films of pure MeO-TPD and pure Bphen have been deposited as inter-layers to avoid quenching, due to the presence of dopants. Regarding the double-cavity device, the active layer consists of two complementary colored fluorescent compounds, namely the yellow emitter 5,6,11,12-tetraphenylnaphthacene (rubrene), dispersed in 4,4,4-tris-*N*-2-naphthyl-*N*-phenylamino triphenylamine (NPB), and the blue emitter 4,4-bis-2,2-diphenylvinyl-1,1-spirobiphenyl (Spiro-DPVBi) (blue emitter). For the triple-cavity device, a hole-transporting host material [TCTA: 4,4',4''-tris(*N*-carbazolyl)-triphenylamine] and an electron-transporting one [TPBi: 2,2',2''(1,3,5-benzenetriyl) tris-(1-phenyl-1*H*-benzimidazole)] have been partially doped with the following phosphorescent emitters: Firpic [iridium-bis-(4,6-difluorophenyl-pyridinato-*N*,C2) picolinate] for blue, Ir(ppy)3 [fac-tris(2-phenylpyridine) iridium] for green, and Ir(MDQ)2(acac) [iridium(III) bis(2methylidibenzo[f,h]quinoxaline) (acetylacetone)] for red.

where the thicknesses of the coupled metallic layers (Fig. 5.14) are continuously tuned.

As is clear in Fig. 5.14(left), when the metallic layer is too thick, only one mode is sustained by the bottom cavity where the

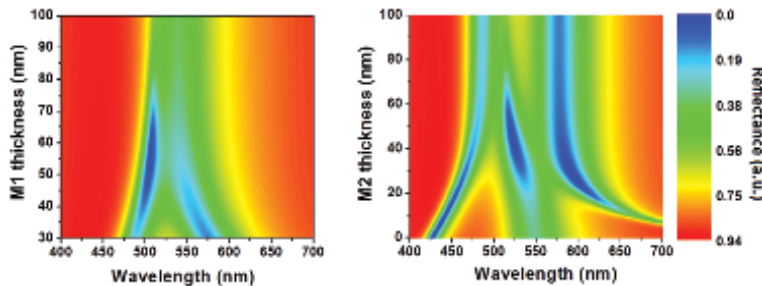


**Figure 5.14** Theoretical simulations of the reflected light intensity from two (left) or three (right) coupled cavity devices, varying the thicknesses of the metallic mirrors M1 and M2.

electroluminescent materials are placed, while below a thickness of 35 nm, two modes appears. As shown in Fig. 5.14(right), the addition of a third cavity onto the thick top-silver layer of the previous double cavity does not have any effect. Nevertheless, a reduction in this silver layer below 40 nm generates three resonant modes, since the three cavities are now coupled to each other. An optimization of organic stacks of the two- or three-cavity architectures guarantees a fine control of the position peaks of resonant modes [16, 17]. If the EM field resonates into one or more cavities through resonance modes, we can force organic molecules to emit light at those specific wavelengths with increased rates. We performed theoretical simulations to preview the behavior of the optical field within single-, double-, and triple-cavity structures.

In Fig. 5.15, the position coordinate represents the field penetration through the device layers, the value 0 being the point of contact of the structure with the substrate; from 0 to 100 nm, there is the bottom cavity, which will be filled by the light-emitting molecules. The colored peaks correspond to the position of the EM modes into the cavity versus the wavelength distribution. We can see that for all the different structures in the bottom cavity, the number of resonant EM modes is equal to the number of coupled cavities. Following these results, we expect that placing the emitters in the position of EM antinodes will result in Purcell effect, thus amplifying both the luminance and the efficiency of the devices. A comparison between reference device (R) made by ITO/Ag electrodes and double-cavity

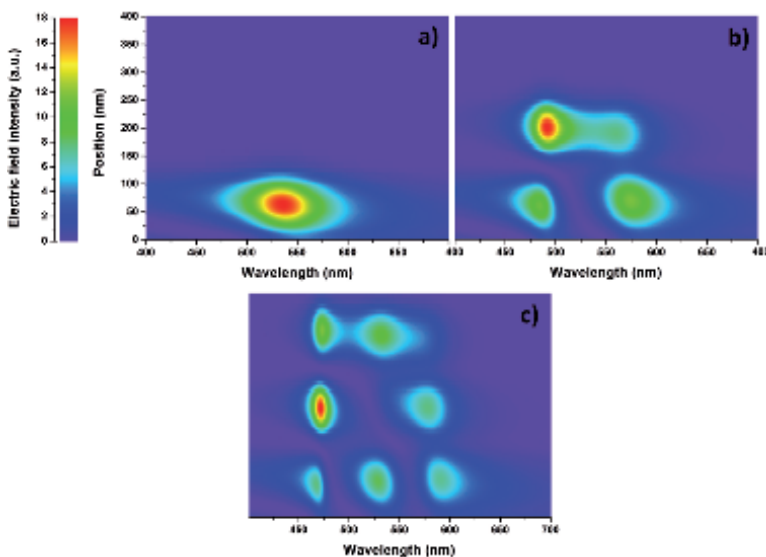


**Figure 5.15** Theoretical simulations showing the behavior of the optical field distribution inside (a) single-, (b) double-, and (c) triple-cavity structures.

device made by both silver layers as electrodes (see Fig. 5.13) is reported in Table 5.1.

As clearly shown, both the power efficiency (namely the lumens emitted normalized to the electrical injected power) and the current efficiency (namely the emission power in candelas normalized to the injected current) are increased by more than 42% in the double cavity compared to reference device, at 1000 cd/m<sup>2</sup>, the minimum luminance required for lighting applications. The quality of white color is kept high, as shown by both the CIE coordinates

**Table 5.1** Electro-optical characteristics comparison between the reference (R) standard ITO-based device and the double cavity

	L [cd/m <sup>2</sup> ] @ 4V			Power Eff. @ 1000 cd/m <sup>2</sup>	Current Eff. @ 1000 cd/m <sup>2</sup>	CRI
		CIE-X	CIE-Y			
R	7260	0.291	0.333	8.4	5.1	71
Double cavity	20000	0.407	0.439	12	7.4	86

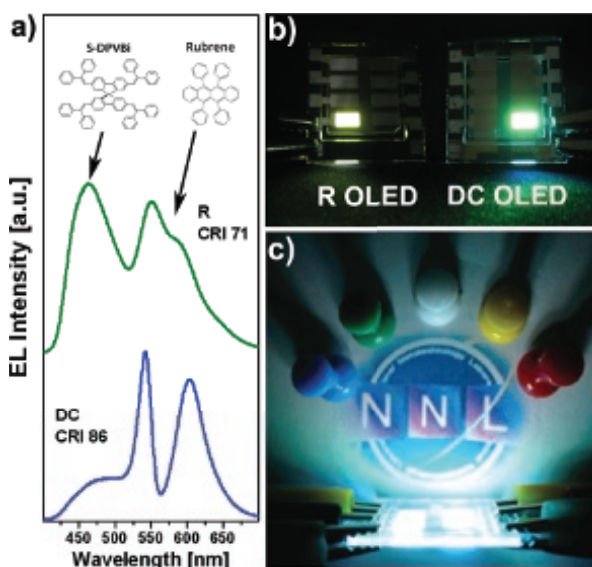


**Figure 5.16** (a) Electroluminescence spectra of reference (R) standard ITO-based device and the double-cavity one. (b) Comparison of the light emission intensity of both R and double-cavity devices, driven at the same current density. (c) Picture of the double-cavity device, showing the high color rendering of the white emitted light.

and color rendering index (CRI) values [16, 17]. In particular, with double-cavity device, CRI is even increased. In Fig. 5.16a, the electroluminescence spectra of the reference (green line) and of the double-cavity device (blue line) are reported, showing that white light is achieved in both the structures. The picture of the two OLEDs driven at the same current clearly shows the higher performance achieved in double-cavity configurations.

Following the same approach, we have developed triple-coupled cavities using phosphorescent emitters. We have fabricated a reference one on ITO anode (R) and a triple-coupled cavity device using only silver as electrodes and mirrors (Fig. 5.16c). Of course, also in this case, both the architectures have been fabricated using the same organic layer sequence. In Fig. 5.17a, the electroluminescence spectra of triple-cavity (blue lines) and R (red lines) devices are displayed, both showing color emission suitable

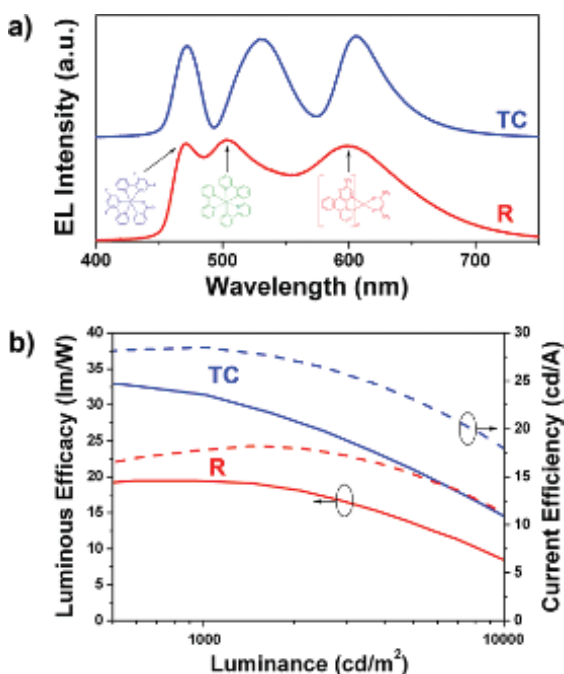


**Figure 5.17** (a) Electroluminescence spectra of reference (R) standard ITO-based device and the triple-cavity (TC) one. (b) Comparison of the current efficiency and luminous efficacy of R and TC devices.

for lighting applications [18–20]. Indeed for the triple-cavity device, the spectrum shows three emission peaks almost resonant with the emission spectrum of the three RGB materials (corresponding to the peaks of the R curve of Fig. 5.17a), and in agreement with the reflectivity measurements (see Fig. 5.14b). Remarkably, the CRI has been improved from 79 (R) to 85 (triple cavity). The reduction in the efficiency when luminance overcomes the value of  $1000 \text{ cd/m}^2$  is associated to quenching phenomena as triplet-triplet annihilation and/or triplet-polaron absorption, which takes place at high current density, and related to the characteristics of the active materials employed [21]. The color coordinates of the OLEDs as function of the visual angle (measured with respect to the forward direction) have been evaluated. The data, in the angle range of  $0\text{--}60^\circ$ , show that this variation is remarkably confined to small intervals of values also

for triple-cavity OLED. In particular, the devices show the following variations:  $\Delta x = 0.020$  and  $\Delta y = 0.020$  for R device, while  $\Delta x = 0.022$  and  $\Delta y = 0.035$  for triple-cavity one, respectively. These results demonstrate that the multicavity technology can overcome the main problems of single microcavity OLEDs.

### 5.2.3 Electroluminescence of Organic Microcavities in Strong-Coupling and USC Regimes

Now we shall discuss OLEDs in the strong-coupling regime and how the electroluminescence mechanism is affected by high light-matter coupling strength. We discuss first the different ways to populate the lower polariton branch. Starting from the pumping (optically or electrically), the system follows different pathways (1–4 in Fig. 5.18). We consider initially an optical pumping (1a) with an external light source at high energies, which are nonresonant with the absorption band of the coupled molecules. After the pump absorption, there is a first relaxation step (2a), which consists in a fast vibrational relaxation of the high-energy molecular excitons. This leads to a fast population of a “reservoir” of a quasi-thermalized excitons. Successively (3a), a slower relaxation step leads to the population of the lower polariton state, from the reservoir. Typical timescales for step 3a are of the order of hundreds of picoseconds [9]. Due to the short lifetime of the polaritons (dominated by the cavity photons lifetime), multiple scattering events are generally not expected, resulting in polaritons trapped (bottlenecked) close to the reservoir, unless they scatter down to the bottom of the lower polariton branch, by interacting with a molecular vibration of sufficiently high energy. Another complementary path to populate the lower polariton branch is the emission from the uncoupled molecules via photoluminescence from reservoir (3b). In this case, the excitons of the reservoir follow the spontaneous decay pathway and emit incoherent photons from the “bare molecules,” which can resonantly couple to the polariton states. For that reason, this mechanism is called radiative pumping. The lower polariton branch can be populated also by injecting opposite charge carriers into the reservoir (1b), employing a microcavity OLED architecture. The dynamics of organic polariton electroluminescence are very

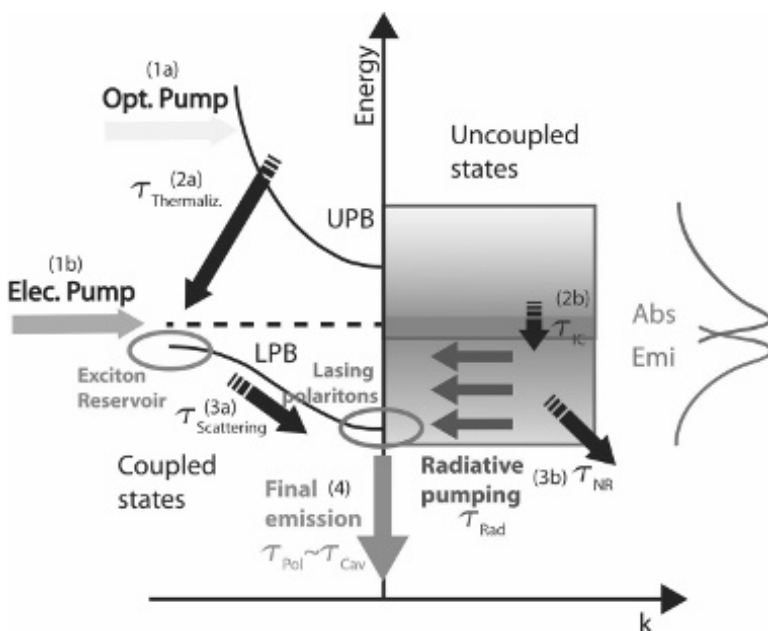


**Figure 5.18** Schematic of polariton decay dynamics. Starting from the optical pumping at high energy (1a), the excitons thermalize in a “reservoir” localized in the high  $k$  zone in the lower polariton branch (2a), where the photon Hopfield coefficient is negligible. Then they have two possible pathways: a dephasing via spontaneous emission dynamics (losses) or a scattering process to the lowest energy state at the bottom of LPB (3a), where now polaritons are affected by the cavity losses (4). In the case of electrical pumping, the excitons are formed directly near the reservoir (1b) and spontaneously decay (2b-3b). Here the timescale of each process was indicated by the lifetime  $\tau$  with the following indices: Thermaliz. stays for thermalized processes; Scattering stays polariton-phonon scattering; Cav. stays for the lifetime of photons into the cavity; Pol. stays for polaritons; IC stays for internal conversion processes; NR stays for non-radiative pathways; Rad. stays for radiative decay.

similar to that previously reported for photoluminescence. Injected electrons and holes first form localized (incoherent) excitons on coupled molecules. Finally, the polaritons emit light by photons escaping from the cavity (4).

Since the first organic polariton electroluminescent device fabricated by Tischler et al. [22] employing J-aggregates of TDBC

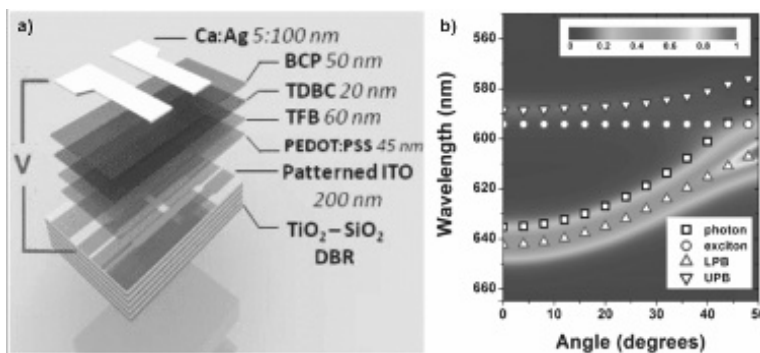


**Figure 5.19** (a) Device structure of SC-OLED with TDBC active molecule. (b) Contour plot of polariton emission dispersion recorded using optical excitation. The open symbols refer to a theoretical fit of polariton branches, cavity, and exciton dispersion. Figure adapted from Ref. [9].

as EML, several OLED structures integrated in the microcavities have been proposed to generate polaritons by electrical injection, with the aim to study the electroluminescence dynamics in strong-coupling regime. A deep analysis on polariton emission dynamics from a microcavity OLED working in strong-coupling regime (SC-OLED) was reported by Christogiannis et al. [21]. They compared the electroluminescence and photoluminescence emissions from the polaritons in an SC-OLED with a reference weak-coupled device (WC-OLED). The structure of the microcavity OLED is shown in Fig. 5.19a. The EML consists of TDBC J-aggregates deposited via the layer-by-layer technique, while the mirrors/electrodes of the cavity are made by a DBR/ITO on the bottom and a metallic layer (Ag) on the top. The EML is placed in the antinode of EM field to maximize the coupling with light. The quality factor of the cavity is about 60, and it is limited by the optical losses of the second metallic mirror. The reference weak-coupled device has the same structure except for the DBR, which is not included in this case, so the cavity is formed by the ITO and Ag layers. The calculated efficiencies of SC-OLED were about six times lower than the reference; thus, the polariton emission intensity was weaker than in WC-OLED despite a similar electrical behavior. The authors argue that exciton–polaritons are not able to efficiently scatter toward the bottom of LPB (at  $k_{\parallel} = 0$ )

because the scattering rate is lower than the spontaneous emission along the branch. For that reason, the emission intensity from LPB is angle dependent, being high at large  $k_{\parallel}$ , namely at momenta near the reservoir. With such high angles, the waveguided and the plasmonic modes couple to emitted radiation from the dipoles, subtracting intensity to the far field emission. The device fabricated by Christogiannis was negatively detuned and Rabi splitting was about 104 meV at room temperature, but higher splitting has been achieved recently in a regime called ultrastrong coupling.

Indeed a new regime of cavity QED, where the vacuum Rabi frequency becomes an appreciable fraction of the unperturbed frequency of the system, has been recently reached experimentally [23–25]. In this so-called USC regime, the routinely invoked RWA is no longer applicable and the antiresonant terms significantly change the standard cavity QED scenarios. When the Rabi energy is a significant fraction of the material transition energy, i.e.,  $g = \Omega/\omega$  is larger than 20%, the USC features start to manifest. In this regime, new phenomena have been predicted such as squeezed ground state with correlated pairs of virtual excitations [26], dynamical Casimir effect [27], and super-radiant phase transitions [28]. Before analyzing the impact of USC on the electroluminescence, we shall discuss what the interaction Hamiltonian of the coupled system becomes in such a high light-matter interaction.

$$\mathcal{H}_{\text{int}} = \hbar\Omega (a + a^\dagger)(b + b^\dagger) + \hbar \frac{\Omega^2}{\omega_{\text{cav}}} (a + a^\dagger)^2 \quad (5.41)$$

The basis previously employed (Eq. 5.35) to make the full Hamiltonian diagonalizable is not valid anymore, being now the following

$$|UP\rangle = \alpha|g, 1\rangle + \beta|e, 0\rangle + \gamma|e, 1\rangle + \delta|g, 0\rangle \quad (5.42)$$

$$|LP\rangle = \alpha'|g, 1\rangle + \beta'|e, 0\rangle + \gamma'|e, 1\rangle + \delta'|g, 0\rangle \quad (5.43)$$

The difference now is that processes involving simultaneous excitation ( $|e, 1\rangle$ ) or de-excitation ( $|g, 0\rangle$ ) of both matter and cavity, namely virtual transitions, have to be taken into account. One of the more interesting effects is that the vacuum state  $|\mathbf{G}\rangle$  of the coupled system in USC has a higher energy compared to the standard ground state of the uncoupled system, namely  $|\mathbf{g}, \mathbf{0}\rangle$ . This means

that the expectation value for the ground state is not null

$$\langle G | a^\dagger a | G \rangle \neq 0 \quad (5.44)$$

or, in other words, there is a population of ground state by virtual bound photons. To reach USC, it is needed to minimize  $\omega_{\text{exc}}$  or maximize  $\Omega_R$  [24]. In the first case, it is possible to use small energy bandgap materials, such as in the THz spectral region [29]. Another way to increase the coupling, given that  $\Omega_R$  is proportional to  $\sqrt{fN/V}$ , is to act on the dipole oscillator strength  $f$ , the number of dipoles coupled to the cavity  $N$ , or the photonic modal volume  $V$ . Organic semiconductors are the ideal candidates for this purpose because, owing to their large oscillator strengths, they can favor very strong light–matter couplings at room temperature. In some structures, the coupling strength was so increased that the cavities reached the USC regime. A Rabi splitting of 700 meV and a normalized coupling factor  $g$  of about 32% have been shown using a spin-coated film of spiropyran molecules in a PMMA matrix [30]. A similar coupling factor has also been reported in a microcavity working in the UV spectral region with a remarkable Rabi splitting ( $\sim 1$  eV) [23]. As an example of USC with organic compounds, we describe here the coupling between a metal microcavity with a squaraine compound as coupling material (see Fig. 5.20 [24]) that featured a record coupling strength value of 60% with Rabi splitting of 1120 meV (Fig. 5.20a).

In the first paragraph, we found that in the strong-coupling case, the polariton eigenvalues, at resonance conditions (namely  $E_0 = E_c$ ), can be approximated by a linear dependence on  $\Omega$ , which can be rewritten as follows:

$$E_\mp \cong E_0 \left( 1 \mp \frac{g}{2} \right) \quad (5.45)$$

Above a coupling value of 25%, the cavity enters in USC regime and the contribution of the antiresonant terms changes significantly the eigenvalues of the light–matter interaction Hamiltonian, whose exact solution is given, at zero detuning, by the following equation [24]:

$$E_\mp = E_0 \left( \sqrt{1 + \frac{g^2}{4}} \mp \frac{g}{2} \right) \quad (5.46)$$

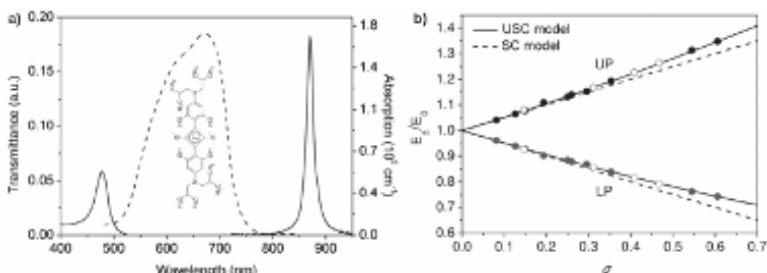


**Figure 5.20** (a) Molecular structure and absorption spectrum of 140 nm Squaraine neat film (dashed line); transmission spectra (solid line) of the Ag/140 nm squaraine/Ag microcavity at normal angle in USC regime with a coupling of 60%. (b) Polariton maximum energies for both upper polariton (UP) and lower polariton (LP) branches at the anticrossing normalized to the exciton energy. Filled dots are the experimental data for the microcavities, while the open dots refer to Sq-OLEDs. Lines represent the calculated polariton eigenvalues neglecting the antiresonant terms (dashed lines), or considering the full Hamiltonian (solid lines). Reprinted (adapted) with permission from Ref. [24], Copyright 2014 American Chemical Society.

In squaraine-filled microcavities,  $g$  could be continuously varied lowering the thickness of the coupled layer and, therefore, decreasing the number of coupled dipoles  $N$ . The total thickness of the cavity was fixed adding two optical spacers between the mirrors and the squaraine layer. Figure 5.20b clearly shows the superlinear behavior of polariton energies going from lower to higher coupling strength when the antiresonant interaction terms are not negligible anymore.

The same coupling material was exploited to realize monolithic p-i-n microcavity OLEDs (Sq-OLEDs) using silver mirrors as both anode and cathode: The device structure is illustrated in Fig. 5.21a. The strongly coupled layer, placed at the antinode position of the EM field to maximize the coupling, is also used as EML of the OLED. Also in this case, the USC regime was reached, with a coupling factor of 48%. The high coupling strength makes the polariton dispersion almost angular independent. Moreover, the polariton FWHM is only 28 meV (Fig. 5.21b), 12-fold narrower than the photoluminescence emission and even narrower than the bare cavity linewidth (50 meV). When the Rabi splitting is larger than

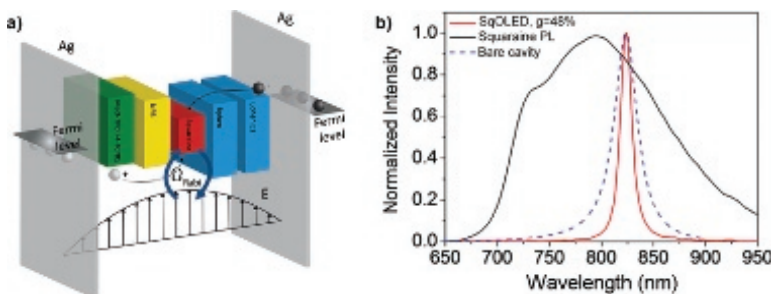


**Figure 5.21** (a) Scheme of Sq-OLED with the energy level diagram of the organic layers illustrating the two-step mechanism of charge injection and exciton formation within the squaraine dye. (b) Normalized electroluminescence spectrum of a Sq-OLED at  $g = 48\%$  (red line), photoluminescence spectrum of a neat film of squaraine (black line), and transmission spectrum of a bare (empty) cavity (dashed line). Reprinted (adapted) with permission from Ref. [24]. Copyright 2014 American Chemical Society.

the inhomogeneous exciton broadening, the polariton linewidths are given by half the sum between the cavity linewidth  $\gamma_c$  and the homogeneous exciton linewidth  $\gamma_{\text{hom}}$ . The collective coupling of the inhomogeneous excitons with the cavity results in a system that behaves like a single exciton with a very strong oscillator strength strongly coupled with the cavity. These results open the way to the development of monochromatic microcavity sources with no angular dependence and with very sharp emission below the limit imposed by the cavity itself.

It is worth to compare the emission properties of Sq-OLEDs in USC regime with another example of organic microcavity OLED working in the same regime reported by Gubbin et al. [31]. The active organic material used was the oligomer 2,7-bis [9,9-di(4-methylphenyl)-fluoren-2-yl]-9,9-di(4-methylphenyl)fluorene (TDAF). The fabricated OLEDs consist of a bottom anode/mirror of Al, followed by an hole injection layer of MoO<sub>3</sub>, the TDAF emissive layer, and a 4,7-diphenyl-1,10-phenanthroline (BPhen) hole blocking layer. The cavity was closed with an LiF/Al cathode. Samples of 55 nm, 60 nm, and 65 nm TDAF thickness resulted in large interaction strength achieved ( $g = 0.21\text{--}0.23$ ), which leads also in this case to a flat dispersion of the polariton branches. A constant optical turn-on voltage of 3.1 V was observed for the three devices,

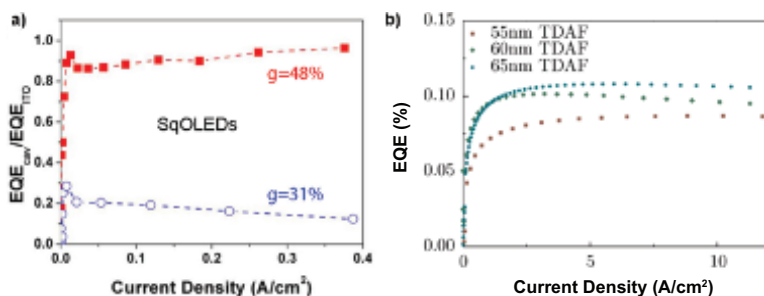


**Figure 5.22** (a) External quantum efficiency (EQE) of Sq-OLEDs at  $g = 31\%$  (blue) and  $g = 48\%$  (red) normalized to the EQE of each reference device. Reprinted from Ref. [34], with the permission from Elsevier. (b) EQE for TDAF OLEDs in USC with different detunings. Thinner devices exhibit smaller EQE due to the presence of leakage currents. Reprinted from Ref. [31], with the permission of AIP Publishing.

despite their different lower polariton energies. Moreover, this value is below that of  $E_{\text{exc}}$  but still higher than lower polariton energy and this suggests that polaritons are not formed directly by injected carriers.

The resulting external quantum efficiency (EQE) for all of the devices was about 0.1%. This value is lower compared to similar weakly coupled TDAF devices (5.3% [32]) due to additional non-radiative decay pathways such as the excitation of dissipating surface plasmon modes on the metallic anode and quenching mechanisms that affect exciton–polaritons before the scattering process from the reservoir [33]. Comparing these results with those obtained with Sq-OLEDs, an intriguing behavior peculiar to devices with a very high coupling strength was found. At small values of  $g$ , Sq-OLEDs' efficiencies are lower than those of the reference uncoupled devices probably due to the same reasons discussed above (quenching processes that affect exciton–polaritons at high  $k$ -vector and plasmonic losses). In this case, the measured emission is only due to the spontaneous emission of the uncoupled portion of molecules filtered by the polariton mode. Nevertheless, as the coupling rate increases, the ratio between Sq-OLEDs EQE and reference samples one approaches the unity: At large couplings, the polariton devices approach the performance of reference OLEDs

[34]. It can be related to the narrowing of the emission linewidth that reveals the homogenous linewidth of the coupled molecular states. When the coupling is so high, the exciton part of polariton states is less subjected to inhomogeneous dephasing and quenching effects and the spontaneous emission rate is enhanced by the Purcell effect leading to an increased efficiency.

## 5.3 Toward Electrically Pumped Organic Lasers

### 5.3.1 Organic Laser under Weak-Coupling Regime

So far we have explored electroluminescence as an incoherent emission of photons produced by electrical injection in both weak- and strong-coupling regimes. In these conditions, the excited states' density does not overcome the ground density and spontaneous emission decay is dominant compared to stimulated one. Nevertheless, by increasing the optical or the electrical pumping, the number of electrons promoted to the excited level may exceed the number of carriers in the ground state, giving rise to the emission of coherent photons by stimulated emission, which can be triggered by a resonant cavity [35]. So far several materials have been used to achieve lasing by optical pumping [36]. Organic materials show gain in the order of  $10\text{--}10^3 \text{ cm}^{-1}$  [37]. An important advantage in using organic compounds for lasing is their low processing cost and wide color tuning in the visible spectrum of light. Unfortunately, despite a huge number of compounds showing lasing action by optical pumping, so far nobody reported lasing by electrical injection. The reason is that, contrarily to more robust inorganic semiconductors, whose photoluminescence efficiency is not dependent on excitation power, for organic compounds several phenomena have been observed at high injection pumping such as: (i) a strong roll-off of electroluminescence quantum efficiency of OLED on the electrical injected current due to several exciton quenching phenomena; (ii) the low thermal resistance of organic layers that show damage before threshold for lasing [37]. Concerning the first point, although OLEDs have also demonstrated a maximum internal efficiency (IQE) approaching 100% at low current density [38], when injected

current is increased several non-radiative losses take place, reducing dramatically the IQE, such as singlet–singlet or singlet–polaron annihilations. A way proposed by Baldo et al. [37] to better understand this point is to estimate the current density threshold  $J_{\text{th}}$  needed for lasing in a general OLED configuration making very general assumptions. Thereafter, we report the main conclusion shown in their work. The external quantum efficiency  $\eta_{\text{ext}}$  of an OLED is related to the spontaneous emission rate  $A_{21}$  from an excited state 2 to the ground state 1, to the current density  $J$  and to the out-coupling factor  $\chi$  by the following relationship:

$$\eta_{\text{ext}} = \chi \frac{A_{21} n}{J/qd} \quad (5.47)$$

where  $n$  is the singlet density,  $d$  is the thickness of exciton layer, and  $q$  is the elementary charge. Taking into account the losses due to the materials filling the cavity ( $\alpha_0$ ) and due to the mirrors (expressed by the reflectivity  $R$ ), the singlet threshold condition is

$$N_s^{\text{th}} = \frac{8\pi n_{\text{cav}}^2}{\Gamma g(\lambda) \lambda^2 k_R} \left( \alpha_0 - \frac{1}{L} \ln(R) \right) = \frac{8\pi n_{\text{cav}}^2}{\Gamma g(\lambda) \lambda^2 k_R} \alpha_{\text{tot}} \quad (5.48)$$

where  $n_{\text{cav}}$  is the cavity refractive index,  $\Gamma$  is the optical confinement factor within the active layer,  $g(\lambda)$  is the normalized fluorescent spectrum lasing of the organic semiconductor,  $L$  is the length of the cavity,  $R$  is the reflectivity of each mirror, assumed equal. Combining the previous equations, we obtain that, in order to achieve lasing, the product between the external efficiency and the threshold current density normalized to the total cavity loss  $\alpha_{\text{tot}}$  at threshold must equal to

$$\frac{\eta_{\text{ext}} J_{\text{th}}}{\alpha_{\text{tot}}} = \chi \frac{8\pi n_{\text{cav}}^2 q c \Delta \lambda}{A_0 \lambda^4} \quad (5.49)$$

where  $\Delta \lambda$  is the linewidth of the emissive spectrum and the normalized spectrum of lasing has been approximated to  $g(\lambda_0) \approx \lambda_0^2/c\Delta\lambda$  [37]. In Fig. 5.23, a typical semiconductor laser configuration is shown, which exploits the waveguide in a half millimeter organic slab embedded between two ITO layers. The light emitted travels along the slab and is reflected back due to the jump in the refractive index between the organic material and air. This kind of resonator works in a multimodal condition. As the reflectivity

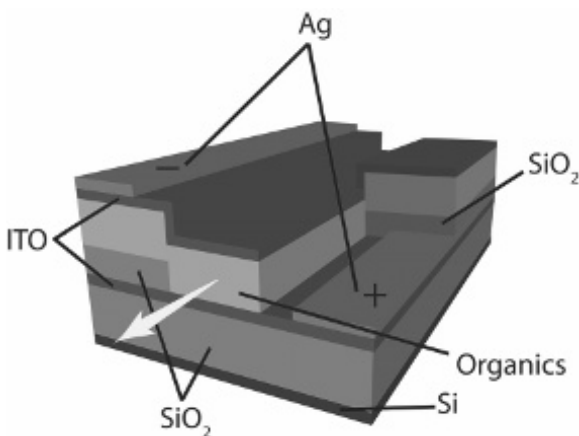


**Figure 5.23** Possible organic laser architecture.

is about 7%, the optical losses ( $-\ln R/L$ ) is about  $32 \text{ cm}^{-1}$ . The losses due to the organic filling material ( $\alpha_0$ ) is about  $27 \text{ cm}^{-1}$  at the lasing wavelength [39]. Therefore, the total losses is near  $60 \text{ cm}^{-1}$ . Note that in this structure, ITO contact layers, which have higher refractive index (1.9) compared to organic stack (1.7), have been used as both electrodes, but their thicknesses were low enough to avoid waveguide effects. The threshold value  $N_s^{\text{th}}$  in this configuration (Eq. 5.48) is about  $5 \times 10^{17} \text{ cm}^{-3}$ , thus producing a minimum external quantum efficiency–threshold current density product (Eq. 5.49) of  $40 \text{ A/cm}^2$ . Even in the case of a 100% internal quantum efficiency and an out-coupling factor of 20%, the required threshold current density for such a laser should be about  $200 \text{ A/cm}^2$ , which is higher than what has been achieved so far in the most common OLED configurations under continuous pumping.

Higher current densities of the order of  $\text{kA/cm}^2$  have been achieved in pulsed OLEDs [40] or in organic light-emitting transistor (OLET) devices [41]. Despite these high current densities, no lasing process has been observed, indicating that electrical losses due to the plasmonic effects or free charge carriers (polarons) take place. In order to reach the lasing threshold, one possibility is to play on the cavity resonator in order to reduce the exciton density needed to trigger stimulated emission. Several resonator architectures can be

able to reduce the threshold energy pumping [42], but it is still high and the integration of an electroluminescent device to such optical feedbacks is very difficult.

### 5.3.2 The Way of Polariton Laser

Recently, an alternative to reduce the lasing threshold through polariton BEC has been proposed. BEC is a process in which bosonic particles begin to occupy the ground state of the system once overcoming critical parameters such as temperature. Superfluidity, superconductivity, and polariton condensates are example of BEC [43]. For an ideal bosonic gas in three dimensions, the critical temperature for BEC occurs when  $n\lambda_D^3 = 2.62$ , where  $n$  is the density of the bosons and  $\lambda_D = \sqrt{2\pi\hbar^2/mk_B T}$  is the de Broglie wavelength in which  $m$  is the mass of the boson,  $k_B$  is Boltzmann's constant, and  $T$  is the temperature. This criterion roughly says that when the density of the bosons is high enough and their de Broglie wavelength is sufficiently large, such that their wavefunctions overlap each other, we can achieve condensation, that is, the bosonic particles may be described by a single phase wavefunction and be detected by interference pattern (see Fig. 5.24).

The mass dependence of the de Broglie wavelength shows that in order to achieve a condensation at room temperature, the mass of the bosons must be low. Polaritons, a mixture between matter and light, are very promising for this purpose, because of their low mass. BECs with polaritons have been realized in CdTe, GaAs, GaN, and ZnO deposited in high quality factor Fabry-Pérot resonators [44]. In Fig. 5.25, a diagram phase is reported for these materials, where BEC is obtained at high temperature, when the materials possess large exciton binding energy, i.e., GaN or ZnO. Indeed, a large binding energy avoids that room temperature dissociates the excitons, thus reducing the exciton-polariton density necessary to trigger the BEC.

Boson condensation may help to realize the so-called polariton lasers. The main difference between polariton and conventional lasers is that in the former case the coherence originates from the condensate which emits coherent photons by spontaneous radiative decay while in latter stimulated radiative emission is required.

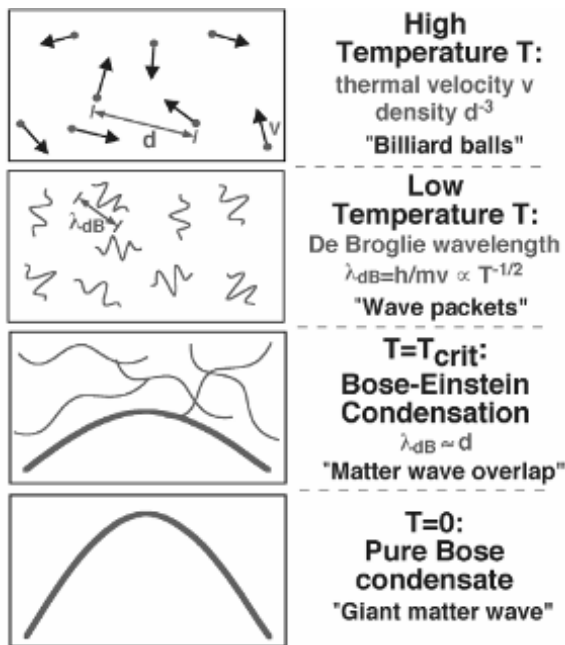


**Figure 5.24** Bose–Einstein condensation of a gas of particles by lowering the temperature from the top to the bottom. As we can see, by reducing the temperature, the de Broglie wavelength of the particle becomes larger and larger until a macroscopic coherent state is reached. Adapted from Ref. [43] (use permitted under the Creative Commons Attribution License CC BY 4.0).

The first proposal to use polaritons as coherent light source was done in 1996 by Imamoglu et al. [45] who proposed that a large number of polaritons can form a condensate in a macroscopically occupied quantum state, via stimulated scattering to the minimum of lower polariton branch, thus emitting coherent light by spontaneous radiative process. The typical architecture for such a laser consists of an optical material placed into a DBR cavity. In 1998, Deng et al. observed polariton lasing at liquid-helium temperature [46], while the first room-temperature polariton laser with optical pumping was realized in 2007 by Christopoulos and colleagues [47]. Recently, organic microcavities in strong-coupling regime have shown BEC at room temperature employing conjugated polymer [48] and organic small molecules [49]. We will thoroughly

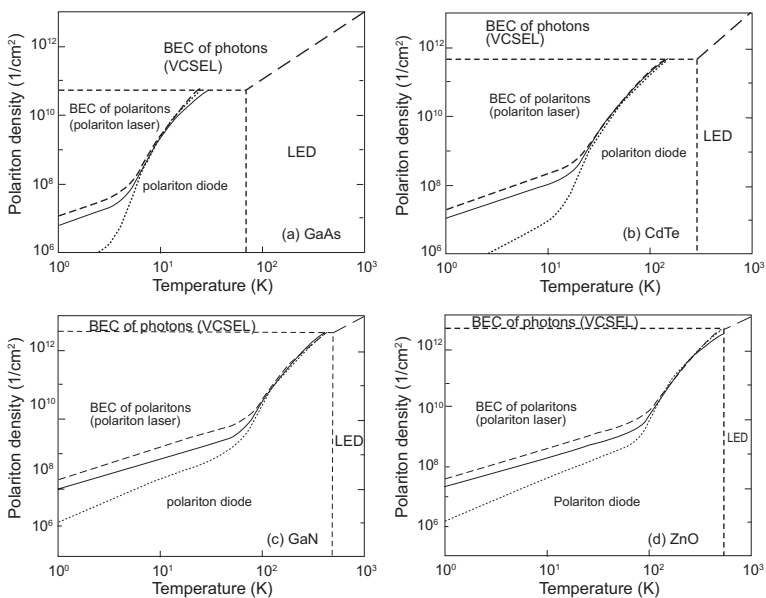


**Figure 5.25** Polariton density–temperature phase diagram of four inorganic compounds that show BEC. Figure adapted from Ref. [50].

discuss these papers as they are the first reported so far that show BEC at room temperature. In the paper by Plumhof et al. [48], the authors placed a thin polymer film of MeLPPP in a Fabry-Pérot microcavity fabricated with  $\text{Ta}_2\text{O}_5/\text{SiO}_2$  DBR. The polymer was deposited on the DBR by spin coating, forming an amorphous and disordered film (Fig. 5.26a). Differently than other common polymers, it exhibits narrow, inhomogeneously broadened exciton linewidths of the order of 60 meV with spectrally resolved vibronic replicas even at room temperature due to a relatively rigid backbone given by the methylene bridge between the phenyl rings, which allows for good coupling even at room temperature. The calculated Rabi splitting is 116 meV with a negative detuning of 77 meV. In the second work, Daskalakis et al. [49] reported room temperature polariton lasing by organic microcavities composed of a single film of thermally evaporated 2,7-bis[9,9-di(4-methylphenyl)-fluoren-2-yl]-9,9-di(4 methylphenyl)fluorine (TDAF) sandwiched between two dielectric mirrors also made of six pairs of  $\text{Ta}_2\text{O}_5/\text{SiO}_2$  (Fig. 5.26b).

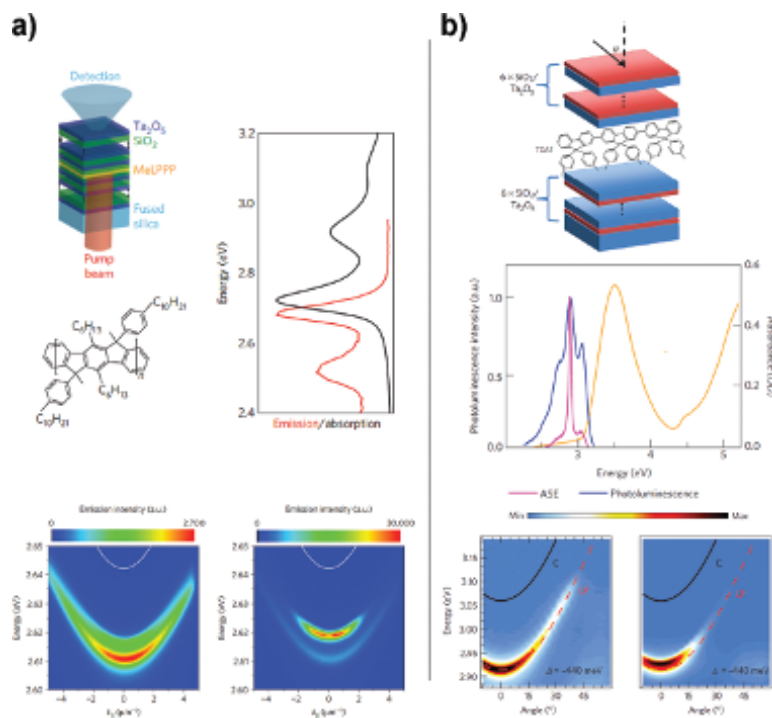


**Figure 5.26** Schematics of the DBR microcavities, optical features of the organic materials (absorption and emission spectra) and photoluminescence emission dispersion before (left) and above (right) threshold, for the structures reported in Refs. [48] (a) and [49] (b). Figures adapted from Refs. [48] and [49].

The absorption exhibits a strong inhomogeneously broadened excitonic resonance at 3.5 eV. Both the reported structures showed BEC, pumping them with a laser at an energy much higher than the coupled transition and above a specific power threshold. The critical threshold of MeLPPP cavity was  $500 \pm 200 \mu\text{J}/\text{cm}^2$ , with a concomitant nonlinear increase in the emission intensity (Fig. 5.27), a sudden decrease in the linewidth and the observation of a blueshift. The emission peak is polarized as the pump beams only above threshold. All these characteristics are markers of polariton BEC. In particular, the blueshift is a signature of the repulsive interactions between the polaritons. Also the TDAF cavity showed

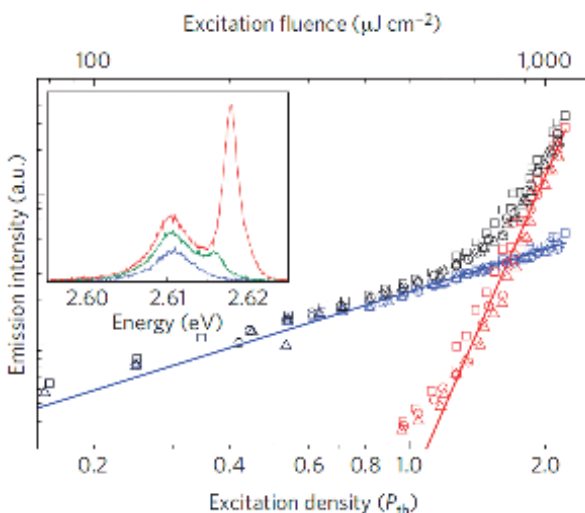


**Figure 5.27** Nonlinear increase in the total emitted intensity (black) above the BEC threshold excitation density  $P_{\text{th}}$  of the MeLPPP microcavity. The spectra (inset:  $P = 0.5/1.0/1.5 P_{\text{th}}$  as blue/green/red lines) show the occurrence of BEC emission narrow peak above threshold. The different symbols (squares, circles, and triangles) represent three consecutive measurement performed on the same sample area, demonstrating the stability of the material. Blue and red solid lines are exponential fits of the lower polariton (blue) and the BEC emission (red). Figure adapted from Ref. [48].

similar features when BEC occurs: on increasing the pump fluence, a threshold is found, which is followed by a superlinear increase in output intensity for transverse magnetic-polarized emission, regardless of the pump polarization. The collapse of linewidth of the emission, that is the increase in temporal coherence, and the collapse in momentum space to the bottom of the lower polariton branch are further indication that BEC was reached (Fig. 5.26). At the threshold, the pump fluence for a TADF cavity with 6-pair-DBRs cavity was  $60 \mu\text{J}/\text{cm}^2$ , while increasing the number of mirrors oxide pairs to 9, the threshold power density decreases to  $30 \mu\text{J}/\text{cm}^2$  due to a better light confinement (high  $Q$ ) and a consequent increase in polariton lifetime.

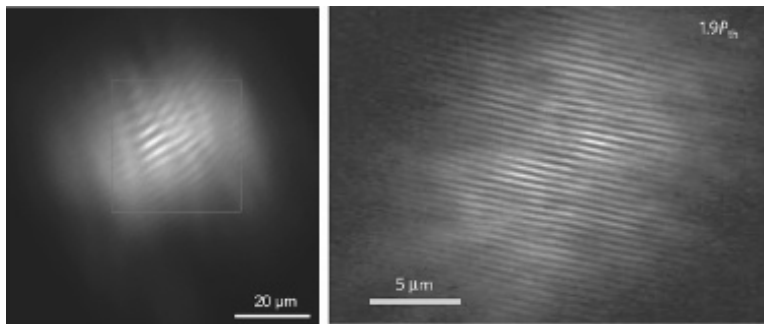


**Figure 5.28** Interferograms recorded in a Michelson interferometer pumping both the cavities above threshold. The MeLPPP microcavity is shown on the left, while the TDAF cavity is on the right. The fringes observed at each point  $\mathbf{r}$  are indicative of the spatial coherence between it and its centro-symmetric counterpart  $\mathbf{r}'$ . Figure adapted from Refs. [48] and [49].

The TDAF cavities showed a lower power threshold compared to MeLPPP probably due to the high intrinsic quantum yield of the blue molecule.

Another peculiar feature of condensate formation is the spontaneous appearance of long-range order [51]: Above threshold, for a homogeneous system, the condensate acquires a constant phase that is spontaneously chosen for each instance of measurement. This effect can be seen through the first-order spatial coherence  $g^{(1)}(\mathbf{r}, \mathbf{r}')$ , which is a measure of the phase coherence between points at  $\mathbf{r}$  and  $\mathbf{r}'$ . A practical method to probe the emergence of spatial coherence is to send the condensate spatial image in a Michelson interferometer with one of the arms replaced by a back-reflector that inverts the image centro-symmetrically [51]. If there is a spatial coherence between points  $\mathbf{r}$  and  $\mathbf{r}'$  with respect to the spot center, then fringes will appear and their contrast will be a measure of  $g^{(1)}$ . **Figure 5.28** shows the images of BECs in the two microcavities recorded above power threshold. Below threshold, the autocorrelation fringe is negligible. As the pump fluence increases to values higher than the threshold, fringes are easily identified over the entire condensate area, a clear marker of long-range order. The TDAF cavity showed a fringe visibility of about 70% within 3  $\mu\text{m}$  of the center point, while the spatial coherence of the MeLPPP was in a

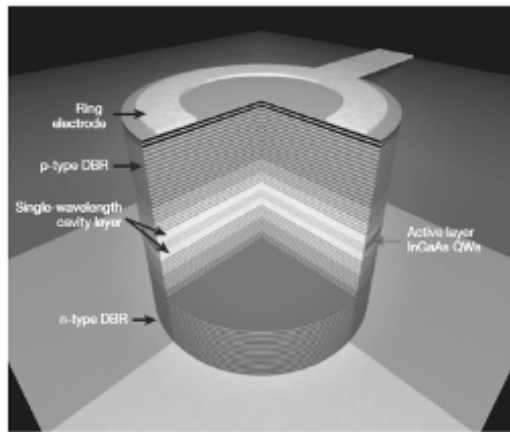


**Figure 5.29** Quantum well microcavity polariton diode and characteristics. Schematics of an electrically contacted 20 mm diameter micropillar with four quantum wells (QWs) in the cavity, sandwiched by gradually doped distributed Bragg reflectors (DBRs). Figure adapted from Ref. [54].

range of about 20  $\mu\text{m}$ : This difference in long-range order depends on the dimensions of the pumping laser spot.

### 5.3.3 Electrical Polariton Lasers: A Brief Overlook in Inorganic World

Despite these progresses by optical pumping, electrical pumping of a polariton laser (crucial for a practical use of polaritonic light sources) was demonstrated only recently, in 2013. At this stage, the electrically driven device operates at very low temperatures around 7 K and needs a magnetic field applied in the Faraday geometry. They achieved a comparably low polariton lasing threshold of  $J_{\text{th}} = 12 \text{ A/cm}^2$  [52].

In 2013, Schneider et al. [53] presented an electrically pumped polariton laser based on a microcavity containing multiple quantum wells. In order to not confuse the coherent photons produced by BEC with weak-coupling lasing regime, the authors showed that the strong-coupling regime is preserved in the device across the polariton laser threshold. Indeed they observed three different regimes

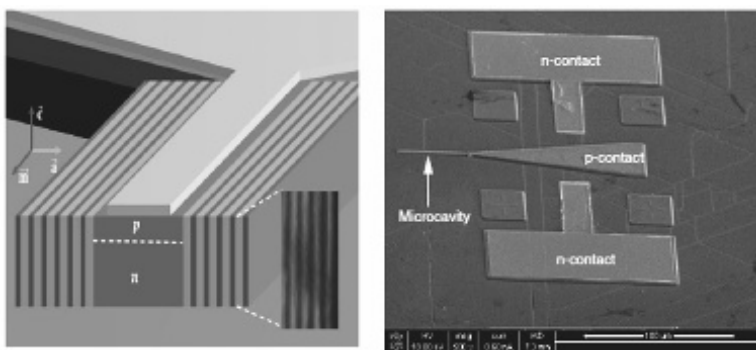


**Figure 5.30** Schematic representation of the GaN microcavity diode. The inset shows a scanning electron microscopy image of the  $\text{SiO}_2/\text{TiO}_2$  DBR mirror on one side (left), scanning electron microscopy image of the fabricated device (right). Figure adapted from Ref. [55].

in the energy–momentum dispersion characteristics, which can be attributed to the regimes of incoherent polariton emission, polariton laser operation, and cavity-mediated laser operation, respectively. The exciton density at the polariton laser threshold is significantly lower than the carrier density required for conventional lasers. They combine together a high value of  $Q$  (about 6.300) and a current confinement achieved by an electrical contact circular pillars of a diameter about 20  $\mu\text{m}$ . The threshold was reached at above 70  $\text{A}/\text{cm}^2$ .

In 2014, Bhattacharya et al. produced the first room-temperature polariton laser, which is pumped by electric current [55].

The structure consists of a p/n junction, which is contacted vertically, while the optical cavity is grown with the confinement direction parallel to the substrate. The metallic narrow contacts inject carriers vertically into the structure, while the EM mode is reflected back and forward along the plane of the substrate. In this way, electrical and optical characteristic of the device can be optimized independently. Also in this case, two different thresholds have been observed associated to polariton and weak-coupling lasing, respectively. At the threshold to BEC ( $169 \text{ A}/\text{cm}^2$ ), the linewidth reduced dramatically by half from 2.8 meV to 1.5 meV (Fig. 5.31).

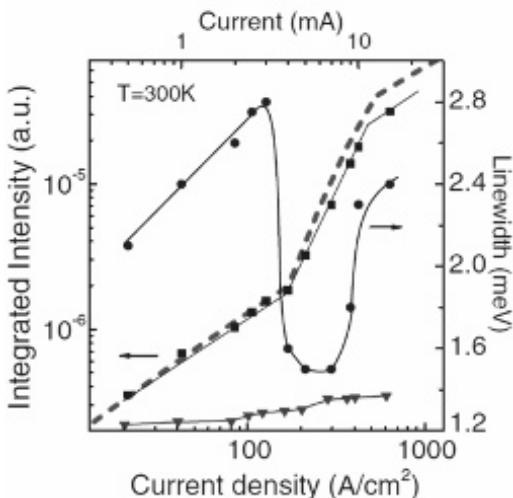


**Figure 5.31** Integrated electroluminescence intensity, LP emission linewidth, and blueshift of peak emission as a function of injected current density of the device shown in Ref. [55]. The solid lines are guides to the eye, and the dashed line shows the calculated intensities. Figure adapted from Ref. [55].

All these results concerning electrical pumping in the inorganic world and optical pumping in the organic one give a real hope for the realization of room-temperature electrically injected organic lasers.

## References

1. L. Novotny. (2010). Strong coupling, energy splitting and level crossing: A classical perspective, *Am. J. Phys.*, **78**, 1199–1202.
2. A. V. Kavokin, J. J. Baumberg, G. Malpuech, and F. P. Laussy. (2007). *Microcavities*, Oxford University Press.
3. R. J. Holmes and S. R. Forrest. (2007). Strong exciton–photon coupling in organic materials, *Org. Electron.*, **8**, 77–93.
4. Yeh, P. (2005). *Optical Waves in Layered Media*, Wiley.
5. E. M. Purcell. (1946). Spontaneous emission probabilities at radio frequencies, *Phys. Rev.*, **69**, 681.

6. J. J. Hopfield. (1958). Theory of the contribution of excitons to the complex dielectric constant of crystals, *Phys. Rev.*, **112**, 1555–1567.
7. E. T. Jaynes and F. W. Cummings. (1963). Comparison of quantum and semiclassical radiation theories with application to the beam maser, *Proc. IEEE*, **51**(1), 89–109.
8. J. R. Tischler, M. S. Bradley, Q. Zhang, T. Atay, A. Nurmikko, and V. Bulovic. (2007). Solid state cavity QED: Strong coupling in organic thin films, *Org. Electron.*, **8**, 94–113.
9. N. Christogiannis, N. Somaschi, P. Michetti, D. M. Coles, P. G. Savvidis, P. G. Lagoudakis, and D. G. Lidzey. (2013). Characterizing the electroluminescence emission from a strongly coupled organic semiconductor microcavity LED. *Adv. Opt. Mater.*, **1**(7), 503–509.
10. S. Reineke, M. Thomschke, B. Lussem, and K. Leo. (2013). White organic light-emitting diodes: Status and perspective, *Rev. Mod. Phys.*, **85**, 1245–1293.
11. S. Reineke, F. Lindner, G. Schwartz, N. Seidler, K. Walzer, B. Lüssem, and K. Leo. (2009). White organic light-emitting diodes with fluorescent tube efficiency, *Nature*, **459**, 234–238.
12. Y. Sun and S. R. Forrest. (2008). Enhanced light out-coupling of organic light-emitting devices using embedded low-index grids, *Nat. Photon.*, **2**, 483–487.
13. S. Moller and S. R. Forrest. (2002). Improved light out-coupling in organic light-emitting diodes employing ordered microlens arrays, *J. Appl. Phys.*, **91**, 3324–3327.
14. K. Walzer, B. Männig, M. Pfeiffer, and K. Leo. (2007). Highly efficient organic devices based on electrically doped transport layers, *Chem. Rev.*, **107**, 1233.
15. S. Chen and H.-S. Kwok. (2011). Alleviate microcavity effects in top-emitting white organic light-emitting diodes for achieving broadband and high color rendition emission spectra, *Org. Electr.*, **12**, 2065–2070.
16. M. Mazzeo, F. Mariano, A. Genco, S. Carallo, and G. Gigli. (2013). High efficiency ITO-free flexible white organic light-emitting diodes based on multi-cavity technology, *Org. Electron.*, **14**, 2840–2846.
17. M. Mazzeo, F. Della Sala, F. Mariano, G. Melcarne, S. D'Agostino, Y. Duan, R. Cingolani, and G. Gigli. (2010). Shaping white light through electroluminescent fully organic coupled-microcavities, *Adv. Mater.*, **22**, 4696–4700.
18. J. P. Spindler and K. H. Hatwar. (2009). Fluorescent-based tandem white OLEDs designed for display and solid-state-lighting applications, *J. Soc. Info. Display*, **17**, 861–868.

19. European academic-industrial research project into OLED lighting website: <http://www.oled100.eu>.
20. Methods of measurement reference standards (a) ANSI ANSLG C78.377-2008: "Specifications for the Chromaticity of Solid State Lighting Products"; (b) IESNA LM-79: "Electrical and Photometric Measurements of Solid-State Lighting Products"; (c) EN 12464-1: "Lighting of work places."
21. N. C. Giebink, B. W. D'Andrade, M. S. Weaver, P. B. Mackenzie, J. J. Brown, M. E. Thompson, and S. R. Forrest. (2008). Intrinsic luminance loss in emitting devices due to bimolecular annihilation reactions, *J. Appl. Phys.*, **103**, 044509-1–044509-9.
22. J. R. Tischler, M. S. Bradley, Q. Zhang, T. Atay, A. Nurmiikko, and V. Bulović. (2007). Strong coupling in a microcavity LED, *Org. Electron.*, **8**(2–3), 94–113.
23. S. Kena-Cohen, S. A. Maier, and D. D. C. Bradley. (2013). Ultrastrongly coupled exciton–polaritons in metal-clad organic semiconductor microcavities. *Adv. Opt. Mater.*, **1**, 827–833.
24. S. Gambino, M. Mazzeo, A. Genco, O. Di Stefano, S. Savasta, S. Patane, D. Ballarini, F. Mangione, G. Lerario, and D. Sanvitto. (2014). Exploring light-matter interaction phenomena under ultrastrong coupling regime, *ACS Photon.*, **1**(10), 1042–1048.
25. G. Günter, A. A. Anappara, J. Hees, A. Sell, G. Biasiol, L. Sorba, S. De Liberato, C. Ciuti, A. Tredicucci, A. Leitenstorfer, and R. Huber. (2009). Sub-cycle switch-on of ultrastrong light-matter interaction, *Nature*, **458**, 178–181.
26. S. De Liberato, C. Ciuti, and I. Carusotto. (2007). Quantum vacuum radiation spectra from a semiconductor microcavity with a time-modulated vacuum Rabi frequency, *Phys. Rev. Lett.*, **98**, 103602.
27. A. Auer and G. Burkard. (2012). Entangled photons from the polariton vacuum in a switchable optical cavity, *Phys. Rev. B*, **85**, 235140.
28. S. De Liberato and C. Ciuti. (2013). Quantum phases of a multimode bosonic field coupled to flat electronic bands, *Phys. Rev. Lett.*, **110**, 133603.
29. Y. Todorov, A. M. Andrews, R. Colombelli, S. De Liberato, C. Ciuti, P. Klang, G. Strasser, and C. Sirtori. (2010). Ultrastrong light-matter coupling regime with polariton dots, *Phys. Rev. Lett.*, **105**, 196402.
30. T. Schwartz, J. A. Hutchison, C. Genet, and T. W. Ebbesen. (2011). Reversible switching of ultrastrong light-molecule coupling, *Phys. Rev. Lett.*, **106**, 196405.

31. C. R. Gubbin, S. A. Maier, and S. Kéna-Cohen. (2014). Low-voltage polariton electroluminescence from an ultrastrongly coupled organic light-emitting diode, *Appl. Phys. Lett.*, **104**, 233302.
32. C. C. Wu, Y. T. Lin, K. T. Wong, R. T. Chen, and Y. Y. Chien. (2004). Efficient organic blue-light-emitting devices with double confinement on terfluorenes with ambipolar carrier transport properties, *Adv. Mater.*, **16**(1), 61–65.
33. M. Litinskaya, P. Reineker, and V. M. Agranovich. (2006). Exciton-polaritons in organic microcavities, *J. Lumin.*, **119–120** 277–282.
34. S. Gambino, A. Genco, G. Accorsi, O. Di Stefano, S. Savasta, S. Patanè, G. Gigli, and M. Mazzeo. (2015). Ultrastrong light-matter coupling in electroluminescent organic microcavities, *Appl. Mater. Today*, **1**(1), 33–36.
35. O. Svelto. (2010). *Principles of Lasers*, Springer.
36. I. D. W. Samuel and G. A. Turnbull. (2007). Organic semiconductor lasers, *Chem. Rev.*, **107**, 1272–1295.
37. M. A. Baldo, R. J. Holmes, and S. R. Forrest. (2002). Prospects for electrically pumped organic lasers, *Phys. Rev. B*, **66**, 035321-1–16.
38. Q. Zang, D. Tsang, H. Kuwabara, Y. Hatae, B. Li, T. Takahashi, S. Y. Lee, T. Yasuda, and C. Adachi. (2015). Nearly 100% internal quantum efficiency in undoped electroluminescent devices employing pure organic emitter, *Adv. Mater.*, **27**, 2096–2100.
39. V. G. Kozlov, G. Parthasarathy, P. E. Burrows, V. B. Khalfin, J. Wang, S. Y. Chou, and S. R. Forrest. (2000). Structures for organic diode lasers and optical properties of organic semiconductors under intense optical and electrical excitations, *IEEE J. Quantum Electron.*, **36**, 18–26.
40. N. Tessler, N. T. Harrison, and R. H. Friend. (1998). High peak brightness polymer light-emitting diodes, *Adv. Mater.*, **10**, 64–68.
41. E. B. Namdas, P. Ledochowitsch, J. D. Yuen, D. Moses, and A. J. Heeger. (2008). High performance light-emitting transistors, *Appl. Phys. Lett.*, **92**, 183304.
42. S. Chénais and S. Forget. (2012). Recent advances in solid-state organic lasers, *Polym. Int.*, **61**, 390–406.
43. W. Ketterle, D. S. Durfee, and D. M. Stamper-Kurn. (1999). Making, probing and understanding Bose–Einstein condensates, <http://arxiv.org/abs/cond-mat/9904034>.
44. Y. Lai, Y. Lan, and T. Lu. (2013). Strong light–matter interaction in ZnO microcavities, *Light Sci. Appl.*, **2**, e76; doi:10.1038/lsa.2013.32.

45. A. Imamoglu, R. J. Ram, S. Pau, and Y. Yamamoto. (1996). Nonequilibrium condensates and lasers without inversion: Exciton–polariton lasers, *Phys. Rev. A*, **53**, 4250–4253.
46. H. Deng, G. Weihs, D. Snoke, J. Bloch, and Y. Yamamoto. (2003). Polariton lasing vs. photon lasing in a semiconductor microcavity, *Proc. Natl. Acad. Sci. USA*, **100**, 15318–15323.
47. S. Christopoulos, G. B. H. von Högersthal, A. J. D. Grundy, P. G. Lagoudakis, A. V. Kavokin, J. J. Baumberg, G. Christmann, R. Butté, E. Feltin, J.-F. Carlin, and N. Grandjean. (2007). Room-temperature polariton lasing in semiconductor microcavities, *Phys. Rev. Lett.*, **98**, 126405.
48. J. D. Plumhof, T. Stöferle, L. Mai, U. Scherf, and R. F. Mahrt. (2014). Room-temperature Bose–Einstein condensation of cavity exciton–polaritons in a polymer, *Nat. Mater.*, **13**, 247–252.
49. K. S. Daskalakis, S. A. Maier, R. Murray, and S. Kena-Cohen. (2014). Nonlinear interactions in an organic polariton condensate, *Nat. Mater.*, **13**, 271–278.
50. G. Malpuech, Y. G. Rubo, F. P. Laussy, P. Bigenwald, and A. V. Kavokin. (2003). Polariton laser: Thermodynamics and quantum kinetic theory, *Semicond. Sci. Technol.*, **18**, S395–S404.
51. J. Kasprzak, M. Richard, S. Kundermann, A. Baas, P. Jeambrun, J. M. J. Keeling, F. M. Marchetti, M. H. Szymańska, R. André, J. L. Staehli, V. Savona, P. B. Littlewood, B. Deveaud, and Le Si Dang. (2006). Bose–Einstein condensation of exciton polaritons, *Nature*, **443**, 404–414.
52. P. Bhattacharya, B. Xiao, A. Das, S. Bhowmick, and J. Heo. (2013). Solid state electrically injected exciton-polariton laser, *Phys. Rev. Lett.*, **110**, 206403, 206403-1-5.
53. C. Schneider, A. Rahimi-Iman, N. Y. Kim, J. Fischer, I. G. Savenko, M. Amthor, M. Lermer, A. Wolf, L. Worschech, V. D. Kulakovskii, I. A. Shelykh, M. Kamp, S. Reitzenstein, A. Forchel, Y. Yamamoto, and S. Höfling. (2013). An electrically pumped polariton laser, *Nature*, **497**, 348–352.
54. C. Wei and Y. S. Zhao. (2014). Electrically pumped polariton lasers, *J. Mater. Chem. C*, **2**, 2295–2297.
55. P. Bhattacharya, T. Frost, S. Deshpande, M. Z. Baten, A. Hazari, and A. Das. (2014). Room temperature electrically injected polariton laser, *Phys. Rev. Lett.*, **112**, 236802, 236802-1-5.



Taylor & Francis  
Taylor & Francis Group  
<http://taylorandfrancis.com>

## Chapter 6

# Vertical External-Cavity Organic Lasers: State of the Art and Application Perspectives

**Sébastien Chénais and Sébastien Forget**

*Université PARIS 13 et CNRS (UMR 7538), 99 Avenue Jean-Baptiste Clément,  
93430 Villetaneuse, France*  
[sebastien.chenais@univ-paris13.fr](mailto:sbastien.chenais@univ-paris13.fr), [sebastien.forget@univ-paris13.fr](mailto:sbastien.forget@univ-paris13.fr)

### 6.1 Introduction: Context and General Description of Vertical External-Cavity Surface-Emitting Organic Lasers

Lasers based on solution-processed thin films have been demonstrated with many different materials (organic dyes and organic semiconductors, hybrid perovskites, colloidal quantum dots, etc.) and also with various designs for the laser resonator [1–3]. Depending on the way feedback is realized, solution-processed lasers (that will be called organic lasers in the following for the sake of simplicity) may fall in four categories: (i) organic vertical cavity surface-emitting lasers (OVCSELs), also called microcavities

---

*Organic Lasers: Fundamentals, Developments, and Applications*

Edited by Marco Anni and Sandro Lattante

Copyright © 2018 Pan Stanford Publishing Pte. Ltd.

ISBN 978-981-4774-46-8 (Hardcover), 978-1-315-10233-7 (eBook)

[www.panstanford.com](http://www.panstanford.com)

when feedback is realized perpendicularly to the thin-film plane by highly reflective mirrors that are in contact with the active film on both sides [4, 5]; (ii) distributed feedback (DFB) lasers when the laser wave is guided inside the active thin film, which supports a periodic modulation of the refractive index, inducing a coherent backscattering of the light at the Bragg wavelength [6, 7]; DFB lasers can work with a simple 1D grating, but lower-thresholds are attained with 2D photonic crystals or some more complex nanostructures; (iii) microdisks or rings or spheres, in which no mirror is intentionally added but where whispering gallery modes with high Q factors exist [8, 9]; and (iv) random lasers, where coherent feedback is provided only by scattering in the medium (either intentionally added or brought by film imperfections) [10, 11].

Since the first demonstration of an organic semiconductor laser in 1996, these four schemes have served as a basis for most, not to say all, laser devices demonstrated with thin-film gain media, with a majority being one of the first two categories listed above (OVCSELs and DFB lasers). Efforts have been essentially focused on minimizing the laser thresholds, in a context where the quest for an electrically pumped laser was the major driving force for research [2, 3, 12].

However, with the advent of new, efficient, robust, and low-cost optical sources such as blue laser diodes and LEDs, optically pumped organic solid-state lasers (OSSLs) have become interesting on their own and have started a career as practical sources to be used in applications [13, 14]. In this context, many aspects of laser engineering that have been regularly overlooked must now be addressed: Optimizing the efficiency, the beam quality, the power scalability, enhancing the photostability, and achieving a better control of the spectrum are questions that matter as much as efforts taken to further reduce thresholds.

Classical laser resonator designs listed above have been considered mostly for their ability to target low thresholds and/or because they are simple to implement, but they produce beams that are unsymmetric and/or highly diverging, conversion efficiencies (ratio of pump power or energy converted into laser light) are small or hardly measurable, and the emission spectrum can be engineered in some quite restricted fashion.

In contrast, external cavities enable a better control of spatial mode matching between pump and cavity modes, the key enabler for a high beam quality and high conversion efficiency. They also enable a high flexibility on the control of the emission since extra elements can be added inside the open cavity. External cavities have been studied with bulk rods of dye-impregnated plastics for instance, or with semiconductors (VECSELs), but were not so far extended to thin-film lasers fabricated from solution-processed materials.

A thin film-based external-cavity device was first reported by Zavelani-Rossi et al. [15]. In this work, a stable plano-concave resonator, containing a 500 nm thick neat film of electroluminescent oligothiophene, deposited directly onto the high reflector via the fast and simple spin-coating technique, was shown. The whole structure was end-pumped with 150 fs long pulses from the second harmonic of Ti:sapphire laser. Using this configuration, a nearly diffraction-limited beam was reported with 1.7% efficiency and a tunability range that was achieved over 30 nm by varying the resonator length (because the laser was single mode), which could be increased up to  $\sim 6 \mu\text{m}$ . No lasing was observed for cavity lengths exceeding this value. This short cavity length limit can be due to the low available gain of the material and the pump length duration that govern the laser pulse buildup time in relation with the cavity length (see [Section 6.2.4](#)). Considering the modest efficiency value together with the short cavity length obtained in their work, the setup is very much similar to a microcavity device. Before this work in 1998, Schülzgen et al. [16] reported on a similar structure based on a conjugated polymer where the cavity length was also limited to  $9 \mu\text{m}$ .

These two examples do not take full benefit of the external cavity, i.e., the cavity is too short to enable the insertion of intracavity elements to control the emission, for instance frequency converters or polarizers; and the conversion efficiency (laser output energy/pump pulse energy) is much lower than what can be expected from such resonators.

In this chapter, we consider vertical external-cavity surface-emitting organic lasers (VECSOL) [17, 18], which are the organic counterparts of inorganic VECSELs [19]. They are composed of a plane mirror coated with a thin film of the organic material and a remote concave mirror to close the cavity (see [Fig. 6.1](#)).

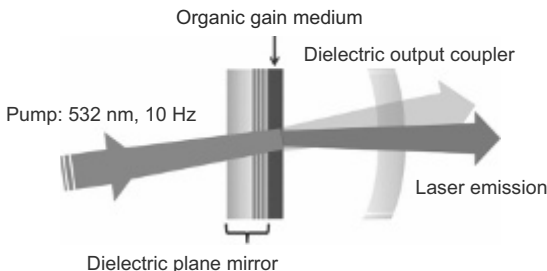


**Figure 6.1** General structure of a VECSOL.

In the first part, we review the main characteristics of laser emission that are directly linked to the macroscopic external cavity. The macroscopic (up to several centimeters long) cavity defines the spatial geometry of the laser mode and enables obtaining a  $\text{TEM}_{00}$  diffraction-limited transverse profile provided that laser and pump modes are properly matched. This matching also leads to one of the highest optical conversion efficiencies reported for thin-film organic lasers (more than 50%). Because the cavity length is large and the overall losses remain low, the photon cavity lifetime is orders of magnitude longer in VECSOLs ( $>\text{ns}$ ) than in other organic laser geometries, which has consequences on the oscillation buildup time, the laser turn-on dynamics, dictates the choice of the pump laser duration, and has also implications on the spectrum produced by the laser.

Power scalability is also one of the important properties of external cavities: hence, the question of thermal limitations, prominent in all domains of solid-state laser engineering, has a specially accurate importance when considering VECSOLs.

In the second part, we review how the empty space left between the two mirrors can be usefully employed to engineer the spectrum of the laser in three different ways that will conduct to discussing three derivations of the VECSOL concept: (a) a laser broadly tunable over the whole visible spectrum, (b) a single-mode organic laser with coherence lengths of the order of 1 m for high-resolution spectroscopy or coherent sensing, thanks to volume Bragg gratings (VBGs), and (c) an organic laser emitting in the deep UV thanks to nonlinear frequency conversion.

## 6.2 General Properties of VECSOLs

### 6.2.1 Setup Description and Fabrication

The resonator ([Fig. 6.1](#)) consists of a highly reflective plane dielectric mirror ( $R > 99.5\%$  in the emission range of the emitter) and a curved output coupler (typically with a 200 mm radius of curvature) with a reflectivity  $R < 100\%$ . The two mirrors are transparent at the pump wavelength. The gain material is usually spin-casted directly on the flat mirror, but other techniques have been successfully employed to realize VECSOLs, such as simple drop casting or inkjet printing of a photo-curable material containing a laser dye. The film must be thick enough to absorb the pump light in a single pass, while keeping a low concentration for the dyes to prevent concentration quenching. Because the thickness of the active medium is unimportant in the laser design, films as thick as necessary can be made, which avoids the use of host/guest systems. This is especially attractive when orange or red laser radiation is desired, since it can be directly obtained under green pumping, a highly preferable solution compared to UV pumping in terms of photostability and reliability.

Different kinds of pump sources can be used (see [Section 6.2.3](#)): pulsed nanosecond lasers with harmonics of Nd lasers (at 532 nm for orange-red emission or in the UV at 355 nm for laser emission in the whole visible spectrum), or pulsed blue laser diodes [[20](#)]. The optimal pulselwidth for the pump is a few tens of nanoseconds, which represents a tradeoff between pulse buildup considerations and triplet piling up in organic media, as discussed in detail in [Section 6.2.4](#).

### 6.2.2 Conversion Efficiency under Laser and Diode Pumping

The key for an efficient conversion of the pump radiation to the laser mode is a good spatial overlap between the pump spot and the (often unique) desired laser mode of the cavity. End-pumping is, in this context, much more favorable than transverse pumping. Furthermore, in close analogy with VECSELs or thin-disk crystalline

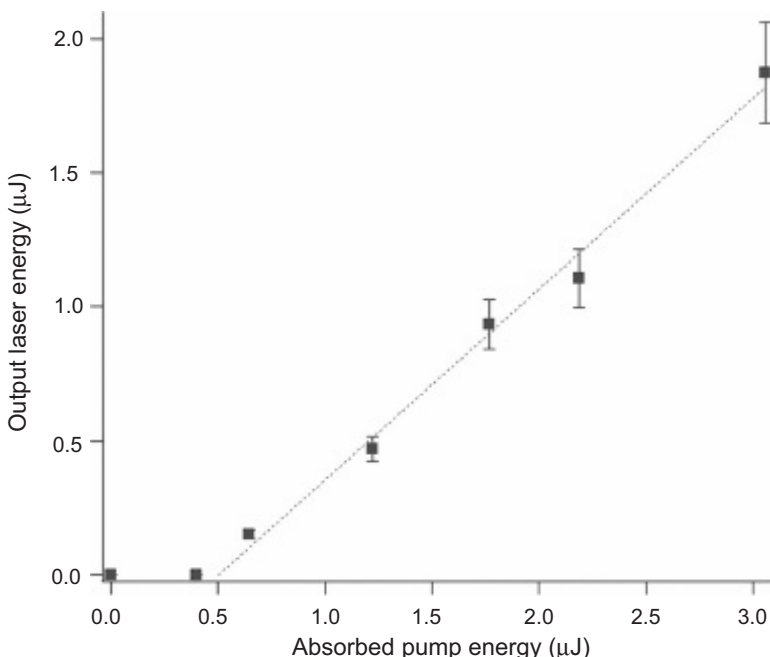


**Figure 6.2** Output pulse energy versus absorbed pump energy in a VECSEL, showing the very high conversion efficiency attainable with such a structure. Here the gain thin film is a 17  $\mu\text{m}$  thick PMMA layer doped with 1 wt.% of Rhodamine 640, spin-coated onto the rear mirror.

lasers, the thin-film nature of the gain material loosens considerably the requirement for a highly spatially coherent pump source, which enables considering pumping VECSELs with non-perfectly coherent sources such as high-power laser diodes.

In Fig. 6.2, the performance of an optimized VECSEL is presented, where the mode matching, reflectivity of the output coupler and cavity length have been optimized in order to reach almost 2  $\mu\text{J}$  of laser emission for 3  $\mu\text{J}$  of absorbed pump power. The pump laser, in this case, is a frequency-doubled Nd:YAG laser emitting 25 ns pulses at 532 nm.

It is also possible to pump VECSELs with blue laser diodes, which add a considerable benefit in terms of cost and compactness [20]. It is also more challenging as the peak power of laser diodes remains

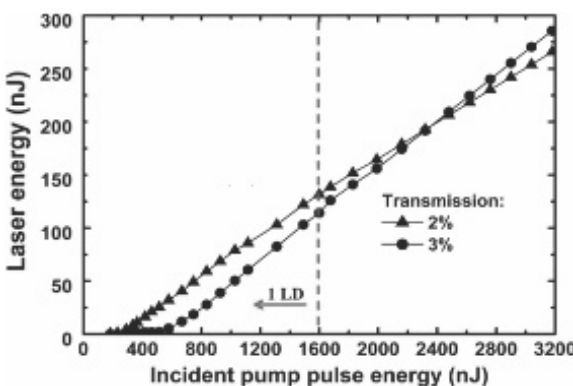


**Figure 6.3** Input–output characteristic of 1% DCM VECSOL, pumped with one laser diode (below 1.6  $\mu\text{J}$ ) and two polarization-coupled laser diodes (above 1.6  $\mu\text{J}$ ). The transmission shown is that of the output coupler (2 or 3%). Adapted from Ref. [20] with permission of AIP Publishing.

in the range of several watts only as opposed to pulsed nanosecond lasers that are typically in the kilowatt range.

For laser diode pumping experiments, the pump laser source is a low-cost high-power blue InGaN laser diode with maximum output power of 1.7 W and a central emission wavelength of 450 nm driven by a pulsed power supply with controllable pulselwidth and repetition rate. With a single laser diode pumping system, the maximum pump pulse energy deposited on the VECSOL chip is 1.6  $\mu\text{J}$  in a 100 ns pulse: Under these pumping conditions and using an output coupler of 2% transmittance, a laser pulse was obtained with 130 nJ pulse energy. To push the output power to its maximum, two laser diodes were driven with a single laser diode driver. The two diodes were polarization-coupled through a polarizing beam splitter to provide incident pump pulse energy on the VECSOL chip of 3.2  $\mu\text{J}$  in a 100 ns pulse. Energy of 280 nJ is obtained with the 3% transmission coupler, and the peak power is around 3.5 W (see Fig. 6.3).

### 6.2.3 Beam Quality and Brightness

Beam quality is essential for many laser applications. It is important to have in mind that in general (and it is always especially true for

thin-film organic lasers) the power or energy emitted by a laser is small compared to the power or energy that can be (much more easily) delivered by an incoherent source such as lamp, LED, or OLED. The power (or energy) brightness is the relevant parameter for a laser beam, defined as  $B = P/(M^2)^2 \cdot \lambda^2$ , where  $P$  is the peak power (or the pulse energy, respectively),  $\lambda$  is the wavelength, and  $M^2$  is the ratio of the divergence of the beam divided by the divergence of a diffraction-limited beam that would have the same size. Hence  $B$  tells us how much power can be concentrated in one or a few modes, giving a direct insight into the directionality and hence the “focussability” of a laser beam.

A major advantage of VECSELs is their ability to produce beams that have an  $M^2$  equal to 1 (i.e., the beam is perfectly diffraction-limited) as far as the pump spot size is correctly matched to the fundamental cavity mode, as shown in Fig. 6.4, whatever the pump source used.

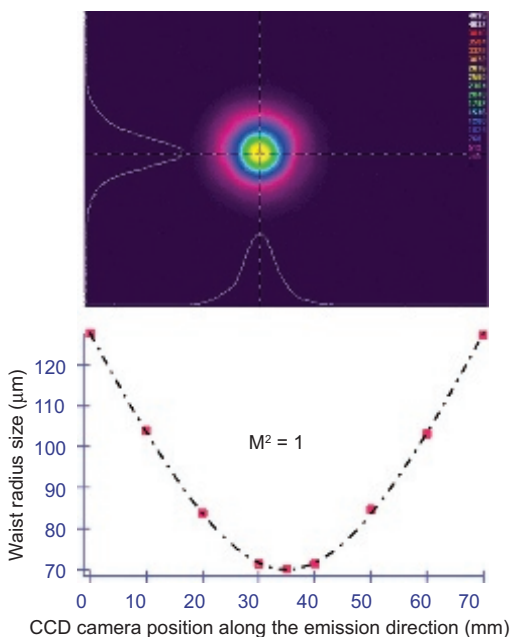


**Figure 6.4** Spatial characterization of the beam emitted by a VECSEL. The  $M^2$  is equal to 1 (diffraction-limited beam) corresponding to a Gaussian beam.

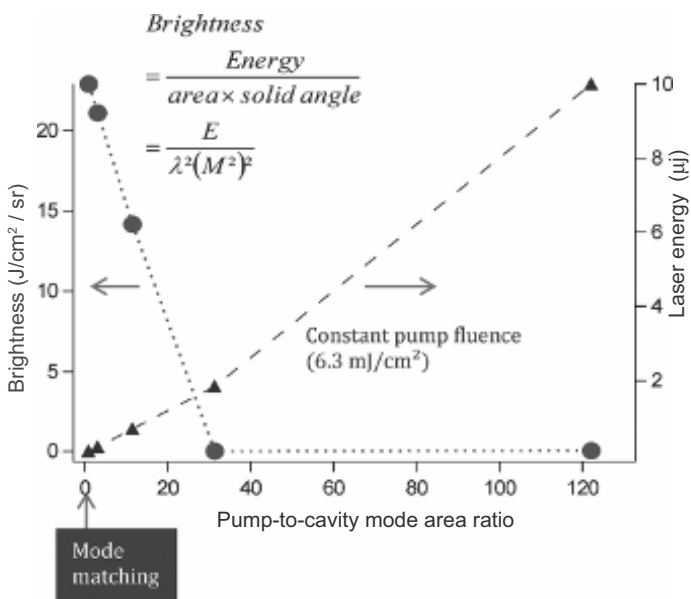


**Figure 6.5** Illustration of energy scaling with VECSOLs: The pump fluence is here kept constant, but the size of the pump spot is increased. The laser energy can be scaled this way (right axis), but at the expense of the beam quality as many transverse modes have enough gain to oscillate, causing a drop in the beam brightness (left axis). Mode matching is obtained when the pump-to-cavity mode area ratio is 1, corresponding to the highest brightness.

When the pump spot is increased, several transverse modes exist and can share the optical gain: While the power measured at the output is scaled, the beam quality vanishes and hence so does the brightness, as shown in Fig. 6.5.

Under diode pumping, the maximum experimentally obtained brightness with VECSOLs is around 9 TW/m<sup>2</sup>/sr at 620 nm. This figure is not easily comparable with other OSSLs, especially DFB resonators, as the  $M^2$  factor is rarely measured. However, for DFB lasers, the beams are generally not diffraction-limited [7, 21]:  $M^2$  values range from a few units (an astigmatic annular mode with an  $M^2$  value as low as 2.2 has been reported in a 2D DFB resonator pumped by a solid-state microchip laser [7]) to several tens (with a high divergence of 5° for example [22]). The power brightness

measured with a diode-pumped VECSOL is then typically two orders of magnitude higher than other reports of diode-pumped OSSLs in the literature.

Under laser (non-diode) pumping, the laser beam produced has a power brightness (of the order of  $10^{14}$  to  $10^{15}$  W/m<sup>2</sup>/sr), a peak power (a few tens of watts up to the kilowatt level under short-pulse pumping), and a pulse energy (in the microjoules range), which are also typically several orders of magnitude higher than the typical values recorded with other types of laser-pumped thin-film OSSLs.

Therefore, VECSOLs are adequate sources for applications requiring a “usable” intense beam that can be coupled to, e.g., an optical fiber, focused and directed as desired, which can be used for remote-sensing experiments or spectroscopy applications among others.

#### 6.2.4 Influence of the Cavity Length on Performance and Pulse Buildup Dynamics

One of the most distinctive features of VECSOLs compared to other designs is the very strong dependence of the laser efficiency on the cavity length, and hence the critical importance of the pump pulselength on the performance of the laser. This dependence originates in the long (nanosecond) oscillation buildup time, which is directly proportional to the length  $L$  of the cavity [23]:

$$\text{Oscillation buildup time, } T_b \propto \frac{L}{gcd}$$

in which  $d$  is the thickness of the active medium,  $c$  is the speed of light, and  $g$  is the linear small-signal gain (formula valid for a true four-level system). This oscillation buildup time is then  $\sim L/d$  times (that is,  $10^3$  to  $10^4$  typ.) longer than in an OVCSEL where  $L = d$ . Taking a crude picture, a photon spends much more time in the air traveling between the two mirrors than it spends inside the active medium, so that it takes quite a long time to reach the saturation intensity and build up a laser pulse.

This long time delay is illustrated in the simulation shown in Fig. 6.6. A simple four-level system is considered, and the set of coupled Statz–DeMars equations (coupling the laser intensity and the population inversion) are numerically solved: For a square

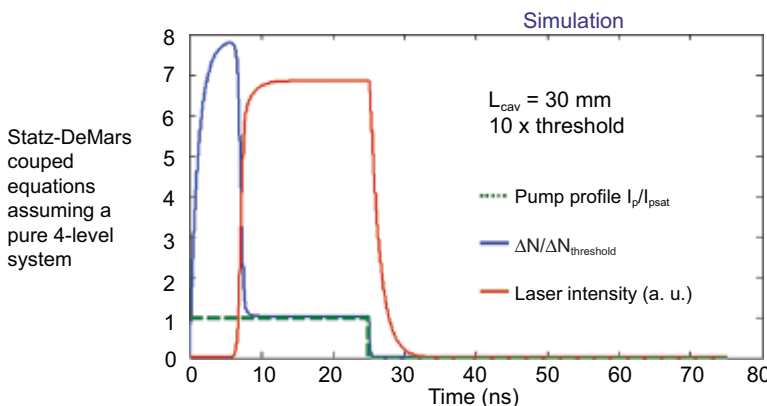


**Figure 6.6** Simulation of the dynamics of the population inversion (in blue, normalized to the threshold (continuous-wave) population inversion) and of the laser pulse intensity, when an ideal four-level system is pumped by a square 25 ns long pulse at the pump saturation intensity. Although inversion surpasses threshold within just a few picoseconds, the oscillation buildup time is as long as several nanoseconds for a centimeter-long cavity.

pump pulse of 25 ns with an intensity (or power density) equal to the pump saturation intensity, it takes roughly 10 ns before the laser pulse emerges for a 3 cm long cavity, whereas the threshold inversion is reached in a few picoseconds only at the beginning of the pulse. Of course this buildup time lengthens when the cavity length is increased, the reflectivity of mirrors reduced, or the pump intensity decreased.

Experimentally, this long delay is directly observed under diode pumping, as shown in Fig. 6.7.

As a consequence, a very intense but too short pump pulse (<ns) creates an optical gain window lasting at most the fluorescence lifetime (ns), which is shorter than  $T_b$  if the cavity length exceeds the millimeter range; this is, therefore, a quite inefficient way to pump VECSOLs, explaining why the first attempts to make external-cavity lasers pumped by femtosecond lasers were only able to produce lasing for cavity as short as a few microns, not developing the full benefit of external cavities. Better conversion efficiencies and lasing with longer cavities can be achieved with pump pulse durations of several to several tens of nanoseconds. This is why

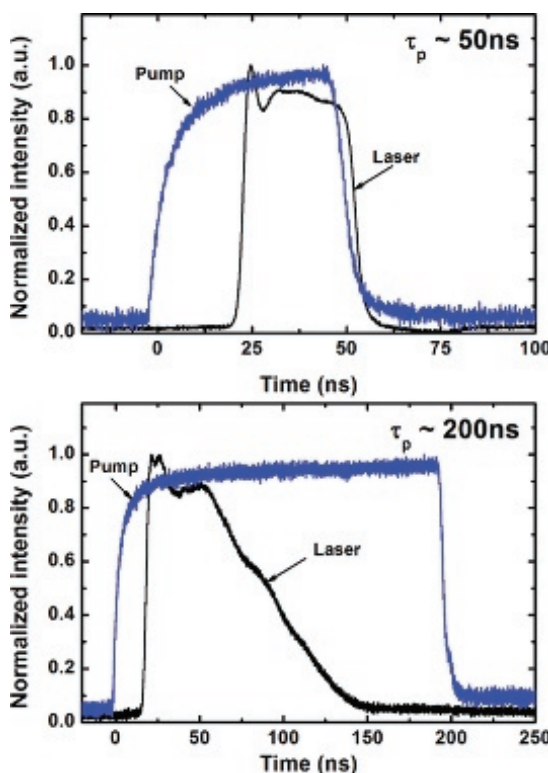


**Figure 6.7** Temporal profile of 1% DCM VECSOL (blue line) pumped with a laser diode with various pulsed widths (black line). The oscillation buildup time is clearly seen as a delay between the onset of the pump and laser pulses. For long pump pulses, the decay of laser emission due to triplet piling up and subsequent induced losses is also visible.

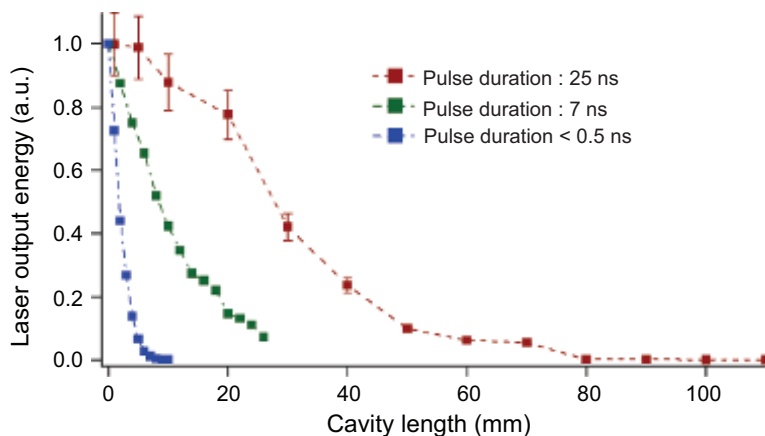
VECSOLs are better when running in “power converting regime” (quasi-CW, the active centers or molecules undergo several cycles of absorption/emission during one pump pulse) while most of organic lasers pumped by ultrashort pulses can be operated in “energy storing” mode (where the laser pulsed width is determined by the photon cavity lifetime).

Figure 6.8 makes a comparison of OVCSEL with VECSOLs, based on the comparison of the photon cavity lifetimes (<ps in OVCSELs due to the very short distance between mirrors, and >ns in VECSOLs).

	Photon cavity lifetime $\tau_{cav}$	Optimal pump pulsedwidth $T_{pump}$	Type of laser regime	Duration of the laser pulse
OVCSEL (microcavity)	 < ps	$T_{pump} < \tau$ ( $\tau$ = Fluorescence lifetime)	Energy storing (gain switch)	$\sim \tau_{cav}$
VECSOL	 > ns	$T_{pump} > \tau$	Power converting (quasi-CW)	$\sim T_{pump}$ (assisted by triplet filling up for long $T_{pump}$ )

**Figure 6.8** Comparison of VECSOLs and OVCSELs.

As another direct consequence, a VECSOL has its performance optimized when the cavity is the shortest, but this dependence will be less critical when long pulses are used. This is shown in Fig. 6.9 when three different pulse durations are used. The details on the experiments conducted with the 0.5 ns and 7 ns pump sources may be found in Ref. [18]. It is clear that the long-pulse laser (25 ns) enables much more flexibility to work with long cavities, as a laser effect was observed up to  $L = 15$  cm with this laser (for 50  $\mu$ J pulses at 532 nm).



**Figure 6.9** Influence of the pump laser pulsedwidth on the performance of a VECSOL.

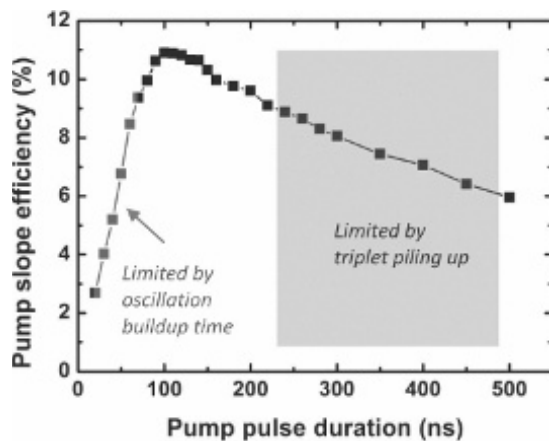


**Figure 6.10** Pump slope efficiency of 1% DCM VECSOLs for different pump pulse durations from 20 ns to 500 ns. The pump is a laser diode with a constant pump power density. The maximum pump slope efficiency was obtained with a pump pulse duration of  $\sim 100$  ns. Adapted from Ref. [20] with permission of AIP Publishing.

In Ref. [1], it is also shown experimentally how increasing the cavity length both shifts and broadens the temporal shape of the laser emission in the case of a short (sub-nanosecond) pump pulses.

It comes to the first conclusion that the pump pulsedwidth is a key design parameter for a VECSOL. As in all organic dyes or organic semiconductors, triplet piling up [1] (accumulation of energy in the triplet state, where triplet absorption to higher-lying triplet states and triplet annihilation create additional losses and reduce the singlet state population) is a fundamental limit to the pulsedwidth, which clearly appears in Fig. 6.8. The pulsedwidth has consequently an optimal value, limited to the short side by oscillation buildup, and to the long side by triplet piling up. This is summarized in Fig. 6.10.

### 6.2.5 Spectrum of VECSOLs

In a simple VECSOL, the peaks of the Fabry-Pérot macroscopic laser cavity are closely spaced (for  $L = 1$  cm, the free spectral range, FSR, is 15 GHz or 2 pm). The measurable output spectrum of a VECSOL

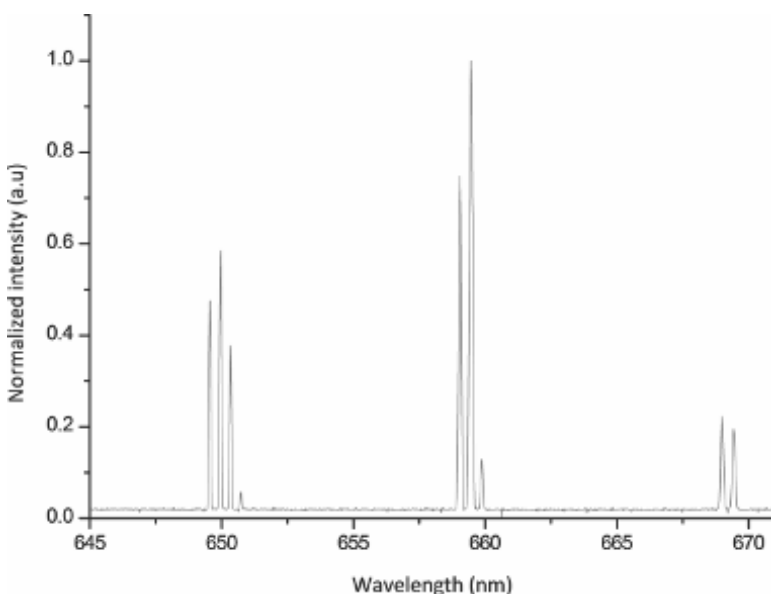


**Figure 6.11** Typical VECSOL spectrum recorded with 0.08 nm resolution spectrometer: The cavity is only 0.5 mm long in order to resolve the cavity peaks.

features the peaks of the sub-cavity formed by the active layer itself, whose FSR is around 10 nm. When the cavity is short enough and the resolution of the spectrometer is good enough to resolve the peaks of the long cavity, the two families of peaks can be clearly observed (Fig. 6.11).

The spectrum of a VECSOL is always highly multimode, even for long pump pulses, betraying a very poor spectral discrimination. In contrast, single longitudinal mode (SLM) lasing has been obtained in inorganic VECSELs without any specific spectral filter inside the cavity [24] or in liquid CW dye lasers lasing even with poorly selective filters, as mode competition can be effective enough in these cases. In OSSLs though, triplet state filling makes laser emission generally last only a few nanoseconds, and up to at most several hundreds of nanoseconds. This happens to be orders of magnitude shorter than the characteristic setting time  $t_c$  needed to reach SLM lasing in an ideal homogeneously broadened

medium [25]:

$$t_c \sim \left( \frac{\Delta v_{f,g}}{FSR} \right)^2 \tau_{cav}$$

where  $\Delta v_{f,g}$  is the spectral filter or gain bandwidth. Indeed, for a 3 mm long cavity, a photon cavity lifetime  $\sim 1$  ns and a  $\sim 50$  nm gain bandwidth typical of dyes,  $t_c$  is orders of magnitude too long, in the millisecond range.

In contrast with OVCSELs with mirrors that would have the same reflectivity, the linewidth of a single peak will be much narrower as the cavity length is much longer. Let us incidentally note that for VECSOLs, the concept of Q factor is irrelevant as it can be made as high as desired upon a simple increase in the cavity length, without of course any incidence on the laser threshold.

In [Section 6.3.2](#), we will see how the spectrum of a VECSOL can be rendered single mode with the help of a VBG inside the cavity.

### 6.2.6 Power Scaling and Photodegradation

The opportunity to obtain high brightness and high energy per pulse with VECSOLs, discussed in the previous section, raises the question of the limitations brought by photodegradation and/or thermal effects. In this section, we do not discuss the nature of photodegradation reactions, which occur in all organic media under intense pump radiation and may have different origins and very different timescales depending on the material, but discuss how the VECSOL structure enables scaling up the laser energy without increasing the rate of photodegradation reactions (power scaling). Higher energies can be obtained from a VECSOL while keeping constant the beam quality and the photodegradation rate, by simply increasing the pump beam size on the sample at constant fluence. Keeping the same beam quality, however, requires that the resonator geometry is slightly modified (through a change in the radius of curvature of the output coupler for instance, or by a change in the cavity length). Power scalability in a VECSOL is illustrated in [Fig. 6.12](#). This strategy for power scaling is, however, limited to pump spots below the millimeter region, as far as the size of higher-

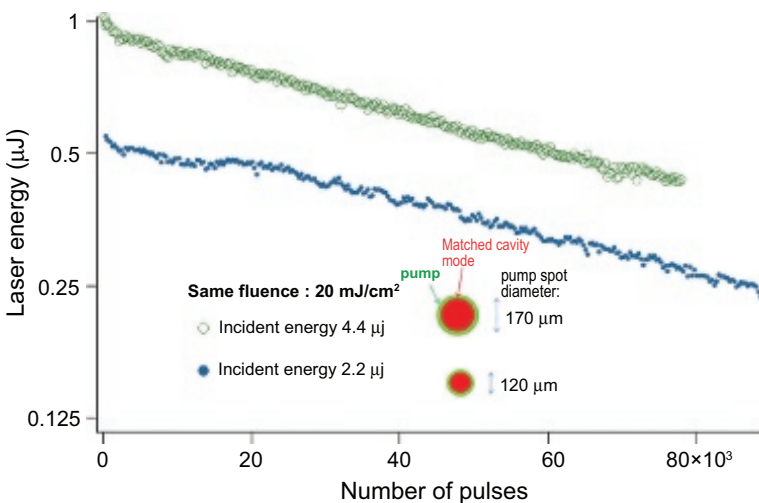


**Figure 6.12** Illustration of the power scaling capability of VECSOLS. The output coupler has a 50 mm radius of curvature. The TEM<sub>00</sub> fundamental mode waist diameter corresponding to this curvature is 104  $\mu\text{m}$ . Therefore, a pump waist diameter of 120  $\mu\text{m}$  was chosen to match the pump and cavity fundamental modes and securing single-transverse mode emission. This corresponds to a pump energy of 2.2  $\mu\text{J}$  (blue curve, down). Then a pump waist diameter of 170  $\mu\text{m}$  was chosen in order to enlarge the pump area by a factor of 2. Meanwhile, the pump energy was doubled to 4.4  $\mu\text{J}$  to ensure that the energy density was still the same at 20  $\text{mJ}/\text{cm}^2$  (approximately two times above threshold). The output coupler was also replaced by an output coupler with 200 mm radius of curvature to match this pump size and the fundamental TEM<sub>00</sub> cavity mode (having, in this case, 150  $\mu\text{m}$  waist size). The experimental results reveal that the output laser energy is almost doubled in the second case, as expected, but they also reveal that the degradation rates are equal in both cases.

transverse modes is different enough to ensure an efficient enough discrimination by mode matching.

In contrast, in a laser structure where the modes have a unique well-defined spatial distribution, such as a DFB or microdisk resonators, the only way to obtain higher output energies consists in increasing the pump energy density, which goes with a faster degradation.

### 6.2.7 Thermal Limitations

As VECSOLs are particularly suited for the production of “high” energies ( $\mu\text{J}$ ) and high-brightness laser beams, the question of the existence of thermal limitations is relevant. This is all the more important that the general trend in OSSL research is to go toward CW regime and electrical pumping, anticipating an evolution from low repetition rate (<kHz) and low pump pulse durations (<10 ns), to a regime where average pump power densities are brought up to the  $\text{kW}/\text{cm}^2$  range and the thermal energy deposited per pulse will be much higher.

To quantify the importance of those thermal effects, measurements and simulations of temperature maps in solid-state organic thin films have been realized [26]. A simplified thermal microscope, home made from a commercial 8–12  $\mu\text{m}$  infrared camera, was used to record temperature maps at the organic thin-film surface during laser action with a 40  $\mu\text{m}$  resolution (see Fig. 6.13), after a proper calibration of the infrared emissivity of the sample; those maps were then compared with time-resolved finite-element thermal simulations. The measured and simulated temperature profiles are in good accordance and reveal that the peak temperature rise remains below a few kelvin in standard operating conditions,

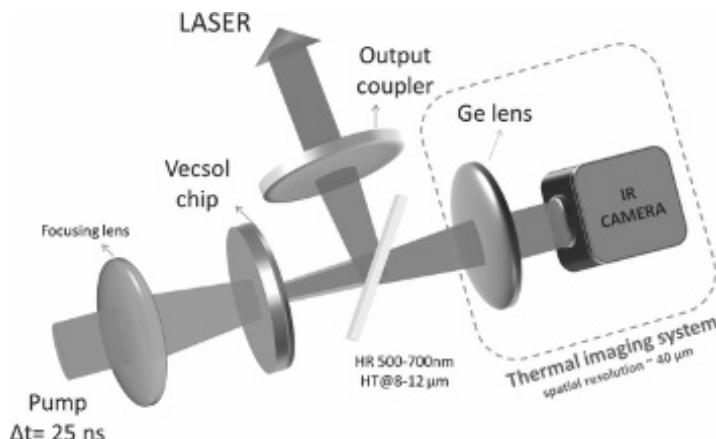


**Figure 6.13** Experimental setup for *in situ* temperature measurements in VECSOL via thermo-imaging method.

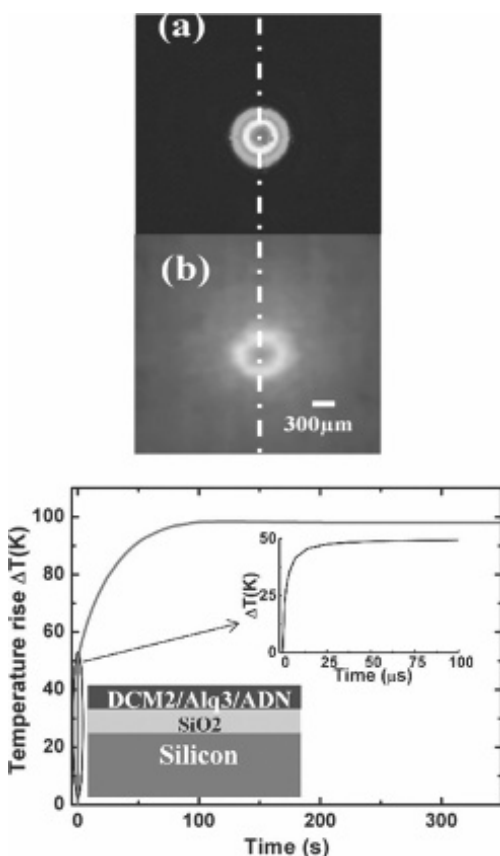


**Figure 6.14** (Top) Pump beam (a) and temperature (b) profile measured at the exit surface of a VECSOL chip under pulsed pumping. (Bottom) Simulation of the temperature rise in polymeric active layers of the device under CW pumping, with a pump intensity of  $2.4 \text{ kW/cm}^2$ .

showing a negligible impact of thermal effects on the performance of VECSOLs (Fig. 6.14, top). Thermal lensing was also estimated to be negligible.

In contrast, thermal effects appear to be significant in long-pulse organic lasers. The validated model was applied to estimate the amplitude of thermal effects in two archetypal laser structures taken from the recent literature: an OVCSEL and a DFB cavity design. Under pulsed pumping and while the repetition rate remains < MHz,

the temperature rise is at most of a few kelvin. It has been recently demonstrated that introducing a triplet manager in an organic active medium can reduce triplet-induced losses and enables laser pulses lasting up to 100  $\mu\text{s}$  under CW pumping, a key step toward true CW lasing. We ran the previously validated thermal simulation on the device presented in Ref. [27]: The temperature rise is calculated to be  $\sim 100$  K at steady state under CW pumping, leading to increased photodegradation rate and altered beam quality (Fig. 6.14 bottom).

## 6.3 VECSOLs for Applications: Three Examples of Intracavity Laser Spectrum Engineering

A major advantage of vertical external cavities lasers is the possibility to insert optical elements inside the resonator to modify the properties of the laser itself (spectral width, emission wavelength, polarization) or to create new functionalities. In this section, we show three examples of spectral engineering, which directly rely on the possibility to add extra elements inside the cavity: (a) a thin-film etalon for a broadly tunable laser, (b) a VBG for a single-mode ultranarrow linewidth laser, and (c) a nonlinear crystal for a deep-UV tunable laser.

### 6.3.1 VECSOLs as Tunable and High Beam Quality “Low-Cost” Lasers over the Visible Spectrum<sup>a</sup>

Widely tunable laser sources in the visible part of the spectrum are required for many applications such as, for instance, spectroscopy [13, 28, 29] or bio-chemo sensing [30]. Liquid dye lasers have been reigning for decades over this spectral region in virtue of their unrivalled spectral coverage and wavelength agility, but they require complex and bulky flow systems and are plagued by stability and toxicity issues. Optical parametric oscillators (OPO) or generators [31, 32] provide a solid-state alternative solution to get tunable visible coherent radiation, but despite many recent improvements [33], they still remain complex, cumbersome, and expensive

---

<sup>a</sup>This section summarizes and reuses material from Ref. [47].

solutions. The landscape of tunable visible sources seemed to change deeply with the advent of supercontinuum sources, which offer broadband spatially coherent light covering the visible and infrared spectrum (400–1800 nm); however, these sources have still low output spectral power densities (typ.  $\sim$ mW/nm) and are hence not ideal whenever only a specific spectral region has to be addressed, since in that case only a tiny fraction of the light is useful after filtering. Tunable visible sources based on nonlinear fibers and frequency conversion recently appeared on the marketplace but are available at a cost comparable with that of dye lasers or OPOs. In pulsed regime, OSSLs [2, 3] are then appealing devices, which combine the advantages of dye lasers with those of conventional solid-state lasers, with a “low-cost” advantage.

Two types of OSSLs are usually distinguished: lasers with bulk ( $\approx$  cm) dye-doped polymer chips, characterized by an open resonator, allowing for a perfect beam quality and enabling an easy insertion of optical elements inside the cavity for wavelength tuning [34]. These lasers can attain nearly four-level limit efficiencies [35]; however, the gain chip (typically a dye-doped polymer block prepared by radical polymerization or sol-gel [36]) might be long and complex to produce and mandatorily requires optical polishing before use [37]. Conversely, thin film-based OSSLs, typically an organic semiconductor DFB laser, has a low-loss resonator with a very low laser threshold, but will not be so easily tuned. Continuous wavelength tunability of a solid-state organic DFB laser requires modifying the active medium shape in some way, either through a modification of the effective index of the layer (which can be done by playing on the index [38, 39], the film thickness [40, 41], or the grating depth [42]), or by mechanical means upon applying a stress to the active layer in order to induce a shift of the Bragg wavelength [43, 44]. Their tuning range is limited to a few nanometers for a single grating and is at most limited by the gain bandwidth of a given material; a full coverage of the visible spectrum requires dozens of gratings with different pitches, leading to increased cost and fabrication issues. Moreover, DFB laser devices have a few drawbacks like a poorly defined spatial beam quality [45, 46], a low optical conversion efficiency, and a related low output energy.

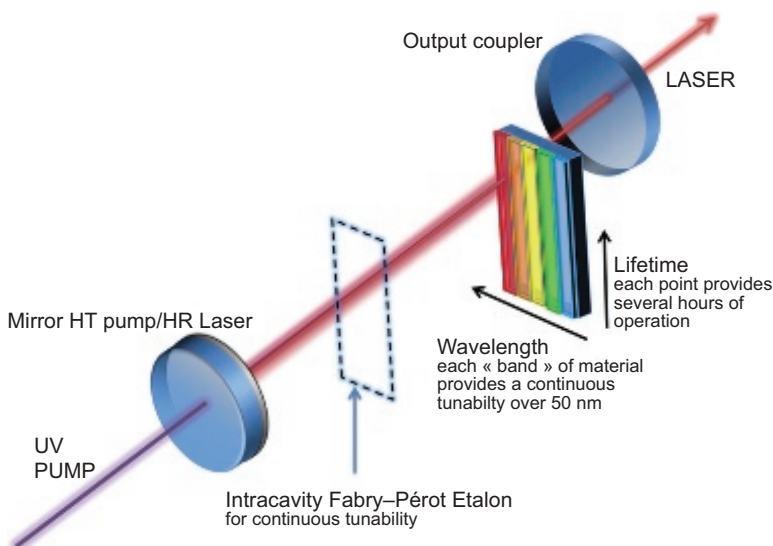


**Figure 6.15** Laser architecture with several disposable capsules. Rotating the Fabry-Pérot intracavity etalon allows fine and continuous tunability within the  $\sim 50$  nm tuning range offered by a given material. Vertical translation of the sample is a way to address different spots and to consequently increase the lifetime of the capsule.

Vertical external-cavity organic lasers are an interesting option to get best of both worlds and combine a thin-film solid-state organic laser with a wide and continuous tunability covering the whole visible spectrum. Another advantage is the possibility to bypass the photodegradation issue, which is common to all organic lasers, based on the use of a very simple “gain capsule” that can be produced at negligible cost, and which can be easily replaced or exchanged without alignment once the material is degraded.

The experimental setup is described in Fig. 6.15. It consists of a modified version of the VECSOL architecture described above, where the gain medium is coated on a simple glass slide inserted in the cavity rather than directly onto one of the cavity mirrors. As antireflection coatings cannot be easily implemented onto low-index organic thin films, the VECSOL emission spectrum, as previously described (see Section 6.2.5), is comb shaped since the several-micrometer-thick active layer, directly deposited onto the rear

mirror, acts as a Fabry-Pérot intracavity etalon. In order to ensure a continuous tunability with a reduced linewidth, the gain medium was physically separated from the rest of the cavity backbone to take the form of a “capsule.” This capsule consists in a glass substrate (low-cost, commercially available microscope plain-glass slides) onto which a film of dye-doped polymer was spin-coated. The pump beam (either a laser or a laser diode can be used) was focused onto the active “capsule” placed close to the input mirror and positioned at Brewster angle to remove the remaining etalon effect, which arises from the index mismatch between the dye-doped polymer film and the glass plate.

To cover a wavelength range going from blue to red, five dyes belonging to three dye families, namely, coumarins, pyrromethenes, and xanthenes, have been chosen for their well-established laser performance. All active materials were dispersed into PMMA either alone or in the form of donor/acceptor mixtures according to their absorption properties at 355 nm.

As discussed in a previous paragraph of this chapter ([Section 6.2.4](#)), oscillation buildup considerations lead to laser performances that drop significantly with the cavity length. Hence, the cavity length must be carefully chosen as a compromise between keeping some space to set intracavity elements and maintaining a correct efficiency. Each dye material has typically a bandwidth of 50 nm. To finely tune the wavelength within this range, an etalon with a FSR higher than 50 nm is required, which corresponds to a  $\sim 2\text{ }\mu\text{m}$  thick etalon assuming an index of 1.5. Such an etalon is difficult to realize from bulk glass plates, which can hardly be made thinner than  $\sim 20\text{ }\mu\text{m}$ . To overcome this limitation, we used a home-made free-standing PMMA film as an etalon: a mixture (1:1) of two PMMA solutions with different viscosities (PMMA A15, molar mass 950,000 and PMMA A6 with molar mass 495,000, from MicroChem Corp.) were used to obtain homogenous spin-coated films with a thickness in the desired micron range. After spin coating (3500 rpm for 75 s), the PMMA-coated glass samples were transferred to the oven and annealed at 50°C during 30 s to evaporate the solvent while keeping the film soft enough to enable the layer to be peeled off gently. The free-standing film was then glued to an annular mount ([Fig. 6.16](#)).

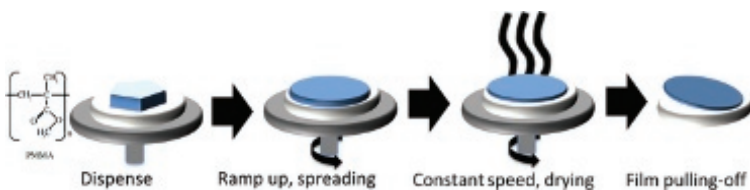


**Figure 6.16** Experimental procedure for a few micrometer thick self-standing PMMA film.

**Figure 6.17** shows the lasing spectra recorded using a spectrometer with a resolution of 0.8 nm. The wavelength can be continuously tuned over 40 nm for each dye material by tilting the etalon. Each peak has a full-width half maximum (FWHM) of 3 nm due to the

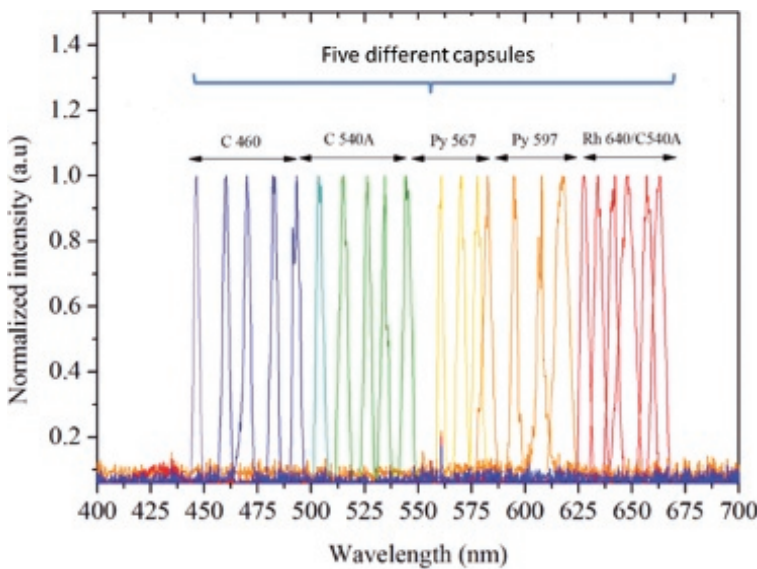


**Figure 6.17** Tunability results with five capsules: coumarin 460 (C 460, blue solid line), coumarin 540 A (C 540A, green), pyrromethene 567 (Py 567, light orange solid line), pyrromethene 597 (Py 597, dark orange solid line), and with a blend of Rhodamine 640 (Rh 640) and C 540A (red solid line). Continuous tunability is obtained through a slight tilting of 2  $\mu\text{m}$  thick free-standing polymer film acting as an intracavity Fabry-Pérot etalon. Adapted from Ref. [47] with the permission of AIP Publishing.



**Figure 6.18** Long-exposure photograph of the setup showing the UV pump beam (coming from the right), and the output coupled beam (on the left). The material used here is pyrromethene 597.

weak finesse of the etalon and contains many modes of the external cavity, which cannot be resolved here. *In fine* a continuous tunability is possible between 440 and 670 nm using only five dye capsules.

The laser efficiency was identical in a VECSOL configuration (i.e., with the gain medium directly spin-coated onto the rear mirror) with the same cavity length, proving that the Brewster-angled gain chip and the tuning etalon only brought negligible additional losses.

While photostability is a crucial issue for organic lasers, most efforts directed toward solving photodegradation issues have been focused either on the development of encapsulation techniques [48] or on improved chemical designs of the chromophores [49]. However, enhancing stability and lifetime at any price might be based on an inadequate idea of the targeted applications for OSSLs. Indeed, as the latter will never be able to compete with crystalline or semiconductor solid-state systems in terms of reliability and stability, most applications that strongly demand a truly tunable visible laser (e.g., biophotonics, spectroscopy, sensing, or more generally applications based on image capture or measurement) will need a laser with a stable intensity only for a limited amount of time, that is maybe only a few thousands pulses, depending on the required signal-to-noise ratio, which is absolutely compatible with OSSLs operating in ambient conditions.

Here the output emission decreased to half its initial value after only a few hundred pulses for a fixed position of the pump spot. This modest one-spot lifetime is the result of the energetic UV pumping and the absence of any encapsulation. To maintain stable lasing performance during hours of operation, the gain capsule could be translated to illuminate a fresh spot after degradation. As an example, a pump spot of diameter 100  $\mu\text{m}$  and a 25 mm  $\times$  8 mm capsule allows  $\approx$ 25,000 spots equivalent to  $\approx$ 833 h of operation at 10 Hz ( $\approx$ 3  $\times$  10<sup>7</sup> pulses).

This type of laser structure can consequently be thought of as an innovative solution to photodegradation issues if the gain capsule is regarded as a disposable element. Adding the costs of dye powder, optical grade PMMA solution and glass slide, the cost of a single capsule does not exceed 1 euro.

To further investigate the low-cost potential of these capsules, the spin-coating process can be replaced by an inkjet process, which enables printing side by side different “pixels” on the same substrate.

The laser ink has been formulated in order to obtain thick films (>10  $\mu\text{m}$ ) to obtain full absorption of the 532 nm pump light with low dye concentration to avoid aggregation. A good optical quality and transparency are also required for laser applications. For this purpose, we used a commercial UV-curable dielectric ink, EMD6415 from Sun Chemical, known for its dielectric properties but which had never been used in the context of printed photonics. A small (<1% vol.) fraction of dye is added after dissolution in ethanol. After UV curing at 365 nm, 20  $\mu\text{m}$  thick nonporous films are obtained for a drop spacing of 20  $\mu\text{m}$ , in the form of square-millimeter-sized pixels. The films show good planarity without any scalloped effect, a low roughness (<2 nm RMS), and high transparency (>95%). The laser performance is shown to be comparable to the reference device made from a spin-coated PMMA uniform layer.

This kind of widely tunable laser source is likely to find applications in spectroscopy or sensing, where a high-brightness laser beam at a controllable visible wavelength is needed, but where stability is not a stringent requirement beyond the time needed for a single set of measurements.

### 6.3.2 VECSOLs as Ultranarrow Linewidth Single-Mode Organic Lasers<sup>b</sup>

Most solid-state organic laser devices demonstrated so far have been able to operate in SLM. However, the first-order coherence of the laser field, a direct measure of the spectral width, is typically very low. The coherence length in all thin-film lasers reported so far is no longer than a few millimeters, or stated differently, the linewidth is not below a tenth of nanometer [50–56].

For applications such as holography, phase-sensitive sensing techniques, quantum information processing or high-resolution spectroscopy, though, longer coherence lengths are strongly desired. A too large linewidth is also a drawback for sensors based on a measurement of a wavelength shift.

Thanks to its open structure, one of the cavity mirrors of a VECSOL (the remote dielectric output coupler) is here replaced by a VBG [57] (Fig. 6.19). This spectrally narrow reflective mirror enables coherence lengths up to 1 m (200 MHz or 0.26 pm linewidth), representing a linewidth reduction of two to three orders of magnitude compared to state-of-the-art thin-film lasers. The simple experimental arrangement enables a considerable gain in compacity and simplicity when compared to dye lasers, in which linewidths < GHz are obtained but with much more complex grazing-incidence gratings [58] or grating + prism combinations [59].

Narrow linewidths (sub-pm or sub-GHz) are challenging to obtain in classical (non-external) geometries of laser resonators. The first reason is that as the inverse of the target linewidth is at most equal to the laser pulse duration  $\tau_L$  (for a Fourier-transform limited pulse), the laser pulse must last some nanoseconds at least, but must also be temporally “smooth,” that is, it should not be structured with relaxation oscillation peaks. This condition is met when the photon cavity lifetime  $\tau_{\text{cav}}$  is longer than the photoluminescence lifetime  $\tau_f$  (class A laser), which happens to fall in the nanosecond range for all organic fluorescent visible emitters. Hence sub-pm SLM lasing can be achieved when time constants

---

<sup>b</sup>This section summarizes and reuses parts of Ref. [65].

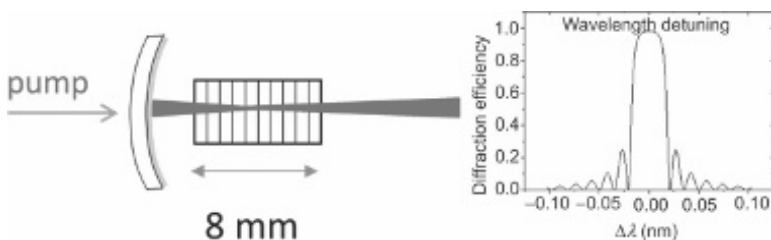


**Figure 6.19** Schematic representation of the VBG-VECSOL setup. Right: calculated diffraction efficiency at normal incidence versus wavelength of the VBG used in this work. The central wavelength is 633.14 nm.

involved obey:

$$\tau_{\text{cav}} \sim \tau_L > \tau_f (\sim ns)$$

As a distinctive feature of VECSOLs is their nanosecond photon cavity lifetimes, they are adequate for this purpose together with nanosecond-long pump pulses. In contrast, in OVCSELs the cavity is too short ( $<\mu\text{m}$ ) so that with finesse typically  $<10^2$  to  $10^3$ , the photon cavity lifetime is less than 1 ps; hence one of the lowest reported OVCSEL linewidths is as broad as 0.02 nm [5] and corresponds to the Fourier limit of the first 100 ps oscillation relaxation pulse. In DFB planar resonators, although propagation distances are much longer, scattering losses are high and lead to photon cavity lifetimes that are only a few hundreds of femtoseconds [60, 61].

However, obtaining SLM lasing in a very multimode “long” external cavity requires very selective additional spectral filtering with a bandwidth of the order of the FSR. The reason for such a stringent requirement originates in the ineffectiveness of mode competition in OSSLs, briefly discussed in [Section 6.2.5](#). To do so, VBGs [57] are the ideal choice in virtue of their unique combination of high spectral and angular selectivity. The use of VBGs as parts of lasers resonators enabled demonstration of dramatic spectral and angular narrowing of emission in semiconductor, solid-state and fiber lasers [62]. Moreover, VBGs recorded in photo-thermo-refractive glass provide optical gratings with high diffraction efficiency, with also good thermal stability, large transparency range

from 350 nm to 2700 nm, and high laser damage threshold (typically  $>40 \text{ J/cm}^2$ ) [57].

Here we designed a reflective VBG with a long interaction length (the VBG length is  $L_{\text{VBG}} = 8.3 \text{ mm}$ ) and a small index modulation, in order to get a very narrow stopband (35 pm FWHM, see inset of Fig. 6.19) and a high diffraction efficiency (around 98%).

The setup (Fig. 6.19) consists of a highly reflective dielectric spherical mirror onto which a film of Rhodamine 640 doped PMMA is spin-casted. The VBG closes the cavity and acts as the flat output coupler.

A frequency-doubled Nd:YAG laser (PowerChip from TeemPhotonics) emitting 0.4 ns FWHM pulses (at 10 Hz rep. rate) was used as a pump source. The narrow linewidth of the VBG-VECSOL laser is too narrow to be measured with a standard grating spectrometer and was derived from a coherence length measurement performed with a Michelson interferometer, ideally suited for single-pulse measurements: The laser beam was collimated and split into two equally intense beams by a beam splitter and superimposed onto a CCD camera with a variable propagation time delay  $\tau$ . A fringe pattern was obtained by making the two beams interfere with a small angle, enabling the measurement of the visibility  $V = \frac{I_{\max} - I_{\min}}{I_{\max} + I_{\min}}$  from the central fringes in one single image for a given optical path difference. Hence, the measured linewidth reflects the single-pulse linewidth, which is found to be stable from pulse to pulse. From the measured data, numerical integration yields a coherence time defined by [63]:

$$\tau_c = \int_{-\infty}^{+\infty} |V^2(\tau)| d\tau \quad (6.1)$$

VBG lasing occurs as a single peak at the expected design wavelength of 633.14 nm. From the variation of visibility  $V$  versus time delay, we found upon numerical integration (using Eq. 6.2) a coherence time  $\tau_c = 0.7 (\pm 0.05) \text{ ns}$ , or a corresponding coherence length  $c\tau_c = 20 \text{ cm}$ . Assuming a Gaussian shape for the power density, the FWHM spectral width is  $\Delta\nu = 0.66/\tau_c = 930 \text{ MHz}$  ( $\Delta\lambda = 1.25 \text{ pm}$ ). In order to infer whether the laser pulse is Fourier-transform limited,  $V(\tau)$  has to be compared with the autocorrelation

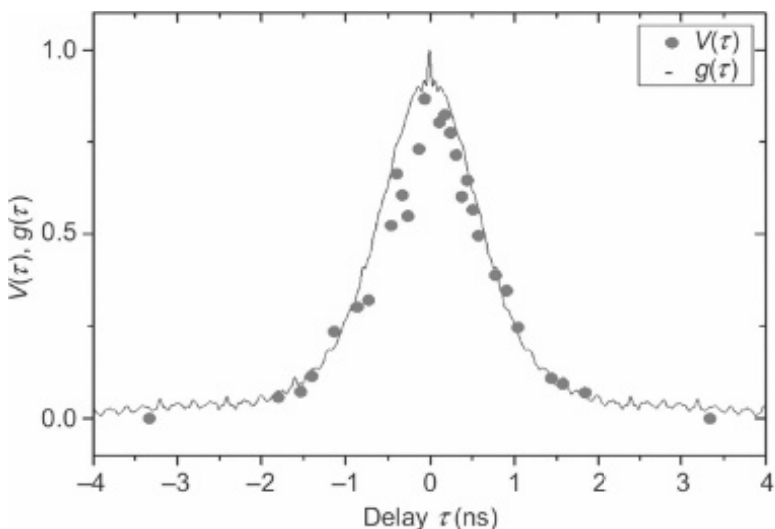


**Figure 6.20** Comparison of measured fringe visibility  $V(\tau)$  with a Michelson interferometer (dots) with the autocorrelation function  $g(\tau)$  of the square root of the laser pulse intensity (solid line), for a VBG-VECSOL pumped with a 0.4 ns FWHM pump source. Adapted from Ref. [65] with permission of Nature Publishing Group.

function of the field envelope [63]:

$$g(\tau) = \frac{\int \sqrt{I(t)}\sqrt{I(t+\tau)}dt}{\int I(t) dt} \quad (6.2)$$

where  $I(t)$  is the measured laser pulse intensity profile, which has a width of 0.8 ns (FWHM). The function  $g(\tau)$  is computed from  $I(t)$ , neglecting instrumental response function. The good matching between  $V(\tau)$  (measured with a  $\pm 10\%$  uncertainty) and  $g(\tau)$  is apparent in Fig. 6.20: The reduced  $\chi^2$  factor testing the goodness of curve matching [64] is around 4, showing that the pulse is, within experimental uncertainty, Fourier-transform limited.

In order to obtain a longer coherence length, the pump source can be replaced by a laser emitting 20 ns pulses. Under this regime, the laser pulse lasts about 15 ns. A visibility curve with a coherence time  $\tau_c = 3.3$  ns is derived, i.e., a coherence length of 1 m (corresponding to a linewidth of 0.26 pm), although in this case the laser pulse is not Fourier-transform limited any more.

The spectral purity of a thin-film organic solution-processed solid-state laser can thus be enhanced by several orders of magnitude, down to 0.26 pm, thanks to the combination of a VBG with a vertical external-cavity architecture.

Remarkably, continuous tunability is also possible using a transversally chirped VBG [66]. We used interference of spherical wavefronts to make a VBG with a transverse chirp. The grating had a peak reflectivity of 99% for 610 nm, a transverse chirp of 60 pm/mm. By translating the grating and with no impact on the cavity alignment, the laser emission wavelength has been tuned over 3 nm with sub-GHz spectral bandwidth and output peak power in the kilowatt range.

This work opens new perspectives for developing compact, ultranarrow linewidth, low-cost, and ultimately broadly tunable laser sources.

### 6.3.3 VECSOLs as Deep-UV Lasers by Intracavity Nonlinear Optics<sup>c</sup>

Organic lasers essentially emit in the visible range: Deep-blue or UV organic emitters are difficult to find, although there exists some UV emitters with good photoluminescence quantum yields. For instance, the theoretical quantum yields of fluorescence in the acene series does not vary in a simple way starting from naphthalene (two benzene rings stuck together, deep-UV emission, quantum yield 31%) to pentacene (five benzene rings, emission in the red, quantum yield 23%), and some UV dyes like coumarin 1 emitting around 380 nm have quantum yields as high as 0.85 in oxygen-free solutions. As far as organic lasing is concerned, the most relevant issue about UV emitters is more practical in nature and deals with photostability. As a laser effect in the UV requires excitation with photons of higher energy in the UV or the deep UV (although there has been a demonstration of two-photon pumping of a blue polyfluorene laser [67]), this causes extremely fast degradation of the molecule, as high-energy photons have enough energy to cause direct bond breaking with creation of reactive radicals. Because of

<sup>c</sup>This section summarizes and reuses parts of Ref. [71].

the large potential interest for spectroscopy, substantial efforts have, however, been made to look for stable and efficient UV emitters, but the lowest lasing wavelength achieved to date directly from an organic semiconductor film is 361.9 nm [68], obtained with a thermally evaporated spiro-terphenyl film.

Consequently, in many application domains where tunable UV (200–400 nm) laser sources are needed (such as atmospheric spectroscopy, ionization spectrometry, chemical or biological hazard detection, laser-induced fluorescence spectroscopy, combustion diagnostics, or photobiology [69]), bulky and complex solid-state laser with multiple nonlinear optical conversion stages are still the dominant solution.

An alternative route exists to reach the UV domain with a compact and low-cost organic thin-film device, while not compromising photostability, by using a VECSOL with intracavity frequency. Whereas frequency doubling has been commonly used in liquid dye lasers to obtain tunable UV light [70], it has remained largely unexplored in solid-state dye lasers, presumably because available intensities were too weak.

The design of an efficient frequency-doubled organic thin-film laser is based on two simple building principles: (i) The laser beam at the fundamental wavelength must have high peak brightness, and (ii) the resonator must be open to allow for intracavity mixing (upon insertion of an efficient nonlinear crystal inside the cavity).

Neither condition is actually met in traditional organic thin-film laser structures, such as DFB or DBR lasers, microcavities and microdisks. Inserting a nonlinear crystal inside the open cavity of a VECSOL is comparatively straightforward, as shown in Fig. 6.21: The VECSOL is made to emit in the red part of the spectrum (with Rhodamine 640 dye), with tunability around a central wavelength of 625 nm, and the nonlinear crystal (BBO) is cut for type-I phase matching at this wavelength.

In order to maximize the intracavity peak power for the fundamental radiation, both mirrors were chosen highly reflective in the 600–650 nm range, and the concave mirror was also coated for high reflectivity in the 300–330 nm range to enable conversion of the red beam in both propagating directions. The VECSOL efficiency drops as the cavity length increases, as discussed in Section 6.2.4.

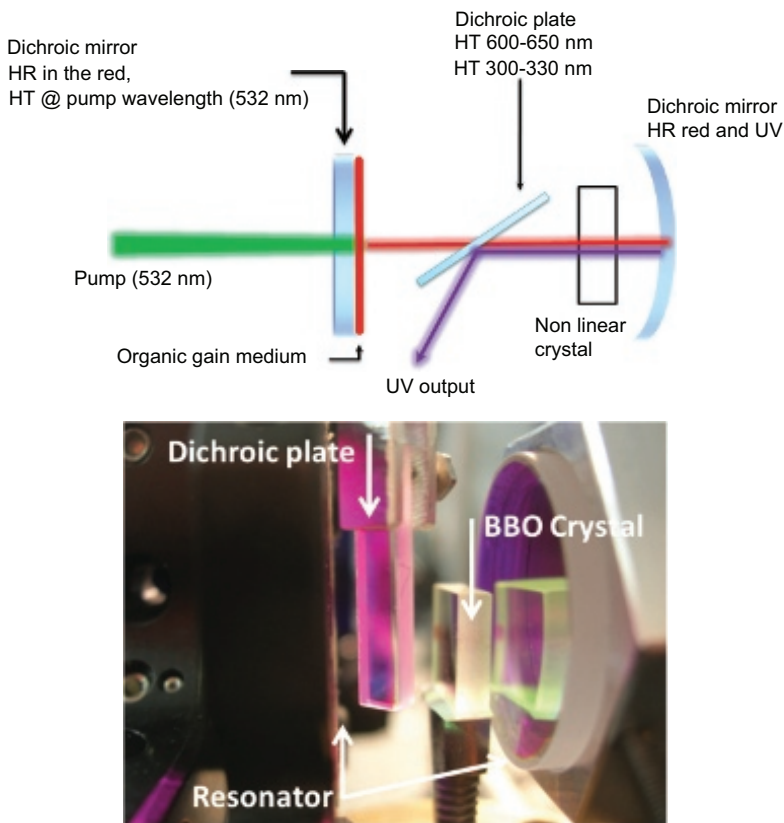


**Figure 6.21** Experimental setup (photograph: close-up of the cavity with dichroic plate and BBO crystal. The length of the cavity is 10 mm). The organic layer is spun cast onto the plane mirror; the concave mirror is highly reflective for both red and UV beams. Adapted from Ref. [71] with permission of AIP Publishing.

Here the total length of the cavity was set to 10 mm, which was the minimum length practically achievable given the extent of intracavity elements. The setup remains consequently extremely compact (see Fig. 6.21) and could be further miniaturized.

A dichroic plate was inserted at Brewster angle inside the cavity, with one face having a high-reflectivity coating in the UV for s-polarization along with a high p-polarization transmission coating in the 600–650 nm range. The role of this plate was to allow an

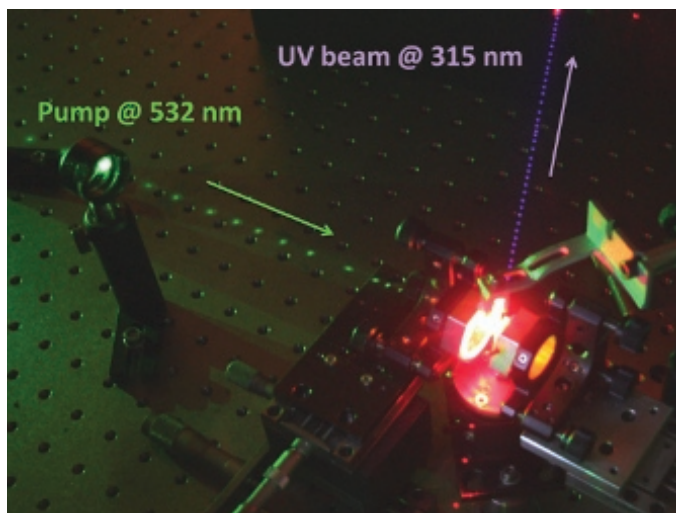


**Figure 6.22** Long-exposure photograph of the setup showing the pump beam (green, coming from the left), a faint red beam leaking from the dichroic plate (bottom), and the UV beam (on top). Reproduced from Ref. [71] with permission of AIP Publishing.

efficient type-I phase-matching scenario by forcing the red laser emission to be p-polarized, and also enabled an efficient outcoupling of the UV beam, while making sure that UV photons never encounter the organic film. This avoids any UV-enhanced photodegradation and decouples degradation issues from UV generation.

The input–output characteristics of the source are shown in Fig. 6.23; the UV emission exhibits a parabolic evolution versus pump power, as expected when pump depletion is negligible. The UV output is  $1 \mu\text{J}$  per pulse, corresponding to a peak power of 250 W; the optical-to-optical conversion efficiency (UV energy divided by the absorbed pump energy) is 2%. For higher pump power levels, photodegradation provoked a sub-linear behavior of the laser efficiency curve and a reduced lifetime. The spatial profile of the UV beam as well as that of the fundamental red beam is diffraction-limited.

The spectrum of the red laser is controlled by the sub-cavity formed by the organic thin film acting as a Fabry–Pérot etalon (see Section 6.2.5 and Fig. 6.24); it comprises several peaks spaced by

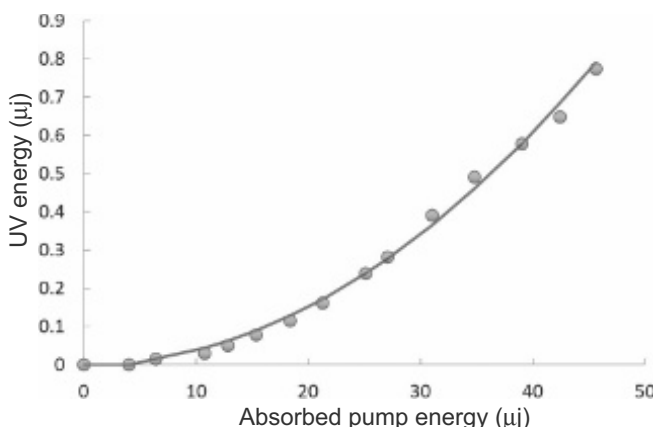


**Figure 6.23** Energy of the UV output (at 315 nm) versus absorbed laser pump energy at 532 nm. The full line is a parabolic fit started from laser threshold.

6 nm corresponding to the FSR of a 21.7  $\mu\text{m}$  thick etalon. The UV spectrum, in contrast, exhibits a single peak, because the spectral acceptance of the nonlinear process (on the order of 0.5 nm) allows only one of the red peaks to fulfill the phase-matching condition at a given crystal angle. The UV emission is consequently tunable by discrete steps upon BBO orientation from 309.5 to 316 nm. Interestingly, the device is also continuously tunable between these values in virtue of the non-perfect thickness homogeneity of the film, especially near the edges where the spin-casting process causes the film to be thicker than at the center [17]. It was then possible to obtain continuous tunability from 309 to 322 nm, by combining a scan of the pump spot location to a fine control of BBO orientation.

VECSOLs can be used to produce tunable ultraviolet radiation (here between 309 and 322 nm, but of course other wavelengths can be obtained with another combination of organic gain material and nonlinear crystal), based on intracavity sum-frequency mixing. Several characteristics that are specific to the VECSOL architecture are used here: a wide open cavity to insert multiple optical elements (crystal, dichroic plate), high energy with short pulses and diffraction-limited beam to reach the level of power brightness required to achieve efficient nonlinear conversion.

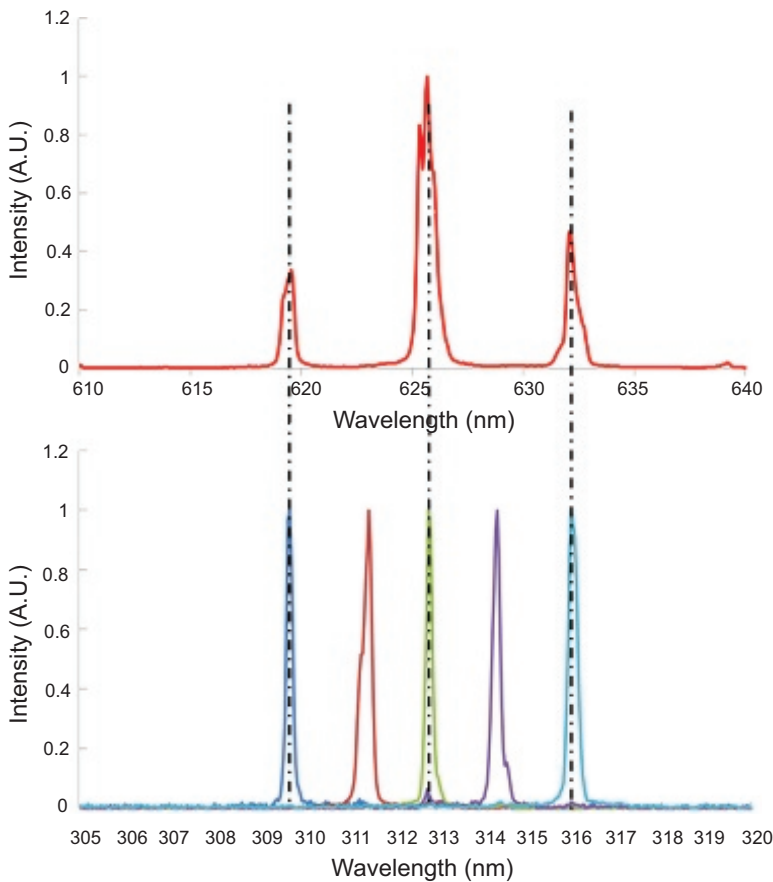


**Figure 6.24** (Top) typical emission spectrum of the red laser. (Bottom) several individual UV peaks obtained for a given pump spot location onto the organic layer, for different orientations of the BBO crystal (arbitrary units, normalized). In addition to second harmonic generation associated to the red peaks, non-degenerate sum-frequency mixing of adjacent red peaks occurs and produces extra UV wavelengths between the SHG peaks. Reproduced from Ref. [71] with permission of AIP Publishing.

## Acknowledgments

The authors acknowledge Oussama Mhibik, Zhuang Zhao, Hadi Rabbani-Haghghi, Malik Nafa, Nordine Diffallah, Ivan Divlansky,

Sébastien Sanaur, Tatiana Leang, MC Castex, Alain Siove, and Thomas Gallinelli for their contributions to the works presented in this chapter. We also thank Thierry Billeton, Albert Kaladjian, and Fabrice Wiotte for technical assistance. We thank the Agence Nationale de la Recherche (Bachelor ANR-07-JCJC-0029, Vecpresso ANR-12-EMMA-0040-01, Edelveis ANR-2012-BS09-0012-01), the C'nano Ile de France, the LABEX SEAM, CNRS and Université Paris 13 (BQR grants) for funding one or several of the works presented in this chapter.

## References

1. S. Forget and S. Chénais, *Organic Solid-State Lasers* (Springer-Verlag, 2013).
2. S. Chénais and S. Forget, *Polym. Int.* **61**, 390 (2012).
3. I. D. W. Samuel and G. A. Turnbull, *Chem. Rev.* **107**, 1272 (2007).
4. N. Tessler, G. J. Denton, and R. H. Friend, *Nature* **382**, 695 (1996).
5. V. Bulovic, V. G. Kozlov, V. B. Khalfin, and S. R. Forrest, *Science* **279**, 553 (1998).
6. M. D. McGehee, M. A. Diaz-Garcia, F. Hide, R. Gupta, E. K. Miller, D. Moses, and A. J. Heeger, *Appl. Phys. Lett.* **72**, 1536 (1998).
7. G. A. Turnbull, P. Andrew, W. L. Barnes, and I. D. W. Samuel, *Appl. Phys. Lett.* **82**, 313 (2003).
8. S. V. Frolov, M. Shkunov, Z. V. Vardeny, and K. Yoshino, *Phys. Rev. B* **56**, R4363 (1997).
9. M. Lebental, J. S. Lauret, R. Hierle, and J. Zyss, *Appl. Phys. Lett.*, **88**, 031108 (2006).
10. R. C. Polson and Z. V. Vardeny, *Phys. Rev. B* **71**, 045205 (2005).
11. M. Anni, S. Lattante, R. Cingolani, G. Gigli, G. Barbarella, and L. Favaretto, *Phys. Status Solidi* **1**, 450 (2004).
12. M. A. Baldo, R. J. Holmes, and S. R. Forrest, *Phys. Rev. B* **66**, 35321 (2002).
13. T. Woggon, S. Klinkhammer, and U. Lemmer, *Appl. Phys. B Lasers Opt.* **99**, 47 (2010).
14. J. Clark and G. Lanzani, *Nat. Photonics* **4**, 438 (2010).
15. M. Zavelani-Rossi, G. Lanzani, M. Anni, G. Gigli, R. Cingolani, G. Barbarella, and L. Favaretto, *Synth. Met.* **139**, 901 (2003).

16. A. Schulzgen, C. Spiegelberg, M. M. Morrell, S. B. Mendes, B. Kippelen, N. Peyghambarian, M. F. Nabor, E. A. Mash, and P. M. Allemand, *Appl. Phys. Lett.* **72**, 269 (1998).
17. H. Rabbani-Haghghi, S. Forget, S. Chénais, and A. Siove, *Opt. Lett.* **35**, 1968 (2010).
18. Rabbani-Haghghi, H., Forget, S., Siove, A., and Chénais, S., *Eur. Phys. J. Appl. Phys.* **56**, 34108 (2011).
19. M. Kuznetsov, F. Hakimi, R. Sprague, and A. Mooradian, *IEEE Photonics Technol. Lett.* **9**, 1063 (1997).
20. Z. Zhao, O. Mhibik, M. Nafa, S. Chénais, and S. Forget, *Appl. Phys. Lett.* **106**, 051112 (2015).
21. G. Heliotis, R. D. Xia, G. A. Turnbull, P. Andrew, W. L. Barnes, I. D. W. Samuel, and D. D. C. Bradley, *Adv. Funct. Mater.* **14**, 91 (2004).
22. X. Liu, S. Lebedkin, T. Mappes, S. Köber, C. Koos, M. Kappes, and U. Lemmer, *Proc. SPIE*, **9137**, 91370Y (2014).
23. A. E. Siegman, *Lasers* (University Science Books, 1986).
24. A. Laurain, M. Myara, G. Beaudoin, I. Sagnes, and A. Garnache, *Opt. Express* **18**, 14627 (2010).
25. M. Jacquemet, M. Domenech, G. Lucas-Leclin, P. Georges, J. Dion, M. Strassner, I. Sagnes, and A. Garnache, *Appl. Phys. B Lasers Opt.* **86**, 503 (2006).
26. Z. Zhao, O. Mhibik, T. Leang, S. Forget, and S. Chénais, *Opt. Express* **22**, 30092 (2014).
27. Y. Zhang and S. R. Forrest, *Phys. Rev. B* **84**, 241301 (2011).
28. F. Duarte, *Tunable Laser Applications*, Second Edition (CRC, New York, 2009).
29. D. Schneider, T. Rabe, T. Riedl, T. Dobbertin, M. Kroger, E. Becker, H. H. Johannes, W. Kowalsky, T. Weimann, J. Wang, P. Hinze, A. Gerhard, P. Stössel, H. Vestweber, M. Kröger, E. Becker, H. H. Johannes, W. Kowalsky, T. Weimann, J. Wang, P. Hinze, A. Gerhard, P. Stössel, and H. Vestweber, *Adv. Mater.* **17**, 31 (2005).
30. A. Rose, Z. G. Zhu, C. F. Madigan, T. M. Swager, and V. Bulovic, *Nature* **434**, 876 (2005).
31. S. Forget, F. Balembois, G. Lucas-Leclin, and P. Georges, *Opt. Commun.* **220**, 187 (2003).
32. O. Mhibik, D. Pabœuf, C. Drag, and F. Bretenaker, *Opt. Express* **19**, 18049 (2011).
33. I. Breunig, D. Haertle, and K. Buse, *Appl. Phys. B* **105**, 99 (2011).

34. R. Bornemann, E. Thiel, and P. H. Bolívar, *Opt. Express* **19**, 26382 (2011).
35. M. Faloss, M. Canva, P. Georges, A. Brun, F. Chaput, and J. P. Boilot, *Appl. Opt.* **36**, 6760 (1997).
36. A. Costela, I. Garcia-Moreno, J. M. Figuera, F. Amat-Guerri, and R. Sastre, *Laser Chem.* **18**, 63 (1998).
37. I. Garcia-Moreno, A. Costela, V. Martin, M. Pintado-Sierra, and R. Sastre, *Adv. Funct. Mater.* **19**, 2547 (2009).
38. S. Klinkhammer, N. Heussner, K. Huska, T. Bocksrocker, F. Geislhöringer, C. Vannahme, T. Mappes, and U. Lemmer, *Appl. Phys. Lett.* **99**, 023307 (2011).
39. B. H. Wallikewitz, G. O. Nikiforov, H. Sirringhaus, and R. H. Friend, *Appl. Phys. Lett.* **100**, 173301 (2012).
40. S. Klinkhammer, T. Grossmann, K. Lull, M. Hauser, C. Vannahme, T. Mappes, H. Kalt, and U. Lemmer, *IEEE Photonics Technol. Lett.* **23**, 489 (2011).
41. M. Stroisch, T. Woggon, C. Teiwes-Morin, S. Klinkhammer, K. Forberich, A. Gombert, M. Gerken, and U. Lemmer, *Opt. Express* **18**, 5890 (2010).
42. V. Navarro-Fuster, I. Vragovic, E. M. Calzado, P. G. Boj, J. A. Quintana, J. M. Villalvilla, A. Retolaza, A. Juarros, D. Otaduy, S. Merino, and M. A. Diaz-Garcia, *J. Appl. Phys.* **112**, 43104 (2012).
43. B. Wenger, N. Tetreault, M. E. Welland, and R. H. Friend, *Appl. Phys. Lett.* **97** (2010).
44. P. Görrn, M. Lehnhardt, W. Kowalsky, T. Riedl, and S. Wagner, *Adv. Mater.* **23**, 869 (2011).
45. G. Heliotis, R. Xia, D. D. C. Bradley, G. A. Turnbull, I. D. W. Samuel, P. Andrew, and W. L. Barnes, *Appl. Phys. Lett.* **83**, 2118 (2003).
46. D. Schneider, T. Rabe, T. Riedl, T. Dobbertin, M. Kroger, E. Becker, H. H. Johannes, W. Kowalsky, T. Weimann, J. Wang, and P. Hinze, *Appl. Phys. Lett.* **85**, 1659 (2004).
47. O. Mhibik, T. Leang, A. Siove, S. Forget, and S. Chenais, *Appl. Phys. Lett.* **102**, 41112 (2013).
48. P. E. Burrows, V. Bulovic, S. R. Forrest, L. S. Sapochak, D. M. McCarty, and M. E. Thompson, *Appl. Phys. Lett.* **65**, 2922 (1994).
49. M. Morales-Vidal, P. G. Boj, J. M. Villalvilla, J. A. Quintana, Q. Yan, N.-T. Lin, X. Zhu, N. Ruangsupapichat, J. Casado, H. Tsuji, E. Nakamura, and M. A. Díaz-García, *Nat. Commun.* **6**, 8458 (2015).
50. F. J. Duarte, *Prog. Quantum Electron.* **36**, 29 (2012).
51. T. Voss, D. Scheel, and W. Schade, *Appl. Phys. B Lasers Opt.* **73**, 105 (2001).

52. K. Baumann, T. Stöferle, N. Moll, G. Raino, R. F. Mahrt, T. Wahlbrink, J. Bolten, and U. Scherf, *J. Opt.* **12**, 065003 (2010).
53. P. B. Deotare, T. S. Mahony, and V. Bulović, *ACS Nano* **8**, 11080 (2014).
54. H. Coles and S. Morris, *Nat Phot.* **4**, 676 (2011).
55. M. Sudzius, M. Langner, S. I. Hintschich, V. G. Lyssenko, H. Fröb, and K. Leo, *Appl. Phys. Lett.* **94**, 2009 (2009).
56. K. Yamashita, T. Nakahata, T. Hayakawa, Y. Sakurai, T. Yamao, H. Yanagi, and S. Hotta, *Appl. Phys. Lett.* **104**, 253301 (2014).
57. O. M. Efimov, L. B. Glebov, L. N. Glebova, K. C. Richardson, and V. I. Smirnov, *Appl. Opt.* **38**, 619 (1999).
58. T. W. Hänsch, *Appl. Opt.* **11**, 895 (1972).
59. A. Costela, I. García-Moreno, and R. Sastre, *Solid-State Dye Lasers* (CRC, New York, USA, 2009).
60. M. Zavelani-Rossi, S. Perissinotto, G. Lanzani, M. Salerno, and G. Gigli, *Appl. Phys. Lett.* **89**, 181105 (2006).
61. Z. V. Vardeny, *Ultrafast Dynamics and Laser Action of Organic Semiconductors* (CRC Press, 2009).
62. L. Glebov, *Rev. Laser Eng.* **41**, 684 (2013).
63. B. E. A. Saleh and M. C. Teich, *Fundamentals of Photonics* (John Wiley & Sons, Inc., New York, USA, 1991).
64. John Taylor, *Introduction to Error Analysis: The Study of Uncertainties in Physical Measurements* (University Science Books, 1997).
65. O. Mhibik, S. Forget, D. Ott, G. Venus, I. Divliansky, L. Glebov, and S. Chénais, *Light Sci. Appl.* **5**, e16026 (2016).
66. K. Seger, B. Jacobsson, V. Pasiskevicius, and F. Laurell, *Opt. Express* **17**, 2341 (2009).
67. G. Tsiminis, A. Ruseckas, I. D. W. Samuel, and G. A. Turnbull, *Appl. Phys. Lett.* **94**, 253304 (2009).
68. T. Spehr, A. Siebert, T. Fuhrmann-Lieker, J. Salbeck, T. Rabe, T. Riedl, H. H. Johannes, W. Kowalsky, J. Wang, T. Weimann, and P. Hinze, *Appl. Phys. Lett.* **87**, 161103 (2005).
69. M. A. Dubinski and P. Misra (Eds.), *Ultraviolet Spectroscopy and UV Lasers, Practical Spectroscopy Series*, vol. **30** (Marcel Dekker, New York, 2002).
70. A. Hirth, K. Vollrath, and J. Y. Allain, *Opt. Commun.* **20**, 347 (1977).
71. S. Forget, H. Rabbani-Haghghi, N. Diffalah, A. Siove, and S. Chenais, *Appl. Phys. Lett.* **98**, 131102 (2011).

## Chapter 7

# Organic Lasers with Distributed Feedback: Threshold Minimization and LED Pumping

**Guy L. Whitworth and Graham A. Turnbull**

*School of Physics and Astronomy, SUPA, University of St Andrews,  
North Haugh, St Andrews, Fife, KY16 9SS, United Kingdom  
[gl.whitworth@gmail.com](mailto:gl.whitworth@gmail.com), [gat@st-andrews.ac.uk](mailto:gat@st-andrews.ac.uk)*

In this chapter, the fundamental concepts behind distributed feedback (DFB) lasing will be introduced, beginning with the underlying perturbation theory, which describes the lasing modes of a DFB laser. This will be followed by the basic characterization/operation of an organic semiconductor DFB laser and a discussion of various fabrication techniques used to create organic DFB lasers. The chapter will conclude by exploring various design approaches to minimize the laser threshold, and the demonstration of indirect electrical pumping of an OSL using LEDs.

### 7.1 Introduction

Solid-state DFB lasers were first established by Kogelnik and Shank in the early 1970s, who proposed that optical feedback in

---

*Organic Lasers: Fundamentals, Developments, and Applications*

Edited by Marco Anni and Sandro Lattante

Copyright © 2018 Pan Stanford Publishing Pte. Ltd.

ISBN 978-981-4774-46-8 (Hardcover), 978-1-315-10233-7 (eBook)

[www.panstanford.com](http://www.panstanford.com)

waveguide structures could be achieved via a periodic modulation of either the refractive index or the gain along the waveguide [1]. This method of optical feedback was shown to exhibit narrow linewidth laser emission, widely tuneable in wavelength [2–7]. Unlike conventional laser resonators in which feedback is provided by discrete reflections at local interfaces, in the DFB laser the feedback is distributed throughout the entire gain medium. This confines a standing-wave optical mode in the periodic waveguide's core and allows for a high “single-pass” gain to be achieved in a relatively thin film of gain medium.

The first organic DFB laser by Kogelnik and Shank was created by incorporating a Rhodamine dye into a gelatin thin-film waveguide, which was optically pumped with a spatially modulated laser source to create an edge-emitting organic DFB laser [8]. These first-generation DFB lasers were all pumped by table-top systems such as regenerative amplifiers or Nd:YAG lasers [9–12]. With the development of high-gain organic media and improved resonator designs, DFB lasing thresholds have been continuously reduced over the years. Combined with an increase in the performance of compact laser pump systems, the overall spatial footprint of organic DFB laser setups has been dramatically reduced, such that they can be pumped by microchip lasers [11, 13, 14], diode lasers [15, 16], and even light-emitting diodes (LEDs) [17–19]. While electrical pumping still remains a significant challenge, the onset of indirect electrical pumping from LEDs (made capable through the low thresholds of DFB lasers) can offer many of the advantages of an electrically pumped organic laser. This advance allows for small portable organic lasers to be used in applications such as lab-on-a-chip experiments [20, 21], photometry [22], and chemical sensing [18, 23].

## 7.2 A Simple Model for Distributed Feedback

To determine the basic condition for distributed feedback, one can start from a simple picture of conservation of the optical wavevector in one dimension. We consider an optical wave with in-plane wavevector  $+\vec{\beta}$  propagating in a periodic slab waveguide, with

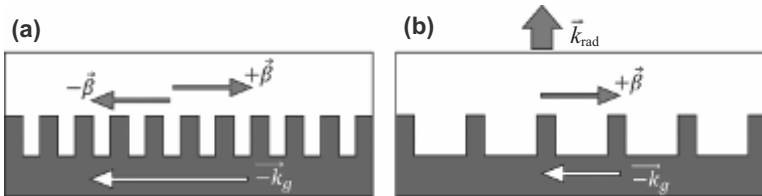


**Figure 7.1** Diagrams of first- and second-order scattering in periodic waveguide structures for (a) a first-order DFB grating, providing feedback and (b) a second-order DFB grating outcoupling a radiating wave.

grating period  $\Lambda$ , and corresponding reciprocal lattice vector  $\vec{k}_g$ :

$$|\vec{k}_g| = \frac{2\pi}{\Lambda} \quad (7.1a)$$

$$|\vec{\beta}| = \frac{2\pi n_{\text{eff}}}{\lambda} \quad (7.1b)$$

where  $m$  is an integer number and  $n_{\text{eff}}$  is the effective refractive index of the waveguide mode [24]. In order for the grating to scatter the wave into counter propagation with wavevector  $-\vec{\beta}$ , momentum must be conserved such that:

$$\vec{\beta} - m\vec{k}_g = -\vec{\beta} \quad (7.2)$$

where  $m$  is an integer. Using Eq. 7.1, this can be rearranged to give the Bragg condition for distributed feedback

$$m\lambda_b = 2n_{\text{eff}} \quad \Lambda \quad (7.3)$$

Figure 7.1 shows examples of scattering in both first-order ( $m = 1$ ) and second-order ( $m = 2$ ) DFB gratings. In the case of the second-order, a higher harmonic of the lattice momentum is being used to create feedback for the in-plane propagating waves. First-order scattering is still present in this case, which results in a zero in-plane wavevector; and a wave is radiated normal to the surface to conserve energy (Fig. 7.1b). When the Bragg condition is met and a net positive gain is introduced to the waveguide, a DFB laser can be formed.

## 7.3 Coupled Mode Theory

### 7.3.1 First-Order Distributed Feedback

For a more complete picture of first-order DFB, we can model the electric field using the scalar Helmholtz wave equation (Eq. 7.4) in a periodic waveguide, a method known as coupled mode theory, as developed by Kogelnik and Shank [1]:

$$[\nabla^2 + k^2] E(x, z) = 0 \quad (7.4)$$

In this section we assume that  $E(x, z) = E(z)\phi(x)$ , where  $E(z)$  is the amplitude of the optical electric field as a function of the propagation  $z$  along the waveguide,  $\phi(x)$  is the transverse mode profile, and  $k$  is the wave number. The general propagation constant for the travelling wave can be defined as

$$\beta \equiv \frac{n_{\text{eff}}\omega}{c} \quad (7.5a)$$

and at the Bragg condition

$$\beta = \beta_0 \equiv \frac{n_{\text{eff}}\omega_0}{c} \quad (7.5b)$$

In a lossless planar waveguide, the propagation constant is equal to the  $z$ -component of the wave number ( $k_z = \beta$ ). However, the presence of gain and/or a refractive index modulation (with frequency  $2\beta_0$ ) introduces a perturbation into the Helmholtz equation such that

$$k_z^2 = \beta^2 + 2i\beta g_\omega - \frac{\omega^2}{c^2} \Delta\varepsilon \sum_{m \neq 0} \int \xi_m(x)\phi(x) dx e^{2mi\beta_0 z} \quad (7.6)$$

where  $g_\omega$  is the net gain at frequency  $\omega$ ,  $\Delta\varepsilon$  is the difference in dielectric constant across the modulated interface, and  $\sum_{m \neq 0} \xi_m(x)e^{2mi\beta_0 z}$  is a Fourier series for the periodic structure, with Fourier coefficients  $\xi_m(x)$ . Combining Eqs. 7.4 and 7.6 gives the perturbed Helmholtz equation for a periodic waveguide (Eq. 7.7).

$$\left[ \frac{\partial^2}{\partial z^2} + \beta^2 + 2i\beta g_\omega - \frac{\omega^2}{c^2} \Delta\varepsilon \sum_{m \neq 0} \int \xi_m(x)\phi(x) dx e^{2mi\beta_0 z} \right] E(z) = 0. \quad (7.7)$$

As a test solution, we assume we have two counter propagating waves with propagation constant matching the DFB Bragg condition, as depicted in Fig. 7.2.

$$E(z) = A(z) e^{i\beta_0 z} + B(z) e^{-i\beta_0 z} \quad (7.8)$$

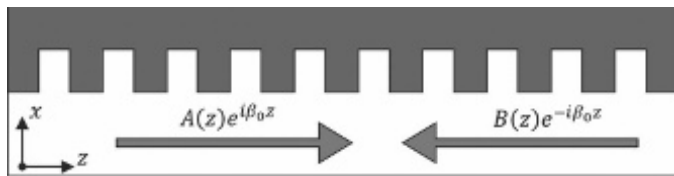


**Figure 7.2** Periodic waveguide with a general electric field of two counter propagating waves.

Assuming that no high-order waves are supported modes of the waveguide, then only the  $m = \pm 1$  terms need to be considered in the Fourier series. Additionally,  $A(z)$  and  $B(z)$  are assumed to be slowly varying functions such that  $\nabla^2 A = \nabla^2 B = 0$ . Hence, after substituting Eq. 7.8 in Eq. 7.7 and gathering like terms, we find

$$\begin{aligned} & \left[ (\beta^2 + 2i\beta g_\omega - \beta_0^2) A - 2i\beta \frac{dA}{dz} - \frac{\omega^2}{c^2} \Delta \varepsilon \int \xi_1 \phi dx B \right] e^{i\beta_0 z} \\ & + \left[ (\beta^2 + 2i\beta g_\omega - \beta_0^2) B + 2i\beta \frac{dB}{dz} - \frac{\omega^2}{c^2} \Delta \varepsilon \int \xi_{-1} \phi dx A \right] e^{-i\beta_0 z} \\ & + [\dots] e^{-3i\beta_0 z} + [\dots] e^{3i\beta_0 z} = 0 \end{aligned} \quad (7.9)$$

Equating the sum of the coefficients of the  $e^{\pm i\beta_0 z}$  waves to zero defines the coupled mode equations for first-order DFB lasers:

$$(g_\omega - i\Delta\beta) A + \frac{dA}{dz} = i\kappa B \quad (7.10a)$$

$$(g_\omega - i\Delta\beta) B + \frac{dB}{dz} = i\kappa A \quad (7.10b)$$

Here we have assumed a symmetric structure  $\Rightarrow \xi_m = \xi_{-m}$  and defined the coupling constant  $\kappa$  and the frequency detuning  $\Delta\beta$  as

$$\kappa = -\frac{\omega^2}{2\beta c^2} \Delta \varepsilon \int \xi_m(x) \phi(x) dx \quad (7.11)$$

$$\Delta\beta \equiv \frac{\beta^2 - \beta_0^2}{2\beta} \approx \beta - \beta_0 \quad (7.12)$$

The coupled mode equations allow one to determine the coupled wave amplitudes,  $A(z)$  and  $B(z)$ . An appropriate test solution for the coupled mode equations is a sum of exponentials

$$A(z) = a_1 e^{\gamma z} + a_2 e^{-\gamma z} \quad (7.13a)$$

$$B(z) = b_1 e^{\gamma z} + b_2 e^{-\gamma z} \quad (7.13b)$$

where  $\gamma$  is known as the complex propagation constant and defined as

$$\gamma^2 = (g_\omega - i\Delta\beta)^2 + \kappa^2 \quad (7.14)$$

The first-order coupled mode equations (Eq. 7.10) describe a self-oscillating device with gain. We assume that there are no external incoming waves to the system, and that the initial wave amplitudes are zero at the device boundaries. Considering a DFB structure of length  $L$ , we define the boundary conditions  $A(0) = B(L) = 0$ . If we assume that the grating structure is symmetric, it follows that the electric field must take either a symmetric ( $E(z) = E(-z)$ ) or an anti-symmetric ( $-E(z) = E(-z)$ ) solution. Imposing these conditions on the test solution (Eq. 7.13), it is easy to see that the travelling wave coefficients are of the form

$$A(z) = \sinh \gamma z \quad (7.15a)$$

$$B(z) = \pm \sinh \gamma(z - L). \quad (7.15b)$$

By substituting this solution (Eq. 7.15) into the coupled mode equations (Eq. 7.10), two relations are obtained. Taking both the sum and the difference of the resulting equations, like terms can be gathered and cancelled. Repeating this process an additional two more times yields a complex transcendental eigenvalue equation for  $\gamma$ ,

$$\gamma = \pm i\kappa \sinh \gamma L \quad (7.16)$$

and the lasing mode relation

$$(g_\omega - i\Delta\beta) = \gamma \coth \gamma L \quad (7.17)$$

These above solutions tell us that for a given coupling constant  $\kappa$ , there is an infinite series of complex propagation constants  $\gamma$ , each representing a different DFB laser mode with a specific value of net threshold gain  $g_\omega$ , and frequency detuning  $\Delta\beta$  from the Bragg condition, as defined through the real and imaginary solutions to Eq. 7.17. At the end of this section, we will see that modes with the smallest detuning factors have significantly lower net gain thresholds than modes with high detuning giving DFB lasers their characteristic high degree of lasing wavelength selectivity.

### 7.3.2 Second-Order Distributed Feedback

We next extend the coupled mode theory to the case for second-order DFB. Now the problem is complicated by the addition of a first-order scattered wave, radiating at an angle perpendicular to the surface of the waveguide. This requires the electric field test in the Helmholtz scalar equation to take the form

$$E(x, z) = [A(z) e^{i\beta_0 z} + B(z) e^{-i\beta_0 z}] \phi(x) + \Delta E(x, z) \quad (7.18a)$$

where  $\Delta E(x, z)$  represents the radiated wave, normal to the waveguide. Additionally, the perturbation is altered to be a grating of half the frequency compared to that of the case for the first-order DFB laser

$$k_z^2 = \beta^2 + 2i\beta g_\omega - \frac{\omega^2}{c^2} \Delta\epsilon \sum_{m \neq 0} \int \xi_m(x) \phi(x) dx e^{mi\beta_0 z} \quad (7.18b)$$

The solution to the wave equation for these new conditions was first obtained by Kazarinov and Henry in 1985 [25]. Their analysis showed that the coupled mode equations for second-order DFB can be written as

$$\frac{dA}{dz} = (g_\omega - i\Delta\beta - \kappa_r) A + (i\kappa_f - \kappa_r) B \quad (7.19a)$$

$$-\frac{dB}{dz} = (g_\omega - i\Delta\beta - \kappa_r) B + (i\kappa_f - \kappa_r) A \quad (7.19b)$$

Here  $\kappa_f$  and  $\kappa_r$  are the feedback and radiative coupling coefficients, respectively, and are given by

$$\kappa_f = \frac{-\omega^2 \Delta\epsilon}{2\beta_0 c^2} \int dx \phi(x)^2 \xi_2(x) \quad (7.20)$$

$$\kappa_r = \frac{\omega^4 \Delta\epsilon}{4\beta_0 \beta_x c^4} \left| \int dx e^{i\beta_x x} \phi(x) \xi_1(x) \right|^2 \quad (7.21)$$

Note that here we use the opposite sign for the definition of the detuning term from that used by Kazarinov and Henry. Due to the reduced grating frequency defined in Eq. 7.18 (compared to Eq. 7.6), it is the second-order Fourier coefficient ( $\xi_2$ ), which is responsible for feedback. The first-order coefficient ( $\xi_1$ ) governing the strength of the radiated wave effectively acts as a loss mechanism in the laser.

Comparing the second-order coupled mode equations (Eq. 7.19) to those for the first-order DFB laser (Eq. 7.10), it can be seen

that they have the same general form but with the following substitutions:

$$(g_\omega - i\Delta\beta) \rightarrow (g_\omega - i\Delta\beta - \kappa_r) \quad (7.22a)$$

$$i\kappa \rightarrow (i\kappa_f - \kappa_r) \quad (7.22b)$$

As such, the second-order DFB coefficients  $A(z)$  and  $B(z)$  have the same  $\sinh(\gamma z)$  functional form as in the first-order case but now with the complex propagation constant defined as

$$\gamma^2 = (g_\omega - i\Delta\beta - \kappa_r)^2 - (i\kappa_f - \kappa_r)^2 \quad (7.23)$$

[Equation 7.17](#), which defined the locations of the lasing modes in threshold gain-frequency detuning space for first-order feedback, is now replaced by

$$(g_\omega - i\Delta\beta - \kappa_r) = \gamma \coth \gamma L \quad (7.24)$$

for a second-order DFB laser.

### 7.3.3 DFB Modal Structure

To determine the modal structure of a DFB laser, one needs first to calculate the radiative and feedback coefficients for a given grating shape, so as to parameterize [Eq. 7.24](#). To solve the DFB modal equation exactly, one can use complex contour integration and a regression algorithm in a process known as the argument principle method [26]. Alternatively, a simple graphical method can yield the approximate solutions for the threshold gains of the laser modes.

[Equation 7.24](#) can be rearranged and multiplied through by the length of the laser cavity to define a complex surface  $D$  [27]:

$$D \equiv \gamma L \cosh \gamma L - (g_\omega - i\Delta\beta - \kappa_r) L \sinh \gamma L = 0 \quad (7.25)$$

The laser modes are located at the zeros of  $D$ . To visualize this, one can computationally plot contours of this complex surface to locate the minima. Multiplying the equation through by the cavity length allows this equation to be plotted in terms of the unit-less quantities  $g_\omega L$  and  $\Delta\beta L$ .

[Figure 7.3](#) shows an example of such a contour plot using typical values of  $\kappa_r$  and  $\kappa_f$  for an MEH-PPV DFB laser [28]. Local minima can be seen to emerge as the contours approach zero ( $|D| \rightarrow 0$ ).

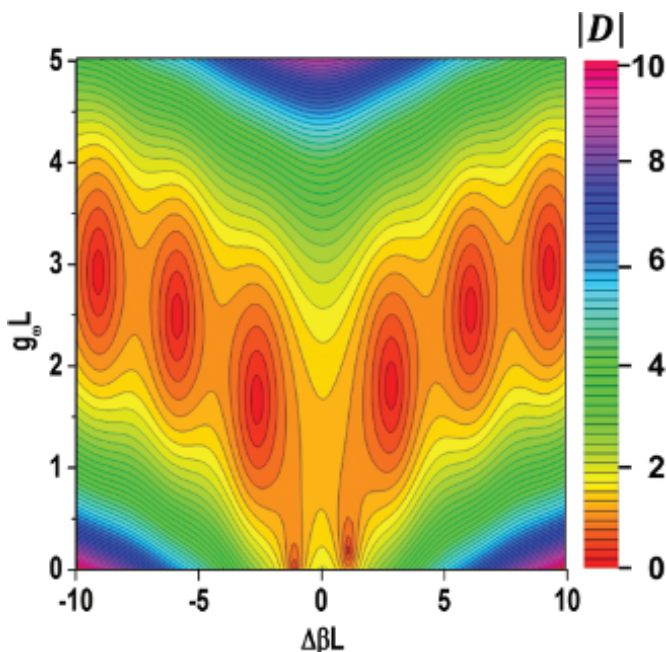


**Figure 7.3** Color-mapped contour plot of  $|D|$  for a typical MEH-PPV laser ( $\kappa_r = 10 \text{ cm}^{-1}$ ,  $\kappa_f = 110 \text{ cm}^{-1}$ ,  $L = 100 \mu\text{m}$ ) [28]. Red regions indicate areas where lasing modes occur ( $|D| \rightarrow 0$ ).

The location of these minima can be determined with increasing precision by reducing the vertical contour interval. The first thing to note is that there is no lasing mode for  $\Delta\beta = 0$  as there exists a photonic stopband centered at the Bragg frequency, within which light cannot propagate. Instead there are two series of laser modes one on each side of the stopband. The two modes on the stopband edges have dramatically lower net gain threshold than all other modes and so are most likely to undergo laser action. Lastly, we note that the stopband edge mode with negative detuning from the stopband has the lowest threshold of all, which is due to a phase slip between the positive and negative detuning edges breaking the symmetry of the system [25]. Having a singular mode with drastically lower threshold than all other possible ones in the system gives DFB lasers exceptional single wavelength selectivity with

narrow linewidth output. As seen from Fig. 7.3, this low-threshold lasing mode occurs at the lower frequency edge of the DFB photonic bandgap.

## 7.4 Experimental Characteristics

### 7.4.1 Spectral Characteristics

In this section, we will discuss some of the typical operation characteristics of organic DFB lasers. Figure 7.4a shows typical output spectra from a second-order organic DFB laser when light is collected normal to the surface. At low pump fluence, below lasing threshold (black), a characteristic spectral double peak is evident, arising from waveguided photoluminescence, which has been Bragg scattered out of the film by the periodic grating. The dip in between the peaks is the signature of the photonic stopband of the grating, within which the propagation and emission of light is suppressed along the grating axis. As the pump fluence is increased, a narrow lasing peak emerges on the long wavelength (lower frequency) edge of the stopband as predicted by Fig. 7.3, collapsing to a single narrow peak [14].

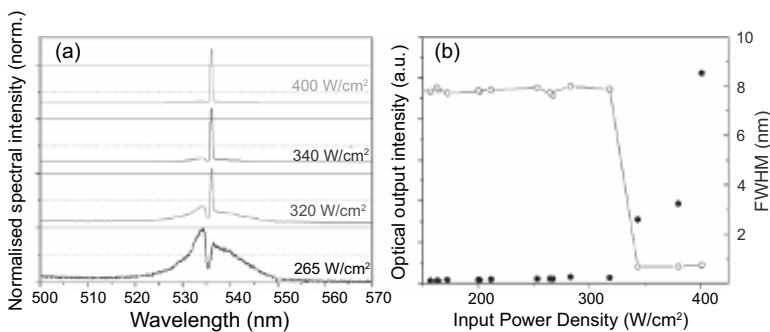


**Figure 7.4** (a) Typical output spectra of a BBEHP-PPV distributed feedback laser at varying input power density, above and below lasing threshold. (b) Optical output intensity as a function of input power density with corresponding spectral full-width half maximum.

In Fig. 7.4b, the intensity of the outcoupled light in the lasing region is plotted against the input pump power density. Above  $300 \text{ W/cm}^2$ , we see a distinct increase in the slope of the output intensity, accompanied by a dramatic reduction in the full-width half maximum (FWHM) of the surface-emitted spectrum from  $\sim 8 \text{ nm}$  to  $< 1 \text{ nm}$ . These indicate that the threshold pump density for laser action in this device is around  $320 \text{ W/cm}^2$ . It is important to note that the threshold pump density in DFB lasers is strongly dependent on the size of the gain region. From Fig. 7.3, we recall that the lasing modes each have a fixed value of  $g_\omega L$ , the product of the threshold gain and laser length. Long lasers will need lower threshold gains and, therefore, lower pump power densities. The cavity length in practice is either defined by the physical length of the grating or defined approximately by the diameter of the pump beam (if smaller than the grating). As such smaller pump spots require a higher gain (exciton density) to achieve lasing [16]. The threshold density cannot, however, be continuously reduced by a larger and larger grating/pump spot as eventually the intrinsic waveguide loss (which is assumed to be zero in the coupled mode model) will dominate.

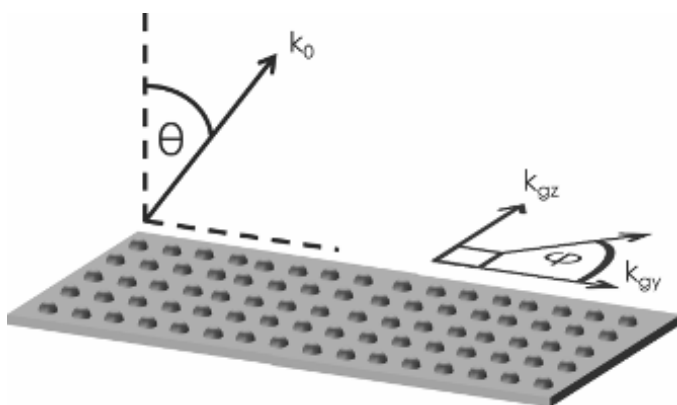
#### 7.4.2 Second-Order Outcoupling Characteristics

As mentioned above, the output beam from a second-order DFB laser is emitted normal to the waveguide surface. The angle of surface emission of light diffracted out of the waveguide is determined by conservation of in-plane wavevector when the waveguide mode is diffracted by the grating. This relation for a 2D grating may be written as

$$|\vec{\beta}|^2 = (mk_{gy} - k_0 \sin \theta \cos \phi)^2 + (pk_{gz} - k_0 \sin \theta \sin \phi)^2. \quad (7.26)$$

The angle  $\theta$  is the out-of-plane polar propagation angle with respect to the normal, and  $\phi$  is the in-plane azimuthal propagation angle with respect to a chosen grating vector, as depicted in Fig. 7.5. The integers  $m$  and  $p$  indicate the order of scattering,  $k_0$  is the free-space wavenumber, and  $k_{gy}$  and  $k_{gz}$  are the magnitudes of the grating vectors in the  $y$  and  $z$  directions, respectively.

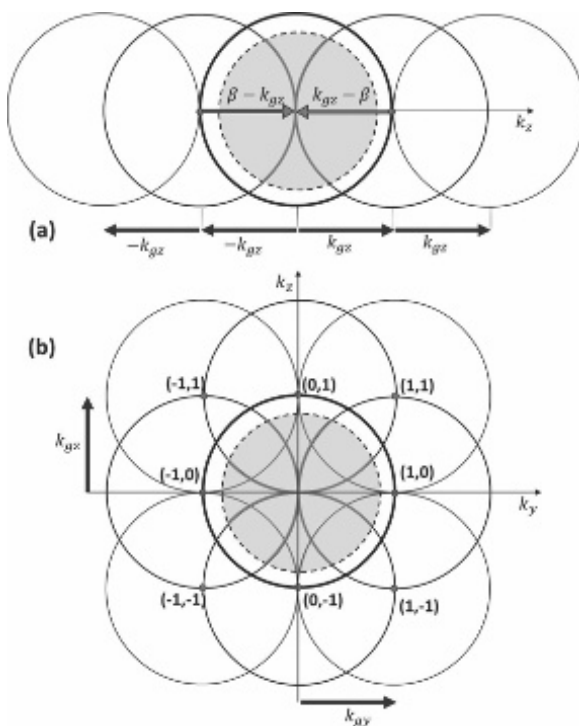
Equation 7.26 describes an infinite array of circles of radius  $\beta$  (the wavenumber of the optical mode) spaced on a rectangular



**Figure 7.5** Diagram defining the angles  $\theta$  and  $\phi$ , with respect to a 2D DFB grating with relevant  $k$ -vectors.

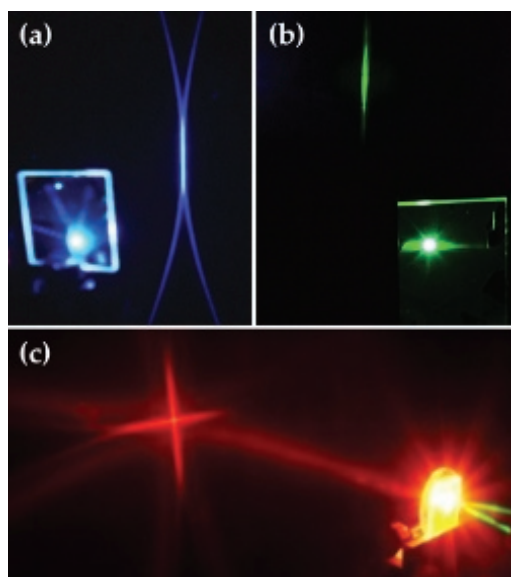
array of reciprocal lattice constants  $k_{gy}$ ,  $k_{gz}$  (see Fig. 7.6). The circles represent the loci of  $k$ -space wavevectors in the planar waveguide after ( $mn$ ) diffractions from the respective gratings. Where scattered modes fall within the light cone of the waveguide (i.e., the red arcs within the dashed circle), these modes are outcoupled into free-space with polar and azimuthal angles ( $\theta\phi$ ) according to Eq. 7.26. For the case of a freely propagating guided wave with a wavenumber close to the Bragg condition of a second-order grating, this outcoupling pattern is a pair of arcs of emission that touch at  $\theta = 0$  (red lines in Fig. 7.6a). For a 2D square-array grating, the emission takes the form of a cross-like structure of four of these arcs (red lines in Fig. 7.6b). Above laser threshold, the amplified light experiences most effective feedback (i.e., with low transverse walk-off) for angles approximately perpendicular to the grating axis, which confines the emission to a tighter arc where the scattered modes overlap.

Figure 7.7 shows three examples of the emission patterns of organic DFB lasers with different gain media and grating structures, each when driven many times above laser threshold. The first two images show 1D second-order DFB lasers for a blue- and a green-emitting semiconducting polymer gain medium. In Fig. 7.7(a), two arcs of scattered emission from the device can be seen, with



**Figure 7.6** Bragg-scattered mode circles representing the loci of  $k$ -space wavevectors in the plane of the waveguide after  $(m, n)$  diffractions from the respective gratings; (a) a 1D grating, (b) a 2D square-array grating. The bold circles of radius  $\beta = 2\pi n_{\text{eff}}/\lambda$  represent the loci of wavevectors of the unscattered waveguide mode. The shaded region inside the dashed circle represents the range of scattered in-plane wavevectors  $|\bar{k}| = 2\pi \sin \theta/\lambda$  where light escapes to free-space radiation at angle  $(\theta, \phi)$ .

the coherent laser mode being confined to the bright stripe at the intersection of the two arcs. The laser in Fig. 7.7c is a red DFB laser with a 2D micropillar grating. Evident in the image is a cross-like laser emission, which eventually separates into pairs of arcs at higher angles. The broader, fainter arcs surrounding the bright laser emission are due to Bragg-scattered ASE at slightly longer wavelength than the laser emission. It is worth noting that the emission from these lasers is shown for optical pumping far above laser threshold. For pump densities a few times threshold,



**Figure 7.7** Photographs of a variety of organic DFB lasers. (a) A 1D dioctyl-polyfluorene (PFO) (Courtesy: Georgios Tsiminis, Ref. [29]); (b) a 1D poly[2,5-bis(2',5'-bis(2"-ethylhexyloxy)phenyl)-p-phenylenevinylene] (BBEHP-PPV) (Courtesy: Nedyalka Panova); (c) a 2D poly[2-methoxy-5-(2-ethylhexyloxy)-1,4-phenylenevinylene] (MEH-PPV) (Courtesy: Georgios Tsiminis, Ref. [29]).

these 2D square-array gratings are often seen to emit a low-divergence annular beam along the normal to the film. This emission arises from a 2D Bloch wave resonance in the DFB structure, and for TE polarized transverse modes will be emitted with an azimuthal polarization. The arcs of light scattered from each grating component begin to dominate as the pump power increases well above threshold.

## 7.5 Fabrication Techniques

Fabrication of the DFB resonator requires the nanostructuring of an organic semiconductor waveguide on a sub-wavelength scale. For visible wavelength emission, the period of these feedback gratings

is typically in the 250–500 nm range. The main techniques used to write the patterns are e-beam lithography and holography. Various types of nanoreplication have been developed to imprint copies of master structures for high throughput manufacturing. In this section, these various fabrication methods will be described in further detail, as well as discussing their advantages and disadvantages.

### 7.5.1 Electron Beam Lithography

Electron beam lithography is a precise, fine, and complicated technique used to create nanostructures. The principle lies in focusing an electron beam down to a tight spot onto an electron-sensitive material known as a resist. The beam is then scanned across the film to create the desired pattern (e.g., a diffraction grating). The film is washed with a solvent to remove the unwanted areas of resist to form a topological profile, and the pattern can then be etched into the underlying substrate. This process allows for the creation of fine structures with resolutions down to  $\sim 20$  nm, often etched into silicon or fused silica. E-beam lithography can be used to write arbitrary shapes with very high resolution and so is very versatile when compared with holography, which, we will see later, is somewhat limited in scope. However, e-beam lithography is an expensive and slow method, making it undesirable for use over large areas and in industrial production of photonic structures. As such e-beam is commonly used to create a master structure to be used in additional replication processes. There are various methods in which the master structure can be quickly and inexpensively replicated, which opens the door to high-throughput fabrication of DFB gratings for organic lasers.

### 7.5.2 Holography

Another commonly used method to fabricate DFB gratings is laser interference lithography, or holography. Gratings are created by exposing a photo-polymerizable film with two or more interfering laser beams (Fig. 7.8) [30]. For a negative photoresist, the interference pattern causes the material to polymerize at locations of constructive interference, leaving destructive locations

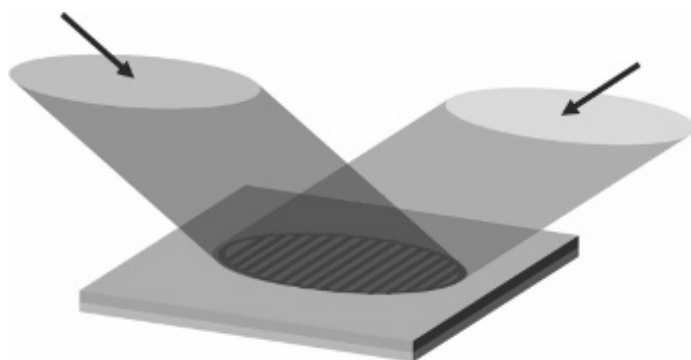


**Figure 7.8** Diagram of two interfering beams used to give a structured exposure to a UV resist layer.

unreacted. Following exposure, the film may be baked to complete the polymerization reaction, before the unpolymerized material is washed off. The grating defined in the resist may subsequently be etched into the substrate prior to the deposition of an organic semiconductor layer to make a DFB laser.

Compared with techniques involving an e-beam master structure, holographic fabrication is less versatile as it is limited to periodic interference patterns, for example 1D sinusoidal gratings. However, this technique does readily create large-area gratings and is much faster than e-beam writing.

### 7.5.3 UV Nanoimprint Lithography

UV nanoimprint lithography (UV-NIL) is an advanced soft-lithographic technique, which can be used to replicate large-area nanostructures with a high resolution [12, 31, 32]. Soft lithographies are a family of fabrication processes in which a soft elastomeric “stamp” is used to imprint structures into/onto another material. This soft stamp is usually cast from a rigid master e-beam nanostructure used as a mold. The fabrication process of a soft stamp, cured using UV light, is illustrated in Fig. 7.9a–c. First the silicon master (grey) is used to mold the liquid stamp material (yellow), which is then cured with UV light to create a

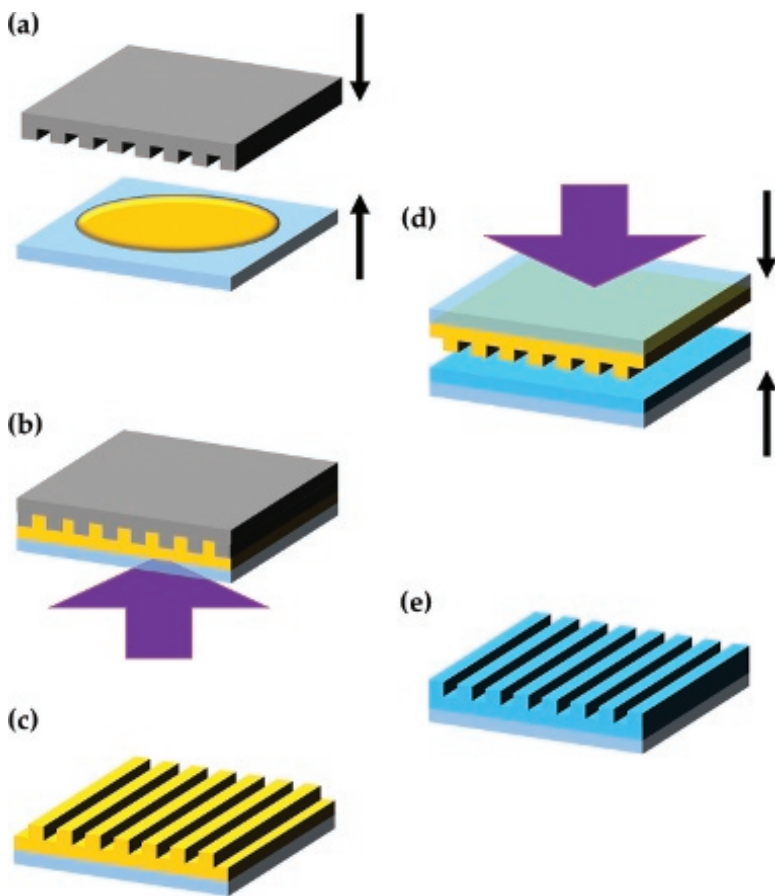


**Figure 7.9** (a) The perfluoropolyether stamp material (yellow) is cast onto a silicon master structure and (b) UV (purple) cured create a daughter stamp for soft-lithography (c). (d) The soft daughter stamp is pressed into a NIL photoresist (UV-Cur06 (blue)) and exposed to UV. (e) The result is a hardened grating substrate made out of the resist layer. Adapted from Ref. [33] with permission.

flexible “daughter” copy of the master grating with the inverse nanostructure.

Figure 7.9d,e shows the subsequent UV-NIL steps that are performed using the soft daughter stamp. The soft stamp is pressed into a polymer UV-NIL resist (blue) with typically 1 bar

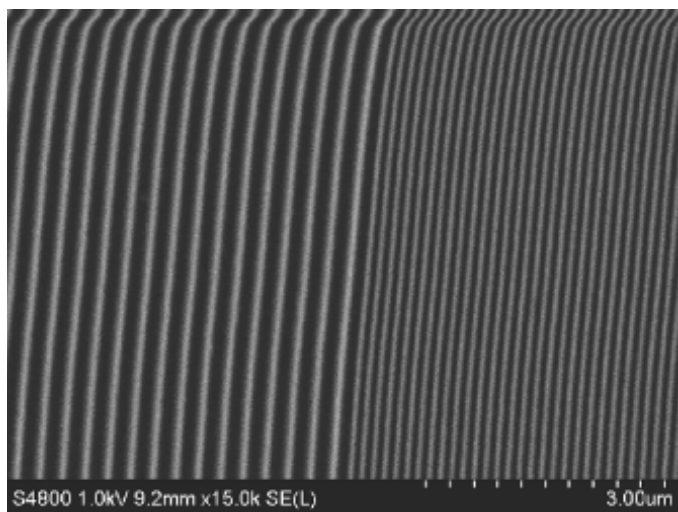


**Figure 7.10** An SEM image of a UV-Cur06 grating manufactured by UV-NIL. The image shows a mixed period grating structure with 280 nm (left) and 140 nm (right) periods. The curves at the top of the image are an artifact due to charging of the film by the SEM.

of pressure while simultaneously exposing to UV light to cure the resist layer. This process creates a polymer replica of the master grating onto which an organic semiconductor layer can be spin-coated or evaporated, to fabricate the DFB laser (Fig. 7.10). This nanoimprinting process can be repeated in quick succession using the same soft stamp, making it a potentially high-throughput method of replicating large-area gratings.

#### 7.5.4 Solvent Imprint Lithography

Solvent imprint lithography (SIL) is another soft-lithography method in which the stamp can be used to imprint directly a pattern into a layer of organic semiconductor. The principle behind the SIL process is to use an organic solvent to treat the surface of an organic semiconductor film so as to make it malleable. Once in this state, the soft stamp can be used to mold the flat film with a nanostructure. The solvent used to treat the film is sorbed into the elastomeric soft stamp while in contact with the film before the two are separated.

One of the early SIL techniques used to create polymer nanostructures was known as solvent-assisted micro-molding (SAMiM) [34]. This technique involved treating the soft stamp with a strong solvent suitable for dissolving the target organic semiconductor. Once pressed into the film, the stamp would dissolve the top layer of the organic semiconductor film in order to form a grating. This method is very successful for making deep patterns in small solution-processed molecules; however, it often produces gratings of limited imprint depths when patterning high molecular weight polymers.

More recently, an improved technique known as solvent immersion imprint lithography (SIIL) was developed by Vasdekis et al., which has been shown to produce reliable and deep microstructures [35]. In the SIIL process, the polymer film is fully immersed into a weakly interacting organic solvent. While the immersion solvent is not strong enough to dissolve the polymer film, it still must be sorbed into the film to form a gel-like material. When a soft stamp is pressed into the immersed polymer film, it can imprint the film with the desired structure and, in the process, isolate the film from the immersion bath for removal. This technique was extended further to nanoimprint directly into conjugated polymer films for fabrication of organic semiconductor DFB lasers [36].

Examples of nanostructures created by this process can be seen in Fig. 7.11 where dioctyl-polyfluorene (PFO) has been imprinted using acetone as the SIIL solvent. Figure 7.11a shows the same

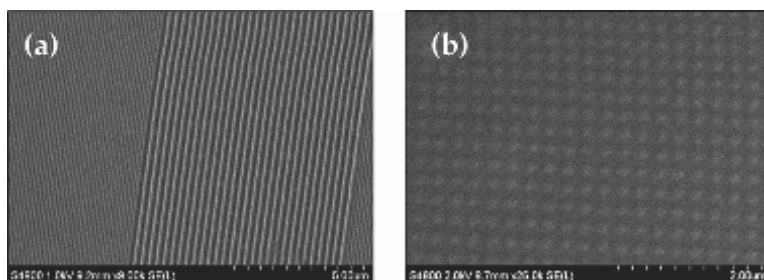


**Figure 7.11** SEM images of two dioctyl-polyfluorene gratings fabricated by SIIL. (a) A 1D mixed-order structure with 280 nm and 140 nm periods. (b) A 2D micropillar array with a 280 nm period.

structure that was shown in Fig. 7.10 with a mixed period of 280 nm and 140 nm. Figure 7.11b shows a micropillar array with a 280 nm period. Such DFB laser structures have been demonstrated to be just as effective as those fabricated through the more established technique of UV-NIL.

### 7.5.5 Thermal Imprint Lithography

An alternative direct imprinting method that can mold the organic semiconductor layer is thermal imprint lithography (TIL) [37]. TIL, however, does not necessarily need to be a “soft” process and can be performed by either a soft daughter stamp or the hard master structure directly. This process involves heating the (thermoplastic) polymer film up to its glass transition temperature, while in pressure contact with the nanopatterned stamp. After reflowing of the softened polymer to conform to the applied nanostructure, the film is cooled back below its glass transition temperature before separation from the stamp to lock in the new conformation.

## 7.6 Minimizing DFB Lasing Threshold

DFB lasers are highly affected by the particular design of grating used to create the cavity. This is because a variety of grating properties can control the radiative and feedback coefficients, as seen in Eqs. 7.20 and 7.21, which in turn determine the thresholds of the laser modes. In this section, various methods by which grating design can be exploited to reduce the threshold of surface-emitting DFB lasers will be explored. Surface-emitting cavities (using second-order DFB gratings) are advantageous for good output beam quality, as it is difficult to fabricate high-quality facets in semiconducting polymer films for edge emission. This means that second-order structures are often preferred, although surface output coupling does act as an additional loss mechanism in the laser cavity. First-order DFB lasers will have a lower threshold than those with second-order feedback and do have potential for efficient waveguide coupling for lab-on-a-chip experiments [21], but their typically poor quality output beam is less desirable for free-space emission.

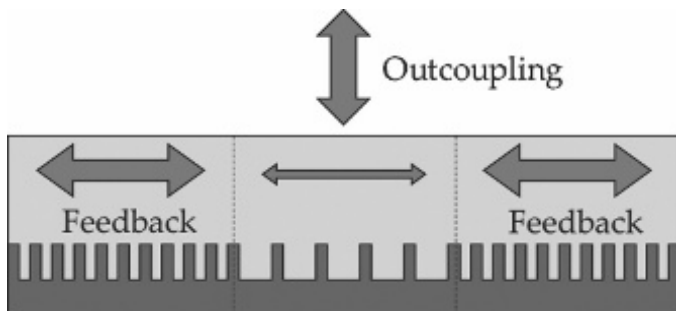


**Figure 7.12** Mixed-order grating indicating first-order regions used for high feedback and a central second-order region for outcoupling.

Consequently, many of the methods developed for reducing second-order lasing thresholds center around the concept making them more first-order-like to reduce output coupling loss and maximize (the relative strength of) optical feedback.

### 7.6.1 Mixed-Order Gratings

The first example of a threshold reduction technique has already been seen in Figs. 7.10 and 7.11a and illustrated in Fig. 7.12. The feedback in a DFB laser is distributed over an area, and as such, the waveguide can be split up into separate regions of first-order and second-order gratings to reduce the length of the lossy second-order section, providing they are tuned to the same feedback wavelength. In such a “mixed-order” structure, the first-order locations act as primary feedback regions (with only intrinsic waveguide losses), while the (central) second-order region out-couples light into free space [38].

As demonstrated by Wang et al., the use of mixed-order structures can reduce lasing thresholds by more than a factor of 2 compared with a similar second-order DFB cavity [39]. Figure 7.13a shows a mixed-order DFB laser (red) with a threshold of  $52 \text{ W/cm}^2$  compared to a reference second-order laser with a threshold of  $126 \text{ W/cm}^2$ . Figure 7.13b,c shows the output spectra just above and below lasing threshold for a second order (Fig. 7.13b) and a mixed order (Fig. 7.13c). Due to the reduction in

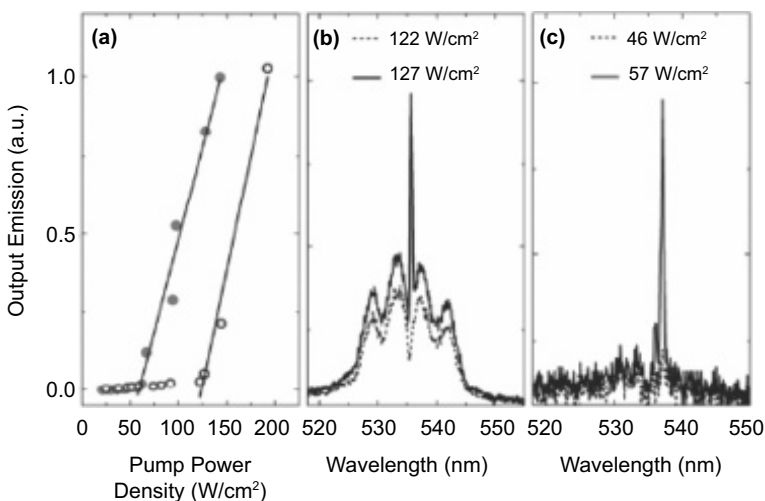


**Figure 7.13** (a) Output intensity as a function of pump power for NIL second-order DFB (open circles) and mixed-order DFB (closed circles); surface emission spectra below (dashed line) and above (solid line) the lasing threshold for (b) second-order and (c) mixed-order DFB. The lasing wavelengths are 536 and 537 nm, respectively. Reprinted from Ref. [39] with permission from Optical Society of America.

the second-order outcoupling, the mixed-order cavity scatters less photoluminescence out of the film below lasing threshold.

### 7.6.2 Controlling Fourier Coefficients

A key parameter that controls the radiative and feedback coupling in second-order DFB lasers is the shape of the unit cell of the grating. This can be described mathematically by the grating's first- and second-order Fourier coefficients  $\xi_{1,2}(x)$ , as seen in Eqs. 7.20 and 7.21. For top-hat gratings, these coefficients are constant in the  $x$  direction ( $\xi_m(x) \rightarrow \xi_m$ ) and so are independent from the integrals for the coupling coefficient relations. The Fourier coefficients are given by the following relation:

$$\xi_m = \frac{\sin\left(\frac{\pi m w}{\Lambda}\right)}{m\pi} \quad (7.27)$$

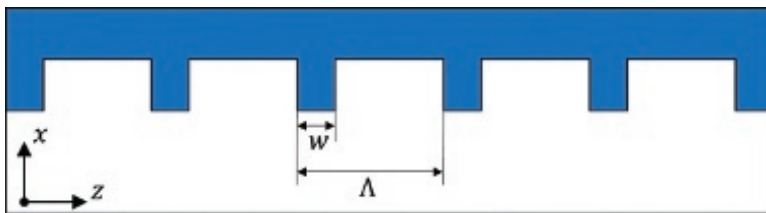


**Figure 7.14** Schematic of a DFB waveguide with indicated period and grating width.

The ratio  $w/\Lambda$  of the grating ridge width  $w$  to the grating period  $\Lambda$  is known as the grating fill factor, as shown in Fig. 7.14.

By tuning this fill factor, the Fourier coefficients can be altered and in turn control the relative size of the radiative and feedback coefficients. Figure 7.15 shows a graph of the normalized first and second Fourier coefficients plotted as a function of the fill factor.

Studying Fig. 7.15a, it can be seen that the second-order Fourier coefficient, primarily responsible for the feedback in the system, is zero for a 50% fill factor, making it a poor choice for achieving low-threshold lasing. Figure 7.15b shows the calculated threshold gain plotted against duty cycle (fill factor), alongside experimentally measured DFB lasing thresholds by Turnbull et al. [40]. This data confirms that a 50% fill factor gives the highest lasing threshold and

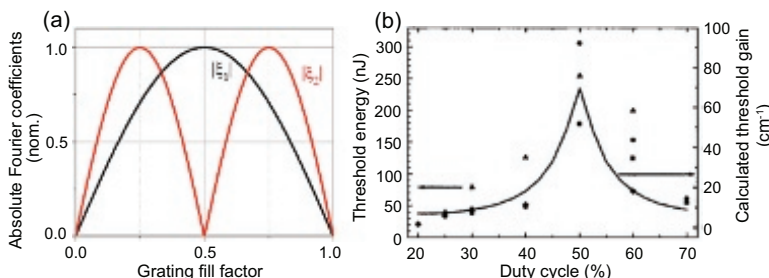


**Figure 7.15** (a) Absolute normalized value of the first (black) and second (red) Fourier coefficients for a square grating as a function of fill factor. (b) Experimentally measured threshold energy (points) and calculated threshold gain (line) as a function of the grating duty cycle. The triangles, circles, diamonds, and squares represent the data for different polymer films. Reprinted from Ref. [40] with the permission of AIP Publishing.

is reduced as the second-order coefficient (feedback) increases and the first-order coefficient (radiative) decreases.

### 7.6.3 Sub-structured Gratings

This concept of controlling the grating Fourier coefficients to fabricate ultralow threshold lasers can be further exploited by designing more complicated sub-structured gratings, as first developed by Martins et al. [41]. The rationale behind the sub-structured grating design starts from the definition of a DFB grating figure of merit as the ratio ( $\xi_2/\xi_1$ ) of the Fourier coefficients for in-plane feedback and surface output coupling. This quantity is maximized when the relative strength of feedback is highest compared to radiative coupling. In a standard second-order DFB, this ratio has a maximum possible value of unity as the fill factor approaches 0 or 1. However, in a first-order DFB device, this value tends to infinity as the radiative Fourier coefficient is zero. [Figure 7.16](#) shows a strategy by which this ratio can be tuned between these two extremes to create

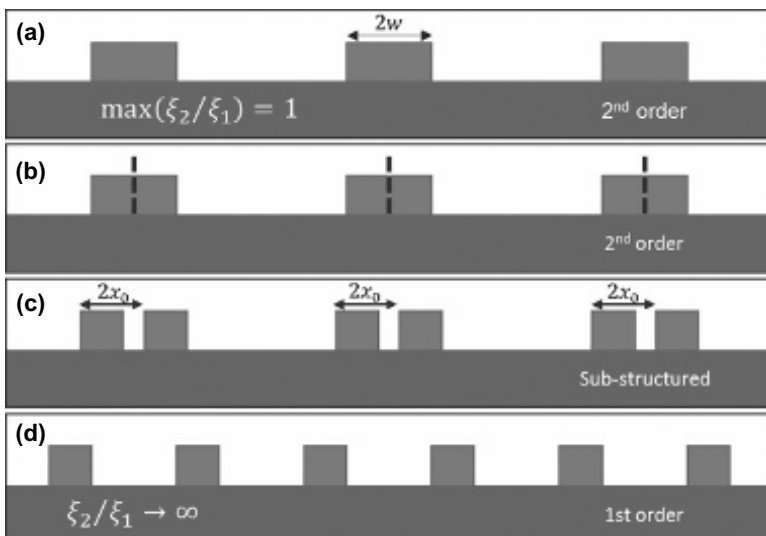


**Figure 7.16** Diagrams depicting the separation of second-order ridges (a, b), to create a sub-structured grating (c) and eventual first-order grating (d).

surface-emitting lasers with managed output loss and, therefore, low threshold.

Starting from a standard second-order design in Fig. 7.16a, each ridge in the grating can be divided into two adjacent ridges of width  $w$  (Fig. 7.16b). By displacing one ridge by a distance  $2x_0$ , the Fourier coefficients are modified from Eq. 7.27 to become

$$\xi_m = 2 \frac{\sin\left(\frac{\pi mw}{\Lambda}\right)}{m\pi} \cos\left(\frac{2\pi mx_0}{\Lambda}\right) \quad (7.28)$$

The additional independent parameter  $x_0$  allows the second-order Fourier coefficient to be increased while decreasing the first-order coefficient. If displaced by a distance of  $\Lambda/2$ , the grating becomes a first-order DFB resonator and the radiative coupling drops to zero. Sub-structured gratings, therefore, allow second-order DFB lasers to have an increased first-order DFB character, reducing the lasing threshold while retaining surface emission.

Figure 7.17 shows the lasing threshold measured for three different organic DFB devices, a reference second-order device with a Fourier ratio of 0.7, and two sub-structured devices with ratios

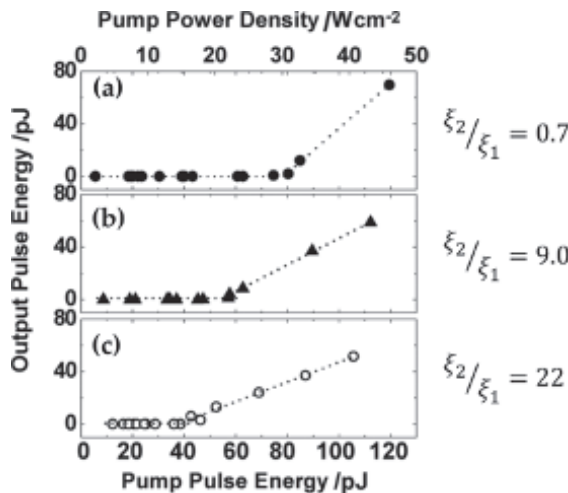


**Figure 7.17** Input/output laser threshold graphs for (a) a reference second-order grating and (b, c) two different sub-structured gratings with indicated Fourier coefficient ratios. Reprinted from Ref. [41], with permission from John Wiley & Sons.

of 9 and 22. As is evident, the higher ratio devices have reduced threshold compared to the reference DFB laser. Sub-structured DFB lasers have exhibited among the lowest recorded power density thresholds for organic lasers.

## 7.7 LED-Pumped Organic DFB Lasers

The low lasing thresholds of DFB lasers have made it possible for them to achieve laser action under LED pumping—the only organic laser design for which this has been reported to date [17, 19]. As well as the use of low-threshold DFB cavities, this achievement has required the development of high-gain conjugated polymer materials [42] and advances in high-power nitride LEDs.

Figure 7.18 shows a photograph of a BBEHP-PPV DFB laser under LED pumping. The green laser beam is typical of the emission from a 1D second-order DFB resonator and is superimposed on a background of the residual transmitted blue pump light. As can be seen, the blue LED is directly butt-coupled to the surface of

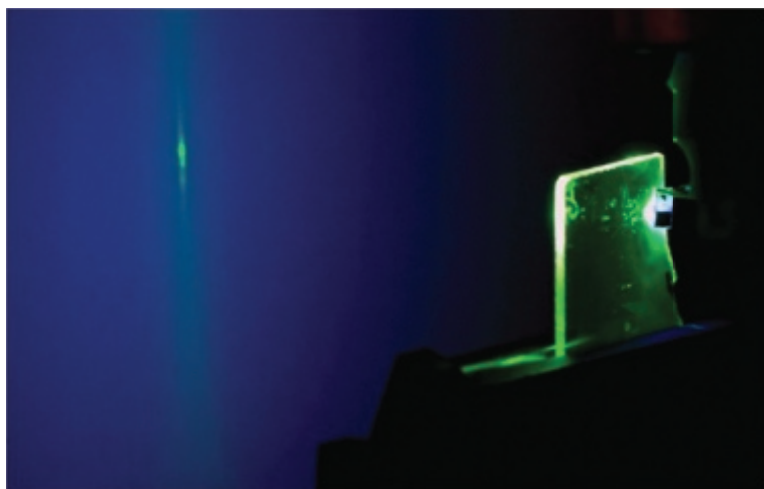


**Figure 7.18** Photograph of a holographically produced LED-pumped BBEHP-PPV second-order DFB laser. Reprinted from Ref. [18] with permission of John Wiley and Sons.

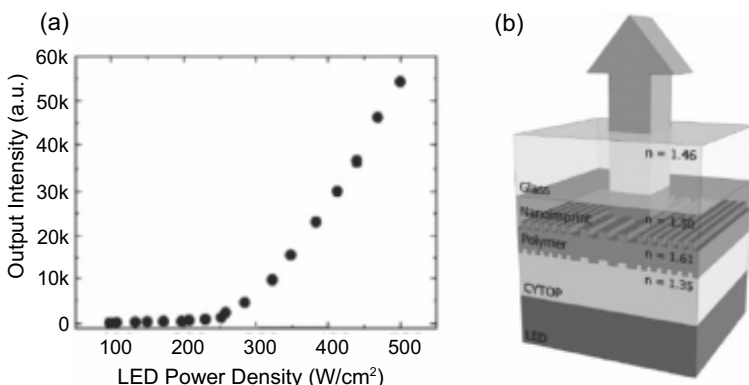


**Figure 7.19** (a) Laser intensity output as a function of LED output power density for an LED-pumped OSL. (b) Device structure of the measured LED/OSL hybrid. Reprinted from Ref. [39] with permission from Optical Society of America.

the organic film to achieve maximum light intensity on the laser resonator. The divergent and incoherent nature of the LED makes it difficult to implement intermediate optics to intensify the pump power density without introducing optical losses.

Figure 7.19 shows the power characteristics of an LED-pumped polymer laser based on a mixed-order DFB grating; the same device used under laser excitation in Fig. 7.13a. A notable difference between the power characteristics in these two figures is the substantial increase in lasing threshold (by a factor of  $\sim 5$ ) under LED excitation. This effect has been explored by Wang et al., identifying that the rise time of the pump source has a significant effect on the laser threshold [18]. In Fig. 7.13, the mixed-order laser is pumped by the 450 nm output from an optical parametric oscillator with 4 ns pulsewidth (FWHM). The LED, however, has an FWHM pulse duration of 20–45 ns with at least 5 ns of rise time. Longer rise times allow for the accumulation of triplet exciton states prior to laser turn-on, increasing the level of loss that must be overcome to exceed threshold. Herrnsdorf et al. further developed this by using micro-LED arrays in a stripe configuration [43]. The integration with micro-LEDs allows for the pixilation of organic OSLs with future potential for hybrid integration on CMOS chips.

This could create arrays of tuneable hybrid laser diodes with easy integration to modern electronics.

## 7.8 Conclusion

DFB structures have proven to be a very successful resonator design for organic semiconductor lasers. They combine properties of low threshold and excellent spectral control to select specific wavelength operation within the broad tuning spectrum of organic gain materials. While the laser cavities necessarily use sub-wavelength structures to provide feedback, these can readily be fabricated using a range of simple and scalable soft-lithographic processes. By using second-order DFB gratings, it is possible to generate low-divergence good-quality laser beams emitted from the surface of the organic film. Through careful design of the grating period, depth, and the shape of the unit cell, it is possible to control the laser wavelength, threshold, slope efficiency, and beam profile.

Organic DFB lasers have been used to achieve indirect electrical excitation, through integration with nitride LEDs. They have been used in recent applications of organic lasers for spectroscopy and chemical sensing and have been integrated into lab-on-a-chip systems. It is likely that they will continue to be a favored design in the future applications of organic lasers, and with ongoing advances in nanoimprint lithography, the organic DFB laser has great potential for inexpensive mass production.

## References

1. H. Kogelnik and C. V. Shank. (1972). Coupled-wave theory of distributed feedback lasers. *J. Appl. Phys.* **43**, pp. 2327–2335.
2. C. Grivas and M. Pollnau. (2012). Organic solid-state integrated amplifiers and lasers. *Laser Photonics Rev.* **6**, pp. 419–462.
3. V. G. Kozlov and S. R. Forrest. (1999). Lasing action in organic semiconductor thin films. *Curr. Opin. Solid State Mater. Sci.* **4**, pp. 203–208.

4. G. Kranzelbinder and G. Leising. (2000). Organic solid-state lasers. *Rep. Prog. Phys.* **63**, pp. 729.
5. S. Chénais and S. Forget. (2012). Recent advances in solid-state organic lasers. *Polym. Int.* **61**, pp. 390–406.
6. I. D. W. Samuel and G. A. Turnbull. (2007). Organic semiconductor lasers. *Chem. Rev.* **107**, pp. 1272–1295.
7. M. D. McGehee and A. J. Heeger. (2000). Semiconducting (conjugated) polymers as materials for solid-state lasers. *Adv. Mater.* **12**, pp. 1655–1668.
8. H. Kogelnik and C. V. Shank. (1971). Stimulated emission in a periodic structure. *Appl. Phys. Lett.* **18**, pp. 152–154.
9. V. G. Kozlov, G. Parthasarathy, P. E. Burrows, V. B. Khalfin, J. Wang, S. Y. Chou, and S. R. Forrest. (2000). Structures for organic diode lasers and optical properties of organic semiconductors under intense optical and electrical excitations. *Quantum Electron. IEEEJ.* **36**, pp. 18–26.
10. G. A. Turnbull, T. F. Krauss, W. L. Barnes, and I. D. W. Samuel. (2001). Tuneable distributed feedback lasing in MEH-PPV films. *Synth. Met.* **121**, pp. 1757–1758.
11. G. Heliotis, R. Xia, D. D. C. Bradley, G. A. Turnbull, I. D. W. Samuel, P. Andrew, and W. L. Barnes. (2003). Blue, surface-emitting, distributed feedback polyfluorene lasers. *Appl. Phys. Lett.* **83**, pp. 2118–2120.
12. M. Berggren, A. Dodabalapur, R. E. Slusher, A. Timko, and O. Nalamasu. (1998). Organic solid-state lasers with imprinted gratings on plastic substrates. *Appl. Phys. Lett.* **72**, pp. 410–411.
13. S. Riechel, U. Lemmer, J. Feldmann, S. Berleb, A. G. Mückl, W. Brüttling, A. Gombert, and V. Wittwer. (2001). Very compact tunable solid-state laser utilizing a thin-film organic semiconductor. *Opt. Lett.* **26**, pp. 593–595.
14. G. A. Turnbull, P. Andrew, W. L. Barnes, and I. D. W. Samuel. (2003). Operating characteristics of a semiconducting polymer laser pumped by a microchip laser. *Appl. Phys. Lett.* **82**, pp. 313–315.
15. A. E. Vasdekis, G. Tsiminis, J.-C. Ribierre, L. O' Faolain, T. F. Krauss, G. A. Turnbull, and I. D. W. Samuel. (2006). Diode pumped distributed Bragg reflector lasers based on a dye-to-polymer energy transfer blend. *Opt. Express.* **14**, pp. 9211–9216.
16. T. Riedl, T. Rabe, H. H. Johannes, W. Kowalsky, J. Wang, Weimann, H. P. B. Nehls, T. Farrell, and U. Scherj. (2006). Tunable organic thin-film laser pumped by an inorganic violet diode laser. *Appl. Phys. Lett.* **88**, pp. 241116.

17. Y. Yang, G. A. Turnbull, and I. D. W. Samuel. (2008). Hybrid optoelectronics: A polymer laser pumped by a nitride light-emitting diode. *Appl. Phys. Lett.* **92**, pp. 163306.
18. Y. Wang, P. O. Morawska, A. L. Kanibolotsky, P. J. Skabara, G. A. Turnbull, and I. D. W. Samuel. (2013). LED pumped polymer laser sensor for explosives. *Laser Photon. Rev.* **76**, pp. 71–76.
19. G. Tsiminis, Y. Wang, A. L. Kanibolotsky, A. R. Inigo, P. J. Skabara, I. D. W. Samuel, and G. A. Turnbull. (2013). Nanoimprinted organic semiconductor laser pumped by a light-emitting diode. *Adv. Mater.* **25**, pp. 2826–2830.
20. C. Vannahme, S. Klinkhammer, U. Lemmer, and T. Mappes. (2011). Plastic lab-on-a-chip for fluorescence excitation with integrated organic semiconductor lasers. *Opt. Express.* **19**, pp. 8179–8186.
21. X. Liu, S. Prinz, H. Besser, W. Pfleging, M. Wissmann, C. Vannahme, M. Guttmann, T. Mappes, S. Koeber, C. Koos, and U. Lemmer. (2014). Organic semiconductor distributed feedback laser pixels for lab-on-a-chip applications fabricated by laser-assisted replication. *Faraday Discuss.* **174**, pp. 153–164.
22. T. Woggon, S. Klinkhammer, and U. Lemmer. (2010). Compact spectroscopy system based on tunable organic semiconductor lasers. *Appl. Phys. B Lasers Opt.* **99**, pp. 47–51.
23. D. Tyler McQuade, A. E. Pullen, and T. M. Swager. (2000). Conjugated polymer-based chemical sensors. *Chem. Rev.* **100**, pp. 2537–2574.
24. G. R. Fowles. (1975). *Introduction to Modern Optics*, Second Edition (Holt, Rinehart and Winston, Inc., New York).
25. R. F. Kazarinov and C. H. Henry. (1985). Second-order distributed feedback lasers with mode selection provided by first-order radiation losses. *IEEE J. Quantum Electron.* **21**, pp. 144–150.
26. G. F. Barlow and K. A. Shore. (2001). Application of the argument principle method to the calculation of DFB laser diode modes. *Int. J. Numer. Model. Electron. Networks, Devices Fields.* **14**, pp. 291–302.
27. D. Park and M. Kim. (1996). Mode analysis of DFB SE lasers. *IEEE J. Quantum Electron.* **32**, pp. 1432–1440.
28. G. F. Barlow, K. A. Shore, G. A. Turnbull, and I. D. W. Samuel. (2004). Design and analysis of a low-threshold polymer circular-grating distributed-feedback laser. *J. Opt. Soc. Am. B* **21**, pp. 2142–2150.
29. G. Tsiminis. (2009). One- and two-photon pumped organic semiconductor lasers. University of St Andrews, PhD thesis.

30. M. G. Ramírez, J. A. Quintana, J. M. Villalvilla, P. G. Boj, A. Retolaza, S. Merino, and M. A. Díaz-García. (2013). Perylenediimide-based distributed feedback lasers with holographic relief gratings on dichromated gelatine. *J. Appl. Phys.* **114**, doi:10.1063/1.4813873.
31. B. H. Wallukewitz, G. O. Nikiforov, H. Sirringhaus, and R. H. Friend. (2012). A nanoimprinted, optically tuneable organic laser. *Appl. Phys. Lett.* **100**, doi:10.1063/1.4705303.
32. C. Kallinger, M. Hilmer, A. Haugeneder, M. Perner, W. Spirk, U. Lemmer, J. Feldmann, U. Scherf, K. Müllen, A. Gombert, and V. Wittwer. (1998). Flexible conjugated polymer laser. *Adv. Mater.* **10**, pp. 920–923.
33. G. L. Whitworth. (2016). Nanoengineered solution processed solid-state semiconductor lasers. University of St Andrews, PhD thesis.
34. J. R. Lawrence, G. A. Turnbull, and I. D. W. Samuel. (2003). Polymer laser fabricated by a simple micromolding process. *Appl. Phys. Lett.* **82**, pp. 4023–4025.
35. A. E. Vasdekis, M. J. Wilkins, J. W. Grate, R. T. Kelly, A. E. Konopka, S. S. Xantheas, and T.-M. Chang. (2014). Solvent immersion imprint lithography. *Lab Chip.* **14**, pp. 2072–2080.
36. G. L. Whitworth, S. Zhang, J. R. Y. Stevenson, B. Ebenhoch, I. D. W. Samuel, and G. A. Turnbull. (2015). Solvent immersion nanoimprint lithography of fluorescent conjugated polymers. *Appl. Phys. Lett.* **107**, pp. 163301.
37. M. G. Ramirez, P. G. Boj, V. Navarro-Fuster, I. Vragovic, J. M. Villalvilla, I. Alonso, V. Trabadelo, S. Merino, and M. A. Díaz-García. (2011). Efficient organic distributed feedback lasers with imprinted active films. *Opt. Express.* **19**, pp. 22443.
38. C. Karnutsch, C. Pflumm, G. Heliotis, J. C. DeMello, D. D. C. Bradley, J. Wang, T. Weimann, V. Haug, C. Gärtner, and U. Lemmer. (2007). Improved organic semiconductor lasers based on a mixed-order distributed feedback resonator design. *Appl. Phys. Lett.* **90**, doi:10.1063/1.2717518.
39. Y. Wang, G. Tsiminis, A. L. Kanibolotsky, P. J. Skabar, I. D. W. Samuel, and G. A. Turnbull. (2013). Nanoimprinted polymer lasers with threshold below  $100 \text{ W/cm}^2$  using mixed-order distributed feedback resonators. *Opt. Express.* **21**, pp. 14362–14367.
40. G. A. Turnbull, A. Carleton, G. F. Barlow, A. Tahraoui, T. F. Krauss, K. A. Shore, and I. D. W. Samuel. (2005). Influence of grating characteristics on the operation of circular-grating distributed-feedback polymer lasers. *J. Appl. Phys.* **98**, doi:10.1063/1.1935131.
41. E. R. Martins, Y. Wang, A. L. Kanibolotsky, P. J. Skabar, G. A. Turnbull, and I. D. W. Samuel. (2013). Low-threshold nanoimprinted lasers using

- substructured gratings for control of distributed feedback. *Adv. Opt. Mater.* **1**, pp. 563–566.
42. G. Tsiminis, Y. Wang, A. L. Kanibolotsky, A. R. Inigo, P. J. Skabara, I. D. W. Samuel, and G. A. Turnbull. (2013). Nanoimprinted organic semiconductor laser pumped by a light-emitting diode. *Adv. Mater.* **25**, pp. 2826–2830.
43. J. Herrnsdorf, Y. Wang, J. J. D. Mckendry, Z. Gong, D. Massoubre, B. Guilhabert, G. Tsiminis, G. A. Turnbull, I. D. W. Samuel, N. Laurand, E. Gu, and M. D. Dawson. (2014). Micro-LED pumped polymer laser: A discussion of future pump sources for organic lasers. *Laser Photon. Rev.* **1078**, pp. 1065–1078.

# Index

- active layer 24, 44, 45, 52, 128, 162, 213–215, 229, 259, 263, 265, 266  
active material 11, 24, 25, 35, 36, 48, 87, 122, 155, 162, 164, 219, 267  
active medium 249, 254, 264  
active molecule 37, 53, 62, 165, 222  
active waveguide 36, 41, 53  
amplified spontaneous emission (ASE) 9, 23, 24, 34–40, 44–46, 48, 50, 54–58, 60, 62–64, 66, 70–72, 74–76, 105, 106, 110, 111, 155  
angle 13, 14, 25, 28, 166, 179, 208, 209, 223, 273, 295–297  
acceptance 14  
azimuthal 296  
critical 26, 27, 29  
refraction 26  
visual 219  
zero 208  
anthracene 101, 105, 111  
antinode 214, 216, 222  
ASE *see* amplified spontaneous emission  
ASE intensity 9, 14, 17, 24, 55–57  
ASE peak wavelength 46, 51, 52, 58  
ASE threshold 9, 15, 16, 24, 35–39, 41, 43, 45, 46, 48–53, 57–59, 61, 64–66, 71–74, 76, 96, 106  
ASE wavelength 47, 51, 52  
beam 246, 252, 253, 269, 273, 299  
diffraction-limited 247, 252, 279  
high-brightness laser 262, 270  
BEC *see* Bose-Einstein condensation  
blend 14, 37, 63, 69–76, 108, 118, 127, 160, 268  
Bloch wave resonance 298  
BODIPY *see* BOron DIPYrrhomethene  
Boltzmann's constant 231  
BOron DIPYrrhomethene (BODIPY) 89–91, 93, 94, 97, 98, 126  
Bose-Einstein condensation (BEC) 194, 231–238  
 $\beta$ -phase content 36, 38–44  
Bragg condition 287, 288, 290, 296  
Bragg frequency 293  
Bragg mirrors 103  
Bragg reflectors 105  
Bragg wavelength 246, 265  
Brewster angle 267, 277  
Brownian motion 152  
  
cesium atoms 215  
cavity 152, 179, 180, 194–214, 216, 218, 220–226, 228–230, 232, 236–238, 247–249, 254, 255, 259–261, 264–266, 272, 273, 276, 277  
bare 210

- high-finesse 211  
low-threshold DFB 310  
resonant 9, 35, 228  
second-order DFB 305  
triple-coupled 218  
cavity length 200, 247, 248, 250, 254, 255, 257, 258, 260, 267, 269, 276, 292, 295  
cavity mirrors 214, 266, 271  
cavity modes 200–203, 247, 252, 261  
cavity resonator 197, 201, 230  
chromophores 87, 90, 94, 97, 99, 105, 110, 269  
compounds 2, 3, 6, 9, 85, 94, 101, 105, 106, 111, 122, 126, 127, 160, 228  
benzene-cored 114  
carbon-rich 159  
first-generation 110  
fluorescent 215  
hybrid 85, 122–126, 128  
inorganic 233  
mature 88, 126  
molecular 203  
non-oligomeric 127  
organic 2, 4, 6–9, 23, 87, 88, 120, 122, 158, 162, 175, 224, 228  
pyrene-core 115  
single-crystal 102  
spiro 109–111  
synthetic 99  
conjugated polymers 2–4, 88, 108, 111, 115–121, 126–129, 159, 232, 247  
organic 1, 156  
copolymers 37, 116, 118, 121, 127  
coumarins 89, 91, 93, 267, 268, 275  
coupled mode equations 289–291  
coupled systems 193, 207, 210, 223  
coupling 11, 15, 18, 19, 173, 193, 195–198, 203, 213, 214, 222–226, 228, 254, 304  
DBR *see* distributed Bragg reflector  
de Broglie wavelength 231, 232  
decay 33, 202, 203, 221, 256  
exponential 34  
non-radiative 8  
pump laser intensity 54  
defects 37, 162, 199  
detuning 203, 212, 213, 227, 290  
negative 209, 233, 293  
positive 209  
zero 208, 224  
devices 122, 128, 158, 162, 175–177, 180, 194, 195, 212–214, 216–218, 220, 223, 226, 227, 237–239, 263–265, 295, 296  
biocompatible 175  
double-cavity 215, 218  
electronic 175  
flexible 117, 124  
integrated 123, 163  
microcavity 247  
multicavity 214  
optical 180  
paper-based 176  
planar 162  
random-laser 180  
self-oscillating 290  
triple-cavity 215, 219  
weak-coupled 222  
DFB *see* distributed feedback  
DFB grating 287, 296, 299, 308  
mixed-order 311  
second-order 304, 312  
DFB lasers 91, 95, 100, 108, 120, 246, 253, 285–287, 290, 292, 293, 295, 300, 302, 304, 305, 310  
edge-emitting organic 286

- first-generation 286
- mixed-order 305
- organic 285, 294, 296, 298, 312
- organic semiconductor 265, 285, 303
- solid-state organic 265
- surface-emitting 304
- DFB resonators 59, 253, 288, 298, 306, 309, 310
- distributed Bragg reflector (DBR) 2, 198, 199, 212, 222, 233, 237
- distributed feedback (DFB) 2, 58, 59, 164, 246, 285–288, 290–292, 294, 296, 298, 300, 302, 304, 306, 308, 310
- dye lasers 88, 97, 265, 271
  - solid-state 129, 276
- dyes 85, 88, 89, 97, 98, 100, 108, 125, 126, 128, 170, 249, 260, 270, 276
  - blue 125
  - blue-emitting 98
  - fluorescent 176
  - nitrobenzoxadiazolyl 98
  - squaraine 226
  - synthetic 98, 100
  
- eGFP *see* enhanced green fluorescent protein
- electroluminescence 103, 194, 212, 222, 223, 228
  - organic polariton 220
  - strong-coupling 211
- electron-transporting layer (ETL) 211, 212
- emissions 7, 9, 93, 96, 99, 102, 121, 122, 124, 170, 172, 201–203, 212, 213, 226–228, 247, 296–298
  - coherent 195
  - deep-UV 275
  
- free-space 304
- incoherent 228
- magnetic-polarized 235
- photoluminescence 222, 225
- scattered 296
- emission spectrum 2, 9–11, 38, 50, 108, 153, 155, 157, 166, 170–172, 180, 219, 234, 246, 280
- emission wavelength 58, 90, 93, 116, 118, 251, 264
- enhanced green fluorescent protein (eGFP) 99, 100
- EQE *see* external quantum efficiency
- ETL *see* electron-transporting layer
- excited state 3–5, 7, 12, 106, 107, 196, 197, 204, 205, 228, 229
- exciton density 57, 230, 238, 295
- excitons 4, 5, 194, 196, 197, 206, 208, 209, 211, 212, 220–222, 226, 227, 231
- external cavity 164, 247, 248, 255, 269, 272
- external quantum efficiency (EQE) 227, 229, 230
  
- FET *see* transistor, field-effect
- film 23, 25–30, 32–38, 41, 43, 44, 47–50, 57, 59–63, 71–73, 75, 76, 110, 111, 249, 279, 298–300, 302–304
  - active 23, 25, 44, 45, 47, 52–54, 57, 59, 60, 62, 78, 246
- disordered 233
- free-standing 267
- metallic 198
- organic 23, 24, 28, 29, 46, 158, 278, 311, 312
- photo-polymerizable 299
- polymer 113, 159, 160, 268, 303, 304, 307

- thin 38, 60, 61, 78, 96, 106, 110, 115, 117, 119, 124, 126, 159, 163, 247, 250  
vacuum-evaporated 106  
fluctuations 71, 155, 170, 172, 173  
random 50  
shot-to-shot 170  
fluorescence 6, 17, 18, 88, 105, 201, 275  
fluorescent protein (FP) 99, 100, 126, 203  
Fock states 203, 204  
Förster radius 42  
Förster resonance energy transfer (FRET) 37, 63, 69, 70, 72–74, 76, 108  
Fourier coefficients 306, 307, 309  
Fourier series 288, 289  
FP *see* fluorescent protein  
free spectral range (FSR) 200, 258, 259, 267, 272, 279  
Frenkel excitons 4, 5  
Fresnel diffraction effect 15  
FRET *see* Förster resonance energy transfer  
FSR *see* free spectral range  
full-width half maximum (FWHM) 9, 10, 16, 41, 66, 200, 201, 268, 274, 294, 295, 311  
FWHM *see* full-width half maximum  
  
gain coefficient 9, 13, 14, 18, 19, 39, 41  
gain material 2, 123, 156, 249  
    organic 279, 312  
gain medium 128, 152, 161, 176, 266, 267, 269, 286, 296  
gain properties 9, 37  
    intrinsic 36, 38  
    optical 19, 36, 114, 116  
Gaussian profile 14, 15  
grating 58, 246, 265, 271, 275, 287, 291, 294, 295, 297, 299, 300, 303, 304, 306, 307, 309  
guided modes 19, 28–31, 34, 44, 45, 49, 51–53  
  
highest occupied molecular orbital (HOMO) 3, 4, 94, 95, 114, 115  
hole 4, 102, 105, 129, 164, 212, 221, 226  
hole mobility 111, 120, 121, 124  
hole-transporting layer (HTL) 211, 212  
HOMO *see* highest occupied molecular orbital  
homopolymer 116, 121, 127  
Hopfield coefficient 208, 209  
HTL *see* hole-transporting layer  
human tissue 152, 157, 175  
  
intramolecular charge transfer 93  
  
J-aggregates 106, 221  
  
lab-on-a-chip system 312  
laser 24, 35, 36, 86, 90, 91, 113, 115, 116, 122, 123, 152, 153, 230, 232, 234, 245–250, 254, 264–267, 297  
argon ion 86  
blue polyfluorene 275  
external-cavity 255  
femtosecond 255  
fiber 272  
four-level 107  
long-pulse 257  
microchip 286  
mirrorless optofluidic 180  
mixed-order 311  
neodymium 86

- nitrogen 86  
 organic microcavity 161  
 organic semiconductor 161,  
     246, 312  
 red 278, 280  
 ring-shaped 170  
 semiconductor diode 86  
 solid-state microchip 253  
 surface-emitting 309  
 thin-film 247, 271  
 laser action 174, 262, 293, 295,  
     310  
 laser beam 252, 254, 273, 276  
 laser cavity 45, 101, 153, 162, 258,  
     292, 304, 312  
 laser device 2, 101, 117, 151, 160,  
     194, 246  
 laser dye 89, 125, 157, 160, 177,  
     249  
 laser emission 93, 99, 100, 105,  
     106, 108–110, 115, 118, 126,  
     180, 248–250, 256, 258, 259,  
     297  
     bichromatic 97  
     blue 93, 125  
     photostable 97  
     polariton 105  
     random 179  
     red 105, 278  
 laser energy 253, 260, 261  
 laser materials 86, 87, 94, 97, 113,  
     121, 124  
     organic 88, 98, 126, 128  
 laser modes 156, 248, 249, 292,  
     293, 297, 304  
 laser pulse 20, 50, 251, 254–256,  
     264, 271, 273, 274  
 laser threshold 87, 100, 108, 121,  
     129, 156, 246, 260, 279, 285,  
     296, 297, 311  
 LED *see* light-emitting diode  
 light-emitting diode (LED) 36,  
     156, 194, 195, 246, 285, 286  
     lower polariton (LP) 207, 208,  
         210, 220, 221, 223, 225, 227,  
         232, 235  
     lower polariton branch 220, 221,  
         232, 235  
     lowest unoccupied molecular  
         orbital (LUMO) 3, 4, 94, 95,  
         114, 115  
     LP *see* lower polariton  
     LUMO *see* lowest unoccupied  
         molecular orbital  
  
     microcavity 157, 161, 194,  
         198–201, 205, 213, 214, 222,  
         224, 225, 236, 237, 245, 276  
     molecular crystal 88, 100–102,  
         105, 106, 108, 111, 126, 127,  
         129  
     molecular glass 88, 108–111, 113,  
         114, 118, 126–128  
  
     Occam's razor principle 73  
     OLED *see* organic light-emitting  
         diode  
     oligofluorenes 108–111, 113,  
         127  
     oligomers 1, 19, 88, 111, 113,  
         160  
     OPO *see* optical parametric  
         oscillator  
     optical cavity 152, 155, 175, 180,  
         198, 200, 202, 212, 238  
     optical feedback 231, 285, 286,  
         305  
     optical gain 2, 9–11, 14–16, 18, 19,  
         24, 35, 36, 45, 58, 62, 69, 70,  
         72, 103, 122, 152, 153, 180  
     optical parametric oscillator (OPO)  
         264, 265, 311  
     optical pumping 35, 50, 156, 220,  
         221, 228, 232, 237, 239, 297

- organic light-emitting diode
  - (OLED) 2, 158, 211–213, 215, 217–221, 223, 225, 227–229, 252
- organic semiconductor laser diode 2
- organic semiconductors 85, 88, 122, 126, 128, 129, 156, 159, 160, 224, 229, 245, 258, 302, 303
- organic solid-state laser (OSSL) 246, 253, 259, 265, 269, 272
- organic vertical cavity surface-emitting laser (OVCSEL) 245, 254, 256, 257, 260, 263, 272
- oscillators 195–198, 201
  - mechanical 196
- OSSL *see* organic solid-state laser
- OVCSEL *see* organic vertical cavity surface-emitting laser
- photodegradation 20, 35, 57, 87, 124, 260, 278
- photoluminescence 35, 220, 221, 294, 306
- photon 5, 16, 42, 85, 152, 194, 202, 203, 205–209, 211, 221, 228, 233, 254, 275
  - coherent 228, 231, 237
  - high-energy 275
  - incoherent 194, 220
  - microcavity 204
  - pump laser 56
  - virtual bound 224
- photonic mode density (PMD) 201, 202
- PMD *see* photonic mode density
- PMO *see* pump-mode overlap
- polariton laser 105, 231, 233, 237
- polaritons 193, 195, 208, 211, 220–222, 227, 231–234, 238
- polymer optical fiber 63
- polymers 19, 50, 60, 62, 70, 72, 73, 76, 89, 98, 111, 117, 122, 127, 160, 233
  - blue-emitting 117
  - high molecular weight 303
  - organic 3, 73
- propagation 11, 26, 27, 53, 71, 152, 169, 288, 294
  - counter 287
  - free 154
  - partial 26
  - transversal 27
- pulse 111, 119, 124, 170, 173, 247, 255, 257, 260–262, 269, 270, 273, 274, 278
  - ultrashort 88, 256
- pulsewidth 42, 249, 251, 256, 258
- pump 8, 54, 107, 125, 247–249, 256, 258, 261, 277
- pump beam 234, 263, 267, 278, 295
- pump energy 166, 172, 173, 250, 261, 278, 279
- pump fluence 235, 236, 253, 294
- pump laser 37, 55, 57, 59, 61, 63, 156, 172, 250
- pump light 37, 108, 249, 270, 310
- pump-mode overlap (PMO) 53–55
- pump power 246, 250, 278, 298, 306
- pump spot 249, 253, 260, 270, 295
- pump wavelength 53, 55, 249, 277
- Purcell effect 193, 194, 201, 203, 213, 214, 216, 228
- quantum dots 156, 202
- quantum wells 204, 237
- quenching effects 76, 95, 108, 111, 113, 228
- Rabi energy 208, 223
- Rabi frequency 197, 206, 211

- Rabi splitting 210, 223–225, 233  
radiation 8, 9, 11, 86, 152, 154,  
  264  
  amplifying 9  
  free-space 297  
  fundamental 276  
  ultraviolet 279  
random laser 151–160, 162, 164,  
  168, 170, 173–176, 179–181,  
  246  
random-laser emission 157, 158,  
  164, 171, 172  
reactive-ion etching 103  
refractive index 23, 26, 28–30, 41,  
  44, 46, 51, 71, 75, 154, 157,  
  198, 203, 229, 246  
resonance 38, 39, 156, 202, 203,  
  213, 234  
resonators 58, 161, 197, 247, 249,  
  264, 265, 272, 276  
low-loss 265  
microdisk 261  
microring 161  
plano-concave 247  
ring 100  
rhodamines 91, 97, 176, 177  
rotating wave approximation  
  (RWA) 206, 207  
RWA *see* rotating wave  
approximation
- scattering 20, 71, 153–156, 162,  
  164, 179, 200, 221, 246, 287,  
  295  
Bragg 180  
Mie 156  
multiple 152, 153, 162  
optical 125  
phonon 221  
photon 176  
second-order 287  
single longitudinal mode (SLM)  
  259, 271
- SLM *see* single longitudinal mode  
Snell's law 25  
solvent immersion imprint  
  lithography 303  
solvent imprint lithography 302  
spectroscopy 88, 264, 269, 270,  
  276, 312  
atmospheric 276  
high-resolution 248, 271  
laser-induced fluorescence 276  
spectrum 9, 154, 155, 180, 213,  
  219, 246, 248, 259, 260, 264,  
  276, 278  
emissive 229  
fluorescence 18  
infrared 265  
optical mode 201  
random-laser 157  
thickness-independent 48  
visible 19, 87, 88, 90, 102, 228,  
  248, 249, 265, 266
- STD technique *see* technique,  
surface tension-driven
- technique 11, 18, 19, 61, 160, 163,  
  249, 299, 300, 303, 304  
advanced lithography 163  
advanced soft-lithographic 300  
crystal growth 102  
layer-by-layer 222  
lithographic 165  
phase-sensitive sensing 271  
soft-lithography 164, 175  
spin-coating 247  
surface tensiondriven (STD)  
  163, 165  
threshold reduction 305  
thermal effects 260, 262, 263  
transistors 175  
  field-effect (FET) 2, 36, 158  
  thin-film 158  
transitions 2, 5, 8, 53, 122, 123,  
  201, 205, 207

- coupled 234
- electronic 5, 204, 206, 214
- electro-vibronic 6
- excitonic 209, 210
- geometry-induced 179
- quantum phase 194
- radiative 152
- super-radiant phase 223
- vibrational 5
- virtual 207, 223
  
- variable stripe length (VSL) 11, 13, 18, 19
- VBG *see* volume Bragg grating
- VECSOL *see* vertical external-cavity surface-emitting organic laser
- vertical external-cavity surface-emitting organic laser (VECSOL) 247–250, 252–254, 256–265, 267, 269, 271, 273, 275–277, 279
  
- volume Bragg grating (VBG) 248, 260, 264, 271–273, 275
- VSL *see* variable stripe length
  
- wavefunction 4, 5, 231
- waveguide 10, 12, 14, 28, 29, 32, 44, 45, 49, 58, 71, 229, 286–289, 291, 295–297, 305
- asymmetric 29, 30
- organic semiconductor 298
- patterned 58
- periodic 288, 289
- plasmonic 156
- symmetric 28, 29
- thin-film 286
- waveguide gain 64
- waveguide loss 35, 39, 40, 42, 43, 71, 295, 305
- waveguide modes 33, 287, 295
- wavevector 27, 154, 200, 205, 286, 287, 296, 297